

Complexity

Fractional-Order and Memristive Nonlinear Systems: Advances and Applications

Lead Guest Editor: Ahmed G. Radwan

Guest Editors: Ahmad T. Azar, Sundarapandian Vaidyanathan,
Jesus M. Munoz-Pacheco, and Adel Ouannas





Fractional-Order and Memristive Nonlinear Systems: Advances and Applications

Complexity

Fractional-Order and Memristive Nonlinear Systems: Advances and Applications

Lead Guest Editor: Ahmed G. Radwan

Guest Editors: Ahmad T. Azar, Sundarapandian Vaidyanathan,
and Jesus M. Munoz-Pacheco



Copyright © 2017 Hindawi. All rights reserved.

This is a special issue published in "Complexity." All articles are open access articles distributed under the Creative Commons Attribution License, which permits unrestricted use, distribution, and reproduction in any medium, provided the original work is properly cited.

Editorial Board

José Ángel Acosta, Spain
Rodrigo Aldecoa, USA
Juan A. Almendral, Spain
David Arroyo, Spain
Arturo Buscarino, Italy
Guido Caldarelli, Italy
Danilo Comminiello, Italy
Manlio De Domenico, Spain
Pietro De Lellis, Italy
Albert Diaz-Guilera, Spain
Joshua Epstein, USA
Thierry Floquet, France

Mattia Frasca, Italy
Carlos Gershenson, Mexico
Peter Giesl, UK
Sergio Gómez, Spain
Sigurdur F. Hafstein, Iceland
Alfred Hubler, USA
Giacomo Innocenti, Italy
Jeffrey H. Johnson, UK
Vittorio Loreto, Italy
Didier Maquin, France
Eulalia Martínez, Spain
Ch. P. Monterola, Philippines

Roberto Natella, Italy
Daniela Paolotti, Italy
Luis M. Rocha, USA
Miguel Romance, Spain
Hiroki Sayama, USA
Michele Scarpiniti, Italy
Enzo Pasquale Scilingo, Italy
Samuel Stanton, USA
Roberto Tonelli, Italy
Shahadat Uddin, Australia
Gaetano Valenza, Italy
Dimitri Volchenkov, Germany

Contents

Fractional-Order and Memristive Nonlinear Systems: Advances and Applications

Ahmed G. Radwan, Ahmad Taher Azar, Sundarapandian Vaidyanathan, Jesus M. Munoz-Pacheco, and Adel Ouannas

Volume 2017, Article ID 3760121, 2 pages

Understanding the Resistive Switching Phenomena of Stacked Al/Al₂O₃/Al Thin Films from the Dynamics of Conductive Filaments

Joel Molina-Reyes and Luis Hernandez-Martinez

Volume 2017, Article ID 8263904, 10 pages

CMOS Realization of All-Positive Pinched Hysteresis Loops

B. J. Maundy, A. S. Elwakil, and C. Psychalinos

Volume 2017, Article ID 7863095, 15 pages

Application of Topological Degree Method for Solutions of Coupled Systems of Multipoints Boundary Value Problems of Fractional Order Hybrid Differential Equations

Muhammad Iqbal, Yongjin Li, Kamal Shah, and Rahmat Ali Khan

Volume 2017, Article ID 7676814, 9 pages

Generalized Fractional-Order Discrete-Time Integrator

Dorota Mozyrska and Piotr Ostalczyk

Volume 2017, Article ID 3452409, 11 pages

Fractional Order Memristor No Equilibrium Chaotic System with Its Adaptive Sliding Mode Synchronization and Genetically Optimized Fractional Order PID Synchronization

Karthikeyan Rajagopal, Laarem Guessas, Anitha Karthikeyan, Ashokkumar Srinivasan, and Girma Adam

Volume 2017, Article ID 1892618, 19 pages

Dynamics, Circuit Design, and Synchronization of a New Chaotic System with Closed Curve Equilibrium

Xiong Wang, Viet-Thanh Pham, and Christos Volos

Volume 2017, Article ID 7138971, 9 pages

A Novel Chaotic System without Equilibrium: Dynamics, Synchronization, and Circuit Realization

Ahmad Taher Azar, Christos Volos, Nikolaos A. Gerodimos, George S. Tombras,

Viet-Thanh Pham, Ahmed G. Radwan, Sundarapandian Vaidyanathan,

Adel Ouannas, and Jesus M. Munoz-Pacheco

Volume 2017, Article ID 7871467, 11 pages

Editorial

Fractional-Order and Memristive Nonlinear Systems: Advances and Applications

Ahmed G. Radwan,^{1,2} Ahmad Taher Azar,^{2,3} Sundarapandian Vaidyanathan,⁴ Jesus M. Munoz-Pacheco,⁵ and Adel Ouannas⁶

¹Engineering Mathematics and Physics Department, Faculty of Engineering, Cairo University, Giza 12613, Egypt

²NISC Research Center, Nile University, Giza 12588, Egypt

³Faculty of Computers and Information, Benha University, Benha 13511, Egypt

⁴Research and Development Centre, Vel Tech University, 400 Feet Outer Ring Road, Avadi, Chennai, Tamil Nadu 600062, India

⁵Facultad de Ciencias de la Electrónica, Autonomous University of Puebla, Av. San Claudio y 18 Sur, Edif. FCEI, 72570 Puebla, PUE, Mexico

⁶Laboratory of Mathematics, Informatics and Systems, University of Larbi Tebessi, 12002 Tebessa, Algeria

Correspondence should be addressed to Ahmed G. Radwan; agradwan@ieee.org

Received 20 July 2017; Accepted 20 July 2017; Published 28 September 2017

Copyright © 2017 Ahmed G. Radwan et al. This is an open access article distributed under the Creative Commons Attribution License, which permits unrestricted use, distribution, and reproduction in any medium, provided the original work is properly cited.

Due to the significance of nonlinear systems and circuits in many applications such as physics, control, biophysics, and bioengineering, enormous research activities have been highlighted to model the practical and experimental insights of such phenomena. Chaotic systems are nonlinear dynamical systems which are sensitive to initial conditions, topologically mixing, and with dense periodic orbits [1–3]. The chaos phenomenon was first observed in weather models by Lorenz in 1963. This was followed by a discovery of a large number of chaotic systems in many different fields like computer sciences, mechanics, communication, economics and finance, biology, chemistry, medicine, and geology.

Recently, the developments of nonlinear circuits and memristors [4] have had a big impact on the way scientists and engineers apply analytical and computational techniques. In the last four years, many systems have been investigated using the innovative features of mem-elements in the analysis and designs of nonlinear circuits and systems, such as chaotic systems. Due to the difficulties of nonlinear circuit design, contributions towards new ideas, techniques, modeling, analysis, design, or fabrication will have a direct impact on future applications and the industry.

The chaotic dynamics of fractional-order systems began to attract a great deal of attention in recent years due to the ease of their electronic implementations. Due to the very

high sensitivity of these chaotic systems which is required for many applications, there was a need to discuss the coupling of two or more dissipative chaotic systems which is known as synchronization. Chaotic synchronization has been applied in many different fields, such as biological, physical systems, structural engineering, and ecological models [1–4].

This special issue aims at presenting the latest developments, trends, research solutions, and applications of fractional-order and memristive chaotic systems with emphasis on real-world applications.

We received a total of twenty submissions, and after two rounds of rigorous review, seven papers were accepted.

In the paper “Fractional Order Memristor No Equilibrium Chaotic System with Its Adaptive Sliding Mode Synchronization and Genetically Optimized Fractional Order PID Synchronization,” K. Rajagopal et al. introduce a new memristor based novel fractional order no equilibrium chaotic system (FOMNE) and investigate its adaptive sliding mode synchronization. Firstly the dynamic properties of the integer order memristor based novel no equilibrium system are analyzed. The fractional order memristor no equilibrium system is then derived from the integer order model. Lyapunov exponents and bifurcation with fractional order are investigated. An adaptive sliding mode control algorithm is derived to globally synchronize the identical

fractional order memristor systems and genetically optimized fractional order PID controllers are designed and used to synchronize the FOMNE systems. Finally the fractional order memristor no equilibrium system is realized using FPGA.

In the paper “Generalized Fractional-Order Discrete-Time Integrator,” D. Mozyrska and P. Ostalczyk investigate a generalization of discrete-time integrator. The proposed linear discrete-time integrator is characterized by the variable-fractional-order of integration/summation. Graphical illustrations are presented for an analysis of particular vector matrices. Numerical examples show the relations between the order functions and element responses.

In the paper “Dynamics, Circuit Design, and Synchronization of a New Chaotic System with Closed Curve Equilibrium,” X. Wang et al. propose a new system with an infinite number of equilibrium points located on a closed curve. It is worth noting that the new system generates chaotic behavior as well as hidden attractors. Dynamics of the system with closed curve equilibrium have been investigated by using phase portraits, bifurcation diagram, maximal Lyapunov exponents, and Kaplan–York dimension. In addition, they introduce an electronic implementation to verify its feasibility. Antisynchronization ability of the new system with infinite equilibria is studied by applying an adaptive control. This study suggests that there exist other chaotic systems with uncountable equilibria in need of further investigation.

In the paper “Application of Topological Degree Method for Solutions of Coupled Systems of Multipoints Boundary Value Problems of Fractional Order Hybrid Differential Equations,” M. Iqbal et al. have established the theory to a coupled systems of multipoints boundary value problems of fractional order hybrid differential equations with nonlinear perturbations of second type involving Caputo fractional derivative. For obtaining sufficient conditions on existence and uniqueness of positive solutions to the system under consideration, the authors have used the technique of topological degree theory. Finally, main results are illustrated by a concrete example.

In the paper “CMOS Realization of All-Positive Pinched Hysteresis Loops,” B. J. Maundy et al. have proposed two novel nonlinear circuits that exhibit an all-positive pinched hysteresis loop. These circuits employ two NMOS transistors, one of which operates in its triode region, in addition to two first-order filter sections. The authors show the equivalency to a charge-controlled resistance (memristance) in a decremental state via detailed analysis. Simulation and experimental results verify the proposed theory.

In the paper “A Novel Chaotic System without Equilibrium: Dynamics, Synchronization, and Circuit Realization,” A. T. Azar et al. have proposed a novel unusual chaotic system without equilibrium. The authors discover dynamical properties as well as the synchronization of the new system. Furthermore, a physical realization of the system without equilibrium is also implemented to illustrate its feasibility.

In the paper “Understanding the Resistive Switching Phenomena of Stacked Al/Al₂O₃/Al Thin Films from the Dynamics of Conductive Filaments,” J. Molina and L. Hernandez-Martinez present the resistive switching characteristics of

Metal-Insulator-Metal (MIM) devices based on amorphous-Al₂O₃ and deposited by Atomic-Layer Deposition (ALD). A maximum processing temperature for this memory device is 300°C, making it ideal for Back-End-Of-Line (BEOL) processing. Even though some variations in the forming, set, and reset voltages (V_{FORM} , V_{SET} , and V_{RES}) are obtained for many of the measured MIM devices (mainly due to roughness variations of the MIM interfaces as observed after atomic-force microscopy analysis), the memristor effect has been obtained after cyclic I - V measurements. These resistive transitions in the metal oxide occur for both bipolar and unipolar conditions while the $I_{\text{OFF}}/I_{\text{ON}}$ ratio is around 4–6 orders of magnitude and is formed at gate voltages of $V_g < 4$ V. In unipolar mode, a gradual reduction in V_{SET} is observed and is related to a combined (a) incomplete dissolution of conductive filaments (made of oxygen vacancies and metal ions) that leaves some residuals and (b) thickening of chemically reduced Al₂O₃ during localized Joule heating. In conclusion, low-thermal budget MIM based memories using Al/Al₂O₃/Al structures have been fabricated and the memristor effect has been observed for the bipolar and unipolar switching modes, which are dependent on the amount of electrons tunneling through the device.

Acknowledgments

The guest editorial team would like to thank authors of all the papers submitted to this special issue. The editors also wish to thank the anonymous reviewers, some of whom helped with multiple review assignments. Finally, we would like to thank the journal’s Editorial Board for being very encouraging and accommodative regarding this special issue. We hope that you will enjoy reading this special issue devoted to this exciting and fast-evolving field as much as we have done.

Ahmed G. Radwan
Ahmad Taher Azar
Sundarapandian Vaidyanathan
Jesus M. Munoz-Pacheco
Adel Ouannas

References

- [1] A. T. Azar and S. Vaidyanathan, *Chaos Modeling and Control Systems Design*, vol. 581 of *Studies in Computational Intelligence*, Springer, Berlin, Germany, 2015.
- [2] A. T. Azar and S. Vaidyanathan, *Advances in Chaos Theory and Intelligent Control*, vol. 337 of *Studies in Fuzziness and Soft Computing*, Springer, Berlin, Germany, 2016.
- [3] A. T. Azar, S. Vaidyanathan, and A. Ouannas, *Fractional Order Control and Synchronization of Chaotic Systems*, vol. 688 of *Studies in Computational Intelligence*, Springer, Berlin, Germany, 2017.
- [4] A. G. Radwan and M. E. Fouda, *On The Mathematical Modeling of Memristor, Memcapacitor, and Meminductor*, vol. 26 of *Studies in Systems, Decision and Control*, Springer, 2015.

Research Article

Understanding the Resistive Switching Phenomena of Stacked Al/Al₂O₃/Al Thin Films from the Dynamics of Conductive Filaments

Joel Molina-Reyes and Luis Hernandez-Martinez

National Institute of Astrophysics, Optics and Electronics, Luis Enrique Erro No. 1, 72840 Tonantzintla, PUE, Mexico

Correspondence should be addressed to Joel Molina-Reyes; jmolina_molina@hotmail.com

Received 5 May 2017; Accepted 11 July 2017; Published 20 September 2017

Academic Editor: Sundarapandian Vaidyanathan

Copyright © 2017 Joel Molina-Reyes and Luis Hernandez-Martinez. This is an open access article distributed under the Creative Commons Attribution License, which permits unrestricted use, distribution, and reproduction in any medium, provided the original work is properly cited.

We present the resistive switching characteristics of Metal-Insulator-Metal (MIM) devices based on amorphous Al₂O₃ which is deposited by Atomic Layer Deposition (ALD). A maximum processing temperature for this memory device is 300°C, making it ideal for Back-End-of-Line (BEOL) processing. Although some variations in the forming, set, and reset voltages (V_{FORM} , V_{SET} , and V_{RESET}) are obtained for many of the measured MIM devices (mainly due to roughness variations of the MIM interfaces as observed after atomic-force microscopy analysis), the *memristor* effect has been obtained after cyclic I - V measurements. These resistive transitions in the metal oxide occur for both *bipolar* and *unipolar* conditions, while the $I_{\text{OFF}}/I_{\text{ON}}$ ratio is around 4–6 orders of magnitude and is formed at gate voltages of $V_g < 4$ V. In unipolar mode, a gradual reduction in V_{SET} is observed and is related to combined (a) incomplete dissolution of conductive filaments (made of oxygen vacancies and metal ions) which leaves some residuals and (b) thickening of chemically reduced Al₂O₃ during localized Joule heating. This is important because, by analyzing the macroscopic resistive switching behavior of this MIM structure, we could indirectly relate it to microscopic and/or nanoscopic phenomena responsible for the physical mechanism upon which most of these devices operate.

1. Introduction

Since the invention and experimental demonstration of the *memristor* (an integrated device with *memory-resistance* properties, able to correlate electric charge to magnetic flux q - ϕ [1]), several materials in the form of thin dielectric films or solid electrolytes have been tested for these emergent non-volatile memory devices in order to produce reliable and reversible switching cycles of the resistive state of the oxide. Thin film based materials able to switch from a high resistance state (HRS/OFF) to a low resistance state (LRS/ON) and vice versa are responsible for the typical “*pinched hysteresis loops*,” which are observed during cyclic current-voltage (I - V) measurements of these devices. This has contributed to the development of important applications like nonlinear circuits, chaotic systems, highly dense neural networks, and even neuromorphic computing, where the diffusive dynamics of memristors can be used as synaptic emulators. Nevertheless,

all these highly dynamic applications exploiting the memristor effect do so without considering complex microscopic and nanoscopic phenomena, mainly related to the evolution and migration dynamics of atomic elements within the integrated device. Recently, several Metal-Insulator-Metal structures have shown the ability to switch between these two resistive states (HRS \leftrightarrow LRS) after promoting resistive switching phenomena (by forming/dissolving conductive filamentary paths in mostly binary oxides) or ion migration mechanisms (by cation or anion species in solid electrolytes) during high electrical stress of the devices [1, 2]. In this sense, Resistive switching Random Access Memory (ReRAM) devices have attracted considerable attention in the recent years due to their superior characteristics for nonvolatile data storage. Some of these advantages are a simple memory structure (usually composed of MIM stacks), deep scalability, ultralow power consumption, fast write/erase speed, and long retention times [3]. Also, even though the precise physics behind

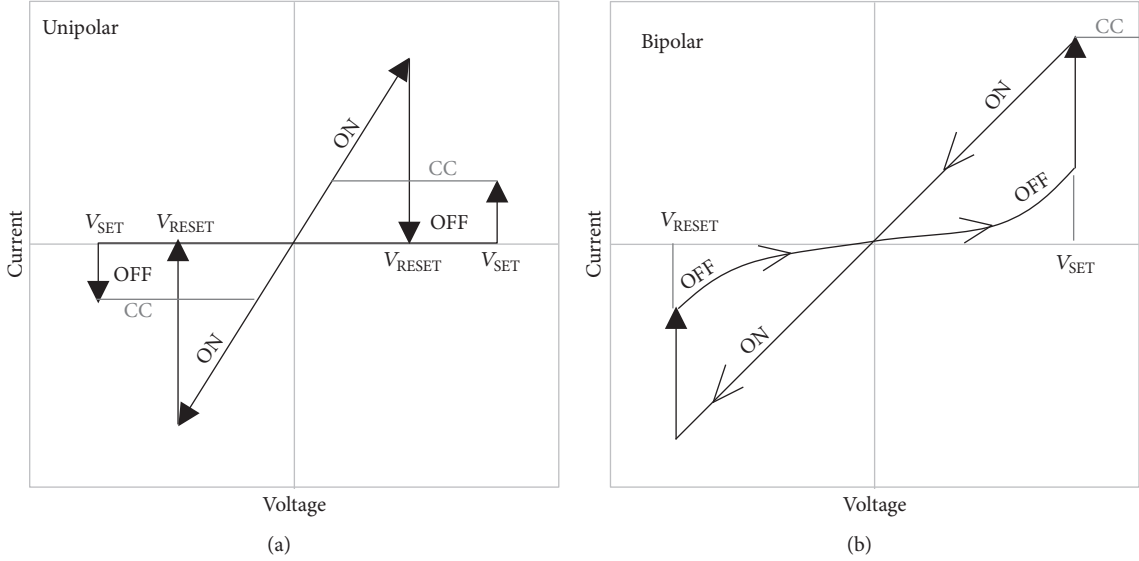


FIGURE 1: $I-V$ diagrams showing the (a) unipolar and (b) bipolar operation modes for ReRAM devices where no dependence of the “*pinched hysteresis loops*” to frequency is involved (DC conditions). The unipolar mode is able to promote resistive switching using a positive or negative polarity with $V_{\text{SET}} > V_{\text{RESET}}$ and $CC_{\text{SET}} < CC_{\text{RESET}}$.

the operation mechanism is still not fully understood, by using resistive switching and/or ion migration phenomena, there have been some advances in which, for many cases, single and/or multiple filamentary conduction paths can be formed or dissolved in the oxide, thus connecting or disconnecting both metal electrodes and, therefore, giving origin to both LRS and HRS [4, 5]. This is important because a better understanding of the resistive switching phenomena could enable enhanced nonlinear applications like the ones previously described, while also providing better modeling tools for nonlinear devices and systems. ReRAM switching modes can be classified into two groups: unipolar switching and bipolar switching. In unipolar mode, the resistive switching transitions (HRS \leftrightarrow LRS) of the oxide layer are obtained using the same polarity but different magnitudes of applied bias (while limiting the gate current at two current compliance levels). In bipolar mode, these transitions are obtained using different polarities of applied bias so that typical hysteresis loops in the $I-V$ characteristics (*Lissajous* curves) are observed [3, 5]. In any case, these resistive switching transitions require specific voltages so that V_{SET} and V_{RESET} would promote HRS \rightarrow LRS (ON) and HRS \leftarrow LRS (OFF) transitions, respectively (see Figures 1(a)-1(b)).

Depending on the MIM structure, an additional forming voltage V_{FORM} is necessary in order to force the initial HRS \rightarrow LRS transition and, generally, $V_{\text{FORM}} > V_{\text{SET}} > V_{\text{RESET}}$. It is important to consider that, for any operation mode, a limit in the current flowing through the MIM device should be established in order to prevent permanent oxide breakdown and, therefore, losing the memory effect. In the unipolar mode, two different current limits must be used so that during the creation of a conductive path/filament by V_{SET} a low current compliance limit CC_{SET} would enable a controlled formation of these conductive paths, while a higher current

compliance limit CC_{RESET} would be required for the dissolution of this conductive path/filament by V_{RESET} (much like the breakdown of a *fuse* after passing a large current density through it). Usually, more reproducible characterization of ReRAM devices based on MIM structures would require that $V_{\text{FORM}} > V_{\text{SET}} > V_{\text{RESET}}$ and $CC_{\text{RESET}} > CC_{\text{SET}}$ and doing so by also using specific time-dependent waveforms as polarization sources so that the time-dependent properties of these devices could also be extracted (like the well-known poor frequency dependence of experimental memristors, where the total area of the *pinched hysteresis loops* decreases with the frequency of applied bias). On the other hand, it is known that, during the reset process in the unipolar switching mode, a large current flow (needed to dissolve an already formed conductive filament (CF)) would produce localized Joule heating at this conductive filament which, in turn, could lead to its partial dissolution and, therefore, to a large amount of residuals around it (oxygen vacancies and/or metal ions) [6, 7]. The amount and type of these residuals are largely dependent on the CC levels as well as the velocity during the voltage sweeps needed for the cyclic HRS \leftrightarrow LRS transitions. The residual combination of metal atoms/complexes/compounds within the remaining oxide could contribute to higher leakage currents as well as electrical instabilities (like charge trapping-detrapping events or a gradual reduction in V_{SET}) of ReRAM devices upon more switching cycles, leading to narrowing of the resistive window and, thus, lower endurance. Here, we monitor the gradual reduction in V_{SET} after the 5 initial switching cycles of an Al/Al₂O₃/Al structure (unipolar operation) and we relate this reduction of V_{SET} to residuals of aluminum ions (during partial dissolution of the conductive filament by a large current flow) which act as trap centers that lower the energy barrier of Al₂O₃ while decreasing the set

voltage (25th International Conference on Amorphous and Nanocrystalline Semiconductors).

2. Materials and Methods

For MIM device fabrication, stacked Al/Al₂O₃/Al thin films were sequentially deposited on previously cleaned Corning glass slides and standard photolithography steps were used for gate pattern definition, while the whole stack is finally annealed in N₂ at 300°C. Initially, all glass slides were cleaned by sequential immersion in trichloroethylene (TCE) and acetone (10/10 min) within an ultrasonic vibrator. This is followed by rinsing in deionized water (DI water) by 10 min and the slides are gently dried using an ultrahigh purity N₂ blow. Aluminum is used as bottom and top electrode (BE/TE) for the MIM device. The BE/TE consist of aluminum layers each with 500 nm in physical thickness and they were deposited by E-beam evaporation (Temescal BJD-1800 from Edwards) under ultrahigh vacuum conditions using a deposition rate of 1-2 Å/sec. Al₂O₃ with 20 or 10 nm in thickness were deposited on the BE by thermal ALD at 250°C (Savannah S100 from Cambridge NanoTech) using H₂O and Trimethylaluminum (TMA) as chemical precursors for the oxygen and aluminum elements of Al₂O₃. Also, a thinner Al₂O₃ = 6 nm was used in Metal-Insulator-Semiconductor (MIS) structures in order to confirm the high electrical quality of this metal oxide via *I-V* and *C-V* measurements. The ALD process was performed at 250°C/200 mTorr of temperature/pressure for all 200, 100, or 60 deposition cycles of Al₂O₃ deposition. All these samples were quickly introduced into the e-beam evaporator after ALD of Al₂O₃. There, the evaporation chamber was vacuumed down to 1×10^{-7} Torr in order to minimize the exposure time of the Al₂O₃ surfaces to atmospheric oxygen or any other contaminant of the clean room. Standard photolithography steps followed after complete metallization of these MIM devices. For this, all samples were covered with positive photoresist using standard spinning/baking conditions and exposed to an UV system (Karl Suss MA6) in order to transfer gate patterns to the TE. Gate capacitor areas of 36×10^{-6} cm² and 64×10^{-6} cm² were used for the MIS and MIM devices, respectively. After gate pattern definition, only the Al/Al₂O₃/Al/Glass (MIM) structures were annealed in pure N₂ (99.999% purity) at 300°C in order to promote densification of Al₂O₃ along with interfacial layer development of this metal oxide with BE/TE (nonstoichiometric Al_xO_y interfacial layers are expected). The complete fabrication procedure is very simple (see Figure 2), while the maximum processing temperature is 300°C. A low thermal budget in the processing of these devices makes them ideal for their integration in the BEOL stages of an integrated circuit, thus further increasing the integration density of memory devices.

3. Results and Discussion

Given the thin physical thickness for Al₂O₃ used in the MIM structures (20 and 10 nm), we have electrically characterized MIS devices in which an even thinner Al₂O₃ = 6 nm has been deposited on silicon by using the same ALD conditions (without thermal annealing). Therefore, by using a silicon

surface with very low atomic surface roughness (as compared to a metallic bottom electrode), we are able to assess the intrinsic electrical quality of Al₂O₃. Figures 3(a)-3(b) show the *I-V* and *C-V* characteristics of several Al/Al₂O₃/n-Si MIS devices in which good uniformity is observed after measuring at least 15 MIS devices for each data set. The *I-V* data (normalized to gate area and oxide thickness) show a high electric field required for oxide breakdown ($E_{bkd} = 7.1$ MV/cm) (under accumulation or substrate injection condition), while the resistivity window before and after hard breakdown can be as high as 10 orders of magnitude (for $E_g \leq 2$ MV/cm). The *C-V* data, on the other hand, show a large hysteresis window *H* (measured at flat-band voltage) which is characteristic of a bad Al₂O₃/Si interface, so that several defects (from a large density of dangling bonds to chemical reduction of Al₂O₃ into AlSi_xO_y silicates) would promote higher densities of charge trapping.

Also, moderate capacitance in accumulation turns into a dielectric constant of $k \sim 6$, a relatively low value compared to what is expected for bulk Al₂O₃ ($k \sim 9$) and yet the good uniformity in the *C-V* data is again observed for all measured MIS devices. For the MIM structures, we could expect some deviations from *I-V* data in particular, since large defects are found at the interfaces of Al₂O₃ with both the bottom and top metallic electrodes.

In order to show the cyclic resistive switching characteristics of the metal oxide film, thicker Al₂O₃ = 20 nm (deposited by ALD with the same conditions) was used in an Al/Al₂O₃/Al/Glass stacked structure and electrically characterized before and after the final thermal treatment applied to the device. Figures 4(a)-4(b) show the resistive switching characteristics (in unipolar mode) of this structure. Even though the gate current levels are increased for the annealed sample (especially during the HRS condition), we notice that different current compliance levels are needed for both samples whenever we promote a transition from the HRS to the LRS condition and vice versa. For this thicker Al₂O₃, the limit in CC_{SET} is set to 100 μA, whereas $CC_{RESET} = 100$ mA; both are large current densities flowing through the oxide layer and that would increase the chances for leaving large amount of residuals (after the RESET condition which produce localized Joule heating in the previously formed conductive filament) in the form of a high density of oxygen vacancies (neutral or charged) and/or metal ions. We also observe that some electrical instabilities in the gate current *I_g* do occur after the initial resistive switching cycles, where the as-deposited and annealed samples produce 8 and 16 cycles (HRS ↔ LRS transitions), respectively. These electrical instabilities are due to charge trapping-detrapping events that, later, are related to conduction mechanisms, where trap-energy levels are responsible for these phenomena.

The conduction mechanisms initially considered for modeling these gate tunneling currents were Ohmic Conduction (OC), Thermionic Emission (TE), Space-Charge Limited Current (SCLC), Trap-Assisted Tunneling (TAT), Poole-Frenkel (PF), and Fowler-Nordheim (FN). After linear fitting of the experimental *I-V* data (only for the HRS condition just before oxide breakdown or conductive filament formation),

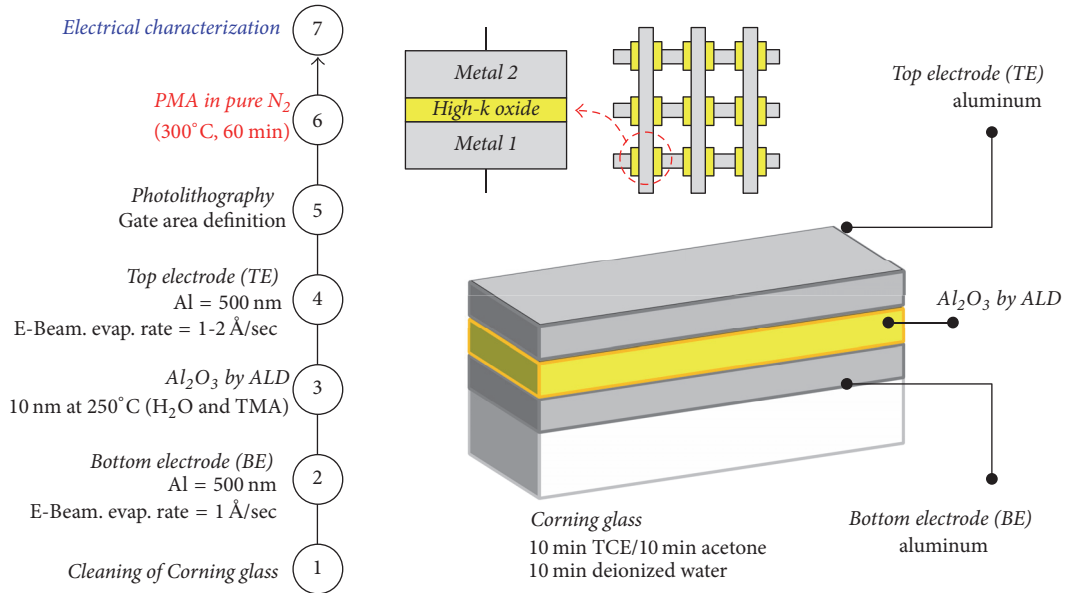


FIGURE 2: Process flow for fabrication of Al/Al₂O₃/Al stacked structures using a maximum temperature of 300°C, ideal for BEOL processing. Traverse cut of an ideal MIM device (where M1 = M2 = aluminum) as well as possible MIM arrays that could be densely integrated within the BEOL stages of an integrated circuit.

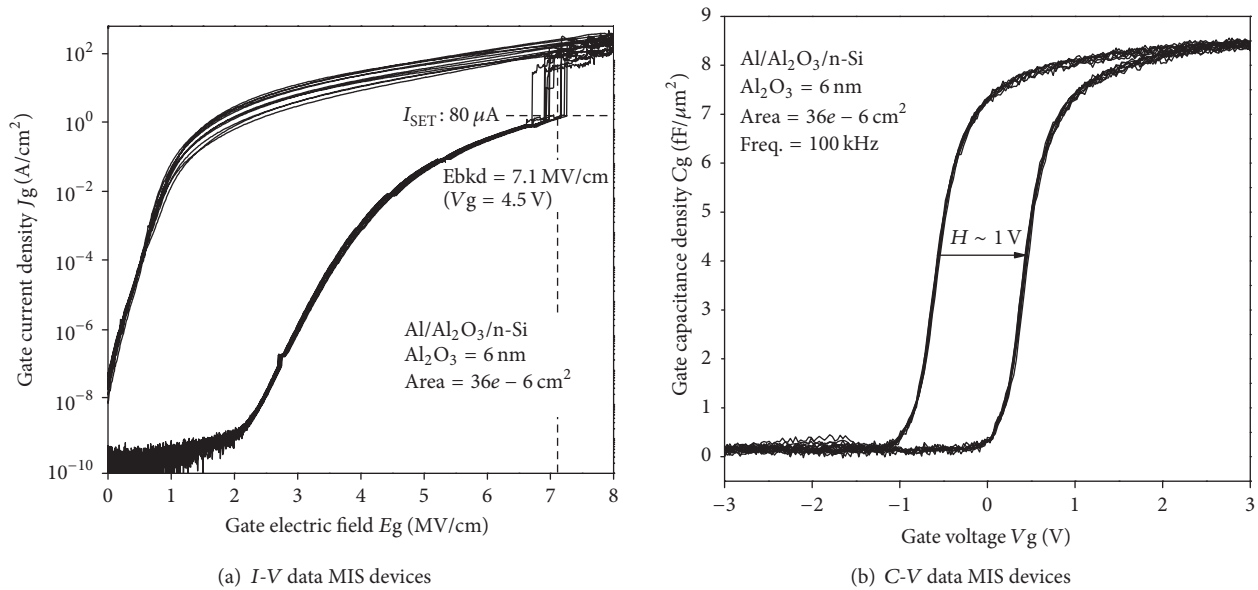


FIGURE 3: Electrical characteristics of MIS devices based on thinner Al₂O₃ = 6 nm and without thermal annealing. Outstanding uniformity is observed for both (a) *I-V* and (b) *C-V* data after testing at least 15 different MIS devices for each measurement. This confirms the good quality of ALD method for deposition of thin Al₂O₃.

PF and FN mechanisms were confirmed as the main conduction models with specific trap/barrier energy levels Φ_t/Φ_B for Al₂O₃ [8]. This Φ_t level (PF model) is often associated with some defects and/or impurities in the oxide layer and this makes sense if we consider that some residuals could remain after partial dissolution of the conductive filament. This would impact the reliable operation of a ReRAM device because it will also produce a gradual decrease in the voltage needed for a new SET operation as will be shown later. Also,

it is important to notice that a broad resistivity window between the HRS and LRS is obtained for these samples, where 4–6 orders of magnitude secure high endurance during continuous *I-V* resistive cycling of these devices.

For the annealed Al/Al₂O₃/Al/Glass MIM device (with thicker Al₂O₃ = 20 nm), monitoring of the gate current *I_g* with time during a constant gate voltage *V_g* applied (in the two resistive states HRS and LRS) produces the results shown in Figure 5(a). Initially, large $V_{SET} = 3.5$ V forces *I_g* to

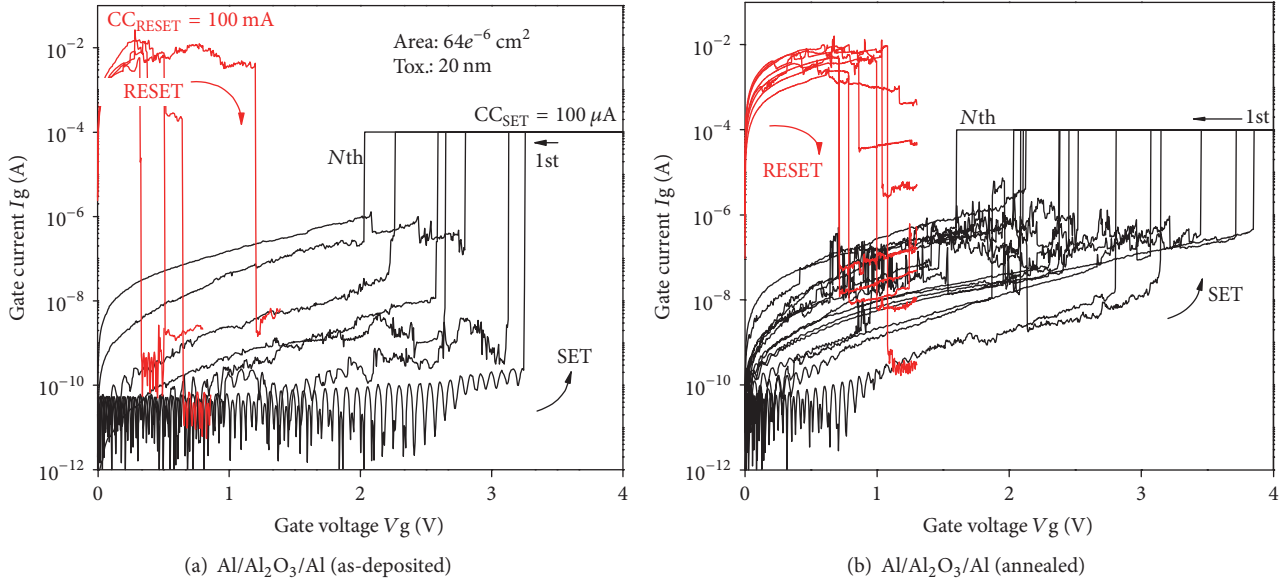


FIGURE 4: Resistive switching of Al/Al₂O₃/Al stacked structures (using thicker Al₂O₃ = 20 nm) for the (a) as-deposited and (b) annealed devices in N₂ at 300°C conditions. The unipolar mode for resistive switching is obtained after using $CC_{SET} = 100 \mu A$ and $CC_{RESET} = 100 mA$. A large resistivity window is also observed for both samples.

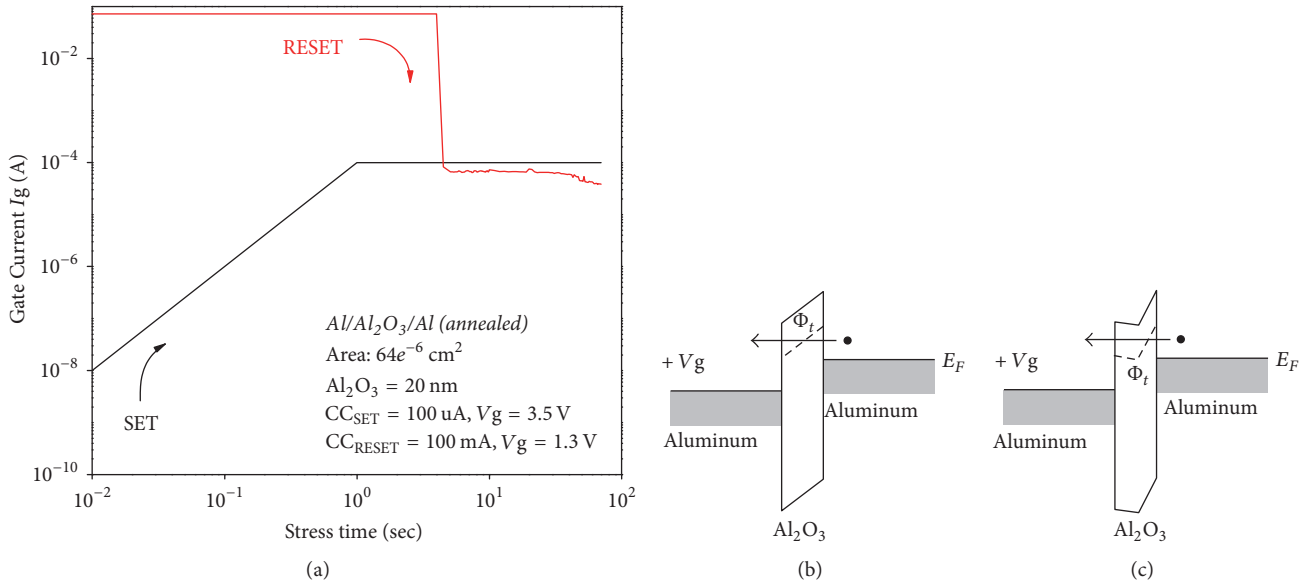


FIGURE 5: (a) Gate current versus stress time for Al/Al₂O₃/Al structure during the SET and RESET conditions. A gradual increase in I_g during the SET condition is evidence of positive charge trapping in the MIM device. Ideal energy band diagrams for the MIM structure under positive bias and where (b) PF tunneling conduction through Φ_t is initiated; (c) a large density of trapped positive charge modifies the energy gap of Al₂O₃.

reach the LRS almost immediately (formation of conductive filament) and it is only limited by $CC_{SET} = 100 \mu A$. We notice a gradual increase in I_g with time until CC_{SET} is reached and this is related to continuous trapping of positive charge [9] in the bulk and/or interfaces of Al₂O₃ (enabled by a PF model with a given Φ_t level; see Figure 5(b)). It is thought that a high density of trapped positive charge would be able to modify

the energy barriers of Al₂O₃ during tunneling of carriers [9–12] (see Figure 5(c)), so that I_g conduction enhances while progressively reducing V_{SET} . For dissolution of the conductive filament, large $CC_{RESET} = 100 mA$ is required (producing Joule heating) and this produces a sudden decrease in gate current I_g which, in this case, is obtained after the first seconds of stressing bias.

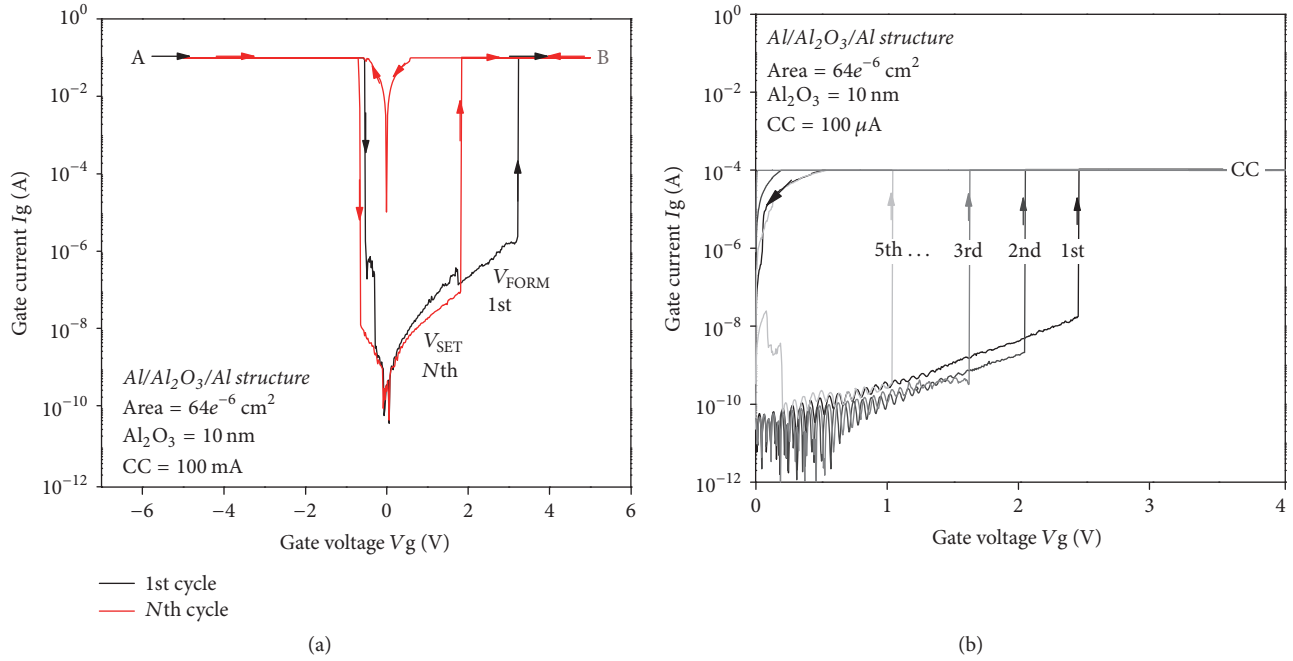


FIGURE 6: Resistive switching for annealed Al/Al₂O₃ (10 nm)/Al stacked structures. (a) Bipolar mode with CC = 100 mA and (b) unipolar mode with CC_{SET} = 100 μA. The $I_{\text{OFF}}/I_{\text{ON}}$ ratio for these structures is 10^4 – 10^6 for both operation modes. For the unipolar mode, a decrease in V_{SET} is observed during continuous resistive switching.

Having a large density of trapped positive charge (after the partial dissolution of a conductive filament) will have a profound impact on the endurance characteristics of a ReRAM device. For this, we will examine the electrical characteristics of annealed Al/Al₂O₃/Al/Glass stacked structures having thinner Al₂O₃ = 10 nm. Figure 6(a) shows the first breakdown voltage (forming voltage V_{FORM}) of the memory cell which is larger than the N th set voltage (V_{SET}) and also the initial current in the HRS is much smaller compared to the current in the LRS as expected. These I - V characteristics correspond to the bipolar switching mode, where a double sweep of voltage (using both polarities) is applied to the same MIM device and I - V hysteretic loops are obtained, while the maximum current is limited to CC = 100 mA. It is important to notice that limiting the maximum current flowing through the device helps to prevent permanent damage of the oxide and therefore more resistive switching cycles could be obtained. For this MIM device, $V_{\text{FORM}} > V_{\text{SET}}$ and the $I_{\text{OFF}}/I_{\text{ON}}$ ratio is ~ 6 orders of magnitude, a large resistivity window able to promote higher endurance during cyclic ReRAM operation. Here, the N th cycle is the 8th I - V cycle and the gate current at this 8th HRS is lower compared to the 1st HRS, which indicates trapping of negative charge. Whether it was a positive or negative charge, it is clear that a high density of trapped charge is able to decrease V_{SET} in both modes.

For the same MIM structure in the unipolar mode, Figure 6(b) shows that the first transitions to a LRS condition cause a progressive reduction in V_{SET} (during sequential switching from HRS to LRS, up to 5 cycles) in the same device. Here, the corresponding HRS \leftarrow LRS transitions are

not shown for clarity purposes. Again, even though a large resistivity window is also obtained (4–6 orders of magnitude), a progressive reduction in V_{SET} will compromise both the endurance and other reliability parameters for these memory devices. The exact physical origin for this reduced V_{SET} is out of the scope of this work but there is plenty of evidence pointing to (1) the chemical reduction of Al₂O₃ into off-stoichiometric Al _{x} O _{y} after oxygen scavenging by the BE/TE metal layers [13, 14] (thus decreasing the total dielectric constant) and/or (2) metal migration from the BE/TE into Al₂O₃ so that a localized conductive nanofilament (formed by a SET process) could be partially dissolved by a RESET process [6, 7], thus reducing both the effective oxide thickness and the next V_{SET} needed for a new HRS \rightarrow LRS transition (see Figure 7(a)). Since these memory devices can have two types of switching modes (unipolar and bipolar), each switching mode will mainly depend on the applied bias conditions, on the magnitude of the compliance currents that will limit the total current after breakdown, and, more importantly, on the energy required to transport electronic and/or ionic (oxygen vacancies and metal ions) charge for cyclic formation and rupture of conductive filaments. It is important to notice that, for both the bipolar and unipolar modes, the minimum current compliance during continuous resistive switching of this device is set to CC \geq 100 μA. It has been recently demonstrated that the level of CC fixed for memory switching is quite important for transitioning between two resistive states of a binary metal oxide [6, 7]. At lower CC < 10 μA, the switching occurs due to a conductive path formed mainly by charged oxygen vacancies [Vo⁺], while for CC > 10 μA, the conduction path is formed by metal ions [M⁺] that

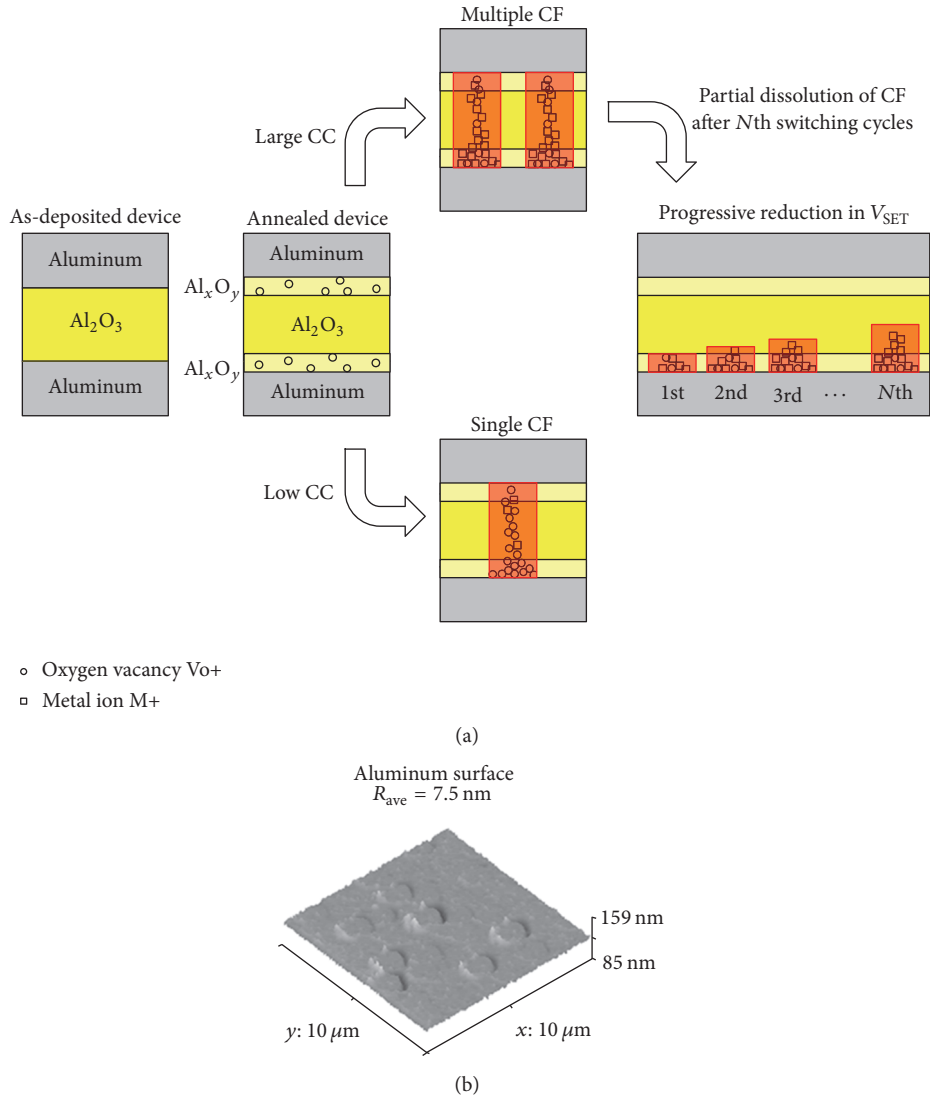


FIGURE 7: (a) Proposed physical mechanism for the origin of single and/or multiple conductive filaments (CFs) for Al/Al₂O₃/Al structure during the SET process (depending on the current compliance limit) and the effect that partial dissolution of this previously formed CF has on the progressive reduction of V_{SET} . For larger CC, multiple formation of CFs should be expected, with their composition being mostly based on metal ions [M^+]. (b) Average surface roughness of the BE (after AFM) showing large surface roughness which is close to the physical Al₂O₃ thickness of the MIM device. High surface roughness would promote local electric-field enhancements.

diffuse or migrate from the metal electrodes (BE/TE) into the oxygen vacancy-rich oxide defect network [15–17]. This is very important, since, depending on the type of species forming the conductive filament (Vo^+ or M^+), any residual left after dissolution of the conductive filament (RESET process) would make the detrapping process from a shallow/deep trap-energy level easier/harder, thus affecting the resistivity windows, endurance, and other reliability issues. Of course, a more precise estimation of the current needed to induce Vo^+ or M^+ based formation of conductive filaments would be normalizing I_g to smaller device areas or, even better, integrating the injected charge with time [18, 19] because, due to highly different oxide thicknesses, very different current levels would be required. Nevertheless, the oxide thickness regime in our samples is in concordance with the migration

thermodynamics for Vo^+/M^+ , described quite recently [6, 7]. In our samples, the I - V data of Figure 6 already show that CC is set to 100 mA and 100 μA for the bipolar and unipolar switching modes, respectively, thus suggesting that the main species forming the conductive filament (by a SET process) are based on metal ions [M^+] which, in this case, would be some specific oxidation states of aluminum (the same metal material for both the BE and TE). A simplified model showing the physical mechanisms behind a progressive reduction in V_{SET} as well as the surface roughness of the BE is illustrated in Figures 7(a)-7(b). During formation of single/multiple conductive filaments, not only the current compliance but also the surface roughness at the metal/oxide interfaces are important, since this would lead to local electric-field enhancements and then early breakdown [20, 21].

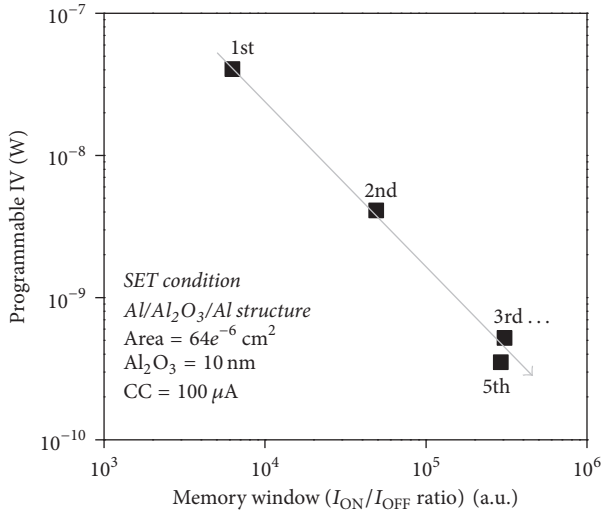


FIGURE 8: Based on the data of Figure 6(b), the power needed to promote continuous resistive switching of that MIM structure is reduced, while the memory window (I_{ON}/I_{OFF} ratios) increases. Even though these are desirable characteristics for a ReRAM device, this behavior is a consequence of the progressive reduction in the V_{SET} parameter which, in turn, will compromise endurance and the general reliability of these memory devices.

Figure 7(a) suggests that, by using large CC, generation of a single broad conductive filament or generation of more than one conductive filament occurs. Generation of single or multiple conductive filaments is in the end promoted by the total current flowing through the device. We also notice that, by using a sufficiently large CC limit during each switching cycle, a partial dissolution of the CF would mostly leave a high density of metal ions (close to the biased anode) which then results in the progressive reduction of V_{SET} (as observed in Figure 6(b)). Figure 7(b) shows the surface morphology of the first aluminum layer which was used as bottom electrode in the Al/Al₂O₃/Al structure. The average roughness for this aluminum layer is 7.5 nm (which could be related to formation of stacking faults during evaporation of this metal) and since the physical thickness of Al₂O₃ = 10 nm, reducing this severe surface roughness is critical in order to enhance the reproducibility of hysteretic I - V characteristics. Therefore, we could relate the observed variations in V_{FORM} , V_{SET} , and V_{RESET} of Figures 4(a)-4(b) to variations in the physical thickness of the effective oxide, since the roughness [22] at the metal/Al₂O₃ interfaces is almost of the same physical thickness as observed after atomic-force microscopy.

Figure 8 shows the power ($V_{SET} \cdot I_{SET}$) needed to promote the HRS \rightarrow LRS transitions already observed in Figure 6(b) versus the memory window (I_{ON}/I_{OFF} ratios) therein obtained. A seemingly desirable tendency is observed, where, for 5 continuous resistive switching cycles (unipolar mode), less power is required to produce these transitions, while the memory window is also increased. This behavior, however, is due to progressively reduced V_{SET} which, in turn, will severely compromise the endurance and the long-lasting performance of these devices.

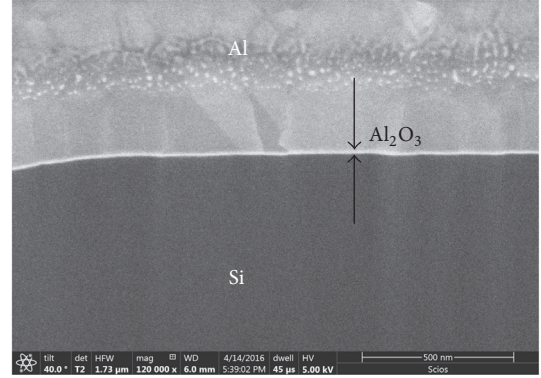


FIGURE 9: Scanning electron microscopy image for Al/Al₂O₃/Si structure (Al₂O₃ = 20 nm, annealing in N₂ at 300°C) after FIB preparation of a traverse-cut face (using secondary electrons of an intralens detector for morphology imaging). A smooth transition between all materials is observed, while the polycrystalline nature of the metal electrode is also visible.

Figure 9 shows the scanning electron microscopy image (secondary electrons using an in-lens detector) of Al₂O₃-based MIS device (Al₂O₃ = 20 nm, annealing in N₂ at 300°C) in which the ultralow atomic surface roughness of the silicon substrate is used in order to show a relatively smooth transition in the morphology and composition of all the materials used for the stacked structure (seen as a sharp difference in the contrast for all films).

The image shows the “curtaining effect” or ripple formation after focused-ion beam (FIB) preparation [23] of a specific face of this MIS device. Because of the sputtering action of the ion beam, the FIB can be used to locally remove or mill away material (exposing the desired face and its interfaces) while getting surface roughening and shadowing effects due to heavy ion bombardment. Although it is difficult to confirm the chemical reduction of Al₂O₃ into Al_xO_y after annealing (as schematically illustrated in Figure 7(a)), we can observe the high uniformity of the Al₂O₃ film after thermal ALD and even the polycrystalline nature of the aluminum electrode which is the material used for the BE and TE in our MIM devices. This is important given the relatively large gate area for these MIM devices (80 μm × 80 μm), where intrinsic defects directly related to the resistive switching of the high- k layer could be masked by extrinsic defects whenever larger areas are under electrical characterization [24–26].

A full understanding of the complex resistive switching phenomena is still a work in progress to which many research labs across the globe have actively contributed so that, by now, microscopic and nanoscopic details related to migration dynamics of atomic elements within stacked MIM structures have emerged. This is quite important since it could contribute to a better definition of the “memristor effect” which by now is still limited to the basic memristor fingerprints [27–29] able to identify a memristive device:

- (1) The device must exhibit a “pinched hysteresis loop” in the voltage-current plane for any bipolar periodic signal excitation. This “pinched hysteresis loop” must

converge and cross the origin of this voltage-current plane.

- (2) The pinched hysteresis loop area should decrease monotonically as the excitation frequency increases.
- (3) The pinched hysteresis loop should shrink to a single-valued function when the frequency tends to infinity, which is similar to turning a memristor into a common resistor, where well-defined linear I - V dependence is observed.

Nevertheless, this work tries to identify and correlate some issues that occur simultaneously in MIM devices during cyclic resistive switching measurements: (a) the origin of variations in the resistive switching phenomena of Al/Al₂O₃/Al devices in both the bipolar and unipolar modes, (b) the modeling of a mechanism responsible for these variations (combining physical, chemical, and electronic phenomena) and whose more accurate details, occurring at the nanoscopic level, have been demonstrated for even higher dielectric constant materials like HfO₂ [24–26, 30, 31], and (c) the connection of the former points from the perspective of the formation/dissolution of conductive filaments. All these issues are of the utmost importance in order to provide a more precise physical explanation regarding the operation mechanism of ReRAM devices and, therefore, enabling the development of accurate electrical models (not only for the DC regime but also for frequency-dependent conditions) that could accelerate the research and application of nonlinear phenomena with these memristive materials and devices.

4. Conclusions

MIM based ReRAM devices (using symmetric Al/Al₂O₃/Al structures) have been fabricated at low processing temperatures and the *resistive switching* effect has been observed for both the bipolar and unipolar operation modes which are dependent on the amount of electrons tunneling through the device. For cyclic ReRAM operation, $V_{\text{FORM}} > V_{\text{SET}} > V_{\text{RESET}}$ was found and a relatively large $I_{\text{OFF}}/I_{\text{ON}}$ ratio of 4–6 orders of magnitude is useful for higher endurance. In the unipolar switching mode and by measuring several resistive switching cycles in the same sample, V_{SET} is progressively reduced and that might be related to a combined mechanism of (a) incomplete dissolution of conductive filaments (made of oxygen vacancies and, mostly, metal ions) which leaves some residuals close to the anode and (b) thickening of chemically reduced Al₂O₃ during localized Joule heating. Also, even though high uniformity of thicker Al₂O₃ films is observed in MIS devices after SEM imaging, the surface roughness of the aluminum-based bottom electrode (after AFM analysis) is close to the physical thickness of Al₂O₃ itself, thus compromising the performance and general reliability of these MIM devices by localized electric-field variations. Nevertheless, these samples have shown the memristor effect while using low-temperature processing and standard materials used in the BEOL stages of an integrated circuit. By optimizing the physical and processing parameters of this structure, vertical integration of dense memory arrays using MIM structures

could be implemented at BEOL processing in order to obtain denser, smarter, and more efficient integrated circuits. Given the importance of memristive devices (also memcapacitive and meminductive elements) for modeling nonlinear phenomena, experimental evidence relating resistive switching behavior to microscopic and nanoscopic details of conductive filament formation is necessary in order to use better models for the analysis, design, and simulation of memristor-based circuits (with analog, digital, logic, neuromorphic, secure communications and several other applications).

Conflicts of Interest

The authors declare that there are no conflicts of interest regarding the publication of this paper.

Acknowledgments

This work was fully supported by the National Council of Science and Technology (CONACYT), Mexico.

References

- [1] D. B. Strukov, G. S. Snider, D. R. Stewart, and R. S. Williams, “The missing memristor found,” *Nature*, vol. 453, pp. 80–83, 2008.
- [2] J.-J. Ke, Z.-J. Liu, C.-F. Kang, S.-J. Lin, and J.-H. He, “Surface effect on resistive switching behaviors of ZnO,” *Applied Physics Letters*, vol. 99, article 192106, 2011.
- [3] R. Waser, R. Dittmann, C. Staikov, and K. Szot, “Redox-based resistive switching memories nanoionic mechanisms, prospects, and challenges,” *Advanced Materials*, vol. 21, no. 25–26, pp. 2632–2663, 2009.
- [4] I. H. Inoue, S. Yasuda, H. Akinaga, and H. Takagi, “Non-polar resistance switching of metal/binary-transition-metal oxides/metal sandwiches: Homogeneous/inhomogeneous transition of current distribution,” *Physical Review B*, vol. 77, article 035105, 2008.
- [5] Y. Fujisaki, “Review of Emerging New Solid-State Non-Volatile Memories,” *Japanese Journal of Applied Physics*, vol. 52, article 040001, 2013.
- [6] K. L. Pey, R. Thamankar, M. Sen, M. Bosman, N. Raghavan, and K. Shubhakar, “Understanding the switching mechanism in RRAM using in-situ TEM,” in *Proceedings of the 21st IEEE Silicon Nanoelectronics Workshop, SNW 2016*, IEEE, Honolulu, Hawaii, USA, June 2016.
- [7] S. Mei, M. Bosman, R. Nagarajan, X. Wu, and K. L. Pey, “Compliance current dominates evolution of NiSi₂ defect size in Ni/dielectric/Si RRAM devices,” *Microelectronics Reliability*, vol. 61, pp. 71–77, 2016.
- [8] J. Molina-Reyes, H. Uribe-Vargas, R. Torres-Torres, P. Mani-Gonzalez, and A. Herrera-Gomez, “Accurate modeling of gate tunneling currents in Metal-Insulator-Semiconductor capacitors based on ultra-thin atomic-layer deposited Al²O₃ and post-metallization annealing,” *Thin Solid Films*, vol. 638, pp. 48–56, 2017.
- [9] Y. Liu, T. P. Chen, W. Zhu et al., “Charging effect of Al₂O₃ thin films containing Al nanocrystals,” *Applied Physics Letters*, vol. 93, Article ID 142106, 2008.
- [10] M. N. Bhuyian, R. Sengupta, P. Vurikiti, and D. Misra, “Oxygen vacancy defect engineering using atomic layer deposited

- HfAlO₃,” *Applied Physics Letters*, vol. 108, no. 18, article 183501, 2016.
- [11] D. Zhou, U. Schroeder, J. Xu et al., “Reliability of Al₂O₃-doped ZrO₂ high-*k* dielectrics in three-dimensional stacked metal-insulator-metal capacitors,” *Journal of Applied Physics*, vol. 108, no. 12, article 124104, 2010.
- [12] B. H. Lee, “Unified TDDDB model for stacked high-*k* dielectrics,” International Conference on IC Design and Technology. pp. 83–87, IEEE, Austin, USA (2009).
- [13] X. Zhong, I. Rungger, P. Zapol, H. Nakamura, Y. Asai, and O. Heinonen, “The effect of a Ta oxygen scavenger layer on HfO₂-based resistive switching behavior: thermodynamic stability, electronic structure, and low-bias transport,” *Physical Chemistry Chemical Physics*, vol. 18, pp. 7502–7510, 2016.
- [14] H. Nakamura and Y. Asai, “Competitive effects of oxygen vacancy formation and interfacial oxidation on an ultra-thin HfO₂-based resistive switching memory: beyond filament and charge hopping models,” *Physical Chemistry Chemical Physics*, vol. 18, pp. 8820–8826, 2016.
- [15] X. Li, C. H. Tung, and K. L. Pey, “The nature of dielectric breakdown,” *Applied Physics Letters*, vol. 93, no. 7, article 072903, 2008.
- [16] X. Wu, D. Cha, M. Bosman et al., “Intrinsic nanofilamentation in resistive switching,” *Journal of Applied Physics*, vol. 113, no. 11, Article ID 114503, 2013.
- [17] X. Wu, S. Mei, M. Bosman et al., “Evolution of Filament Formation in Ni/HfO₂/SiO_x/Si-Based RRAM Devices,” *Advances in Electronics*, vol. 1, Article ID 1500130, 2015.
- [18] J. Molina, R. Ortega, W. Calleja, P. Rosales, C. Zuniga, and A. Torres, “MOHOS-type memory performance using HfO₂ nanoparticles as charge trapping layer and low temperature annealing,” *Materials Science and Engineering: B-Advanced*, vol. 177, pp. 1501–1508, 2012.
- [19] J. Molina, R. Ortega, W. Calleja, P. Rosales, C. Zuniga, and A. Torres, “HfO₂ nanoparticles embedded within a SOG-based oxide matrix as charge trapping layer for SOHOS-type memory applications,” *Journal of Non-Crystalline Solids*, vol. 358, no. 17, pp. 2482–2488, 2012.
- [20] S. K. Nandi, X. Liu, D. K. Venkatachalam, and R. G. Elliman, “Effect of Electrode Roughness on Electroforming in HfO₂ and Defect-Induced Moderation of Electric-Field Enhancement,” *Physical Review Applied*, vol. 4, article 064010, 2015.
- [21] J. Ke, T. Wei, D. Tsai, C. Lin, and J. He, “Surface effects of electrode-dependent switching behavior of resistive random-access memory,” *Applied Physics Letters*, vol. 109, no. 13, article 131603, 2016.
- [22] J. Molina, R. Valderrama, C. Zuniga et al., “Influence of the surface roughness of the bottom electrode on the resistive-switching characteristics of Al/Al₂O₃/Al and Al/Al₂O₃/W structures fabricated on glass at 300°C,” *Microelectronics Reliability*, vol. 54, no. 12, pp. 2747–2753, 2014.
- [23] C. A. Volkert and A. M. Minor, “Focused Ion Beam Microscopy and Micromachining,” *MRS Bulletin*, vol. 32, no. 5, pp. 389–399, 2007.
- [24] R. Thamankar, N. Raghavan, J. Molina et al., “Single vacancy defect spectroscopy on HfO₂ using random telegraph noise signals from scanning tunneling microscopy,” *Journal of Applied Physics*, vol. 119, no. 8, article 084304, 2016.
- [25] A. Ranjan, N. Raghavan, K. Shubhakar et al., “CAFM based spectroscopy of stress-induced defects in HfO₂ with experimental evidence of the clustering model and metastable vacancy defect state,” in *Proceedings of the 2016 International Reliability Physics Symposium, IRPS 2016*, pp. 7A41–7A47, IEEE, Pasadena, California, USA, April 2016.
- [26] A. Ranjan, N. Raghavan, J. Molina, S. J. O’Shea, K. Shubhakar, and K. L. Pey, “Analysis of quantum conductance, read disturb and switching statistics in HfO₂ RRAM using conductive AFM,” *Microelectronics Reliability*, vol. 64, pp. 172–178, 2016.
- [27] S. P. Adhikari, M. P. Sah, H. Kim, and L. O. Chua, “Three fingerprints of memristor,” *IEEE Transactions on Circuits and Systems*, vol. 60, no. 11, pp. 3008–3021, 2013.
- [28] D. Bielek, Z. Bielek, V. Biolkova, and Z. Kolka, “Some fingerprints of ideal memristors,” in *Proceedings of the 2013 IEEE International Symposium on Circuits and Systems, ISCAS 2013*, pp. 201–204, Beijing, China, May 2013.
- [29] L. Chua, “Resistance switching memories are memristors,” *Applied Physics A*, vol. 102, no. 4, pp. 765–783, 2011.
- [30] J. Molina, R. Thamankar, and K. L. Pey, “Performance of ultra-thin HfO₂-based MIM devices after oxygen modulation and post-metallization annealing in N₂,” *Physica Status Solidi (A) Applications and Materials Science*, vol. 213, no. 7, pp. 1807–1813, 2016.
- [31] R. Thamankar, F. M. Puglisi, A. Ranjan et al., “Localized characterization of charge transport and random telegraph noise at the nanoscale in HfO₂,” *Journal of Applied Physics*, vol. 122, no. 2, article 024301, 2017.

Research Article

CMOS Realization of All-Positive Pinched Hysteresis Loops

B. J. Maundy,¹ A. S. Elwakil,^{2,3} and C. Psychalinos⁴

¹Department of Electrical and Computer Engineering, University of Calgary, Calgary, AB, Canada T2N 1N4

²Department of Electrical and Computer Engineering, University of Sharjah, Sharjah, UAE

³Nanoelectronics Integrated Systems Center (NISC), Nile University, Giza 12588, Egypt

⁴Physics Department, Electronics Laboratory, University of Patras, Rio, 26504 Patras, Greece

Correspondence should be addressed to B. J. Maundy; bmaundy@ucalgary.ca

Received 21 March 2017; Accepted 20 June 2017; Published 6 August 2017

Academic Editor: Jesus M. Munoz-Pacheco

Copyright © 2017 B. J. Maundy et al. This is an open access article distributed under the Creative Commons Attribution License, which permits unrestricted use, distribution, and reproduction in any medium, provided the original work is properly cited.

Two novel nonlinear circuits that exhibit an all-positive pinched hysteresis loop are proposed. These circuits employ two NMOS transistors, one of which operates in its triode region, in addition to two first-order filter sections. We show the equivalency to a charge-controlled resistance (memristance) in a decremental state via detailed analysis. Simulation and experimental results verify the proposed theory.

1. Introduction

Pinched hysteresis was proposed to be a signature of memristive devices [1, 2], yet it can also be observed in several other nonlinear devices such as nonlinear inductors (capacitors) with quadratic-type current (voltage) dependence [3]. Finding a general model for pinched hysteresis behavior was attempted in [4] for specific devices labeled as memristors [5]. In [6] and from a simplified mathematical point of view, the following model was proposed and shown to exhibit a pinched hysteresis behavior which can fit both charge-controlled and flux-controlled memristance definitions:

$$y(t) = x(t) \times \left(a + \frac{1}{T} \int_0^t x(\tau) d\tau \right), \quad (1)$$

where if $y(t) = v(t)$ and $x(t) = i(t)$, the charge-controlled memristance is obtained, while for the alternative setting $y(t) = i(t)$ and $x(t) = v(t)$, the flux-controlled memristance is obtained. In (1), the constants a and T are scaling and integration time constants, respectively. Note that circuit realization of this model for the purpose of emulating its pinched hysteresis behavior in non-solid-state devices requires a multiplier block, an integrator block, and an adder [6]. Several other emulator circuits have recently

been proposed in the literature [7–13]. It is important to note that (1) is nonlinear due to the multiplication term and that pinched hysteresis cannot appear in a linear system. It is also possible to include other forms of nonlinearity that apply to the shaping of the loop as a result of shaping the applied excitation. This means replacing $x(t)$ in (1) more generally with $f(x(t))$.

Pinched hysteresis loop is generally observed as a result of applying a bipolar sinusoidal voltage or current excitation signal and is thus symmetrical around the origin. Nonsymmetrical loops can also be obtained when the pinch point is shifted away from the origin. However, an all-positive pinched loop, to the best of our knowledge, has not been demonstrated before. It is the purpose of this work to introduce two simple circuits where this behavior is observed. We rely on the inherent nonlinearity of a MOS transistor to perform the multiplication operation required by (1) in order to obtain a charge-controlled memristance. Recall that a MOS transistor current-voltage relation can be described by

$$i_{ds} = k \left[(v_{gs} - V_T) v_{ds} - \frac{v_{ds}^2}{2} \right], \quad (2)$$

where i_{ds} is the drain-to-source current, v_{gs} and v_{ds} are, respectively, the gate-to-source and drain-to-source voltage, V_T is the threshold voltage, and k is a constant in A/V^2 units. It is obvious from (2) that a multiplication operation is inherent through the term $(v_{gs} - V_T)v_{ds}$. However, for an NMOS transistor, the current is unidirectional and the condition $v_{gs} > V_T$ is necessary for the transistor to switch on. Therefore, if (2) is successfully reconfigured to implement (1), an all-positive pinched hysteresis loop can be obtained. In the first part of this work, we do not attempt to remove the extra nonlinear term $v_{ds}^2/2$ and therefore it remains affecting the pinched loop. However, this effect is minimized via proper selection of the design parameters. In a later section of the work, we employ a linearization circuit to remove this quadratic term and hence ensure that only the multiplication nonlinearity term remains. As a result and comparing (2) to (1) assuming $v_{ds}^2/2$ is minimized or eliminated, it is clear that the mapping $i_{ds} \rightarrow y(t)$, $v_{ds} \rightarrow x(t)$, and $K(v_{gs} - V_T) \rightarrow a + (1/T) \int_0^t x(\tau) d\tau$ is necessary. To achieve this, we adopt a frequency-domain approach which also allows independent adjustment of the fixed part and the charge-controlled part of the memristance. We stress and clarify the role played by the capacitors in the proposed circuits, which is crucial to the understanding of pinched hysteresis behavior in general, as clearly seen in [17, 18] for solid-state devices as well. Note that, in reconfiguring (2) to realize (1) via this mapping, we are essentially modifying the MOS transistor transconductance such that it is state-controlled, with the state variable being the terminal voltage of the transconductance v_{ds} . The time constant T necessary in (1) can only be obtained with an embedded capacitance (physical or parasitic) [17, 18]. Finally, it must be stated that this paper is concerned with the ‘‘pinched hysteresis behavior’’ as a behavior rather than with proposing yet another memristor emulator. The design concept of the circuits under study here is completely new and relies on a frequency-domain approach rather than a time-domain approach. It also shows for the first time that pinched hysteresis can even be unipolar, something not possible with memristors as they are so defined.

This manuscript is organized as follows. Section 2 looks at the proposed circuits and presents the theory behind their operation that leads to pinched hysteresis behavior. Section 3 computes the memristance of the proposed circuits, with numerical simulations, and presents pinch-off analysis of the proposed circuits. In Section 4, a method to linearize the main transistor in triode is presented which removes the extra nonlinear term $v_{ds}^2/2$ in (2). In Section 5, simulation and experimental results are presented, and finally our conclusions are given in Section 6.

2. The Proposed Circuits

Consider the circuits shown in Figure 1 both consisting of opamp A_1 connected as a buffer and opamp A_2 along with the NMOS transistor M_2 as a simple voltage to current converter which converts the voltage of the noninverting terminal of A_2 into a current i_{in} through NMOS transistor

M_1 . It is essential for M_1 to remain in triode, hence acting as a transconductance. Both circuits contain a lossy integrator comprising R_1, C_1 , and a DC bias voltage V_{dc_1} required to maintain M_1 in triode ($V_{dc_1} > V_T$, $V_{DS_1} < V_{dc_1} - V_T$). The difference between the two circuits can be seen in their high-pass filter sections. In the case of Figure 1(a), it consists of R_2, C_2 with an additional DC source V_{dc_2} providing a DC voltage to the drain of M_1 . For Figure 1(b), the high-pass filter is made up of $r_{1,2}, C_2$ and here the drain-to-source DC biasing of M_1 comes from V_{dc_1} through $r_{1,2}$ as αV_{dc_1} , where $\alpha = r_1/(r_1 + r_2)$. Note that maintaining transistor M_1 in triode in both circuits requires that $V_{dc_1} - V_{dc_2} > V_T$ and $(1 - \alpha)V_{dc_1} > V_T$ for Figures 1(a) and 1(b), respectively.

The lossy integrator of each circuit has a response given in the frequency domain which can be written as

$$H_1(\omega) = |H_1(\omega)| \angle -\theta_1 = \frac{1}{\sqrt{1 + \omega^2 \tau_1^2}} \angle \tan^{-1}(\omega \tau_1), \quad (3)$$

where $\tau_1 = R_1 C_1$. Meanwhile, the high-pass filter in Figure 1(a) has a response

$$\begin{aligned} H_{2a}(\omega) &= |H_{2a}(\omega)| \angle \theta_{2a} \\ &= \frac{\omega \tau_2}{\sqrt{1 + \omega^2 \tau_2^2}} \angle (90^\circ - \tan^{-1}(\omega \tau_2)), \end{aligned} \quad (4)$$

with $\tau_2 = R_2 C_2$, and likewise the response of the high-pass filter in Figure 1(b) is

$$\begin{aligned} H_{2b}(\omega) &= |H_{2b}(\omega)| \angle \theta_{2b} \\ &= \alpha \sqrt{\frac{1 + \omega^2 \tau_z^2}{1 + \omega^2 \tau_p^2}} \angle \tan^{-1}(\omega \tau_z) - \tan^{-1}(\omega \tau_p), \end{aligned} \quad (5)$$

where $\tau_z = r_2 C_2$ and $\tau_p = (r_1/r_2) C_2$. Clearly, both high-pass filters provide a leading phase shift by different amounts while DC biasing voltages are allowed to be passed on to the transistor M_1 to set V_{DS_1} . For an input voltage of amplitude A and frequency ω_o in the form $v_{in}(t) = A \sin(\omega_o t) + V_{dc_1}$, it follows that the time dependent V_{GS} voltage of M_1 is

$$V_{GS_1}(t) = A |H_1(\omega_o)| \sin(\omega_o t - \theta_1) + V_{dc_1}, \quad (6)$$

while the time dependent V_{DS} voltages in Figures 1(a) and 1(b) are, respectively,

$$\begin{aligned} V_{DS_1}(t) &= A |H_{2a}(\omega_o)| \sin(\omega_o t + \theta_{2a}) + V_{dc_2}, \\ V_{DS_1}(t) &= A |H_{2b}(\omega_o)| \sin(\omega_o t + \theta_{2b}) + \alpha V_{dc_1}, \end{aligned} \quad (7)$$

where, for (7), $A < V_{dc_2}$ and $A < \alpha V_{dc_1}$, respectively. Substituting (6)-(7) into (2) yields after considerable simplification

$$\begin{aligned} i_{in}(t) &= -\hat{A} \cos(2\omega_o t - \theta_1 + \theta_{2a}) + \hat{B} \sin(\omega_o t - \theta_1) \\ &\quad + \hat{C} \sin(\omega_o t + \theta_{2a}) + \hat{D} \cos(2\omega_o t + 2\theta_{2a}) \\ &\quad + \hat{E} + \hat{I}_{off}, \end{aligned} \quad (8)$$

TABLE 1: Summary of the coefficients in (8) and (9) for Figures 1(a) and 1(b).

Coefficient	Figure 1(a)	Figure 1(b)
\widehat{A}	$\frac{1}{2}kA^2 H_1(\omega_o) H_{2a}(\omega_o) $	$\frac{1}{2}kA^2 H_1(\omega_o) H_{2b}(\omega_o) $
\widehat{B}	$kA H_1(\omega_o) V_{dc2}$	$\alpha kA H_1(\omega_o) V_{dc1}$
\widehat{C}	$kA H_{2a}(\omega_o) (V_{dc1} - V_{dc2} - V_T)$	$kA H_{2b}(\omega_o) [(1 - \alpha)V_{dc1} - V_T]$
\widehat{D}	$\frac{1}{4}kA^2 H_{2a}(\omega_o) ^2$	$\frac{1}{4}kA^2 H_{2b}(\omega_o) ^2$
\widehat{E}	$\widehat{A} \cos(\theta_1 + \theta_{2a}) - \widehat{D}$	$\widehat{A} \cos(\theta_1 + \theta_{2b}) - \widehat{D}$
\widehat{I}_{off}	$k[(V_{dc1} - V_T)V_{dc2} - \frac{1}{2}V_{dc2}^2]$	$\alpha k[(1 - \frac{\alpha}{2})V_{dc1} - V_T]V_{dc1}$

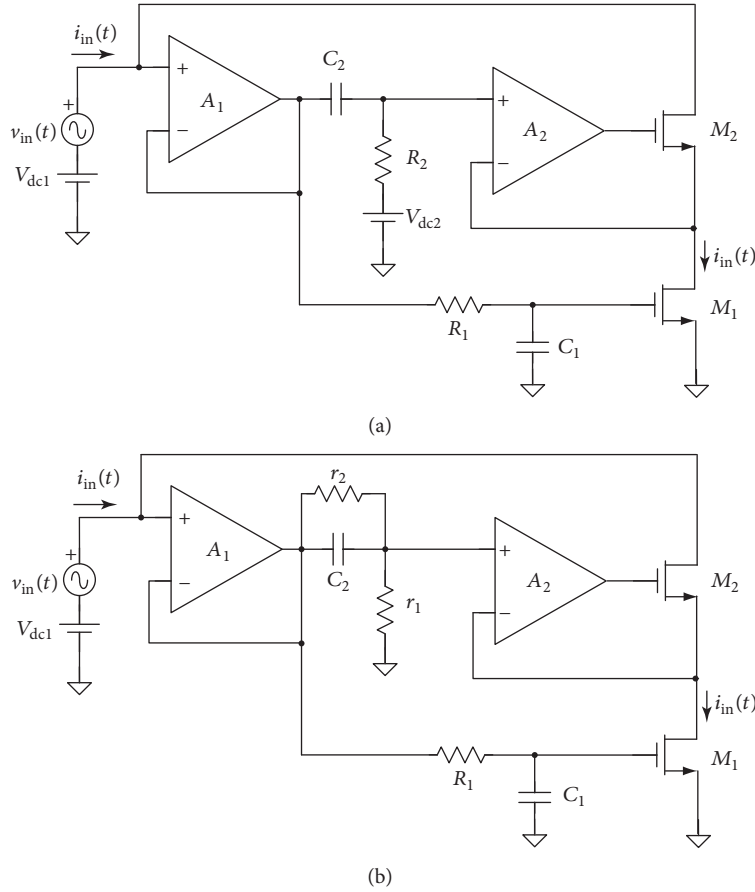


FIGURE 1: The proposed nonlinear circuits with unipolar pinched hysteresis loop.

for Figure 1(a), and

$$\begin{aligned}
 i_{in_b}(t) = & -\widehat{A} \cos(2\omega_o t - \theta_1 + \theta_{2b}) + \widehat{B} \sin(\omega_o t - \theta_1) \\
 & + \widehat{C} \sin(\omega_o t + \theta_{2b}) + \widehat{D} \cos(2\omega_o t + 2\theta_{2b}) \quad (9) \\
 & + \widehat{E} + \widehat{I}_{off},
 \end{aligned}$$

for Figure 1(b). The coefficients of the $\sin(\cdot)$ and $\cos(\cdot)$ terms in (8) and (9) are given in Table 1. Note that, with the exception of \widehat{I}_{off} , all coefficients in Table 1 are frequency dependent. This implies that it is necessary to choose proper values for time constants in order to observe the hysteresis behavior.

Close inspection of (8) under the assumption that $\theta_{2a} \cong \pi/2 - \theta_1$ shows that it can be rewritten in the dimensionless form

$$\begin{aligned}
 & y(t) + y_{off} \\
 & = x(t) |H_1(\omega)| \left[1 - \omega |H_{2a}(\omega)| \int_0^t x(\tau) d\tau \right] \quad (10) \\
 & + \frac{|H_{2a}(\omega)|}{\omega} \dot{x}(t) - \frac{|H_{2a}(\omega_o)|^2}{2\omega^2} [\dot{x}(t)]^2 + x_{off},
 \end{aligned}$$

where $x(t) = \sin(\omega t - \theta_1)$ represents an already phase shifted input signal. The term in the square brackets is clearly similar to (1) while additional $\dot{x}(t)$ and $\dot{x}^2(t)$ terms outside the

TABLE 2: Summary of several analog circuits with pinched hysteresis and actual analog memristor emulators to date and their designs. MB: multiplier block; OPA: operational amplifier; CCI: second-generation current conveyors; AH: additional hardware, which may be in the form of buffers, multiplexers, diodes, inverters, switches, and so forth; I/D: incremental/decremental memristance emulation. The number (#) of transistors refers to the discrete number of external transistors. * An OTA was used here in place of an OPA.

Reference []	MB	OPAs	CCIs	# of trans.	AH	Quadrant	I/D
[6]	1	—	3	—	Yes	2	Both
[7]	—	1*	2	—	No	2	I
[8]	1	—	2	—	No	2	I
[9]	—	2	1	2	No	2	D
[10]	1	5	—	10	Yes	2	Both
[11]	—	2	1	1	No	2	I
[12]	—	—	3	1	No	2	I
[13]	1	2	—	—	Yes	2	D
[14]	1	—	2	—	Yes	2	I
[15]	—	1*	1	2	No	2	Both
[16]	—	—	4	—	Yes	2	NA
This work	—	2	—	2	No	1	D

brackets are unwanted and will result in a nonsymmetrical loop. Note that the offset terms y_{off} and x_{off} present are a result of the input being DC level shifted. However, using (10) and assuming that ω is sufficiently large such that the second and third terms are negligible and in addition translating the origin to $(x_0, y_0) = (x_{\text{off}}, y_{\text{off}})$, we obtain

$$\begin{aligned}
 y(t) &= x(t) \\
 &\times \left[|H_1(\omega)| - \omega |H_{2a}(\omega)| |H_1(\omega)| \int_0^t x(\tau) d\tau \right], \quad (11)
 \end{aligned}$$

which compared to (1) has the slightly modified form $y(t) = x(t) \times (a + (ab/T) \int_0^t x(\tau) d\tau)$, where $a = |H_1(\omega)|$ and $b = -|H_{2a}(\omega)|$.

Finally, in comparison with other circuits which also exhibit pinched hysteresis behavior and some of which are labeled as analog memristor emulators as shown in Table 2, about half of them use discrete multiplier blocks which are inefficient. By far, the vast majority use second-generation current conveyors with the only commercial one being the AD844, and several use additional hardware in the form of buffers, multiplexers, diodes, and switches. If the total component count is used as a figure of merit, then the proposed circuits of Figure 1 have the lowest count with their main drawback being operation in one quadrant. Note that even though our proposed circuits are listed among those identified as “memristors” or “memristor emulators,” we refrain from labeling our proposed circuits as “memristor emulators” and simply label them as among circuits having pinched hysteresis behavior.

3. Charge-Controlled Resistance (Memristance) Calculation

Using (11) and setting $x(t) = i(t)/I_{\text{ref}}$, $y(t) = v(t)/I_{\text{ref}}R_s$, where I_{ref} is an arbitrary reference current and R_s is an arbitrary scaling resistor, the memristance value for Figure 1(a) can be obtained as

$$R_{m_a} = R_s |H_1(\omega)| \left[1 - \frac{\omega |H_{2a}(\omega)|}{I_{\text{ref}}} q(t) \right], \quad (12)$$

where $q(t)$ is the electrical charge. Note that since the input signal has a fixed $\omega = 1/T$, we can rewrite this memristance as

$$R_{m_a} = R_s \left| H_1 \left(\frac{1}{T} \right) \right| \left[1 - \frac{1}{T} \frac{|H_{2a}(1/T)|}{I_{\text{ref}}} q(t) \right], \quad (13)$$

which has a fixed resistive part equal to $R_s |H_1(1/T)|$ and a charge-controlled part equal to $R_s |H_1(1/T)| |H_{2a}(1/T)|$. It is thus clear that while the transfer function H_1 controls the magnitude of both parts, H_{2a} can change the magnitude of the charge-controlled part alone. Note that this memristance is decremental [6]. Furthermore, note that, for sufficiently high frequency such that $\omega \gg 1/\tau_1$, $|H_1(\omega)| \approx 1/\omega\tau_1$ and it follows that the fixed part of the realized memristance is approximately $R_s(T/\tau_1)$. However, for sufficiently high frequency such that $\omega \gg 1/\tau_2$, we also note that $|H_{2a}(\omega)| \approx 1$ and therefore the realized memristance can be approximated as

$$R_{m_a} \approx R_s \left(\frac{T}{\tau_1} \right) \left[1 - \frac{R_s}{T \times 1V} q(t) \right]. \quad (14)$$

We can further express the electrical charge as $q(t) = C_1 v_{C_1}(t)$ since the only capacitor in the circuit in this case capable of

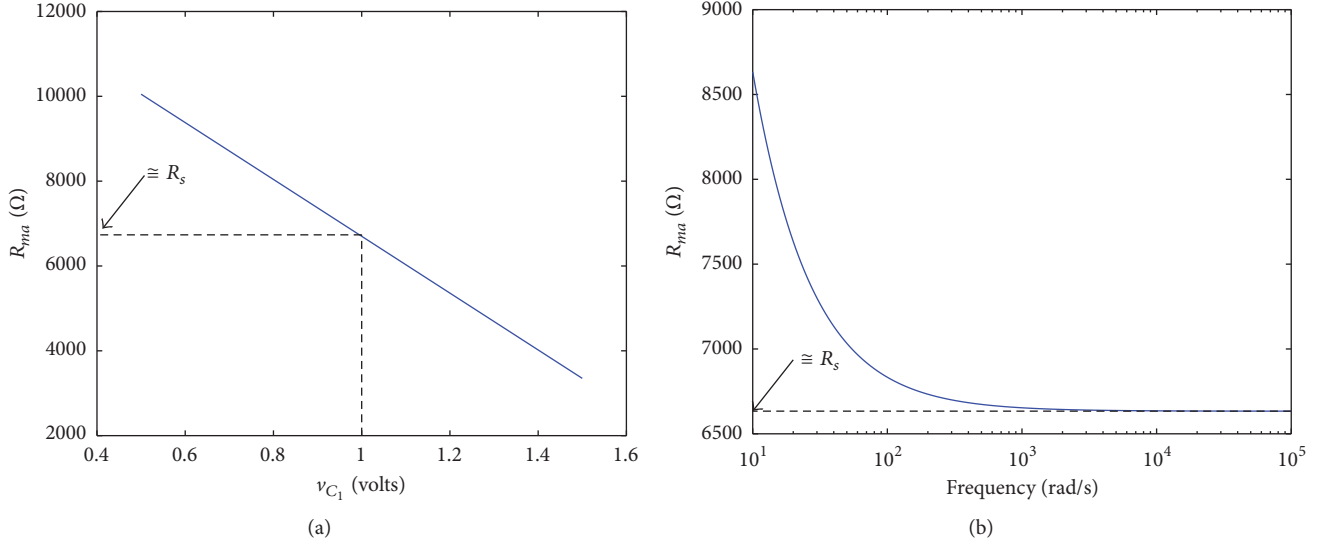


FIGURE 2: (a) Plot of memristance R_{ma} versus capacitor voltage $v_{C_1} = v_{C_1}/1V$ when $m = v_{C_1}/100$, $R_s = 6.7 \text{ k}\Omega$, $R_{\text{off}_a} = 12.67 \text{ k}\Omega$, and $\omega \gg 1/\tau_1$. (b) Plot of R_{ma} versus frequency when $C_1 = 10 \mu\text{F}$.

holding a charge is C_1 following the fact that $|H_{2a}(\omega)| \approx 1$. Accordingly,

$$R_{ma} \approx \left(\frac{R_s T}{R_1 C_1} \right) \left[1 - \frac{R_s}{T} C_1 v_{C_{1n}}(t) \right] \quad (15)$$

$$R_{ma} = \frac{R_s^2}{R_1} \left(\frac{T}{R_s C_1} - v_{C_{1n}}(t) \right),$$

where $v_{C_{1n}}(t)$ is the normalized (by 1V) voltage across C_1 . In a final step, we may freely express the period T of the applied signal as a ratio of $R_s C_1$ (i.e., $T = m R_s C_1$) leading to the simplified expression

$$R_{ma} \approx \frac{R_s^2}{R_1} (m - v_{C_{1n}}(t)) = R_s (m - v_{C_{1n}}(t)), \quad (16)$$

if we select the arbitrary reference resistance as $R_s = R_1$. Note that, for the condition $\omega \gg 1/\tau_1$ to be satisfied, it follows that $m \ll 1$.

The expression in (16) is significantly important for two aspects:

- (i) It shows that although the circuit has an all-positive input resistance, theoretically and according to (16), the memristance is not always positive. However, it remains positive because the origin has been already shifted to $(x_0, y_0) = (x_{\text{off}}, y_{\text{off}})$. With reference back to the origin $(x_0, y_0) = (0, 0)$, (16) then becomes

$$R_{ma} \approx R_s (m - v_{C_{1n}}(t)) + R_{\text{off}_a}, \quad (17)$$

where $R_{\text{off}_a} = V_{d_{c_1}}/V_{d_{c_2}}/k[(2 - V_{d_{c_2}}/V_{d_{c_1}})V_{d_{c_1}} - V_T]$. Figures 2(a) and 2(b) show the variation of the memristance versus the capacitor voltage v_{C_1} and versus frequency ω , respectively. In Figure 2(a), for the values chosen: $m = v_{C_1}/100$, $V_{d_{c_1}} = 1 \text{ V}$, $V_{d_{c_2}} =$

0.4 V , $V_T = 0.35 \text{ V}$, and $k = 0.15 \text{ mA/V}^2$, we obtain $R_{\text{off}_a} = 12.67 \text{ k}\Omega$. Correspondingly, selecting a suitable reference current such as $I_{\text{ref}} = 0.15 \text{ mA}$ leads to a nominal value for R_s of $6.7 \text{ k}\Omega$ (i.e., $I_{\text{ref}} R_s \approx 1 \text{ V}$). For Figure 2(b), we fixed $v_{C_1} = 1 \text{ V}$ and $C_1 = 10 \mu\text{F}$ and show the decremental nature of the memristance whereas the frequency increases when R_{ma} asymptotically approaches R_s .

- (ii) It highlights the significance and necessity of the existence of a capacitor in order to hold the charge. In this circuit, this capacitor is C_1 ; however, in solid-state devices, this capacitor may well be a parasitic capacitor or equivalent of parasitic capacitances as observed in [17, 18]. It thus appears to the authors that it is not possible to isolate the appearance of pinched hysteresis loops from the existence of a capacitive effect.

In a similar manner, the memristance of the circuit in Figure 1(b) can be obtained as

$$R_{mb} = R_s \left| H_1 \left(\frac{1}{T} \right) \right| \left[\alpha - \frac{1}{T} \frac{|H_{2b}(1/T)|}{I_{\text{ref}}} q(t) \right], \quad (18)$$

which unlike (13) has a fixed resistive part equal to $\alpha R_s |H_1(1/T)|$ but an identical charge-controlled part. Noting that $|H_{2b}(1/T)| = \alpha$ for $1/T \gg 1/\tau_1$ and making the same assumptions as before, a generalized expression for R_{mb} can be given as

$$R_{mb} \approx \alpha \frac{R_s^2}{R_1} (m - v_{C_{1n}}(t)) + R_{\text{off}_b} \quad (19)$$

$$R_{mb} = \alpha R_s (m - v_{C_{1n}}(t)) + R_{\text{off}_b},$$

where $R_{\text{off}_b} = 1/\alpha k[(2 - \alpha)V_{d_{c_1}} - V_T]$.

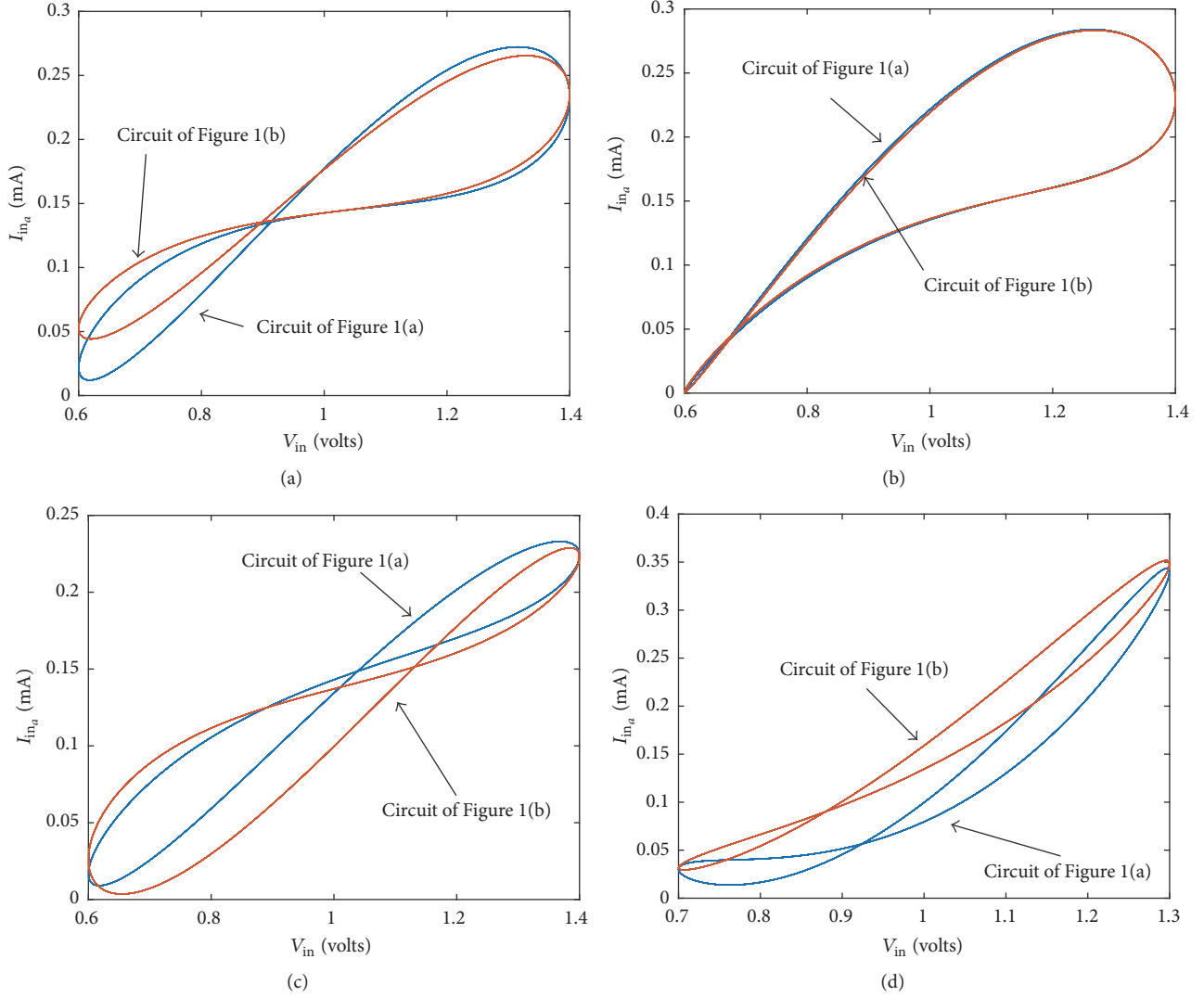


FIGURE 3: Matlab simulation of the I - V characteristics of Figures 1(a) and 1(b) as given by (8) and (9), respectively. (a) $\tau_2 = \tau_1 = \tau_z$, $\tau_p = \alpha\tau_z$ with $\alpha = 0.4$. (b) $\tau_2 = 10\tau_1 = \tau_z$, $\tau_p = \alpha\tau_z$ with $\alpha = 0.4$. (c) $\tau_2 = \tau_1 = \tau_z$, $\tau_p = \alpha\tau_z$ with $\alpha = 0.286$ and $V_{dc_2} = 0.3$ V. (d) $\tau_2 = \tau_1 = 0.1\tau_z$, $\tau_p = \alpha\tau_z$ with $\alpha = 0.33$, $V_{dc_2} = 0.3$ V, and $A = 0.5$ V and $A = 0.3$ V for Figures 1(a) and 1(b), respectively.

3.1. Numerical Simulations. Sample Matlab plots of (8) and (9) are shown in Figures 3(a)–3(c) to normalized values of $k = 1$ mA/V², $A = 0.4$ V, $V_{dc_1} = 1$ V, and $V_T = 0.35$ V. In the first of the plots shown in Figure 3(a), $\tau_2 = \tau_1 = \tau_z$, $\tau_p = \alpha\tau_z$ with $\alpha = 0.4$ and the applied sinusoidal voltage frequency $\omega_o > 1/\tau_1$ and $V_{dc_2} = 0.4$ V. Note that having $\alpha = 0.4$ is equivalent to setting $V_{dc_2} = \alpha V_{dc_1}$ and that $\theta_{2b} \approx \theta_{2a} = \pi/2 - \theta_1$. In this figure, we see that neither loop is symmetrical which is attributed to the $\dot{x}(t)$ and $\dot{x}^2(t)$ terms (see (10)) and the phase shift term introduced by the lossy integrator. In the second plot, shown in Figure 3(b), $\tau_2 = 10\tau_1 = \tau_z$, $\tau_p = \alpha\tau_z$ with $\alpha = 0.4$ and $V_{dc_2} = 0.4$ V as before but $\theta_{2a} \approx \theta_{2b} \approx 0$. The pinched loops from the two circuits are nearly identical and the upper lobe is far bigger than the lower one. In Figure 3(c), $\tau_2 = \tau_1 = \tau_z$, $\tau_p = \alpha\tau_z$ with $\alpha = 0.286$, $V_{dc_2} = 0.3$ V, and $\theta_{2b} \approx \theta_{2a} = \pi/2 - \theta_1$. Clearly, as α or V_{dc_2} decreases, the upper

lobe decreases in size and the pinch point increases. Note the reduced value of A for the circuit (Figure 1(a) or (8)). This implies that the circuit of Figure 1(a) must work with reduced input amplitudes compared to the circuit of Figure 1(b), unless V_{dc_1} and V_{dc_2} are adjusted in tandem. This is not the case for the circuit of Figure 1(b) where DC bias voltages are related by α which is fixed for $\omega_o > 1/\tau_1$.

Finally, in Figure 3(d), $\omega < 1/\tau_1$ with $\tau_2 = \tau_1 = 0.1\tau_z$, $\tau_p = \alpha\tau_z$, $\alpha = 0.33$, and $V_{dc_2} = 0.3$ V. Under these conditions, $\theta_{2b} \ll \theta_{2a} = \pi/2 - \theta_1$, and decreased amplitudes must now be used in the circuit of Figure 1(b) or (9) compared to the circuit of Figure 1(a) or (8). Therefore, we select $A = 0.5$ V and $A = 0.3$ V for the two circuits, respectively, in this case.

3.2. Pinch Point Analysis. The unique form of (8) and (9) allows for a closed-loop solution of the pinch-off point in

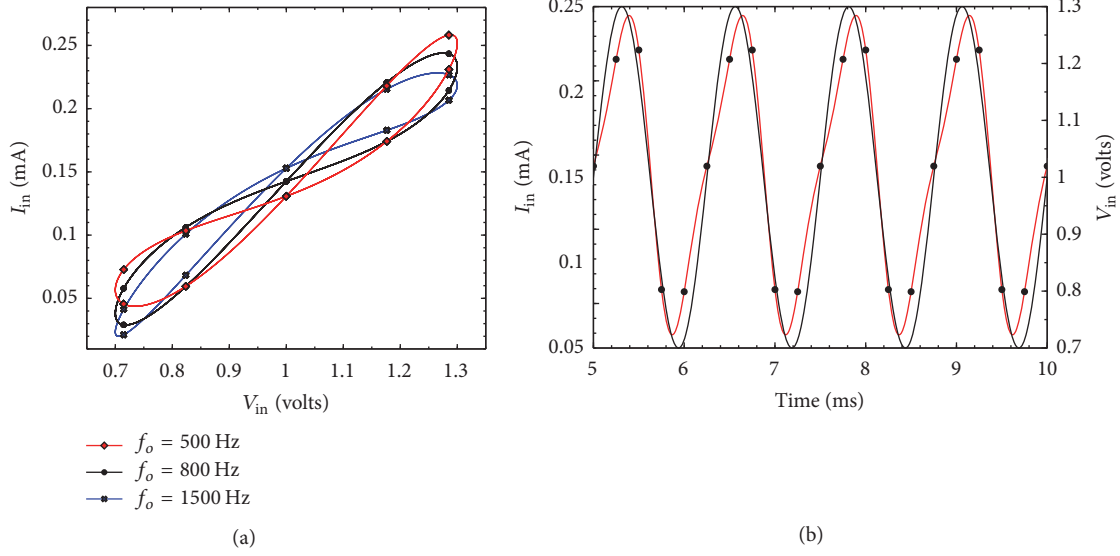


FIGURE 4: (a) Matlab simulation of the I - V characteristic of Figure 1(a) governed by (8) to $A = 0.3$ V, $\tau_2 = \tau_1 = 500$ μ s, $V_{dc_1} = 1$ V, $V_T = 0.35$ V, $k = 1$ mA/V², and $V_{dc_2} = 0.325$ V. (b) Input voltage $v_{in}(t)$ and current $i_{in_a}(t)$ plotted as a function of time at a frequency of $\omega = 2\pi \times 800$ rad/s.

these circuits. It can be shown after considerable simplification that (8) and (9) have a pinch-off point $[\widehat{V}_{in_p}, \widehat{I}_{in_p}]$ given by

$$\begin{aligned} \widehat{V}_{in_p} &= V_{dc_1} - A\widehat{X}(\Theta), \\ \widehat{I}_{in_p} &= -\widehat{A} \cos [2 \sin^{-1} (X(\Theta)) + \theta_{2a,2b} - \theta_1] \\ &\quad - \widehat{B} \sin [\sin^{-1} (X(\Theta)) - \theta_1] \\ &\quad - \widehat{C} \sin [\sin^{-1} (X(\Theta)) + \theta_{2a,2b}] \\ &\quad + \widehat{D} \cos [2 \sin^{-1} (X(\Theta)) + 2\theta_{2a,2b}] + \widehat{E} \\ &\quad + \widehat{I}_{off}, \end{aligned} \quad (20)$$

where

$$\widehat{X}(\Theta) = \frac{(\widehat{B}/2) \sin(-\theta_1) + (\widehat{C}/2) \sin(\theta_{2a,2b})}{\widehat{A} \sin(\theta_{2a,2b} - \theta_1) - \widehat{D} \sin(2\theta_{2a,2b})}, \quad (21)$$

and the subscripts a, b refer to (8) and (9), respectively. The frequency dependent nature of (20) makes their analysis difficult; however, several observations can be deduced. First, $\widehat{X}(\Theta)$ can be positive or negative depending on the values of θ_1 , θ_{2a} , and θ_{2b} as observed in Figure 3. In addition, C_2 plays an important role even though it is not the main charge holding or integrating capacitor. In Figure 1(a), its minor role is to block V_{dc_1} , as V_{dc_2} is passed, but in both circuits, its main contribution is to add a leading phase shift opposed to the lagging phase shift caused by C_1 . For example, in the circuit of Figure 1(b), in the absence of C_2 , that is, if $C_2 = 0$, then $\sin(\theta_{2b}) = \sin(2\theta_{2b}) = 0$, because $\theta_{2b} = 0$, and with $|H_{2b}(\omega)| = \alpha$, (21) reduces to $\widehat{X}(\Theta) = V_{dc_1}/A$, setting $\widehat{V}_{in_p} = 0$. That is, no pinch point will occur.

Secondly, under the assumption $\tau_2 = \tau_1$, we find that $\widehat{V}_{in_p} = V_{dc_1}$ when $\tan(\theta_1) = \widehat{C}/\widehat{B}$ or when $V_{dc_2} = (V_{dc_1} - V_T)/2$. Under this condition, M_1 remains in triode so long as $V_{dc_1} > 3V_T$ which is easily satisfied. For the general case when $\tau_2 = \beta\tau_1$, implying that $\theta_{2a} \neq \pi/2 - \theta_1$ (unless $\beta = 1$), the general solution to $\widehat{X}(\Theta) = 0$ yields

$$V_{dc_2} = \frac{\beta}{(\beta + 1)} \frac{(\tau_1^2 \omega^2 + 1)}{(\beta \tau_1^2 \omega^2 + 1)} (V_{dc_1} - V_T). \quad (22)$$

Likewise, the value for α in the circuit of Figure 1(b) that results in $\widehat{V}_{in_p} = V_{dc_1}$ can be expressed as

$$\alpha = 1 - \frac{V_T}{V_{dc_1}} - \frac{\omega \tau_1 \csc(\theta_{2b})}{(\omega^2 \tau_1^2 + 1)} \sqrt{\frac{1 + \omega^2 \tau_p^2}{1 + \omega^2 \tau_z^2}}. \quad (23)$$

In both general cases, (22) and (23) are frequency dependent, the exception being when $\beta = 1$ for (22), but both can be minimized for frequency dependance by ensuring that $\omega \tau_1 > 1$, $\omega \tau_z > 1$, and $\omega \tau_p > 1$. Sample plots of the I - V characteristic for the circuit of Figure 1(a) governed by (8) to the conditions $A = 0.3$ V, $\tau_2 = \tau_1 = 500$ μ s, $V_{dc_1} = 1$ V, $V_T = 0.35$ V, $k = 1$ mA/V², and $V_{dc_2} = (V_{dc_1} - V_T)/2 = 0.325$ V are shown in Figure 4(a).

Note that because $\beta = 1$ and $V_{dc_2} = (V_{dc_1} - V_T)/2$, $\widehat{V}_{in_p} = V_{dc_1}$ is independent of the input frequency which is verified at the three frequencies $f_o = [500, 800, 1500]$ Hz, as theoretically predicted. In Figure 4(b), $v_{in}(t)$ and $i_{in_a}(t)$ are plotted as a function of time.

TABLE 3: Summary of the coefficients of the input current $i_{in}(t)$ of Figures 1(a) and 1(b) in response to an input voltage $v_{in}(t)$ when M_1 is replaced by a linearized resistor such as the one shown in Figure 5.

Coefficient	Figure 1(a)	Figure 1(b)
\bar{A}	$\frac{1}{2}kA^2 H_1(\omega_o) H_{2a}(\omega_o) $	$\frac{1}{2}kA^2 H_1(\omega_o) H_{2b}(\omega_o) $
\bar{B}	$kA H_1(\omega_o) V_{dc_2}$	$\alpha kA H_1(\omega_o) V_{dc_1}$
\bar{C}	$kA H_{2a}(\omega_o) (V_{dc_1} - V_T)$	$kA H_{2b}(\omega_o) [V_{dc_1} - V_T]$
\bar{I}_{off}	$k [(V_{dc_1} - V_T) V_{dc_2}]$	$\alpha k [V_{dc_1} - V_T] V_{dc_1}$

$\bar{I}_{off} > \hat{I}_{off}$, with all other terms in the coefficients being equal. The corresponding new pinch point $[\bar{V}_{in_p}, \bar{I}_{in_p}]$ is given by

$$\bar{V}_{in_p} = V_{dc_1} - A\bar{X}(\Theta), \quad (31)$$

$$\begin{aligned} \bar{I}_{in_p} = & -\bar{A} \cos [2 \sin^{-1} (\bar{X}(\Theta)) + \theta_{2a,2b} - \theta_1] \\ & - \bar{B} \sin [\sin^{-1} (\bar{X}(\Theta)) - \theta_1] \\ & - \bar{C} \sin [\sin^{-1} (\bar{X}(\Theta)) + \theta_{2a,2b}] \\ & + \bar{A} \cos (\theta_1 + \theta_{2a,2b}) + \bar{I}_{off}, \end{aligned} \quad (32)$$

where

$$\bar{X}(\Theta) = \frac{(\bar{B}/2) \sin(-\theta_1) + (\bar{C}/2) \sin(\theta_{2a,2b})}{\bar{A} \sin(\theta_{2a,2b} - \theta_1)}. \quad (33)$$

The benefits to linearizing M_1 are immediately clear upon close inspection of (31)–(33). In particular, for the circuit of Figure 1(a) in the general case when $\tau_2 = \beta\tau_1$, the general solution to $\bar{X}(\Theta) = 0$ now yields

$$V_{dc_2} = \frac{\beta(\tau_1^2\omega^2 + 1)}{(\beta^2\tau_1^2\omega^2 + 1)} (V_{dc_1} - V_T), \quad (34)$$

which, for $\beta = 1$, implies that, for $\bar{V}_{in_p} = V_{dc_1}$, V_{dc_2} is chosen such that $V_{dc_2} = V_{dc_1} - V_T$. Of course, under these conditions, the composite linearized resistor is at the edge of the triode and a more practical solution would be for a given $\beta \neq 1$, ω , and τ_1 to simply choose $\beta(\tau_1^2\omega^2 + 1)/(\beta^2\tau_1^2\omega^2 + 1) > V_{dc_2}/(V_{dc_1} - V_T)$. For the circuit of Figure 1(b) employing a linearized M_1 , the choice of α does not affect the pinch point; however, the value of V_{dc_1} that results in $\bar{V}_{in_p} = V_{dc_1}$ is given by

$$\begin{aligned} V_{dc_1} \\ = \frac{V_T}{1 - \omega\tau_1 \csc(\theta_{2b}) \sqrt{(1 + \tau_p^2\omega^2)/(1 + \tau_z^2\omega^2)(1 + \tau_1^2\omega^2)}}, \end{aligned} \quad (35)$$

which is still frequency dependent, but minimization is still possible if $\omega\tau_1 > 1$, $\omega\tau_z > 1$, and $\omega\tau_p > 1$. Last but not

least, no pinching occurs for the circuit of Figure 1(a) using the linearized resistor at frequencies

$$\begin{aligned} \omega_1 &= \frac{1}{\tau_1} \sqrt{\frac{V_{dc_2} + V_T}{2V_{dc_1} - V_{dc_2} - V_T}}, \\ \omega_2 &= \frac{1}{\tau_1} \sqrt{\frac{2V_{dc_1} - V_{dc_2} - V_T}{V_{dc_1} + 2V_{dc_2} + V_T}} \end{aligned} \quad (36)$$

assuming $\tau_2 = \tau_1$ and at

$$\omega_1 = \sqrt{\frac{2V_{dc_1} - V_T}{V_{dc_1}\tau_1\tau_p - \tau_1^2(V_{dc_1} - V_T)}}, \quad (37)$$

$$\omega_2 = \sqrt{\frac{(2V_{dc_1} - V_T)\tau_p + V_T\tau_1}{(\tau_1^3 - 2\tau_1^2\tau_p - \tau_p^2)V_{dc_1} + (\tau_p - \tau_1)\tau_1^2V_T}},$$

for the circuit of Figure 1(b) when $\tau_z = \tau_1 = \alpha\tau_p$.

5. Simulation and Experimental Results

The circuits in Figures 1(a) and 1(b) were simulated and built experimentally. In the sections that follow, simulations of Figures 1(a) and 1(b) without and with linearization of M_1 were conducted. For the experiments, off-the-shelf discrete components were used without linearization of M_1 .

5.1. Simulation Results: Without M_1 Linearization. For simulation purposes, Cadence was used employing the Design Kit offered by the AMS 0.35 μm CMOS process. The opamp utilized in simulations is demonstrated in Figure 6, where the bias scheme was $V_{DD} = -V_{SS} = 5\text{V}$ and $I_O = 300\ \mu\text{A}$. The MOS transistors' aspect ratio is given in Table 4 with $R_c = 140\ \Omega$ and $C_c = 2\ \text{pF}$ to achieve a phase margin of 60° . Also, the aspect ratio of transistor M_1 in Figure 1(a) was $100\ \mu\text{m}/1\ \mu\text{m}$; for M_2 , the aspect ratio was $12\ \mu\text{m}/2\ \mu\text{m}$ and thus its gain factor was $k = 1\ \text{mA}/\text{V}^2$.

The resistor and capacitor values used in simulations were $R_1 = 820\ \Omega$ and $C_1 = C_2 = 470\ \text{nF}$ and, therefore, $\tau_1 = \tau_2$. The DC voltages were $V_{dc_1} = 2\ \text{V}$ and $V_{dc_2} = 0.74\ \text{V}$. Considering a sinusoidal input with $700\ \text{mV}$ amplitude and variable frequency, the obtained i_{in} - v_{in} characteristics, for $f = 600\ \text{Hz}$, $1\ \text{kHz}$, and $1.5\ \text{kHz}$, are demonstrated in Figure 7. The time-domain behavior of the scheme in Figure 1(a) is demonstrated in Figure 8 for a $1\ \text{kHz}$ input voltage. Likewise,

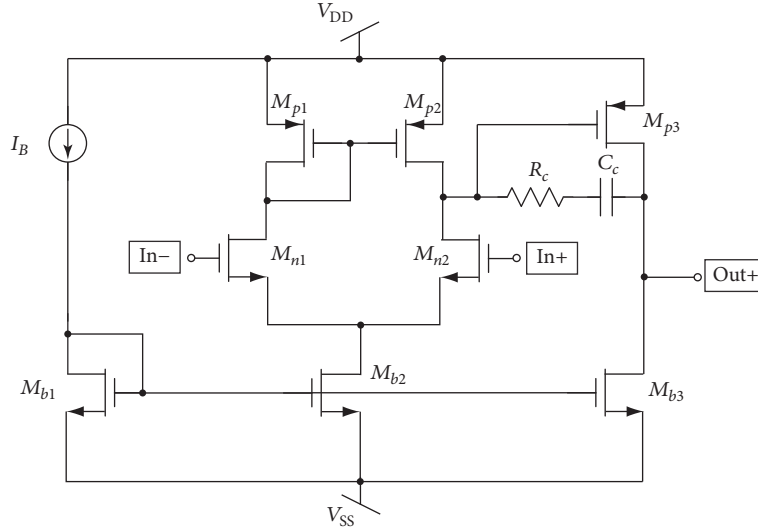


FIGURE 6: Opamp used in simulations.

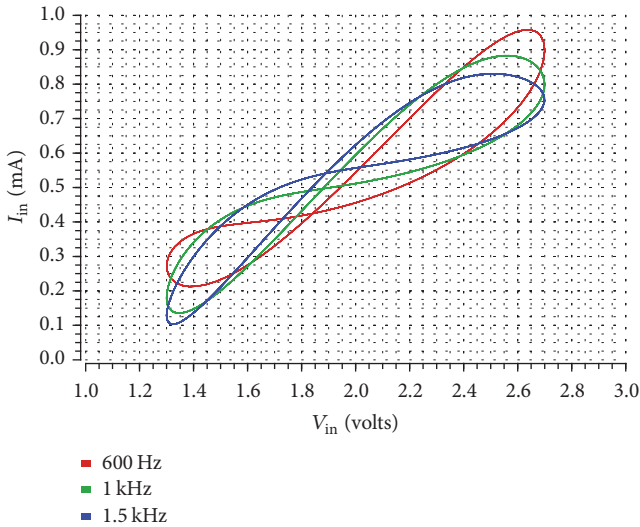
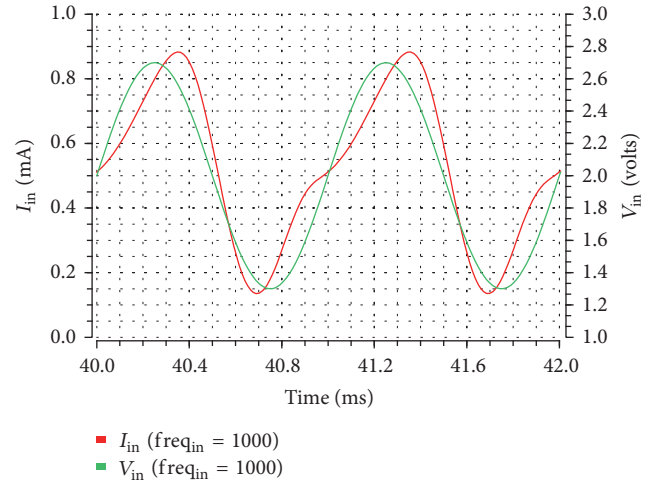
FIGURE 7: Simulated $i_{in} - v_{in}$ characteristics for $f = 600$ Hz, 1 kHz, and 1.5 kHz.

TABLE 4: MOS transistors' aspect ratio for Figure 6.

Transistor	W/L
M_{b1}	$50 \mu\text{m}/2 \mu\text{m}$
$M_{b2}-M_{b3}$	$100 \mu\text{m}/2 \mu\text{m}$
$M_{n1}-M_{n2}$	$200 \mu\text{m}/0.5 \mu\text{m}$
$M_{p1}-M_{p2}$	$50 \mu\text{m}/0.5 \mu\text{m}$
M_{p3}	$200 \mu\text{m}/0.5 \mu\text{m}$

the obtained $i_{in} - v_{in}$ characteristics, for Figure 1(b) for $f = 400$ Hz, 700 Hz, and 2 kHz, are demonstrated in Figure 9 with the corresponding time-domain behavior shown in Figure 10 for a 700 Hz input voltage.

FIGURE 8: Time-domain behavior of the circuit in Figure 1(a) for $f = 1$ kHz.

The effect of r_2 in the operation of the topology in Figure 1(b) has also been studied under the conditions $r_2 = 0.4r_1$, $0.56r_1$, and $0.7r_1$, which sets $\alpha = 0.26$, 0.36 , and 0.41 , respectively. The derived $i_{in} - v_{in}$ characteristics, for $f = 700$ Hz, are given in Figure 11.

5.2. Simulation Results: With M_1 Linearization. The improved linear resistor shown in Figure 5 was also used for linearizing transistor M_1 . The power supply voltage was equal to 2 V and the aspect ratio of M_1-M_2 and M_5-M_6 was $1 \mu\text{m}/2 \mu\text{m}$, while for M_3-M_4 it was $3.2 \mu\text{m}/2 \mu\text{m}$. Considering a sinusoidal input with 700 mV amplitude and variable frequency, the obtained $i_{in} - v_{in}$ characteristics, for the circuit in Figure 1(a), derived at the same conditions as in the previous subsection, and for $f = 600$ Hz, 1 kHz, and 1.5 kHz, are demonstrated in Figure 12. The corresponding

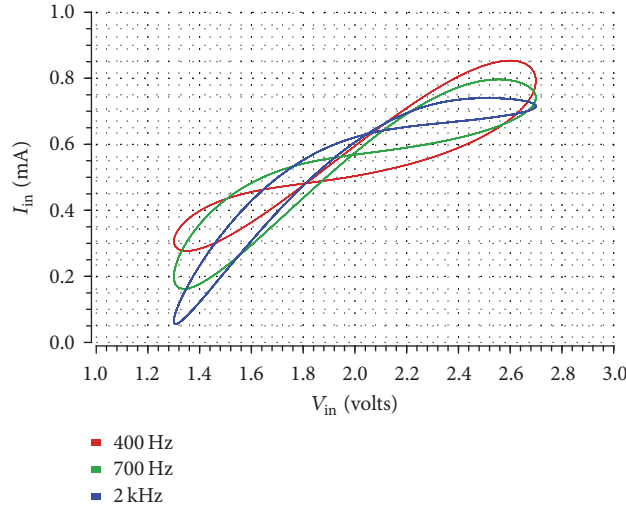


FIGURE 9: Simulated i_{in_b} - v_{in} characteristics for $f = 400$ Hz, 700 Hz, and 2 kHz.

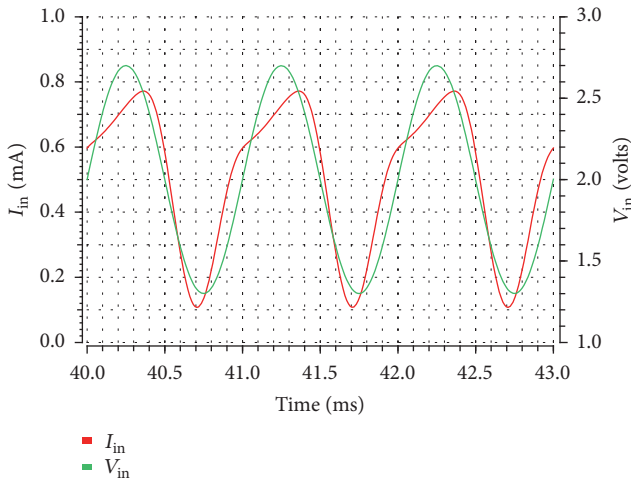


FIGURE 10: Time-domain behavior of the circuit in Figure 1(b) for $f = 700$ Hz.

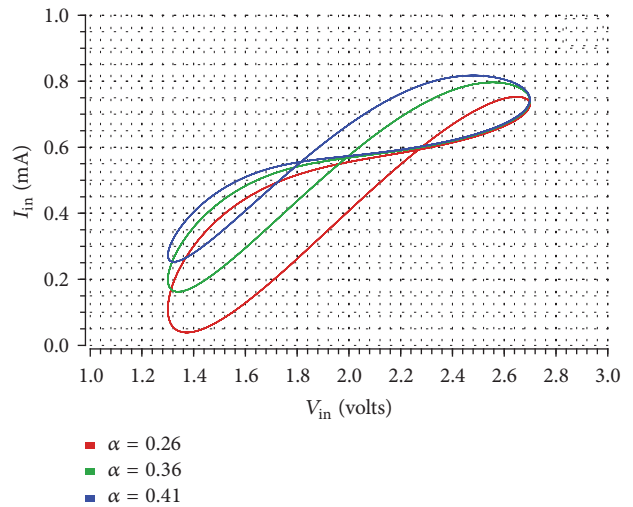


FIGURE 11: Simulated i_{in_b} - v_{in} characteristics for $\alpha = 0.26$, 0.36, and 0.41.

time-domain behavior is depicted in Figure 13 for a 1 kHz input voltage.

In a similar way, the plots for the circuit in Figure 1(b), obtained at the same conditions as in the previous subsection, are given in Figure 14. The time-domain behavior is given in Figure 15 for a 700 Hz input voltage.

5.3. Experimental Results. In the first of a series of experimental tests, the circuit of Figure 1(a) was constructed using 741 opamps powered by a ± 15 V supply. The resistor and capacitor values used were $R_1 = R_2 = 820 \Omega$ and $C_1 = C_2 = 470$ nF ensuring that $\tau_1 = \tau_2$. Transistors M_1 and M_2 were taken from Fairchild's dual complementary pair CD4007CN chip. The DC biasing voltages used were $V_{dc_1} = 4.6$ V, $V_{dc_2} = 1.12$ V, and $= 1$ V_{pp}. The current i_{in_a} was measured by inserting a 10Ω resistor in series with v_{in} and measuring the voltage drop across this resistor using an

instrumentation amplifier with a gain of 10; that is, $i_{in_a} = v_{10\Omega}$. The results of v_{in} versus i_{in_a} are shown in Figure 16 for several frequencies starting at 1 kHz with the pinch point remaining nearly constant for $V_{dc_2} = 1.12$ V. Note that this result is consistent with (22) where SPICE models for the CD4007 (the actual value of V_T is both foundry and process dependent but unfortunately actual data on the CD4007CN chips used was not available) place V_T in the order of around 2~2.3V. Bending of the lobes can be observed towards a downward trend when the frequency is decreased below 1 kHz and upwards when the frequency is increased above 1 kHz. The usable range of this circuit was found to be from 300 Hz to 10 kHz. Note that the lower frequency limit on the operation of the circuit (300 Hz) is also consistent with (25) where, for $V_{dc_2} = (1/2)(V_{dc_1} - V_T)$, $R_1 = 820 \Omega$, $C_1 = 470$ nF, with $\tau_1 = \tau_2$, yields a calculated value of $\omega_{1,2} = 292$ Hz. The upper frequency limit was observed when the lobes

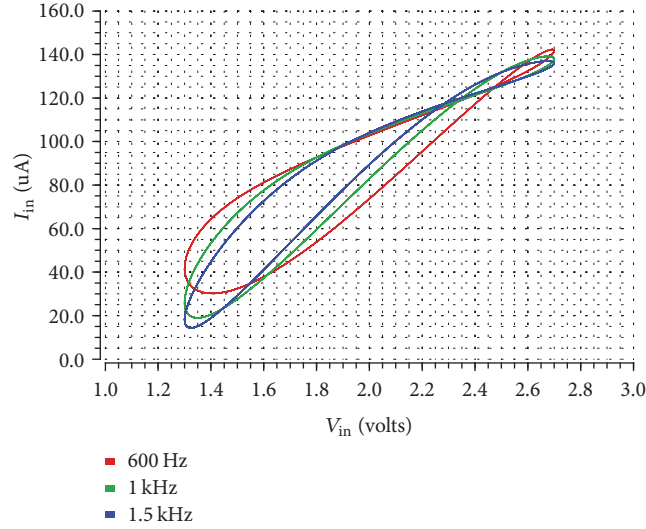


FIGURE 12: Simulated i_{in_a} - v_{in} characteristics for the circuit in Figure 1(a) with $f = 600$ Hz, 1 kHz, and 1.5 kHz and linearization of M_1 .

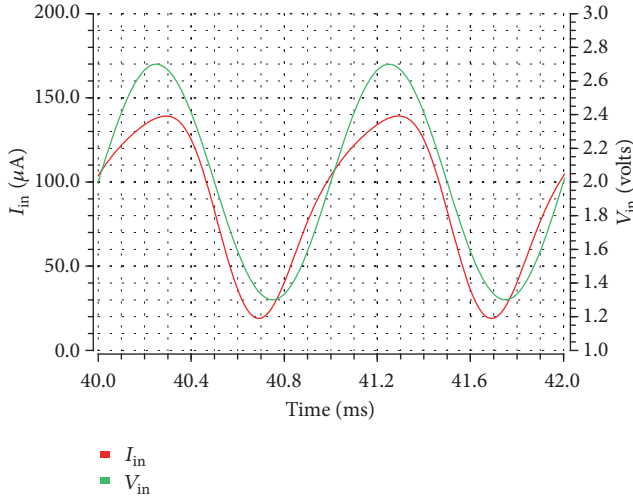


FIGURE 13: Time-domain behavior of the circuit in Figure 1(a) for $f = 1$ kHz and linearization of M_1 .

of the pinch hysteresis were too close to be distinguishable and in addition would also be set by limitations associated with A_2 losing gain in its closed-loop configuration with M_2 .

In a second experimental test, the circuit of Figure 1(b) was set up and the resistor and capacitor values used were $R_1 = r_2 = 2$ k Ω and $C_1 = C_2 = 470$ nF ensuring that $\tau_z = \tau_1$. The current i_{in_b} was likewise measured through a 10 Ω resistor using an instrumentation amplifier set to a gain of 10. Resistor r_1 was adjusted by a potentiometer at a value of $r_1 = 1031$ Ω which set $\alpha = 0.34$. Input voltages were set at $V_{dc} = 4$ V and $A = 3$ V_{pp} and the initial frequency was set at 700 Hz. The results shown in Figure 17 indicate that the pinch point and symmetry of the lobes are highly dependent on the input frequency. For this configuration, pinching was lost for frequencies below 300 Hz and above 10 kHz.

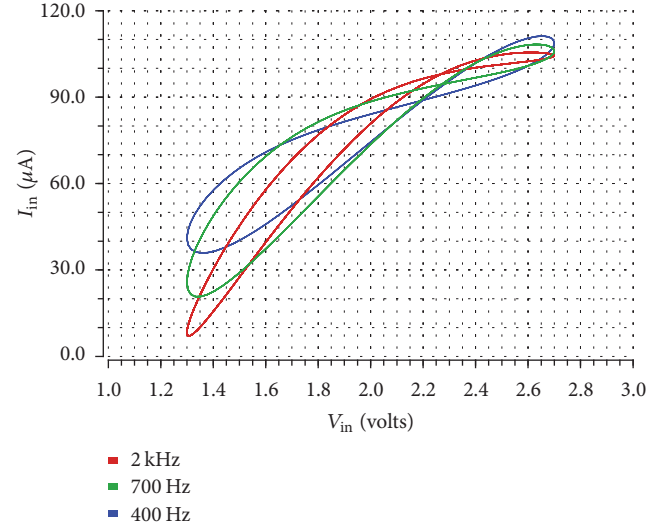


FIGURE 14: Simulated i_{in_b} - v_{in} characteristics for the circuit in Figure 1(b) with $f = 400$ Hz, 700 Hz, and 2 kHz and linearization of M_1 .

Finally, it should be mentioned that the circuits of Figures 1(a) and 1(b) were also tested using different time constants such as $\tau_1 \neq \tau_2$ and $\tau_1 \neq \tau_z$ and all results not shown here were consistent with the expected theory.

6. Conclusion

Two simple nonlinear circuits that exhibit unipolar pinched hysteresis behavior were presented in this paper. The multiplication-type nonlinearity between a state variable and its past history, as given in (1), is fundamental in obtaining pinched hysteresis although the past history can also be replaced by the rate of change of the present state as shown in [3]. In this work, this multiplication is simply achieved

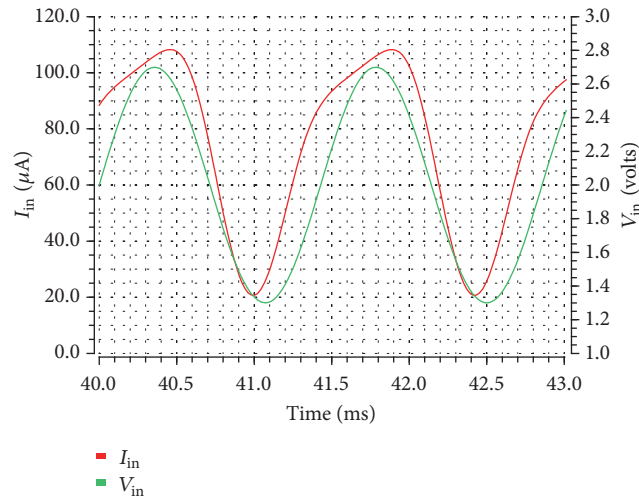
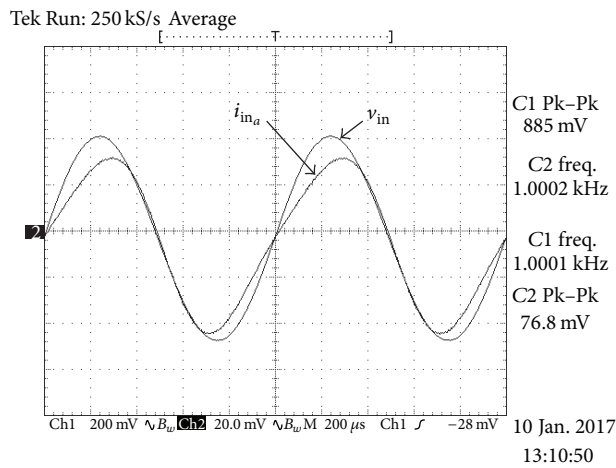
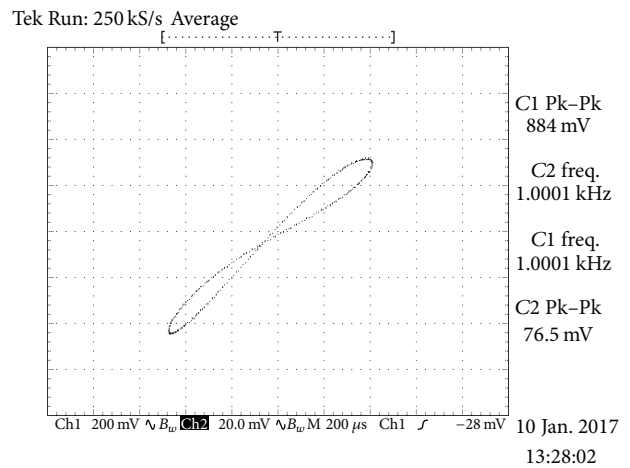


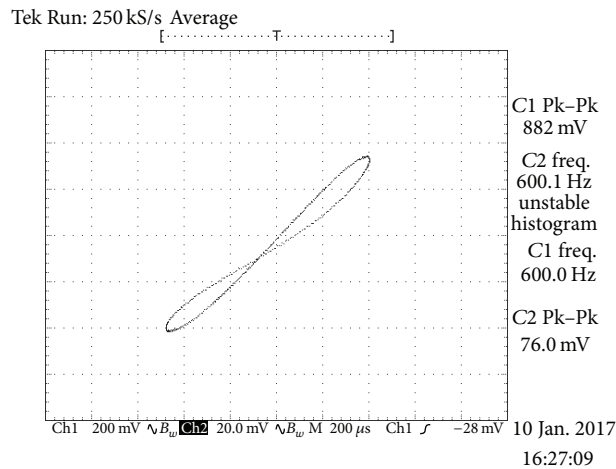
FIGURE 15: Time-domain behavior of the circuit in Figure 1(b) for $f = 700$ Hz and linearization of M_1 .



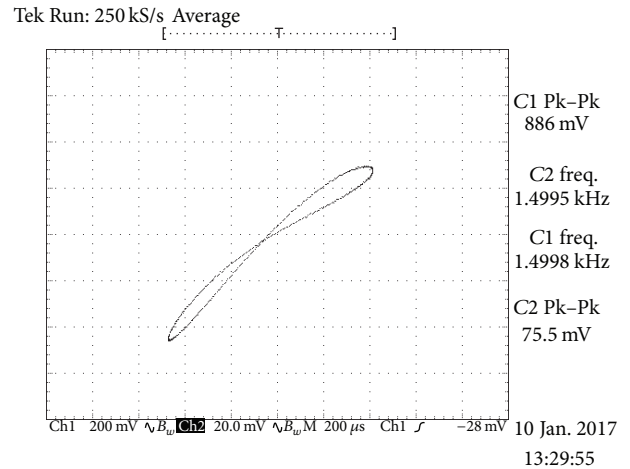
(a)



(b)



(c)



(d)

FIGURE 16: (a) Experimental results of the plot of $v_{in}(t)$ and $i_{in}(t)$ at 1 kHz for the circuit of Figure 1(a). (b) Oscilloscope trace of the pinched hysteresis loop of the memristor emulator circuit of Figure 1(a) at 1 kHz, (c) at 600 Hz, and (d) at 1.5 kHz.

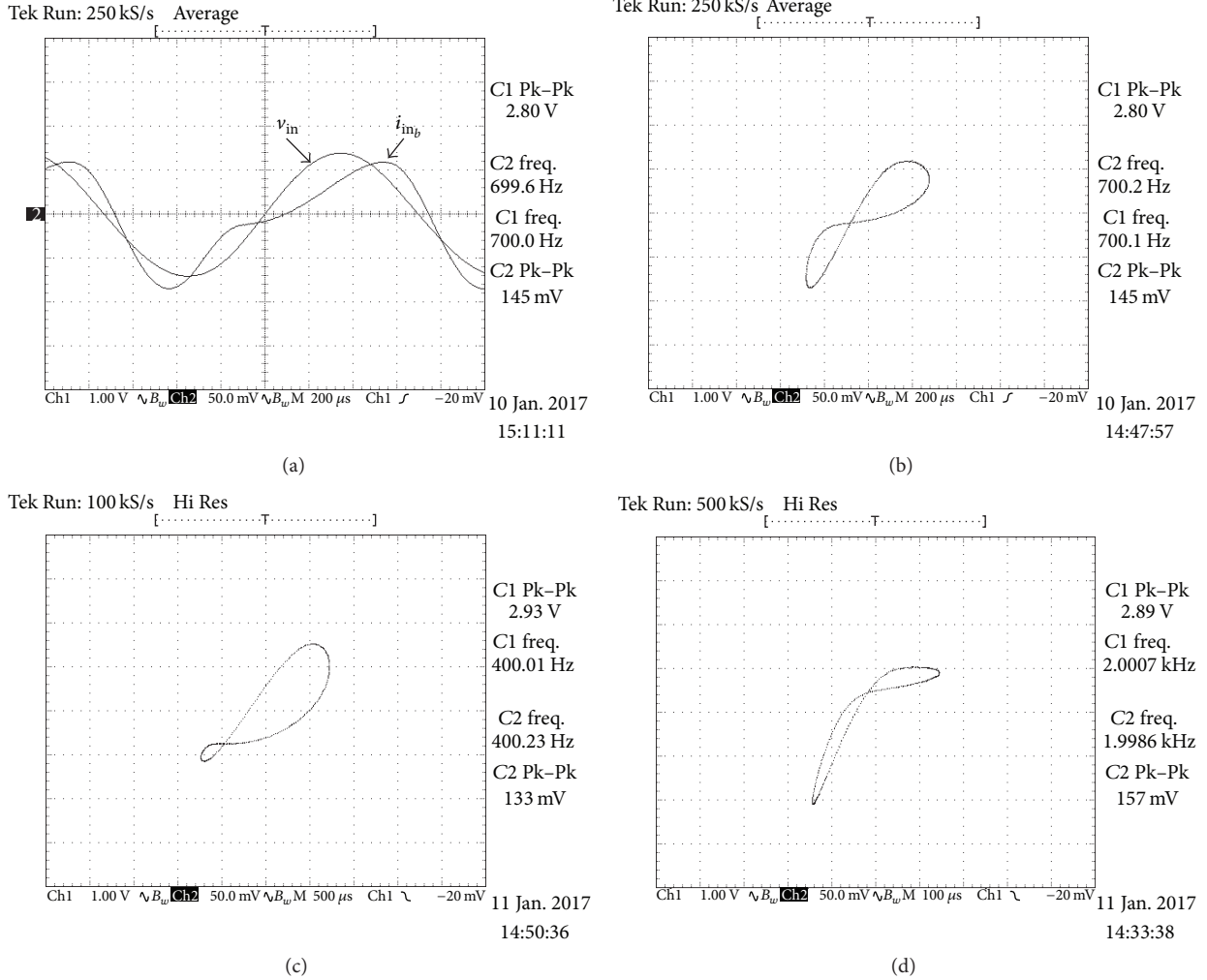


FIGURE 17: (a) Experimental results of the plot of $v_{in}(t)$ and $i_{in_b}(t)$ at 700 Hz for the circuit of Figure 1(b). (b) Oscilloscope trace of the pinched hysteresis loop at 700 Hz, (c) at 400 Hz, and (d) at 2 kHz.

using the MOS transistor transconductance equation. The proposed circuits have been analyzed, their pinch points were determined, and their behavior was verified in Matlab and experimentally. A method of linearization that enables the elimination of undesired higher-order nonlinear terms was also examined and verified via simulations in Cadence. Of significant importance in this work is the clarification of the role played by the charge holding capacitor in the value of the charge-controlled memristance. We argue that, in all solid-state devices that have been fabricated and that show pinched hysteresis, a parasitic capacitor combined with a modulation-type (multiplication-type) nonlinearity is behind the appearance of this behavior. Arguably, the authors of [18] conclude that both “memory resistance and memory capacitance must coexist.”

Conflicts of Interest

The authors declare that they have no conflicts of interest.

Acknowledgments

The authors would like to acknowledge the support of the Natural Sciences and Engineering Research Council (NSERC) of Canada in this work and Mr. Abdulwadood Al-Ali in the preparation and the carrying out of the experiments.

References

- [1] Z. Biolek, D. Biolek, and V. Biolková, “Specification of one classical fingerprint of ideal memristor,” *Microelectronics Journal*, vol. 46, no. 4, pp. 298–300, 2015.
- [2] F. Corinto, P. P. Civalleri, and L. O. Chua, “A theoretical approach to memristor devices,” *IEEE Journal on Emerging and Selected Topics in Circuits and Systems*, vol. 5, no. 2, pp. 123–132, 2015.
- [3] M. E. Fouda, A. S. Elwakil, and A. G. Radwan, “Pinched hysteresis with inverse-memristor frequency characteristics in some nonlinear circuit elements,” *Microelectronics Journal*, vol. 46, no. 9, article no. 3861, pp. 834–838, 2015.

- [4] A. Ascoli, R. Tetzlaff, Z. Biolek, Z. Kolka, V. Biolkova, and D. Biolek, "The art of finding accurate memristor model solutions," *IEEE Journal on Emerging and Selected Topics in Circuits and Systems*, vol. 5, no. 2, pp. 133–142, 2015.
- [5] S. Vongehr and X. Meng, "The missing memristor has not been found," *Scientific Reports*, vol. 5, Article ID 11657, 2015.
- [6] A. S. Elwakil, M. E. Fouda, and A. G. Radwan, "A simple model of double-loop hysteresis behavior in memristive elements," *IEEE Transactions on Circuits and Systems II: Express Briefs*, vol. 60, no. 8, pp. 487–491, 2013.
- [7] M. T. Abuelma'Atti and Z. J. Khalifa, "A continuous-level memristor emulator and its application in a multivibrator circuit," *AEU - International Journal of Electronics and Communications*, vol. 69, no. 4, pp. 771–775, 2015.
- [8] C. Sánchez-López, M. A. Carrasco-Aguilar, and C. Muñoz-Montero, "A 16 Hz-160 kHz memristor emulator circuit," *AEU - International Journal of Electronics and Communications*, vol. 69, no. 9, pp. 1208–1219, 2015.
- [9] A. G. Alharbi, Z. J. Khalifa, M. E. Fouda, and M. H. Chowdhury, "Memristor emulator based on single CCII," in *Proceedings of the 27th International Conference on Microelectronics, ICM 2015*, pp. 174–177, IEEE, Casablanca, Morocco, December 2015.
- [10] C. Yang, S. Cho, M. P. Sah, H. Kim, and K.-S. Jung, "Memristor emulator with off-the-shelf solid state components for memristor application circuits," in *Proceedings of the 2012 13th International Workshop on Cellular Nanoscale Networks and their Applications, CNNA 2012*, IEEE, Piscataway, NJ, USA, August 2012.
- [11] A. I. Hussein and M. E. Fouda, "A simple MOS realization of current controlled memristor emulator," in *Proceedings of the 2013 25th International Conference on Microelectronics, ICM 2013*, IEEE, Beirut, Lebanon, December 2013.
- [12] A. Elwakil, B. Maundy, and C. Psychalinos, "On the pinched hysteresis behavior in a state-controlled resistor," *AEU - International Journal of Electronics and Communications*, vol. 74, pp. 171–175, 2017.
- [13] R. Mutlu and E. Karakulak, "Emulator circuit of TiO_2 memristor with linear dopant drift made using analog multiplier," in *Proceedings of the 2010 7th National Conference on Electrical, Electronics and Computer Engineering, ELECO 2010*, pp. 380–384, Bursa, Turkey, December 2010.
- [14] A. G. Alharbi, M. E. Fouda, Z. J. Khalifa, and M. H. Chowdhury, "Simple generic memristor emulator for voltage-controlled models," in *Proceedings of the 2016 IEEE 59th International Midwest Symposium on Circuits and Systems (MWSCAS)*, pp. 1–4, Abu Dhabi, United Arab Emirates, October 2016.
- [15] Y. Babacan and F. Kaçar, "Floating memristor emulator with subthreshold region," *Analog Integrated Circuits and Signal Processing*, vol. 90, no. 2, pp. 471–475, 2017.
- [16] M. T. Abuelma'Atti and Z. J. Khalifa, "A new floating memristor emulator and its application in frequency-to-voltage conversion," *Analog Integrated Circuits and Signal Processing*, vol. 86, no. 1, pp. 141–147, 2016.
- [17] Z. B. Yan and J.-M. Liu, "Coexistence of high performance resistance and capacitance memory based on multilayered metal-oxide structures," *Scientific Reports*, vol. 3, article no. 2482, 2013.
- [18] I. Salaoru, Q. Li, A. Khat, and T. Prodromakis, "Coexistence of memory resistance and memory capacitance in TiO_2 solid-state devices," *Nanoscale Research Letters*, vol. 9, no. 1, pp. 1–7, 2014.
- [19] N. Tadić and D. Gobović, "A voltage-controlled resistor in CMOS technology using bisection of the voltage range," *IEEE Transactions on Instrumentation and Measurement*, vol. 50, no. 6, pp. 1704–1710, 2001.
- [20] B. Maundy, S. Gift, and P. Aronhime, "Practical voltage/current-controlled grounded resistor with dynamic range extension," *IET Circuits, Devices and Systems*, vol. 2, no. 2, pp. 201–206, 2008.
- [21] M. Kushima, M. Inaba, and K. Tanno, "Linear and compact floating node voltage-controlled variable resistor circuit," *IEICE Transactions on Fundamentals of Electronics, Communications and Computer Sciences*, vol. E89-A, no. 2, pp. 459–460, 2006.
- [22] B. Maundy and M. Maini, "A comparison of three multipliers based on the V_{gs2} technique for low-voltage applications," *IEEE Transactions on Circuits and Systems I: Fundamental Theory and Applications*, vol. 50, no. 7, pp. 937–940, 2003.

Research Article

Application of Topological Degree Method for Solutions of Coupled Systems of Multipoints Boundary Value Problems of Fractional Order Hybrid Differential Equations

Muhammad Iqbal,¹ Yongjin Li,² Kamal Shah,¹ and Rahmat Ali Khan¹

¹Department of Mathematics, University of Malakand, Dir (L), Khyber Pakhtunkhwa, Pakistan

²Department of Mathematics, Sun Yat-Sen University, Guangzhou, China

Correspondence should be addressed to Yongjin Li; stslj@mail.sysu.edu.cn

Received 15 March 2017; Revised 26 April 2017; Accepted 11 May 2017; Published 20 July 2017

Academic Editor: Sundarapandian Vaidyanathan

Copyright © 2017 Muhammad Iqbal et al. This is an open access article distributed under the Creative Commons Attribution License, which permits unrestricted use, distribution, and reproduction in any medium, provided the original work is properly cited.

We established the theory to coupled systems of multipoints boundary value problems of fractional order hybrid differential equations with nonlinear perturbations of second type involving Caputo fractional derivative. The proposed problem is as follows: ${}^c D^\alpha [x(t) - f(t, x(t))] = g(t, y(t), I^\alpha y(t))$, $t \in J = [0, 1]$, ${}^c D^\alpha [y(t) - f(t, y(t))] = g(t, x(t), I^\alpha x(t))$, $t \in J = [0, 1]$, ${}^c D^p x(0) = \psi(x(\eta_1))$, $x'(0) = 0, \dots, x^{n-2}(0) = 0$, ${}^c D^p x(1) = \psi(x(\eta_2))$, ${}^c D^p y(0) = \psi(y(\eta_1))$, $y'(0) = 0, \dots, y^{n-2}(0) = 0$, ${}^c D^p y(1) = \psi(y(\eta_2))$, where $p, \eta_1, \eta_2 \in (0, 1)$, ψ is linear, ${}^c D^\alpha$ is Caputo fractional derivative of order α , with $n - 1 < \alpha \leq n$, $n \in \mathbb{N}$, and I^α is fractional integral of order α . The nonlinear functions f, g are continuous. For obtaining sufficient conditions on existence and uniqueness of positive solutions to the above system, we used the technique of topological degree theory. Finally, we illustrated the main results by a concrete example.

1. Introduction

Due to a wide range of applications of fractional calculus in various scientific disciplines such as optimization theory, electric networks, signal processing, nonlinear control theory, nonlinear biological systems, controlled thermonuclear fusion, viscoelasticity, chemistry, turbulence, mechanics, oscillation, diffusion, fluid dynamics, stochastic dynamical system, polymer physics, plasma physics, astrophysics, chemical physics, and economics [1–4], the subject area has received much attention among the scientific community. Recently, the theory on existence and uniqueness of solutions to boundary value problems (BVPs) of fractional differential equations (DEs) are well studied and many results are available in literature (see, e.g., [5–10] and the references herein). The perturbed DEs are categorized into various types. Dhage [11] classified different types of perturbations for nonlinear integral and DEs. An important class of DEs which captured great attention in last few decades is the

quadratic perturbations of nonlinear differential equations known as hybrid differential equations (HDEs). This class is well studied for BVPs with ordinary DEs. However, existence theory for BVPs with fractional hybrid differential equations (FHDEs) are not well explored and few results are available in the literature (see [12, 13]). This class of DEs includes perturbations of dynamical systems in different ways and hence includes several dynamical systems as special cases. Modern control-command systems often include controllers that perform nonlinear computations to control a physical system, which can typically be described by hybrid automaton containing high dimensional systems of nonlinear DEs. The hybrid systems are dynamical systems that involve the interaction of continuous (real valued) states and discrete (finite valued) states.

Recently, existence of solutions to some classes of HDEs is studied with the use of hybrid fixed point theory (see [14–18]). Dhage and Jadhav [17] developed sufficient conditions for

existence of maximal and minimal solutions to the following first-order HDEs:

$$\begin{aligned} \frac{d}{dt} [r(t) - \Theta(t, r(t))] &= \varphi(t, r(t)), \quad \text{a.e } t \in I, \\ r(t_0) &= r_0 \in \mathbb{R}, \end{aligned} \quad (1)$$

where $I = [t_0, t_0 + a) \in \mathbb{R}$ for some $t_0, a \in \mathbb{R}$ with $a > 0$ and $\Theta, \varphi \in C(I \times \mathbb{R}, \mathbb{R})$. The results of [17] were generalized by Lu et al. [18] to the case of fractional order and developed conditions for existence and uniqueness to the following FHDEs:

$$\begin{aligned} D^q [r(t) - \Theta(t, r(t))] &= \varphi(t, r(t)), \\ \text{a.e } t \in I, \quad 0 < q < 1, \quad (2) \\ r(t_0) &= r_0 \in \mathbb{R}. \end{aligned}$$

Bashiri et al. in [13] used coupled fixed point theorem, a Krasnoselskii type generalization of fixed point theorem of Burton [19] in Banach spaces, to the case of coupled systems and developed sufficient conditions for existence of solutions to the following coupled systems of two-point BVPs for FHDEs:

$$\begin{aligned} D^q [r(t) - \Theta(t, r(t))] &= \psi(t, s(t), I^\alpha(s(t))), \\ \text{a.e } t \in I, \\ D^q [s(t) - \Theta(t, s(t))] &= \psi(t, r(t), I^\alpha(r(t))), \\ \text{a.e } t \in I, \quad 0 < q < 1, \quad \alpha > 0, \quad (3) \\ r(0) &= 0, \\ s(0) &= 0. \end{aligned}$$

Leray Schauder theory is powerful tool in solving operator equations of the form $(I - T)u = w$, where T is compact. But in many situations, T is not compact. Therefore, it is natural to ask whether the solutions of the above operator equation are possible if T is not compact. Schauder constructed an example and showed that it is impossible. But later on Browder, Sadovski and Vath, and so on proved that it is possible to define a complete analogue of the Leray Schauder theory for condensing type mapping with compactness. They called this method the “topological degree method”; see for detail [20]. In 1970, Mawhin introduced the mentioned degree theory for nonlinear Volterra integral equations and differential equations with boundary conditions. On the other hand, using the classical fixed point theory such as “Schauder fixed point theorem” and “Banach contraction principle” required stronger conditions on the nonlinear functions and thus restrict the applicability of these results to limited classes of applied problems and to some specialized systems of BVPs. Finding the fixed points of the respective operator equations corresponding to fractional integral equations needs strong conditions for the compactness of the operator. To relax the criteria and establish weaker conditions in order to extend tools to more classes of BVPs, researchers need to look for some other refined tools of functional analysis. One of such

tools is “topological degree theory.” The topological degree method is a powerful tool for existence of solutions to BVPs of many mathematical models that arise in applied nonlinear analysis. The concerned method is also called the “prior estimate method.” By coincidence degree theory approach, Mawhin [21] studied existence of solutions to the following BVPs:

$$\frac{d}{dt} s(t) = \psi(t, s(t)), \quad t \in [0, 1], \quad (4)$$

$$s(0) = s(1),$$

$$-\frac{d^2}{dt^2} s(t) = \psi\left(t, s(t), \frac{d}{dt} s(t)\right), \quad t \in [0, \pi], \quad (5)$$

$$s(0) = s(\pi) = 0,$$

under appropriate assumptions. Dinca et al. [22] used this method together with Leray Schauder degree to prove the existence of solutions of the Dirichlet problems with p -Laplacian:

$$\begin{aligned} -\Delta_p w &= \psi(t, w), \quad \text{in } \Omega \\ w |_{\partial\Omega} &= 0. \end{aligned} \quad (6)$$

Isaia [23] used this method along with “the degree for condensing maps” and proved the existence of solutions for the following integral equation by using appropriate assumption on the functions φ and Θ , where $\varphi : [a_1, a_2] \times \mathbb{R} \rightarrow \mathbb{R}$ and $\Theta : [a_1, a_2] \times [a_1, a_2] \times \mathbb{R} \rightarrow \mathbb{R}$ are continuous functions, $a_1, a_2 \in \mathbb{R}$,

$$s(t) = \varphi(t, s(t)) + \int_{a_1}^{a_2} \Theta(t, \xi, s(\xi)) d\xi, \quad t \in [a_1, a_2]. \quad (7)$$

Wang et al. [24] used “topological degree method” to a class of “nonlocal Cauchy problems” of the following form to study the existence and uniqueness of solutions:

$${}^c D^p s(t) = \psi(t, s(t)), \quad t \in [0, T], \quad (8)$$

$$s(0) + g(s) = s_0,$$

where ${}^c D^p$ is the Caputo fractional derivative of order $p \in (0, 1]$, $s_0 \in \mathbb{R}$, and $\psi : [0, T] \times \mathbb{R} \rightarrow \mathbb{R}$ is continuous. For more study of fractional DEs via topological degree method, we refer to [6, 24–26]. Recently, Shah et al. [27] applied the “topological degree method” and established sufficient conditions for the existence of at least one solution to the following coupled system of nonlinear ordinary fractional equations with four-point boundary conditions:

$${}^c D^p x(t) = \phi(t, x(t), y(t)), \quad t \in [0, 1],$$

$${}^c D^q y(t) = \psi(t, x(t), y(t)), \quad t \in [0, 1],$$

$$x(0) = f(x),$$

$$x(1) = \lambda x(\eta), \quad \lambda, \eta \in (0, 1),$$

$$y(0) = g(y),$$

$$y(1) = \delta y(\xi), \quad \delta, \xi \in (0, 1), \quad (9)$$

where $p, q \in (1, 2]$ and $\phi, \psi : [0, 1] \times \mathbb{R} \times \mathbb{R} \rightarrow \mathbb{R}$ are continuous, also $f, g \in ([0, 1], \mathbb{R})$. The above system (9) contains two nonlinear functions, namely, ϕ, ψ . While the proposed coupled system contains four nonlinearities as follows:

$$\begin{aligned} {}^c D^\alpha [x(t) - f(t, x(t))] &= g(t, y(t), I^\alpha y(t)), \\ t \in J &= [0, 1], \\ {}^c D^\alpha [y(t) - f(t, y(t))] &= g(t, x(t), I^\alpha x(t)), \\ t \in J &= [0, 1], \\ {}^c D^p x(0) &= \psi(x(\eta_1)), \\ x'(0) &= 0, \dots, x^{n-2}(0) = 0, \\ {}^c D^p x(1) &= \psi(x(\eta_2)), \\ {}^c D^p y(0) &= \psi(y(\eta_1)), \\ y'(0) &= 0, \dots, y^{n-2}(0) = 0, \\ {}^c D^p y(1) &= \psi(y(\eta_2)), \end{aligned} \quad (10)$$

which made the considered problem more general and complicated. Furthermore, in the proposed coupled system (10) of FHDEs, the order of fractional differential operator lies in $(n - 1, n]$. Moreover, the boundary conditions of the proposed problem involve Caputo fractional order derivative as well as ordinary derivative of higher order. Moreover, to the best of our knowledge, the topological degree method has not been applied properly for the systems of nonlinear hybrid fractional differential equations.

Motivated by this consideration, our main focus in the present article is to use topological degree approach for condensing mapping to investigate existence of solutions of coupled system (10). We would like to solve the dynamics of the system to determine how the state will evolve in the future, that is, to find a function $x(t)$ called trajectory or solution of the system.

2. Preliminaries

In the following, we provide some basic definitions and results of fractional calculus and topological degree theory. For detailed study, we refer to [1–4, 10, 28–30].

Definition 1 (see [1]). The fractional integral operator of order $r \in \mathbb{R}^+$ of a function $f : (0, \infty) \rightarrow \mathbb{R}$ is defined as

$$I^r f(t) = \frac{1}{\Gamma(r)} \int_0^t (t - \xi)^{r-1} f(\xi) d\xi, \quad (11)$$

provided that integral on the right is pointwise defined on $(0, \infty)$.

Definition 2 (see [1]). The Caputo fractional order derivative of order $p \in \mathbb{R}^+$ of a continuous function $f : (0, \infty) \rightarrow \mathbb{R}$ is defined as

$${}^c D^p f(t) = \frac{1}{\Gamma(m-p)} \int_0^t (t - \xi)^{m-p-1} f^{(m)}(\xi) d\xi, \quad (12)$$

where $m = [p] + 1$, provided that integral on the right is pointwise defined on $(0, \infty)$.

Lemma 3 (see [1, 28]). *The following results hold for fractional integral and Caputo derivative.*

- (i) ${}^c D^p [\lambda_1 f(t) + \lambda_2 g(t)] = \lambda_1 {}^c D^p f(t) + \lambda_2 {}^c D^p g(t)$, $\lambda_1, \lambda_2 \in \mathbb{R}$.
- (ii) ${}^c D^p I^q f(t) = I^{q-p} f(t)$, ${}^c D^p I^p f(t) = f(t)$.
- (iii) ${}^c D^p t^q = (\Gamma(q+1)/\Gamma(q+1-p))t^{q-p}$, $D^p C = 0$, where C is a constant.
- (iv) $I^q {}^c D^q f(t) = f(t) - \sum_{k=0}^{n-1} (D^k f(0)/\Gamma(k-q+1))t^k = f(t) - d_0 - d_1 t - d_2 t^2 - d_3 t^3 - \dots - d_{n-1} t^{n-1}$, $d_i \in \mathbb{R}$, for $0 \leq i \leq n-1$.

Let $J = [0, 1]$; the spaces of all continuous functions $Y = C(J, \mathbb{R})$ and $Z = C(J, \mathbb{R})$ are Banach spaces under the usual norms $\|y\| = \sup\{|y(t)| : t \in J\}$ and $\|z\| = \sup\{|z(t)| : t \in J\}$, respectively. Moreover, the product space $Y \times Z$ is a Banach space under the norm $\|(y, z)\| = \|y\| + \|z\|$ and norm $\|(y, z)\| = \max\{\|y\|, \|z\|\}$. In the following, Y is a Banach space and $\mathcal{M} \subset P(Y)$ is the family of all its bounded sets.

We recall the following notions, which can be found in [29].

Definition 4. “The function $Y : \mathcal{M} \rightarrow \mathbb{R}^+$ defined as $\mu(M_k) = \inf\{d > 0 : M_k \text{ admits a finite cover by sets of diameter } \leq d\}$, where $M_k \in \mathcal{M}$ is called the (Kuratowski-) measure of noncompactness.”

Some of the properties of this measure are listed below (without proof).

Proposition 5. *The following assertions hold for Kuratowski measure Y :*

- (i) $Y(M_k) = 0$ iff M_k is relatively compact.
- (ii) Y is a seminorm; that is, $Y(\sigma M_k) = |\sigma|Y(M_k)$ and $Y(M_{k1} + M_{k2}) \leq Y(M_{k1}) + Y(M_{k2})$, where $M_{k1}, M_{k2} \in \mathcal{M}$, and $\sigma \in \mathbb{R}$.
- (iii) $M_{k1} \subset M_{k2}$ implies $Y(M_{k1}) \leq Y(M_{k2})$ and $Y(M_{k1} \cup M_{k2}) = \max\{Y(M_{k1}), Y(M_{k2})\}$.
- (iv) $Y(\text{conv } M_k) = Y(M_k)$.
- (v) $Y(\overline{M_k}) = Y(M_k)$.

Definition 6. Let $\mathcal{L} \subset Y$ and $\Theta : \mathcal{L} \rightarrow Y$ be a continuous bounded mapping. Then Θ is Y -Lipschitz if $\exists k \geq 0 \ni$

$$Y(\Theta(L)) \leq kY(L) \quad (\forall) L \subset \mathcal{L} \text{ bounded.} \quad (13)$$

Furthermore, if $k < 1$, then Θ is a strict Y -contraction.

Definition 7. The function Θ is Y -condensing if

$$\begin{aligned} Y(\Theta(L)) &< Y(L) \\ (\forall) L \subset \mathcal{L} \text{ bounded with } Y(L) &> 0. \end{aligned} \quad (14)$$

If $Y(\Theta(L)) \geq Y(L)$, then $Y(L) = 0$.

It may be noted that the class of strict Y -contractions contains the class of Y -condensing maps. Also every member of Y -condensing map is Y -Lipschitz with constant $k = 1$.

Definition 8. $\Theta : \mathcal{L} \rightarrow Y$ is called Lipschitz if $\exists k > 0 \ni$

$$\|\Theta y_1 - \Theta y_2\| \leq k \|y_1 - y_2\| \quad (\forall) y_1, y_2 \in \mathcal{L}. \quad (15)$$

If $k < 1$, then Θ is a strict contraction.

Proposition 9 (see [23]). *If $\Theta : \mathcal{L} \rightarrow Y$ is compact, then Θ is Y -Lipschitz with zero constant.*

Proposition 10 (see [23]). *If $\Theta : \mathcal{L} \rightarrow Y$ is Lipschitz with constant k_1 , then Θ is Y -Lipschitz with the same constant k_1 .*

Proposition 11 (see [23]). *If $\Theta_1, \Theta_2 : \mathcal{L} \rightarrow Y$ are Y -Lipschitz with constants k_1 and k_2 , respectively, then $\Theta_1 + \Theta_2 : \mathcal{L} \rightarrow Y$ is Y -Lipschitz with constant $k_1 + k_2$.*

The following theorem from [23] plays a vital role for our main result.

Theorem 12. *Let $\Theta : Y \rightarrow Y$ be Y -condensing and*

$$S = \{y \in Y : (\exists) \sigma \in J \ni y = \sigma \Theta y\}. \quad (16)$$

If S is a bounded set in Y , so there exist $r > 0 \ni S \subset B_r(0)$; then the degree

$$D(I - \sigma \Theta, B_r(0), 0) = 1 \quad (\forall) \sigma \in J. \quad (17)$$

Consequently, Θ has at least one fixed point and the set of fixed points of Θ lies in $B_r(0)$.

Definition 13 (see [31]). An element $(y_1, y_2) \in Y \times Y$ is called "a coupled fixed point of a mapping" $T : Y \times Y \rightarrow Y$ if $T(y_1, y_2) = y_1$ and $T(y_2, y_1) = y_2$.

3. Main Result

Assume that $f : J \times \mathbb{R} \rightarrow \mathbb{R}$ and $g : J \times \mathbb{R} \times \mathbb{R} \rightarrow \mathbb{R}$ are continuous functions. Consider the following hypotheses:

$$(\mathcal{A}1) \quad (\partial^k / \partial t^k) f(t, x(t))|_{t=0} = 0.$$

$$(\mathcal{A}2) \quad \text{There exist } k_1 \in [0, 1) \ni \forall (t, x), (t, y) \in J \times \mathbb{R},$$

$$|f(t, x) - f(t, y)| \leq k_1 |x - y|. \quad (18)$$

$$(\mathcal{A}3) \quad \text{There exist } c_1, N_1 \geq 0, \ni \forall (t, x) \in J \times \mathbb{R},$$

$$|f(t, x)| \leq c_1 |x|^{p_1} + N_1, \quad \text{where } p_1 \in (0, 1). \quad (19)$$

$$(\mathcal{A}4) \quad \text{There exist } c_2, N_2 \geq 0, \ni \forall (t, x, I^\alpha x) \in J \times \mathbb{R} \times \mathbb{R},$$

$$|g(t, x, I^\alpha x)| \leq c_2 |x|^{p_2} + N_2, \quad \text{where } p_2 \in (0, 1). \quad (20)$$

$$(\mathcal{A}5) \quad \text{There exist a continuous function } h \in Y \ni |g(t, x(t), y(t))| \leq h(t), \text{ for } x, y \in \mathbb{R} \text{ and } t \in J.$$

The following lemma is useful in the existence results.

Lemma 14. *If $\mathcal{H} : J \rightarrow \mathbb{R}$ is α -time integrable and assuming that the hypothesis ($\mathcal{A}1$) holds, then the solutions of the multipoints BVPs:*

$${}^c D^\alpha [x(t) - f(t, x(t))] = \mathcal{H}(t), \quad t \in J,$$

$${}^c D^p x(0) = \psi(x(\eta_1)),$$

$$x'(0) = 0, \dots, x^{n-2}(0) = 0, \quad (21)$$

$${}^c D^p x(1) = \psi(x(\eta_2))$$

$$\text{where } \psi \text{ is linear, } 0 < \eta_1, \eta_2 < 1,$$

are the following integral equation:

$$\begin{aligned} x(t) &= f(t, x(t)) + I^\alpha \mathcal{H}(t) + a_1 t^{n-1} + a_2, \\ &\text{where } a_1, a_2 \in \mathbb{R}. \end{aligned} \quad (22)$$

Proof. Applying I^α on ${}^c D^\alpha [x(t) - f(t, x(t))] = \mathcal{H}(t)$ and using Lemma 3, we obtain

$$\begin{aligned} x(t) &= f(t, x(t)) + I^\alpha \mathcal{H}(t) + d_0 + d_1 t + d_2 t^2 + d_3 t^3 \\ &\quad + d_4 t^4 + \dots + d_{n-2} t^{n-2} + d_{n-1} t^{n-1}, \end{aligned} \quad (23)$$

$$\text{where } d_i \in \mathbb{R}, \text{ for } i = 0, 1, 2, \dots, n-1.$$

Now by conditions $x'(0) = 0, \dots, x^{n-2}(0) = 0$ and hypothesis ($\mathcal{A}1$), (23) implies $d_1 = d_2 = \dots = d_{n-2} = 0$. Hence,

$$x(t) = f(t, x(t)) + I^\alpha \mathcal{H}(t) + d_0 + d_{n-1} t^{n-1}. \quad (24)$$

Applying ${}^c D^p$ on (24) and using Lemma 3

$$\begin{aligned} {}^c D^p x(t) &= {}^c D^p f(t, x(t)) + I^{\alpha-p} \mathcal{H}(t) \\ &\quad + d_{n-1} \frac{\Gamma(n)}{\Gamma(n-p)} t^{n-1-p}. \end{aligned} \quad (25)$$

By conditions ${}^c D^p x(0) = \psi(x(\eta_1))$ and ${}^c D^p x(1) = \psi(x(\eta_2))$ and linearity of ψ ,

$$\begin{aligned} 0 &= \psi(f(\eta_1, x(\eta_1))) + \psi(I^{\alpha-p} \mathcal{H}(\eta_1)) + \psi(d_0) \\ &\quad + d_{n-1} \psi(\eta_1^{n-1}), \end{aligned} \quad (26)$$

$$\begin{aligned} {}^c D^p f(1, x(1)) + I^{\alpha-p} \mathcal{H}(1) + d_{n-1} \frac{\Gamma(n)}{\Gamma(n-p)} \\ = \psi(f(\eta_2, x(\eta_2))) + \psi(I^{\alpha-p} \mathcal{H}(\eta_2)) + \psi(d_0) \\ + d_{n-1} \psi(\eta_2^{n-1}). \end{aligned} \quad (27)$$

Subtracting (26) from (27) and rearranging, we get

$$\begin{aligned} d_{n-1} &= \frac{1}{\{\psi(\eta_2^{n-1}) - \psi(\eta_1^{n-1}) - \Gamma(n)/\delta_2\Gamma(n-p)\}} \left[{}^c D^p f(1, \right. \\ & x(1)) + I^{\alpha-p} \mathcal{H}(1) - \{\psi(f(\eta_2, x(\eta_2))) \\ & \left. - \psi(f(\eta_1, x(\eta_1))) + \psi(I^\alpha \mathcal{H}(\eta_2)) - \psi(I^\alpha \mathcal{H}(\eta_1))\} \right]. \end{aligned} \quad (28)$$

Using (28) in (26), we get

$$\begin{aligned} d_0 &= \frac{-\psi(f(\eta_1, x(\eta_1))) - \psi(I^\alpha \mathcal{H}(\eta_1))}{\psi(1)} \\ & - \frac{\psi(\eta_1^{n-1})}{\psi(1) \{\psi(\eta_2^{n-1}) - \psi(\eta_1^{n-1}) - \Gamma(n)/\delta_2\Gamma(n-p)\}} \left[{}^c D^p f(1, \right. \\ & x(1)) + I^{\alpha-p} \mathcal{H}(1) - \{\psi(f(\eta_2, x(\eta_2))) - \psi(f(\eta_1, x(\eta_1))) \\ & \left. + \psi(I^\alpha \mathcal{H}(\eta_2)) - \psi(I^\alpha \mathcal{H}(\eta_1))\} \right]. \end{aligned} \quad (29)$$

From (24), (28), and (29), it follows that

$$x(t) = f(t, x(t)) + I^\alpha \mathcal{H}(t) + a_1 t^{n-1} + a_2, \quad (30)$$

where $a_1 = \kappa_3 \psi(1)/\kappa_2$, $a_2 = -\kappa_0 - (\kappa_1/\kappa_2)\kappa_3$, $\kappa_0 = (-\psi(f(\eta_1, x(\eta_1))) - \psi(I^\alpha \mathcal{H}(\eta_1)))/\psi(1)$, $\kappa_1 = \psi(\eta_1^{n-1})$, $\kappa_2 = \psi(1) \{\psi(\eta_2^{n-1}) - \psi(\eta_1^{n-1}) - \Gamma(n)/\delta_2\Gamma(n-p)\}$ and $\kappa_3 = {}^c D^p f(1, x(1)) + I^{\alpha-p} \mathcal{H}(1) + \psi(f(\eta_1, x(\eta_1))) - \psi(f(\eta_2, x(\eta_2))) + \psi(I^\alpha \mathcal{H}(\eta_1)) - \psi(I^\alpha \mathcal{H}(\eta_2))$. \square

In view of Lemma 14, system (10) is equivalent to the following coupled systems of integral equations:

$$\begin{aligned} x(t) &= f(t, x(t)) + I^\alpha g(t, y(t), I^\alpha y(t)) + a_1 t^{n-1} \\ &+ a_2, \\ y(t) &= f(t, y(t)) + I^\alpha g(t, x(t), I^\alpha x(t)) + b_1 t^{n-1} \\ &+ b_2, \end{aligned} \quad (31)$$

where $a_1, b_1, a_2, b_2 \in \mathbb{R}$.

Define operators $F_1, F_2, G : Y \rightarrow Y$ by

$$\begin{aligned} (F_1 z)t &= f(t, z(t)) + a_1 t^{n-1} + a_2, \\ (F_2 z)t &= f(t, z(t)) + b_1 t^{n-1} + b_2, \\ (Gz)t &= I^\alpha g(t, z(t), I^\alpha z(t)). \end{aligned} \quad (32)$$

By virtue of these operators, system (31) can be written as

$$\begin{aligned} x(t) &= (F_1 x)t + (Gy)t = T_1(x, y), \\ y(t) &= (F_2 y)t + (Gx)t = T_2(x, y). \end{aligned}$$

Which implies $(x, y) = (T_1, T_2)(x, y)$.

$$\begin{aligned} \text{If } \tilde{F} &= (F_1, F_2), \\ \tilde{G} &= (G, G), \\ \tilde{T} &= (T_1, T_2), \end{aligned} \quad (33)$$

then $(x, y) = \tilde{T}(x, y) \implies$

$$u = \tilde{T}u, \quad \text{where } u = (x, y);$$

and solutions of system (10) are fixed points of \tilde{T} .

Lemma 15. Assume that hypotheses (A2) and (A3) hold, then the operator $\tilde{F} : Y \times Y \rightarrow Y$ is Y -Lipschitz with constant k_1 .

Proof. For $(x_1, y_1), (x_2, y_2) \in Y \times Y$, using (A2), it follows that

$$\begin{aligned} \left\| (\tilde{F}u)t - (\tilde{F}v)t \right\| &= \left\| (F_1, F_2)(x_1, y_1)t - (F_1, F_2)(x_2, \right. \\ & y_2)t \left. \right\| = \sup_{t \in J} \left| ((F_1 x_1)t, (F_2 y_1)t) \right. \\ & \left. - ((F_1 x_2)t, (F_2 y_2)t) \right| = \sup_{t \in J} \left| ((F_1 x_1)t \right. \\ & \left. - (F_1 x_2)t, (F_2 y_1)t - (F_2 y_2)t) \right| = \sup_{t \in J} \left[\left| (F_1 x_1)t \right. \right. \\ & \left. \left. - (F_1 x_2)t \right| + \left| (F_2 y_1)t - (F_2 y_2)t \right| \right] \\ &= \sup_{t \in J} \left[\left| f(t, x_1(t)) + a_1 t^{n-1} + a_2 \right. \right. \\ & \left. \left. - \left\{ f(t, x_2(t)) + a_1 t^{n-1} + a_2 \right\} \right| + \left| f(t, y_1(t)) \right. \right. \\ & \left. \left. + b_1 t^{n-1} + b_2 - \left\{ f(t, y_2(t)) + b_1 t^{n-1} + b_2 \right\} \right| \right] \\ &= \sup_{t \in J} \left[\left| f(t, x_1(t)) - f(t, x_2(t)) \right| + \left| f(t, y_1(t)) \right. \right. \\ & \left. \left. - f(t, y_2(t)) \right| \right] \leq k_1 |x_1(t) - x_2(t)| + k_1 |y_1(t) \\ & - y_2(t)| \leq k_1 (\|x_1 - x_2\| + \|y_1 - y_2\|) = k_1 \|(x_1 \\ & - x_2, y_1 - y_2)\| = k_1 \|u - v\|. \end{aligned} \quad (34)$$

Thus, \tilde{F} is Lipschitz with constant k_1 . Hence, by Proposition 10, \tilde{F} is Y -Lipschitz with constant k_1 . Moreover, by using (A3), we get the following condition for \tilde{F} :

$$\left\| \tilde{F}u \right\| \leq c_1 \|u\|^{p_1} + N_3, \quad \text{where } N_3 = N_1 + a_1 + a_2. \quad (35)$$

\square

Lemma 16. Assume that the hypotheses (A4) and (A5) hold; then the operator $\tilde{G} : Y \times Y \rightarrow Y$ is Y -Lipschitz with zero constant.

Proof. To show that \widetilde{G} is compact it is enough to show that \widetilde{G} is uniformly bounded and equicontinuous. Let $\widetilde{S} = \{u_n = (x_n, y_n) : \|(x_n, y_n)\| \leq R\} \subset Y \times Y \ni (x_n, y_n) \rightarrow (x, y)$ as $n \rightarrow \infty$ in \widetilde{S} . We have to show that $\|\widetilde{G}u_n - \widetilde{G}u\| \rightarrow 0$.

$$\begin{aligned} \lim_{n \rightarrow \infty} \{(\widetilde{G}u_n)t\} &= \lim_{n \rightarrow \infty} \{(G, G)(x_n, y_n)t\} \\ &= \left(\lim_{n \rightarrow \infty} (Gx_n)t, \lim_{n \rightarrow \infty} (Gy_n)t \right) \\ &= \left(\lim_{n \rightarrow \infty} I^\alpha g(t, x_n(t), I^\alpha x_n(t)), \right. \\ &\quad \left. \lim_{n \rightarrow \infty} I^\alpha g(t, y_n(t), I^\alpha y_n(t)) \right) = \left(\frac{1}{\Gamma(\alpha)} \right. \\ &\quad \cdot \lim_{n \rightarrow \infty} \int_0^t (t-\xi)^{\alpha-1} g(t, x_n(t), I^\alpha x_n(t)) d\xi, \frac{1}{\Gamma(\alpha)} \\ &\quad \cdot \lim_{n \rightarrow \infty} \int_0^t (t-\xi)^{\alpha-1} g(t, y_n(t), I^\alpha y_n(t)) d\xi \end{aligned} \quad (36)$$

which by Lebesgue dominated convergence theorem gives

$$\begin{aligned} \lim_{n \rightarrow \infty} \{(\widetilde{G}u_n)t\} &= \left(\frac{1}{\Gamma(\alpha)} \right. \\ &\quad \cdot \int_0^t (t-\xi)^{\alpha-1} g(t, x(t), I^\alpha x(t)) d\xi, \frac{1}{\Gamma(\alpha)} \\ &\quad \cdot \left. \int_0^t (t-\xi)^{\alpha-1} g(t, y(t), I^\alpha y(t)) d\xi \right) \\ &= (I^\alpha g(t, x(t), I^\alpha x(t)), I^\alpha g(t, y(t), I^\alpha y(t))) \\ &= ((Gx)t, (Gy)t) = (\widetilde{G}u)t. \end{aligned} \quad (37)$$

Thus, the image of a convergent sequence is convergent, so \widetilde{G} is a continuous on \widetilde{S} . Moreover, in view of (A4), \widetilde{G} satisfies the following condition:

$$\|\widetilde{G}u\| \leq c_2 \|u\|^{p_2} + N_2. \quad (38)$$

Now, using (A5), we obtain

$$\begin{aligned} |(\widetilde{G}u)t| &= |((Gx)t, (Gy)t)| = |(Gx)t| + |(Gy)t| \\ &= |I^\alpha g(t, x(t), I^\alpha x(t))| + |I^\alpha g(t, y(t), I^\alpha y(t))| \\ &= \frac{1}{\Gamma(\alpha)} \left| \int_0^t (t-\xi)^{\alpha-1} g(t, x(t), I^\alpha x(t)) d\xi \right| \\ &\quad + \frac{1}{\Gamma(\alpha)} \left| \int_0^t (t-\xi)^{\alpha-1} g(t, y(t), I^\alpha y(t)) d\xi \right| \\ &\leq \frac{1}{\Gamma(\alpha)} \int_0^t (t-\xi)^{\alpha-1} |g(t, x(t), I^\alpha x(t))| d\xi \\ &\quad + \frac{1}{\Gamma(\alpha)} \int_0^t (t-\xi)^{\alpha-1} |g(t, y(t), I^\alpha y(t))| d\xi \\ &\leq \frac{2\|h\|}{\Gamma(\alpha)} \int (t-\xi)^{\alpha-1} d\xi = \frac{2\|h\|}{\Gamma(\alpha+1)} t^\alpha. \end{aligned} \quad (39)$$

Upon using $t \leq 1$, (39) implies that

$$\|\widetilde{G}u\| \leq \frac{2\|h\|}{\Gamma(\alpha+1)}. \quad (40)$$

Hence, \widetilde{G} is uniformly bounded. Now, for $t_1, t_2 \in J$, and any $u \in \widetilde{S}$, consider

$$\begin{aligned} |(\widetilde{G}u)t_1 - (\widetilde{G}u)t_2| &= |G(x, y)t_1 - G(x, y)t_2| \\ &= |(Gx)t_1 - (Gx)t_2, (Gy)t_1 - (Gy)t_2| = |(Gx)t_1 \\ &\quad - (Gx)t_2| + |(Gy)t_1 - (Gy)t_2| \\ &= |I^\alpha g(t_1, x(t_1), I^\alpha x(t_1)) \\ &\quad - I^\alpha g(t_2, x(t_2), I^\alpha x(t_2))| \\ &\quad + |I^\alpha g(t_1, y(t_1), I^\alpha y(t_1)) \\ &\quad - I^\alpha g(t_2, y(t_2), I^\alpha y(t_2))| = \frac{1}{\Gamma(\alpha)} \left| \int_0^{t_1} (t_1 \right. \\ &\quad \left. - \xi)^{\alpha-1} g(\xi, x(\xi), I^\alpha x(\xi)) d\xi - \int_0^{t_2} (t_2 - \xi)^{\alpha-1} \right. \\ &\quad \cdot g(\xi, x(\xi), I^\alpha x(\xi)) d\xi \left. + \frac{1}{\Gamma(\alpha)} \left| \int_0^{t_1} (t_1 \right. \right. \\ &\quad \left. \left. - \xi)^{\alpha-1} g(\xi, y(\xi), I^\alpha y(\xi)) d\xi - \int_0^{t_2} (t_2 - \xi)^{\alpha-1} \right. \right. \\ &\quad \left. \left. \cdot g(\xi, y(\xi), I^\alpha y(\xi)) d\xi \right| \\ &= \frac{1}{\Gamma(\alpha)} \left| \left[\int_0^{t_1} (t_1 - \xi)^{\alpha-1} g(\xi, x(\xi), I^\alpha x(\xi)) d\xi \right. \right. \\ &\quad \left. \left. - \int_0^{t_1} (t_2 - \xi)^{\alpha-1} g(\xi, x(\xi), I^\alpha x(\xi)) d\xi \right. \right. \\ &\quad \left. \left. + \int_0^{t_1} (t_2 - \xi)^{\alpha-1} g(\xi, x(\xi), I^\alpha x(\xi)) d\xi \right. \right. \\ &\quad \left. \left. - \int_0^{t_2} (t_2 - \xi)^{\alpha-1} g(\xi, x(\xi), I^\alpha x(\xi)) d\xi \right] \right| \\ &\quad + \frac{1}{\Gamma(\alpha)} \left| \left[\int_0^{t_1} (t_1 - \xi)^{\alpha-1} g(\xi, y(\xi), I^\alpha y(\xi)) d\xi \right. \right. \\ &\quad \left. \left. - \int_0^{t_1} (t_2 - \xi)^{\alpha-1} g(\xi, y(\xi), I^\alpha y(\xi)) d\xi \right. \right. \\ &\quad \left. \left. + \int_0^{t_1} (t_2 - \xi)^{\alpha-1} g(\xi, y(\xi), I^\alpha y(\xi)) d\xi \right. \right. \\ &\quad \left. \left. - \int_0^{t_2} (t_2 - \xi)^{\alpha-1} g(\xi, y(\xi), I^\alpha y(\xi)) d\xi \right] \right| \end{aligned}$$

$$\begin{aligned}
&= \frac{1}{\Gamma(\alpha)} \left| \left[\int_0^{t_1} [(t_1 - \xi)^{\alpha-1} - (t_2 - \xi)^{\alpha-1}] \right. \right. \\
&\quad \cdot g(\xi, x(\xi), I^\alpha x(\xi)) d\xi + \int_0^{t_1} (t_2 - \xi)^{\alpha-1} \\
&\quad \cdot g(\xi, x(\xi), I^\alpha x(\xi)) d\xi + \int_{t_2}^0 (t_2 - \xi)^{\alpha-1} \\
&\quad \left. \left. \cdot g(\xi, x(\xi), I^\alpha x(\xi)) d\xi \right] \right| \\
&+ \frac{1}{\Gamma(\alpha)} \left| \left[\int_0^{t_1} [(t_1 - \xi)^{\alpha-1} - (t_2 - \xi)^{\alpha-1}] \right. \right. \\
&\quad \cdot g(\xi, y(\xi), I^\alpha y(\xi)) d\xi + \int_0^{t_1} (t_2 - \xi)^{\alpha-1} \\
&\quad \cdot g(\xi, y(\xi), I^\alpha y(\xi)) d\xi + \int_{t_2}^0 (t_2 - \xi)^{\alpha-1} \\
&\quad \left. \left. \cdot g(\xi, y(\xi), I^\alpha y(\xi)) d\xi \right] \right| \\
&\leq \frac{\|h\|}{\Gamma(\alpha)} \left| \left[\int_0^{t_1} \{(t_1 - \xi)^{\alpha-1} - (t_2 - \xi)^{\alpha-1}\} d\xi \right] \right| \\
&+ \left| \int_{t_2}^{t_1} (t_2 - \xi)^{\alpha-1} d\xi \right| \\
&+ \frac{\|h\|}{\Gamma(\alpha)} \left| \left[\int_0^{t_1} \{(t_1 - \xi)^{\alpha-1} - (t_2 - \xi)^{\alpha-1}\} d\xi \right] \right| \\
&+ \left| \int_{t_2}^{t_1} (t_2 - \xi)^{\alpha-1} d\xi \right| \leq \frac{2\|h\|}{\Gamma(\alpha+1)} [|t_1^\alpha - t_2^\alpha| + |t_2 \\
&- t_1|^\alpha - |t_2 - t_1|^\alpha] = \frac{2\|h\|}{\Gamma(\alpha+1)} |t_1^\alpha - t_2^\alpha|. \tag{41}
\end{aligned}$$

Since t^α is uniformly continuous on J for $n-1 < \alpha \leq n$, so for $\epsilon > 0 \exists \delta > 0 \ni$ if $|t_1 - t_2| < \delta$, then $|t_1^\alpha - t_2^\alpha| < (\Gamma(\alpha+1)/2\|h\|) \epsilon$. Thus, (41) becomes

$$|(\tilde{G}u)t_1 - (\tilde{G}u)t_2| < \frac{2\|h\|}{\Gamma(\alpha+1)} \frac{\Gamma(\alpha+1)}{2\|h\|} \epsilon. \tag{42}$$

Thus, $|(\tilde{G}u)t_1 - (\tilde{G}u)t_2| < \epsilon$ if $|t_1 - t_2| < \delta$; thus, \tilde{G} is equicontinuous. Hence, by Arzela-Ascoli Theorem \tilde{G} is compact and by virtue of Proposition 9, \tilde{G} is Y -Lipschitz with zero constant. \square

Theorem 17. *If $f : Y \times Y \rightarrow Y$ and $g : Y \times Y \rightarrow Y$ satisfying conditions (A1)-(A5), then the integral equation*

$$\begin{aligned}
u(t) &= (x(t), y(t)) = (f(t, x(t)) + a_1 t^{n-1} + a_2 \\
&+ I^\alpha g(t, y(t), I^\alpha y(t)), f(t, y(t)) + b_1 t^{n-1} + b_2 \tag{43} \\
&+ I^\alpha g(t, x(t), I^\alpha x(t))), \quad t \in J,
\end{aligned}$$

has at least one solution $u \in J$ and the set of solutions of system (10) is bounded in Y .

Proof. Let $\tilde{F}, \tilde{G}, \tilde{T} : Y \times Y \rightarrow Y$ be the operators defined in (32). These are continuous and bounded. By Lemma 15, it follows that \tilde{F} is Y -Lipschitz with constant k_1 . Also by Lemma 16, \tilde{G} is Y -Lipschitz with zero constant. Thus, by using Proposition 11, \tilde{T} is Y -Lipschitz with constant k_1 . Set

$$\tilde{S} = \{u \in Y \times Y : (\exists) \sigma \in J \ni u = \sigma \tilde{T}u\}. \tag{44}$$

We will prove that \tilde{S} is bounded in $Y \times Y$. For this let $u \in \tilde{S}$; then $u = \sigma \tilde{T}u$, where $\sigma \in J$. Now by (35) and (38),

$$\begin{aligned}
\|u\| &= \|(x, y)\| = \|\sigma \tilde{T}(x, y)\| \leq \|\tilde{T}(x, y)\| \\
&= \|\tilde{F}(x, y)\| + \|\tilde{G}(x, y)\| \\
&\leq c_1 \|u\|^{p_1} + N_3 + c_2 \|u\|^{p_2} + N_2 \\
1 &\leq \frac{c_1}{\|u\|^{1-p_1}} + \frac{N_3}{\|u\|} + \frac{c_2}{\|u\|^{1-p_2}} + \frac{N_2}{\|u\|}. \tag{45}
\end{aligned}$$

If $\|u\| \rightarrow \infty$, then $1 \leq 0$, a contradiction. Thus, $\|u\|$ is bounded in $Y \times Y$. Consequently, we deduced by Theorem 12 that \tilde{T} has at least one fixed point which is bounded in $Y \times Y$. \square

Remark 18. Here we remark that the conditions (A3), (A4) hold for $p_1 = p_2 = 1$. Therefore, in view of this remark, Theorem 17 is also valid for $p_1 = p_2 = 1$.

4. Illustrative Example

Example 1. Consider the coupled system of FHDEs given by

$$\begin{aligned}
D^{5/2} \left[x(t) - \frac{\cos t |x(t)|}{4(10 + |x(t)|)} \right] &= \frac{t [y(t) + I^{5/2} y(t)]}{10 + |y(t)|}, \\
t \in J = [0, 1],
\end{aligned}$$

$$\begin{aligned}
{}^c D^{5/2} \left[y(t) - \frac{\cos t |y(t)|}{4(10 + |y(t)|)} \right] \\
= \frac{t [x(t) + I^{5/2} x(t)]}{10 + |x(t)|}, \quad t \in J = [0, 1],
\end{aligned}$$

$${}^c D^{1/2} x(0) = \sum_{k=0}^{10} \frac{1}{20} x\left(\frac{1}{2}\right),$$

$$x'(0) = 0, \dots, x^{n-2}(0) = 0,$$

$$\begin{aligned}
{}^c D^{1/2} x(1) &= \sum_{k=0}^{10} \frac{1}{20} x\left(\frac{1}{2}\right), \\
{}^c D^{1/2} y(0) &= \sum_{k=0}^{10} \frac{1}{20} y\left(\frac{1}{2}\right), \\
y'(0) &= 0, \dots, y^{n-2}(0) = 0, \\
{}^c D^{1/2} y(1) &= \sum_{k=0}^{10} \frac{1}{20} y\left(\frac{1}{2}\right).
\end{aligned} \tag{46}$$

From system (46) we see that $f(t, x(t)) = \cos t|x(t)|/4(10 + |x(t)|)$, $g(t, x(t), I^\alpha x(t)) = t[x(t) + I^{5/2}x(t)]/(10 + |x(t)|)$, $\eta_1 = \eta_2 = 1/2$, $\alpha = 5/2$, $p = 1/2$, $\psi(x(\eta_1)) = \psi(x(\eta_2)) = \sum_{k=0}^{10} (1/20)x(1/2)$. Upon computation, we have $c_1 = 1/4$, $p_1 = 1$, $N_1 = 0$, $p_2 = 1$, $c_2 = 1/4$, $N_2 = 0$, $a_1 = 0.0055$, $a_2 = 1.0852$, and $N_3 = 1.0907$. In view of Theorem 17, $\tilde{S} = \{u = (x, y) \in Y \times Y : u = (1/2)\tilde{T}u\}$ is the solution set; then

$$\begin{aligned}
\|u\| &\leq \|\tilde{T}u\| = \|\tilde{F}u\| + \|\tilde{G}u\| \\
&\leq c_1 \|u\|^{p_1} + N_3 + c_2 \|u\|^{p_2} + N_2.
\end{aligned} \tag{47}$$

From which, we have $\|u\| \leq 2N_3 = 2.1814$. Thus, system (46) has at least one solution and the set of solutions of \tilde{S} is bounded in $C(J, \mathbb{R}) \times C(J, \mathbb{R})$.

Conflicts of Interest

There are no conflicts of interest with regard to this paper.

Authors' Contributions

All authors equally contributed to this paper.

Acknowledgments

This research work was supported by the National Natural Science Foundation of China (11571378). For review, the authors are thankful to Professor Yongjin Li and Dr. Kamal Shah, who helped them in constructing example to demonstrate the main results and in improving the introduction part by adding some recent work about FHDEs and their applications.

References

- [1] A. A. Kilbas, H. M. Srivastava, and J. J. Trujillo, *Theory and Applications of Fractional Differential Equations*, vol. 204 of *New York, NY, USA*, Elsevier, 2006.
- [2] R. Hilfer, *Applications of Fractional Calculus in Physics*, World Scientific, Singapore, 2000.
- [3] K. S. Miller and B. Ross, *An Introduction to the Fractional Calculus and Fractional Differential Equations*, John Wiley & Sons, New York, NY, USA, 1993.
- [4] S. G. Samko, A. A. Kilbas, and O. I. Marichev, *Fractional Integrals and Derivatives, Theory and Applications*, Gordon and Breach, Yverdon, Switzerland, 1993.
- [5] R. P. Agarwal, M. Benchohra, and S. Hamani, "A survey on existence results for boundary value problems of nonlinear fractional differential equations and inclusions," *Acta Applicandae Mathematicae*, vol. 109, no. 3, pp. 973–1033, 2010.
- [6] R. A. Khan and K. Shah, "Existence and uniqueness of solutions to fractional order multi-point boundary value problems," *Communication in Applied Analysis*, vol. 19, pp. 515–526, 2015.
- [7] X. Wang, L. Wang, and Q. Zeng, "Fractional differential equations with integral boundary conditions," *Journal of Nonlinear Science and Its Applications*, vol. 8, no. 4, pp. 309–314, 2015.
- [8] K. Shah, H. Khalil, and R. A. Khan, "Investigation of positive solution to a coupled system of impulsive boundary value problems for nonlinear fractional order differential equations," *Chaos, Solitons & Fractals*, vol. 77, pp. 240–246, 2015.
- [9] J. A. Nanware and D. B. Dhaigude, "Existence and uniqueness of solutions of differential equations of fractional order with integral boundary conditions," *Journal of Nonlinear Science and its Applications. JNSA*, vol. 7, no. 4, pp. 246–254, 2014.
- [10] L. Lv, J. Wang, and W. Wei, "Existence and uniqueness results for fractional differential equations with boundary value conditions," *Opuscula Mathematica*, vol. 31, no. 4, pp. 629–643, 2011.
- [11] B. C. Dhage, "Fixed point theorems in ordered Banach algebras and applications," *Panamerican Mathematical Journal*, vol. 9, no. 4, pp. 93–102, 1999.
- [12] M. A. Herzallah and D. Baleanu, "On fractional order hybrid differential equations," *Abstract and Applied Analysis*, vol. 2014, Article ID 389386, 7 pages, 2014.
- [13] T. Bashiri, S. M. Vaezpour, and C. Park, *Fixed Point Theory and Application to Fractional Hybrid Differential Problems*, Springer, 2016.
- [14] B. C. Dhage, "A fixed point theorem in Banach algebras with applications to fractional integral equations," *Kyungpook Mathematical Journal*, vol. 44, pp. 145–155, 2004.
- [15] B. C. Dhage and S. B. Dhage, "Approximating solutions of nonlinear PBVPs of second-order differential equations via hybrid fixed point theory," *Electronic Journal of Differential Equations*, vol. 20, pp. 1–10, 2015.
- [16] B. C. Dhage and V. Lakshmikantham, "Basic results on hybrid differential equations," *Nonlinear Analysis. Hybrid Systems*, vol. 4, no. 3, pp. 414–424, 2010.
- [17] B. C. Dhage and N. S. Jadhav, "Basic results in the theory of hybrid differential equations with linear perturbations of second type," *Tamkang Journal of Mathematics*, vol. 44, no. 2, pp. 171–186, 2013.
- [18] H. Lu, S. Sun, D. Yang, and H. Teng, "Theory of fractional hybrid differential equations with linear perturbations of second type," *Boundary Value Problems*, vol. 2013, no. 23, 16 pages, 2013.
- [19] T. A. Burton, "A fixed-point theorem of Krasnoselskii," *Applied Mathematics Letters. An International Journal of Rapid Publication*, vol. 11, no. 1, pp. 85–88, 1998.
- [20] D. O'Regan, Y. J. Cho, and Y.-Q. Chen, *Topological Degree Theory and Applications*, vol. 10 of *Series in Mathematical Analysis and Applications*, Chapman & Hall/CRC, Boca Raton, Fla, USA, 2006.
- [21] J. Mawhin, *Topological Degree Methods in Nonlinear Boundary Value Problems*, vol. 40 of *NSFCBMS Regional Conference Series in Mathematics*, American Mathematical Society, Providence, RI, USA, 1979.

- [22] G. Dinca, P. Jebelean, and J. Mawhin, "Variational and topological methods for Dirichlet problems with p -Laplacian," *Portugaliae Mathematica*, vol. 58, no. 3, pp. 339–378, 2001.
- [23] F. Isaia, "On a nonlinear integral equation without compactness," *Acta Mathematica Universitatis Comeniana. New Series*, vol. 75, no. 2, pp. 233–240, 2006.
- [24] J. Wang, Y. Zhou, and W. Wei, "Study in fractional differential equations by means of topological degree methods," *Numerical Functional Analysis and Optimization. An International Journal*, vol. 33, no. 2, pp. 216–238, 2012.
- [25] A. Ali, B. Samet, K. Shah, and R. Khan, "Existence and stability of solution to a toppled systems of differential equations of non-integer order," *Boundary Value Problems*, vol. 2017, 16 pages, 2017.
- [26] K. Shah and R. A. Khan, "Existence and uniqueness results to a coupled system of fractional order boundary value problems by topological degree theory," *Numerical Functional Analysis and Optimization. An International Journal*, vol. 37, no. 7, pp. 887–899, 2016.
- [27] K. Shah, A. Ali, and R. A. Khan, "Degree theory and existence of positive solutions to coupled systems of multi-point boundary value problems," *Boundary Value Problems*, vol. 2016, no. 43, 12 pages, 2016.
- [28] I. Podlubny, *Fractional Differential Equations*, vol. 198 of *Mathematics in Science and Engineering*, Academic Press, San Diego, Calif, USA, 1999.
- [29] K. Deimling, *Nonlinear Functional Analysis*, Springer, Berlin, Germany, 1985.
- [30] V. Lakshmikantham, S. Leela, and J. Vasundhara, *Theory of Fractional Dynamic Systems*, Cambridge Academic Publishers, Cambridge, UK, 2009.
- [31] S. S. Chang, Y. J. Cho, and N. J. Huang, "Coupled fixed point theorems with applications," *Journal of the Korean Mathematical Society*, vol. 33, no. 3, pp. 575–585, 1996.

Research Article

Generalized Fractional-Order Discrete-Time Integrator

Dorota Mozyrska¹ and Piotr Ostalczyk²

¹Faculty of Computer Science, Bialystok University of Technology, Bialystok, Poland

²Institute of Applied Computer Science, Lodz University of Technology, Łódź, Poland

Correspondence should be addressed to Dorota Mozyrska; d.mozyrska@pb.edu.pl

Received 10 February 2017; Accepted 23 April 2017; Published 6 July 2017

Academic Editor: Ahmad T. Azar

Copyright © 2017 Dorota Mozyrska and Piotr Ostalczyk. This is an open access article distributed under the Creative Commons Attribution License, which permits unrestricted use, distribution, and reproduction in any medium, provided the original work is properly cited.

We investigate a generalization of discrete-time integrator. Proposed linear discrete-time integrator is characterised by the variable, fractional order of integration/summation. Graphical illustrations of an analysis of particular vector matrices are presented. In numerical examples, we show relations between the order functions and element responses.

1. Introduction

In order to build a dynamic system, one should define specifications to be met, apply synthesis techniques, if available, analyse a mathematical model of a system, and simulate the model on a computer to test the effect of various inputs on the behavior of the resulting system. New classes and categories of systems that could be used as new models are still needed. One of the most important tools is an element called “integrator.” In measurements and control applications, an integrator is an element whose output signal is the time integral (in continuous case) or summation (in discrete case) of its input signal. It accumulates the input quantity over a defined time to produce a representative output. For the classical theory, see, for instance, [1, 2]. An integrator may be treated as a fundamental and is commonly used in constructions of more complicated systems via Kelvin’s scheme [2]. This leads to a variety of structures known as realizations. As crucial realizations, those, which reveal such important dynamic properties as stability, controllability, and so forth, are considered. The first-order differential equations can be generalized to the fractional-order ones [3–10]. Hence, we get the fractional-order integrator, which can be used in a modelling of fractional-order dynamic systems.

For discrete-time systems, an equivalent element is called a summator or discrete integrator. This dynamic element is described by linear time-invariant first-order difference equation; see [11, 12]. As a generalization of the classical discrete integrator, we can consider discrete summation of

fractional order [3, 13–20]. In this paper, we propose a generalization of the fractional-order discrete integrator and call it the variable-, fractional-order discrete-time integrator.

Besides applications of integrators in mentioned realizations, another important use is the integration action in the PID controllers; see [1, 21]. The integration action preserves a zero steady state in the closed-loop systems with typical plants. Different types of the variable-, fractional-order elements have been proposed in [22, 23]. For constant orders (fractional or integer orders), all integrators are identical. This property is not valid in the variable-, fractional-order integrators in the mentioned types. Comparing with the model of integrator described in [22], we state here a different and more general model with better motivated initial conditions. Moreover, our investigations of values of coefficients of matrices, that are used for calculations of models, are much more advanced.

The proposed integrator may be used in the variable-, fractional-order digital filters [11, 12], described by related variable-, fractional-order difference equations. In the paper, an equivalent but very useful vector matrix description of the variable-, fractional-order integrator is applied. It becomes a great tool in the variable-, fractional-order integrators description. One should mention that to variable-, fractional-order difference equations we cannot apply the Z -transform.

The paper is organised as follows. After an introduction to the variable-, discrete-, fractional-order calculus, a description of the variable-, fractional-order discrete integrator is

given in Section 3. The formula for the variable-, fractional-order integrator response is derived. Our investigations are illustrated by numerical examples.

2. Preliminaries

The most important in the evaluation of the variable-, fractional-order backward difference/sum is the kernel function, named after its action the *oblivion function*. For $k, l \in \mathbb{Z}$ and a given order function $\nu(\cdot) : \mathbb{Z} \rightarrow \mathbb{R}$, the function of two discrete variables is defined by its values: $a^{[\nu(l)]}(k)$. We assume that order functions have values in the interval $[0, 1]$.

Definition 1. For $k, l \in \mathbb{Z}$ and a given order function $\nu(\cdot)$, one defines the oblivion function, as a discrete function of two variables, by its values $a^{[\nu(l)]}(k)$ given as

$$a^{[\nu(l)]}(k) = \begin{cases} 0 & \text{for } k < 0 \\ 1 & \text{for } k = 0 \\ (-1)^k \frac{\nu(l) [\nu(l) - 1] \cdots [\nu(l) - k + 1]}{k!} & \text{for } k > 0. \end{cases} \quad (1)$$

It is easy to observe that for opposite values of order function holds the following:

$$a^{[-\nu(l)]}(k) = \begin{cases} 0 & \text{for } k < 0 \\ 1 & \text{for } k = 0 \\ \frac{\nu(l) (\nu(l) + 1) \cdots (\nu(l) + k - 1)}{k!} & \text{for } k > 0. \end{cases} \quad (2)$$

Formula (1) in Definition 1 is equivalent to the following recurrence with respect to $k \in \mathbb{N}$:

$$a^{[\nu(l)]}(0) = 1, \quad (3)$$

$$a^{[\nu(l)]}(k) = a^{[\nu(l)]}(k-1) \left[1 - \frac{\nu(l) + 1}{k} \right] \quad \text{for } k \geq 1.$$

In [24], we have proved the following properties for positive values of order function.

Proposition 2 (see [24]). *Let the order function have values $0 < \nu(l) < 1$ for $l \in \mathbb{Z}$. Then, the following properties hold:*

- (a) For all $l \in \mathbb{Z}$ and $k \in \mathbb{N}_1$, $a^{[\nu(l)]}(k) < 0$.
- (b) For all $l \in \mathbb{Z}$, the sequence $(a^{[\nu(l)]}(k))_{k \in \mathbb{N}_1}$ is increasing.
- (c) For each increasing and bounded order function $\nu(\cdot)$ with values in $(0, 1)$ and for each $l \in \mathbb{N}$, there is m_l such that for $k \geq m_l$ the sequence $(a^{[\nu(l)]}(k))_{l \in \mathbb{N}}$ is increasing;

that is, for $k \geq m_l$,

$$a^{[\nu(l+1)]}(k) > a^{[\nu(l)]}(k). \quad (4)$$

Particularly for order functions with values in $1/2 \leq \nu(l) < 1$, the border $m_l = 2$.

- (d) For each increasing and bounded order function $\nu(\cdot)$ with values in $(0, 1)$, there is $m_k \in \mathbb{N}_1$ such that for $k \geq m_k$

$$a^{[\nu(k+1)]}(k+1) > a^{[\nu(k)]}(k). \quad (5)$$

In the sequel, we need to prove parallel properties for oblivion function with negative values of order function with values $-\nu(l) \in (-1, 0)$ for $l \in \mathbb{Z}$.

Proposition 3. *Let one assume that, $\forall l \in \mathbb{Z}$, $\nu(l) \in (0, 1)$. Then the following properties are satisfied:*

- (a) For all $l \in \mathbb{Z}$ and $k \in \mathbb{N}_1$, $a^{[-\nu(l)]}(k) > 0$.
- (b) For all $l \in \mathbb{Z}$, the sequence $(a^{[-\nu(l)]}(k))_{k \in \mathbb{N}_1}$ is decreasing.
- (c) For decreasing and bounded order function $\nu(\cdot)$ with values in $(0, 1)$ and for each $l \in \mathbb{N}$, the sequence $(a^{[-\nu(l)]}(k))_{l \in \mathbb{N}}$ is decreasing; that is, for $k \geq \mathbb{N}_1$,

$$a^{[-\nu(l+1)]}(k) < a^{[-\nu(l)]}(k). \quad (6)$$

- (d) For decreasing and bounded order function $\nu(\cdot)$ with values in $(0, 1)$ and for each $l \in \mathbb{N}$ holds

$$a^{[-\nu(k+1)]}(k+1) < a^{[-\nu(k)]}(k). \quad (7)$$

Proof. For $l \in \mathbb{Z}$, we have that $a^{[-\nu(l)]}(0) = 1$ and for $k > 0$

$$a^{[-\nu(l)]}(k) = \frac{\nu(l) (\nu(l) + 1) \cdots (\nu(l) + k - 1)}{k!}. \quad (8)$$

Then, we directly have points (a), (b), and (c). In (b), we need additionally to notice that $(\nu(l) - 1)/k < 0$, which gives $a^{[-\nu(l)]}(k+1) < a^{[-\nu(l)]}(k)$. We do the next calculations to receive what we claim in point (d). We have the following:

$$a^{[-\nu(k+1)]}(k+1) - a^{[-\nu(k)]}(k) = \left(1 - \frac{-\nu(k+1) + 1}{k+1} \right) a^{[-\nu(k+1)]}(k) - a^{[-\nu(k)]}(k). \quad (9)$$

Moreover, as $0 < \nu(k+1) < 1$, then $0 < 1 + (\nu(k+1) - 1)/(k+1) < 1$ for $k \leq 1$. Knowing that $a^{[-\nu(k+1)]}(k) > 0$, we receive $(1 - (-\nu(k+1) + 1)/(k+1)) a^{[-\nu(k+1)]}(k) < a^{[-\nu(k+1)]}(k)$. Hence,

$$a^{[-\nu(k+1)]}(k+1) - a^{[-\nu(k)]}(k) < a^{[-\nu(k+1)]}(k) - a^{[-\nu(k)]}(k) \quad (10)$$

and then from point (c) we have the thesis. \square

In the next definition, the Grünwald–Letnikov fractional-order backward difference (GL-FOBD) is generalized to the Grünwald–Letnikov variable-, fractional-order backward difference (GL-VFOBD) in part (a) and to the Grünwald–Letnikov variable-, fractional-order backward difference with initialization (GL-VFOBDwI) in part (b). For definition and properties of the Grünwald–Letnikov fractional-order backward difference (GL-FOBD) for constant order, we refer to [10, 18, 25, 26].

Definition 4. Let f be a discrete-variable bounded real valued function.

- (a) The Grünwald–Letnikov variable-, fractional-order backward difference with initialization (GL-VFOBDwI) with an order function $\nu : \mathbb{Z} \rightarrow \mathbb{R}_+ \cup \{0\}$ is defined as an infinite sum, provided that the series is convergent:

$$\begin{aligned} \left({}_{-\infty}^{GL} \Delta^{[\nu(k)]} f \right) (k) &= \sum_{i=0}^{\infty} a^{[\nu(k)]} (i) f(k-i) \\ &= \begin{bmatrix} 1 & a^{[\nu(k)]} (1) & a^{[\nu(k)]} (2) & \dots \end{bmatrix} \begin{bmatrix} f(k) \\ f(k-1) \\ f(k-2) \\ \vdots \end{bmatrix}. \end{aligned} \quad (11)$$

- (b) The Grünwald–Letnikov variable-, fractional-order backward difference (GL-VFOBD) with an order function $\nu : \mathbb{Z} \rightarrow \mathbb{R}_+ \cup \{0\}$ started at k_0 is defined as a finite sum

$$\begin{aligned} \left({}_{k_0}^{GL} \Delta^{[\nu(k)]} f \right) (k) &= \sum_{i=k_0}^k a^{[\nu(k)]} (i-k_0) f(k+k_0-i) \\ &= \sum_{i=0}^{k-k_0} a^{[\nu(k)]} (i) f(k-i) \\ &= \begin{bmatrix} 1 & a^{[\nu(k)]} (1) & \dots & a^{[\nu(k)]} (k-k_0) \end{bmatrix} \begin{bmatrix} f(k) \\ f(k-1) \\ \vdots \\ f(k_0+1) \\ f(k_0) \end{bmatrix}. \end{aligned} \quad (12)$$

For $k_0 = 0$, the GL-VFOBD becomes a discrete convolution: $\left({}_0^{GL} \Delta^{[\nu(k)]} f \right) (k) = (\mathbf{a} * f)(k) = (f * \mathbf{a})(k)$, where $\mathbf{a}(k) := a^{[\nu(k)]}(k)$. In particular case of constant order function, we have the following (for $k > k_0$ and k_0 can be finite or $k_0 = -\infty$):

- (i) $\left({}_{k_0}^{GL} \Delta^{[0]} f \right) (k) = f(k)$;
(ii) $\left({}_{k_0}^{GL} \Delta^{[1]} f \right) (k) = f(k) - f(k-1)$;

- (iii) $\left({}_{k_0}^{GL} \Delta^{[-1]} f \right) (k) = \sum_{i=0}^{k-k_0} f(k-i)$, if only the summation exists.

Next, one assumes that $\nu(k) = 0$ for $k \leq k_0 - 1$. Equality (11) is defined for any $k \geq k_0 > -\infty$, so it is also valid for any $k-1, k-2, \dots, k_0+1, k_0, k_0-1, \dots$

Collecting all such equalities like (11) in one vector matrix form, one obtains

$$\left({}_{-\infty}^{GL} \Delta^{[\nu(k)]} \mathbf{f} \right) (k) = {}_{-\infty} \mathbf{A}_{k_0, k}^{[\nu(k)]} \begin{bmatrix} \mathbf{f}(k) \\ \mathbf{f}_{k_0-1} \end{bmatrix}, \quad (13)$$

where

$$\begin{aligned} \mathbf{f}(k) &= \begin{bmatrix} f(k) \\ f(k-1) \\ \vdots \\ f(k_0+1) \\ f(k_0) \end{bmatrix}, \\ \mathbf{f}_{k_0-1} &= \begin{bmatrix} f(k_0-1) \\ f(k_0-2) \\ \vdots \end{bmatrix}, \end{aligned} \quad (14)$$

$$\begin{aligned} \left({}_{-\infty}^{GL} \Delta^{[\nu(k)]} \mathbf{f} \right) (k) &= \begin{bmatrix} {}_{-\infty}^{GL} \Delta^{[\nu(k)]} f(k) \\ \vdots \\ {}_{-\infty}^{GL} \Delta^{[\nu(k_0)]} f(k_0) \end{bmatrix}, \\ {}_{-\infty} \mathbf{A}_{k_0, k}^{[\nu(k)]} &:= \begin{bmatrix} \mathbf{A}_{k_0, k}^{[\nu(k)]} & -\infty \mathbf{I}_{k_0-1}^{[\nu(k)]} \end{bmatrix}. \end{aligned} \quad (15)$$

Inside matrix (15) we extract the following parts:

$${}_{k_0} \mathbf{A}_k^{[\nu(k)]} := \begin{bmatrix} 1 & a^{[\nu(k)]} (1) & \dots & a^{[\nu(k)]} (k-k_0) \\ 0 & 1 & \dots & a^{[\nu(k-1)]} (k-k_0-1) \\ \vdots & \vdots & & \vdots \\ 0 & 0 & \dots & 1 \end{bmatrix}, \quad (16)$$

$${}_{-\infty} \mathbf{I}_{k_0-1}^{[\nu(k)]} := \begin{bmatrix} a^{[\nu(k)]} (k-k_0+1) & a^{[\nu(k)]} (k-k_0+2) & \dots \\ a^{[\nu(k-1)]} (k-k_0) & a^{[\nu(k-1)]} (k-k_0+1) & \dots \\ \vdots & \vdots & \\ a^{[\nu(0)]} (1) & a^{[\nu(0)]} (2) & \dots \end{bmatrix}. \quad (17)$$

For $\nu = 1$ and $k_0 = 0$, appropriate matrices have the following forms:

$${}_{k_0}\mathbf{A}_k^{[-1]} = \begin{bmatrix} 1 & 1 & 1 & \cdots & 1 & 1 \\ 0 & 1 & 1 & \cdots & 1 & 1 \\ 0 & 0 & 1 & \cdots & 1 & 1 \\ \vdots & \vdots & \vdots & & \vdots & \vdots \\ 0 & 0 & 0 & \cdots & 1 & 1 \\ 0 & 0 & 0 & \cdots & 0 & 1 \end{bmatrix}, \quad (18)$$

$${}_{k_0}\mathbf{A}_k^{[1]} = \begin{bmatrix} 1 & -1 & 0 & \cdots & 0 & 0 \\ 0 & 1 & -1 & \cdots & 0 & 0 \\ 0 & 0 & 1 & \cdots & 0 & 0 \\ \vdots & \vdots & \vdots & & \vdots & \vdots \\ 0 & 0 & 0 & \cdots & 1 & -1 \\ 0 & 0 & 0 & \cdots & 0 & 1 \end{bmatrix}. \quad (19)$$

Moreover, it is worth noticing that ${}_{k_0}\mathbf{A}_k^{[0]} = \mathbf{1}_{k-k_0+1}$, which is the $(k - k_0 + 1) \times (k - k_0 + 1)$ -dimensional identity matrix.

We give now the series of properties of finite dimensional matrices ${}_{k_0}\mathbf{A}_k^{[\nu(k)]}$ and ${}_{k_0}\mathbf{A}_k^{[-\nu(k)]}$ and their inverses, for order function with values $\nu(k) \in (0, 1]$.

Proposition 5 (see [24]). *Assume that for all $k \geq k_0$, $\nu(k) \in (0, 1]$ and $\nu(k) = 0$ for $k \leq k_0 - 1$. Then, all elements of the inverse matrix $({}_{k_0}\mathbf{A}_k^{[\nu(k)]})^{-1}$ are nonnegative.*

Proposition 6 (see [24]). *For an order function $\nu(k) > 0$ and a constant order $\nu_c > 0$, the following equality holds: ${}_{0}\mathbf{A}_k^{[\nu(k)]} {}_{0}\mathbf{A}_k^{(\nu_c)} = {}_{0}\mathbf{A}_k^{[\nu(k)+\nu_c]}$.*

By direct calculations, one can check that ${}_{0}\mathbf{A}_k^{(\nu_c)} {}_{0}\mathbf{A}_k^{[\nu(k)]} \neq {}_{0}\mathbf{A}_k^{[\nu(k)+\nu_c]}$. Proposition 6 confirms the fact that for $\nu(k) = \nu = \text{const}$, we have ${}_{0}\mathbf{A}_k^{(\nu)} {}_{0}\mathbf{A}_k^{(\nu_c)} = {}_{0}\mathbf{A}_k^{(\nu+\nu_c)}$. As a consequence of the last equality, one has the following ${}_{k_0}\mathbf{A}_k^{(\nu)} = ({}_{k_0}\mathbf{A}_k^{(-\nu)})^{-1}$. By direct calculations, we can check that

$$\left({}_{k_0}\mathbf{A}_k^{[\nu(k)]} \right)^{-1} \neq \left({}_{k_0}\mathbf{A}_k^{[-\nu(k)]} \right). \quad (20)$$

The crucial matrix in the VFODI response is ${}_{k_0}\mathbf{A}_k^{[-\nu(k)]}$. We prove the following in [22].

Proposition 7 (see [22]). *For order functions with values $0 \leq \nu(k) \leq 1$ for $k \geq k_0$, all elements of the matrix ${}_{k_0}\mathbf{A}_k^{[-\nu(k)]}$ are nonnegative.*

Proposition 8 (see [22]). *For two order functions with values $0 < \nu_1(k) < \nu_2(k) \leq 1$, for $k \geq k_0$, all elements of the matrix*

$(a_{ij}) = {}_{k_0}\mathbf{A}_k^{[-\nu_1(k)]}$ are less than or equal to these of the matrix $(b_{ij}) = {}_{k_0}\mathbf{A}_k^{[-\nu_2(k)]}$; that is, $a_{ij} \leq b_{ij}$.

3. Variable-, Fractional-Order Difference Integrator (VFODI)

3.1. Description of the VFODI. Let u be the given function $u : \mathbb{Z} \mapsto \mathbb{R}$ and $f : \mathbb{R}^2 \mapsto \mathbb{R}$ be given bounded function of two variables. Let $\bar{f}(k) := f(y(k-1), u(k))$, $k \in \mathbb{Z}$. The variable-, fractional-order discrete-time difference equation for the pair of orders (ν, μ) is described by the following fractional-order difference equation:

$$\left({}_{-\infty}^{GL}\Delta^{[\nu(k)]} y \right) (k) = \left({}_{k_0}^{GL}\Delta^{[-\mu(k)]} \bar{f} \right) (k), \quad k \geq k_0 \quad (21)$$

with initial conditions

$$\mathbf{y}_{k_0-1} = \begin{bmatrix} y(k_0-1) \\ y(k_0-2) \\ \vdots \end{bmatrix} \quad (22)$$

and values $u(k) = 0$ for $k < k_0$.

From definitions of fractional operators, (21) has the following recurrence solution:

$$\begin{aligned} y(k) &= -\sum_{i=1}^{\infty} a^{[\nu(k)]}(i) y(k-i) \\ &+ \sum_{i=0}^{k-k_0} a^{[-\mu(k)]}(i) f(y(k-1-i), u(k-i)), \end{aligned} \quad (23)$$

$k \geq k_0$.

In the simplest situations, we present solutions given by (23) in the form

(i) for $\nu \equiv 0$, $\mu \equiv 0$,

$y(k) = f(y(k-1), u(k))$ and this looks like classical difference equation;

(ii) for $\nu \equiv 1$, $\mu \equiv 0$,

$y(k) = y(k-1) + f(y(k-1), u(k))$ and this is the case of the so-called nabla operator equation;

(iii) for $\nu \equiv 0$, $\mu \equiv 1$,

$y(k) = \sum_{i=1}^{k-k_0} f(y(k-1-i), u(k-i))$;

(iv) for $\nu \equiv 1$, $\mu \equiv 1$,

$y(k) = y(k-1) + \sum_{i=1}^{k-k_0} f(y(k-1-i), u(k-i))$.

In the next definition of variable-, fractional-order difference integrator (VFODI), we assume that $f(y(k-1), u(k)) = b_0 u(k)$. Let us introduce the following notation:

$$\begin{aligned} \mathbf{y}(k) &= \begin{bmatrix} y(k) \\ y(k-1) \\ \vdots \\ y(k_0+1) \\ y(k_0) \end{bmatrix}, \\ \mathbf{u}(k) &= \begin{bmatrix} u(k) \\ u(k-1) \\ \vdots \\ u(k_0+1) \\ u(k_0) \end{bmatrix}, \\ Y(k) &= \begin{bmatrix} y(k) \\ y(k-1) \\ \vdots \end{bmatrix}, \quad \text{for } k \in \mathbb{Z}. \end{aligned} \quad (24)$$

If $k \geq k_0$, then we can write $Y(k)$ in the following way $Y(k) = \begin{bmatrix} y(k) \\ \mathbf{y}_{k_0-1} \end{bmatrix}$.

The variable-, fractional-order difference integrator (VFODI) is described by the following fractional-order difference matrix-vector equation:

$$\left({}_{-\infty} \mathbf{A}_k^{[\nu(k)]} \right) \cdot Y(k) = b_0 \left({}_{k_0} \mathbf{A}_k^{[-\mu(k)]} \right) \mathbf{u}(k) \quad (25)$$

with initial condition $Y(k_0 - 1) = \mathbf{y}_{k_0-1}$. On the right side of (25), we use finite matrix ${}_{k_0} \mathbf{A}_k^{[-\mu(k)]}$ as on the left side there is a rectangular (finite rows and infinite columns) matrix operator. It is because we claim as in the classical cases that values $u(k) = 0$ for $k < k_0$. Then, even if we write infinite operator matrix on the right side, it will give the same action as multiplication by an infinite number of zeros of $u(\cdot)$.

Proposition 9. Equation (25) with initial condition $Y(k_0 - 1) = \mathbf{y}_{k_0-1}$ has the solution given by the following description:

$$\begin{aligned} \mathbf{y}(k) &= \left({}_{k_0} \mathbf{A}_k^{[\nu(k)]} \right)^{-1} \\ &\cdot \left(b_0 {}_{k_0} \mathbf{A}_k^{[-\mu(k)]} \mathbf{u}(k) - {}_{-\infty} \mathbf{I}_{k_0-1}^{[\nu(k)]} \mathbf{y}_{k_0-1} \right). \end{aligned} \quad (26)$$

Proof. The proof follows from the fact that taking into account the initial conditions vector $Y(k_0 - 1)$ and the partition of the matrices ${}_{-\infty} \mathbf{A}_{k_0, k}^{[\nu(k)]}$, we have from (25)

$$\begin{bmatrix} {}_{k_0} \mathbf{A}_k^{[\nu(k)]} & \\ & {}_{-\infty} \mathbf{I}_{k_0-1}^{[\nu(k)]} \end{bmatrix} \begin{bmatrix} \mathbf{y}(k) \\ \mathbf{y}_{k_0-1} \end{bmatrix} = b_0 \left({}_{k_0} \mathbf{A}_k^{[-\mu(k)]} \right) \mathbf{u}(k). \quad (27)$$

It is possible as matrices ${}_{k_0} \mathbf{A}_k^{[\nu(k)]}$ and ${}_{k_0} \mathbf{A}_k^{[-\mu(k)]}$ are always nonsingular. \square

For example, for $k = 1$ and zero initial conditions vector $Y(k_0 - 1) = 0$ with $k_0 = 0$, we have that

$$\begin{aligned} \mathbf{y}(1) &= \begin{bmatrix} y(1) \\ y(0) \end{bmatrix} = b_0 \left(\mathbf{A}_1^{[\nu(1)]} \right)^{-1} \mathbf{A}_1^{[-\mu(1)]} \begin{bmatrix} u(1) \\ u(0) \end{bmatrix}, \\ \mathbf{y}(1) &= b_0 \begin{bmatrix} u(1) + u(0)(\nu(1) + \mu(1)) \\ u(0) \end{bmatrix}. \end{aligned} \quad (28)$$

Hence, $y(0) = b_0 u(0)$ and $y(1) = b_0(u(1) + u(0)(\nu(1) + \mu(1)))$.

Proposition 10. The VFODI of form (25) with fractional orders satisfying the condition that for each $k \geq k_0$, $\nu(k) + \mu(k) = 1$ and zero initial conditions vector $Y(k_0 - 1) = \mathbf{0}$ is a classical first-order summator (discrete-time integrator).

Proof. By the assumption $-\mu(k) = \nu(k) - 1$, then

$${}_{k_0} \mathbf{A}_k^{[\nu(k)]} \mathbf{y}(k) = b_0 {}_{k_0} \mathbf{A}_k^{[\nu(k)-1]} \mathbf{u}(k). \quad (29)$$

Based on investigations in [24], we know that (29) is equivalent to

$${}_{k_0} \mathbf{A}_k^{[\nu(k)]} \mathbf{y}(k) = b_0 {}_{k_0} \mathbf{A}_k^{[\nu(k)]} {}_{k_0} \mathbf{A}_k^{[-1]} \mathbf{u}(k). \quad (30)$$

Matrix ${}_{k_0} \mathbf{A}_k^{[\nu(k)]}$ is always nonsingular as an upper triangular matrix with ones on the main diagonal. Hence, from (30) one immediately gets $\mathbf{y}(k) = b_0 {}_{k_0} \mathbf{A}_k^{[-1]} \mathbf{u}(k)$ and equivalently

$${}_{k_0} \mathbf{A}_k^{[1]} \mathbf{y}(k) = b_0 \mathbf{u}(k). \quad (31)$$

Matrix ${}_{k_0} \mathbf{A}_k^{(1)}$ has the form (19). From the first row of (31) with (19), one obtains $y(k) - y(k-1) = b_0 u(k)$ or equivalently $y(k) = b_0 \sum_{i=0}^k u(i)$. \square

Example 11. In the numerical example, usefulness of the VFODI is presented. In the first one, the discrete unit step responses of the VFODI for assumed fractional-order functions are presented. In the second example, some particular application of the VFODI is shown.

Let us consider two fractional-order functions given by their values for $k \in \mathbb{N}$:

$$\begin{aligned} \nu(k) &= 0.5 - 0.5e^{-0.01k}, \\ \mu(k) &= -0.5 + 0.5e^{-0.05k}. \end{aligned} \quad (32)$$

In Figure 1, plots of order functions $\nu(k)$, black line, and $\mu(k)$, red line, are presented. As a consequence in Figures 2(a) and 2(b), images and 3D matrix values are presented.

In Figures 3(a) and 3(b), images and 3D matrix values of $[{}_{k_0} \mathbf{A}_k^{[\nu(k)]}]^{-1}$ are presented, where (p_1, p_2) are pixels positions and $c(p_1, p_2)$ are the color representations.

The image and values of matrix $[{}_{k_0} \mathbf{A}_k^{[\nu(k)]}]^{-1} {}_{k_0} \mathbf{A}_k^{[-\mu(k)]}$ are given in Figures 4(a) and 4(b).

3.2. Particular Forms of VFODI. We consider here two special cases of (25), the first one for $\mu(k) \equiv 0$ and the second one for $\nu(k) \equiv 0$.

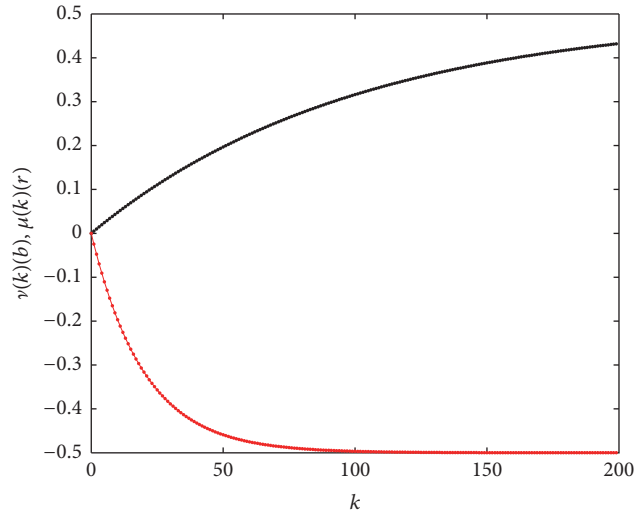
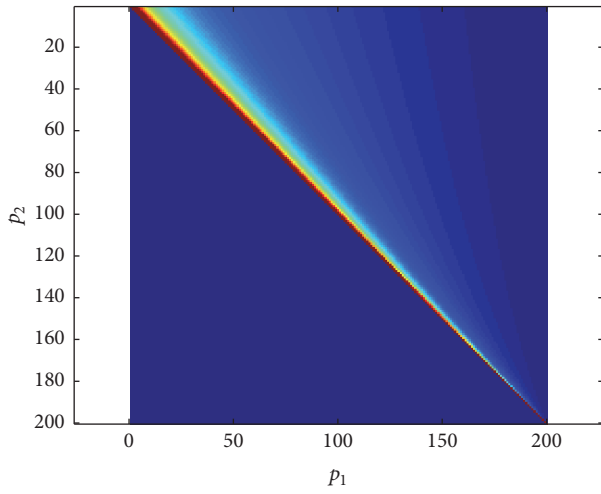
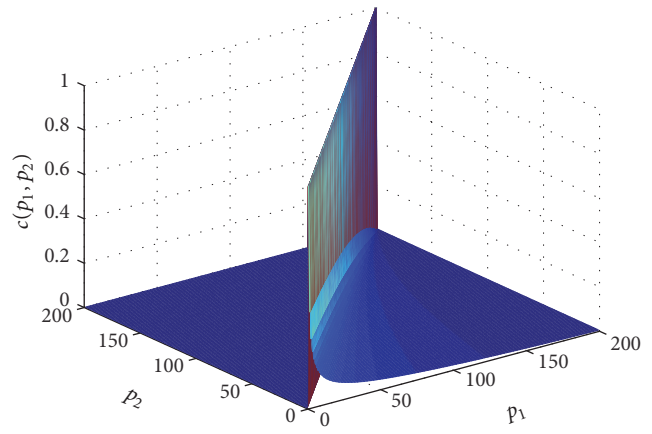


FIGURE 1: Plots of order functions defined by formula (32).

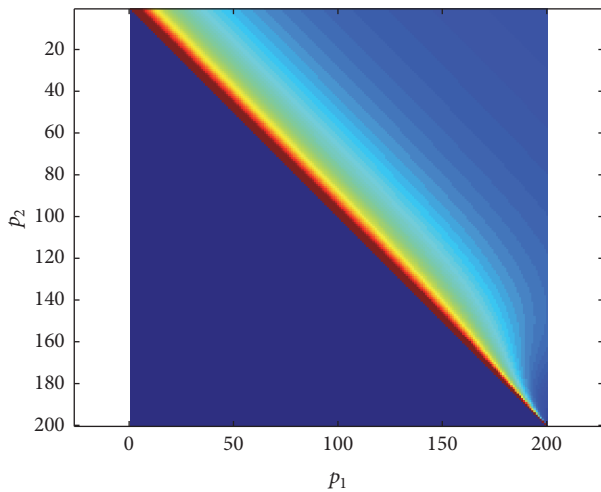


(a) Image of the matrix

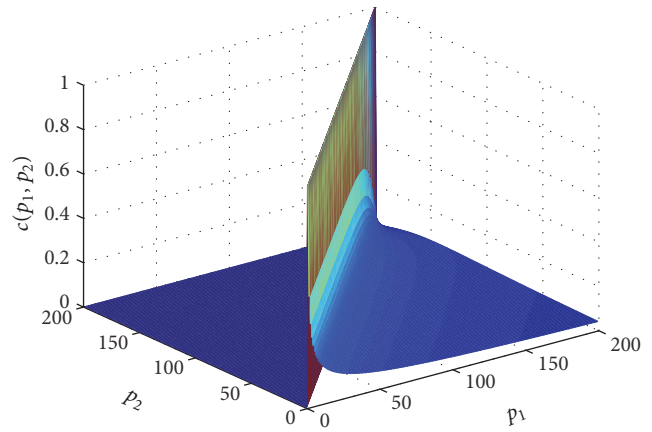


(b) 3D plot of values of the matrix

FIGURE 2: Image of the matrix and 3D plot of values of the matrix $[_{k_0} \mathbf{A}_k^{[\nu(k)]}]^{-1}$.

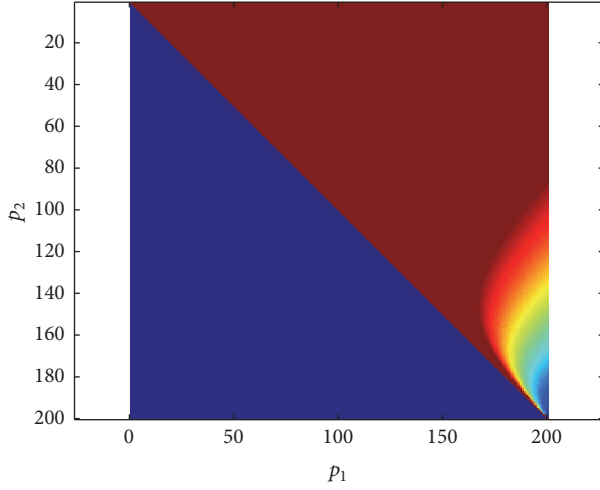


(a) Image of the matrix

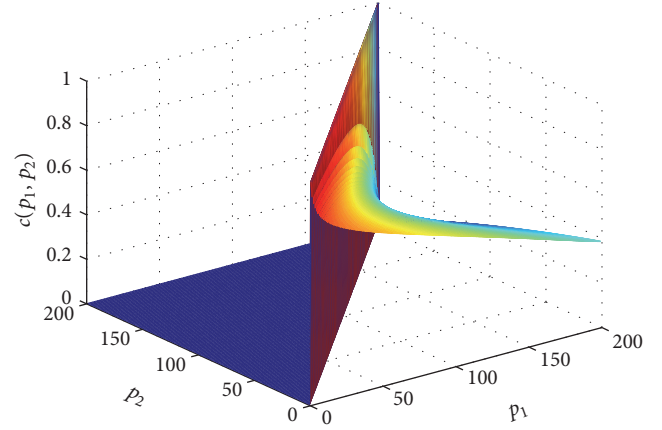


(b) 3D plot of values of the matrix

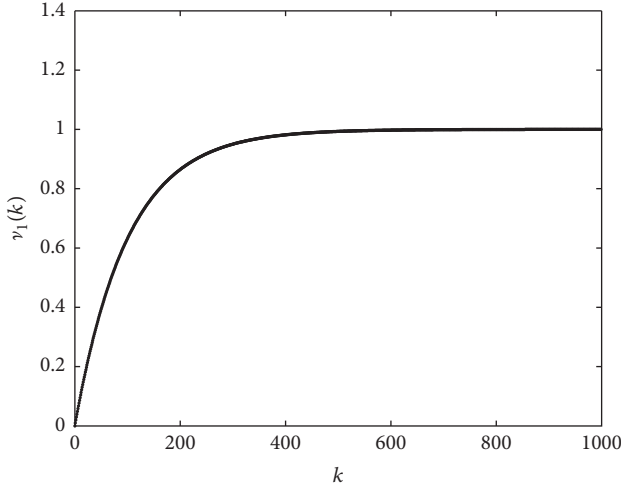
FIGURE 3: Image of the matrix and 3D plot of values of the matrix $[_{k_0} \mathbf{A}_k^{[-\mu(k)]}]$.



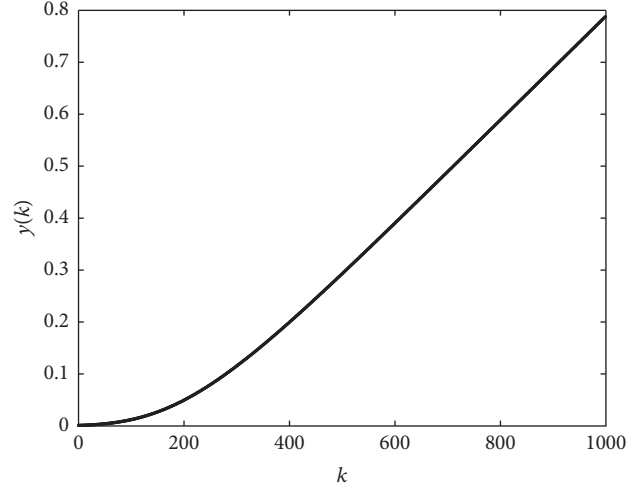
(a) Image of the matrix



(b) 3D plot of values of the matrix

FIGURE 4: Image of the matrix and 3D plot of values of the matrix ${}_{k_0} \mathbf{A}_k^{[\nu(k)]^{-1}} {}_{k_0} \mathbf{A}_k^{[-\mu(k)]}$.

(a) The plot of the order function



(b) The unit step response

FIGURE 5: Plots of the order function ν_1 given by (35) and the unit step response of the 1st form of VFODI represented by formula (34) with $b_0 = 0.001$, $k_0 = 0$.

(i) Let us consider $\mu(k) \equiv 0$. Then, (25) takes form

$$\left({}_{-\infty} \mathbf{A}_k^{[\nu(k)]} \right) \cdot Y(k) = b_0 \mathbf{u}(k) \quad (33)$$

and the VFODI response, with initial condition $Y(k_0 - 1) = \mathbf{y}_{k_0 - 1}$, is described by the formula proved in Proposition 9:

$$\mathbf{y}(k) = b_0 \left({}_{k_0} \mathbf{A}_k^{[\nu(k)]} \right)^{-1} \cdot \mathbf{u}(k) - \left({}_{k_0} \mathbf{A}_k^{[\nu(k)]} \right)^{-1} \cdot {}_{-\infty} \mathbf{I}_{k_0 - 1}^{[\nu(k)]} \mathbf{y}_{k_0 - 1}. \quad (34)$$

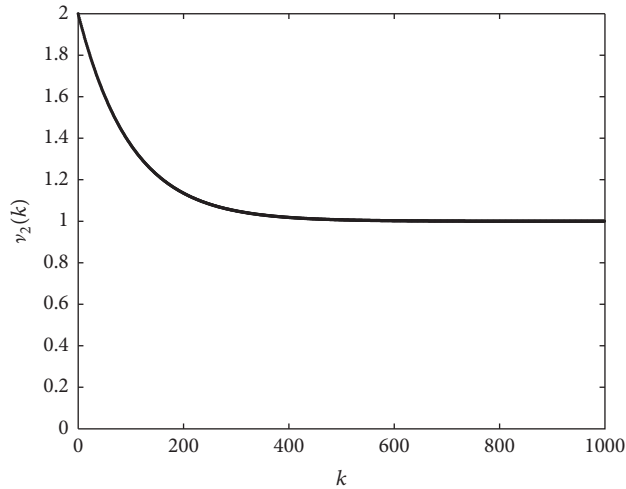
One should emphasise that the initial condition vector is infinite dimensional. This is characteristic for systems with “memory” of the state.

Example 12. In the following numerical example, we examine the discrete unit step responses of the first form of the VFODI. We present plots of order functions and solutions of VFODI, given by (34) with $b_0 = 0.001$, $k_0 = 0$.

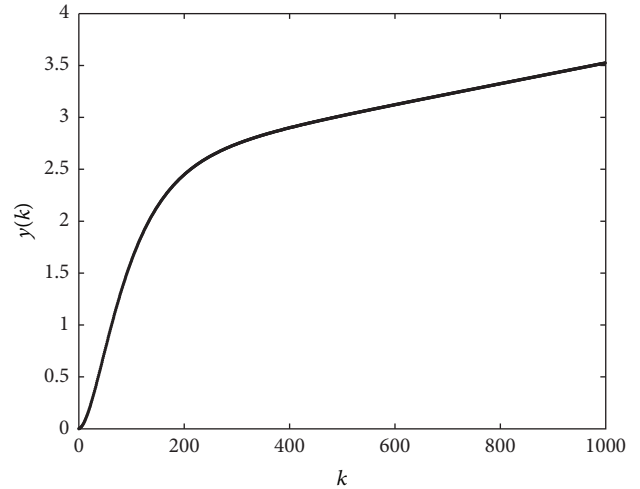
(a) Let us consider order function given by

$$\nu_1(k) = 1 - e^{-0.01k}. \quad (35)$$

The order function ν_1 is plotted in Figure 5(a). The graph of the unit step response is given in Figure 5(b). The considered order function is characterised by two time intervals separated by a time instant $k = 400$. In the first one, the order function increases monotonically from 0 to 1. Hence, the summation force is weaker but growing. In the second interval,



(a) The plot of the order function



(b) The unit step response

FIGURE 6: Plots of the order function v_2 given by (36) and the unit step response of the 1st form of VFODI represented by formula (34) with $b_0 = 0.001$, $k_0 = 0$.

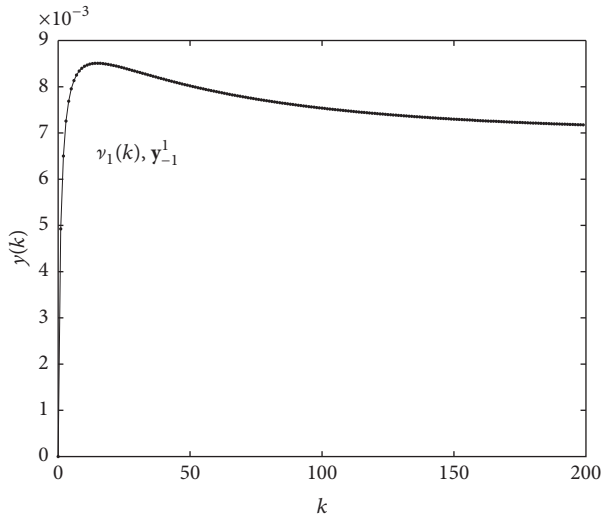
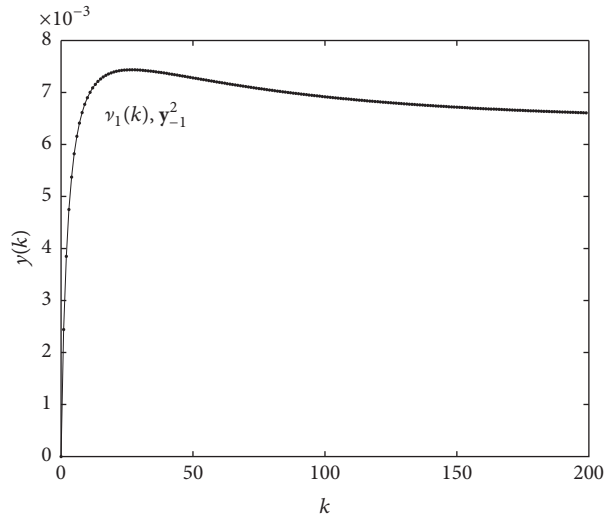
(a) Plot of response to y_{-1}^1 (b) Plot of response to y_{-1}^2

FIGURE 7: The VFOI homogenous responses to y_{-1}^1 and y_{-1}^2 with $b_0 = 0.001$, $k_0 = 0$ in formula (34) and the order $v_1(k) = 1 - e^{-0.01k}$.

the function is almost constant. This means that the VFODI acts as a classical integrator. The VFODI response presented in Figure 5(b) is similar to the response of the ideal summator with lag.

(b) Now we consider decreasing order function given by

$$v_2(k) = 1 + e^{-0.01k}. \quad (36)$$

The graph of the order function (36) is given in Figure 6(a). Values of order function begin at 2 and monotonically tend to 1. This means that summation force successively declines to the classical summator. The response is shown in Figure 6(b).

Example 13. The VFOIE possesses also the property related to the classical integrator. For zero input signal and nonzero

initial conditions, it preserves a nonzero output. In this example, we split our consideration to two different initial conditions:

$$\mathbf{y}_{-1}^1 = \begin{bmatrix} 1 \\ 0 \\ 0 \\ 0 \\ \vdots \end{bmatrix}, \quad (37)$$

$$\mathbf{y}_{-1}^2 = \begin{bmatrix} 0 \\ 0 \\ 1 \\ 0 \\ \vdots \end{bmatrix}.$$

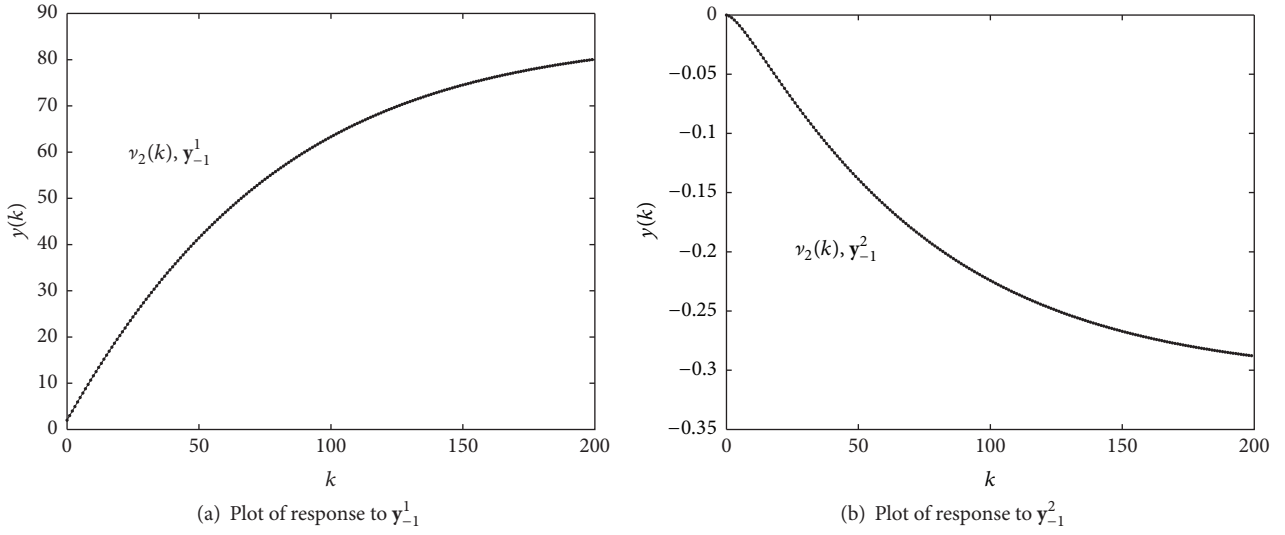


FIGURE 8: The VFOI homogenous responses to y_{-1}^1 and y_{-1}^2 with $b_0 = 0.001$, $k_0 = 0$ in formula (34) and the order $\nu_2(k) = 1 + e^{-0.01k}$.

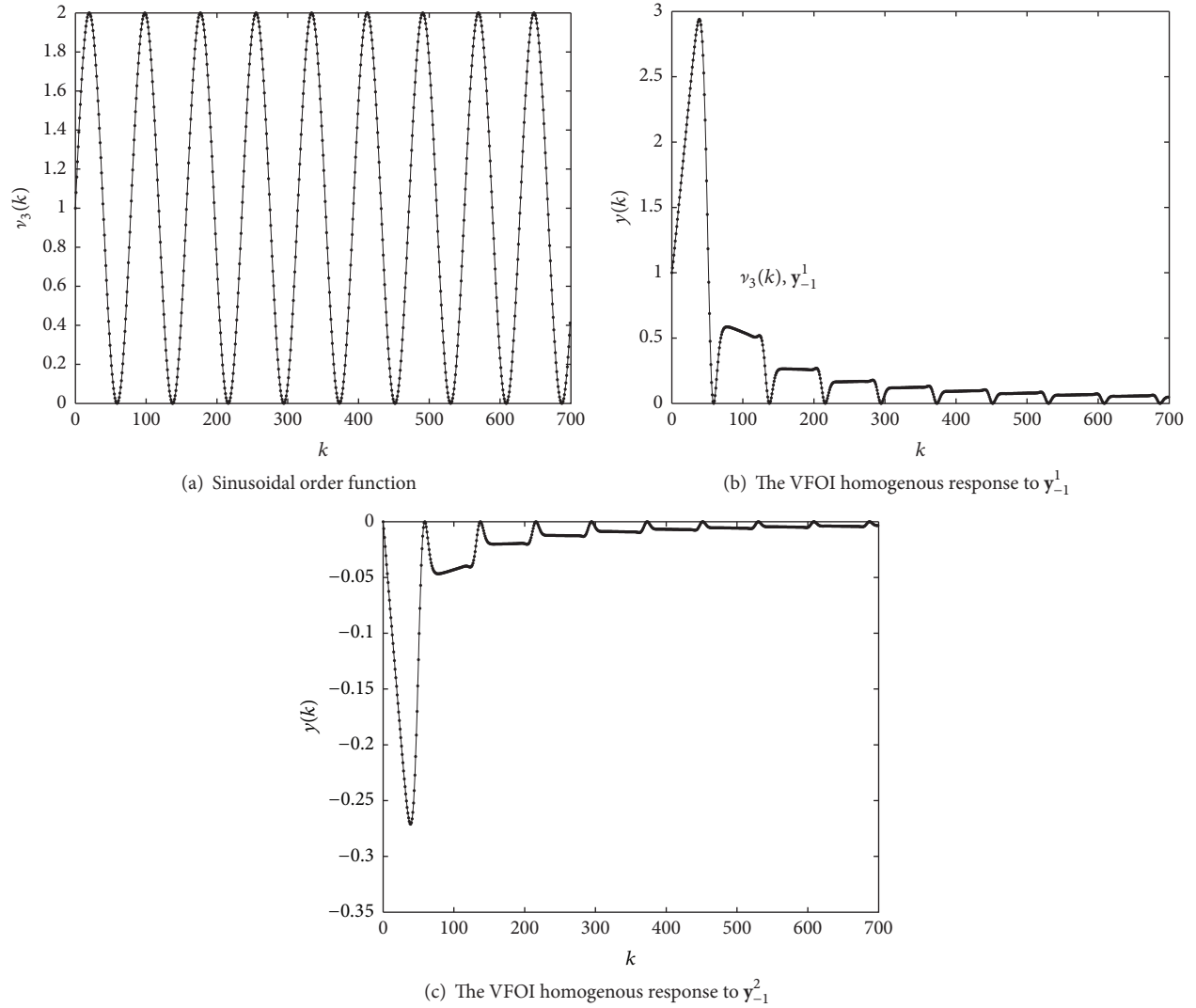


FIGURE 9: Plots of sinusoidal order function $\nu_3(k) = 1 + \sin(\pi k/40)$ and the VFOI homogenous response to y_{-1}^1 and y_{-1}^2 represented by formula (34) with $b_0 = 0.001$, $k_0 = 0$.

We change in the item order functions, considering increasing and decreasing order functions.

(c) For the order function $\nu_1(k) = 1 - e^{-0.01k}$, we obtain the VFOIE homogenous responses presented in Figures 7(a) and 7(b), respectively. Indeed responses differ a little from each other. The second response reaches slightly lower steady state. This statement confirms that the oblivion function decreases due to the initial condition placed in the past. For the order function $\nu_2(k) = 1 + e^{-0.01k}$, we obtain the VFOIE homogenous responses presented in Figures 8(a) and 8(b), respectively.

(d) In this part, we examine the homogenous response to \mathbf{y}_{-1}^1 with a periodic order function given by $\nu_3(k) = 1 + \sin(\pi k/40)$. The plots of order functions and the simulated solutions are presented in Figures 9(a), 9(b), and 9(c), respectively. Values of both responses are tending to zero.

(ii) Let us take $\nu(k) \equiv 0$. Then, (25) takes the form

$$Y(k) = b_0 \left({}_{k_0} \mathbf{A}_k^{[-\mu(k)]} \right) \mathbf{u}(k) \quad (38)$$

and the VFODI response, with initial condition $Y(k_0 - 1) = \mathbf{y}_{k_0 - 1}$, is described by the formula proved in Proposition 9:

$$\mathbf{y}(k) = b_0 {}_{k_0} \mathbf{A}_k^{[-\mu(k)]} \mathbf{u}(k) - {}_{-\infty} \mathbf{I}_{k_0 - 1}^{[\nu(k)]} \mathbf{y}_{k_0 - 1}. \quad (39)$$

4. Final Conclusions

The form of the variable-, fractional-order difference integrator (VFODI) is characterised by the two independent fractional-order functions. Both order functions are assumed to be nonnegative. There is no restriction concerning their equality. There is an immense choice of the fractional-order selection. One of the promising choices appears to be a relation of the order function with the input and output signals $\nu[|u(k)|]$ and $\mu[|u(k)|]$ or $\nu[|y(k)|]$ and $\mu[|y(k)|]$. In the closed-loop systems with VFO PID controller, the order functions can be related to the closed-loop error signal.

Conflicts of Interest

The authors declare that they have no conflicts of interest.

Acknowledgments

This research was partially supported by the Bialystok University of Technology Grant S/WI/1/2016 (Dorota Mozyrska) and the Lodz University of Technology Grant 501\12-24-1-5437 (Piotr Ostalczyk) and funded from the sources for research by Ministry of Science and Higher Education.

References

- [1] T. Kaczorek, *Linear Control Systems: Analysis of Multivariable Systems*, John Wiley & Sons, Inc, New York, NY, USA, 1992.
- [2] T. Kailath, *Linear Systems*, Prentice-Hall, Englewood Cliffs, NJ, USA, 1980.
- [3] R. Abu-Saris and Q. Al-Mdallal, "On the asymptotic stability of linear system of fractional-order difference equations," *Fractional Calculus and Applied Analysis. An International Journal for Theory and Applications*, vol. 16, no. 3, pp. 613–629, 2013.
- [4] D. Baleanu, K. Diethelm, E. Scalas, and J. J. Trujillo, *Fractional Calculus Models and Numerical Methods*, vol. 3 of *Series on Complexity, Nonlinearity and Chaos*, World Scientific, Singapore, 2012.
- [5] D. Baleanu, J. A. T. Machado, and A. C. J. Luo, *Fractional Dynamics and Control*, Springer-Verlag, New York, NY, USA, 2012.
- [6] R. Caponetto, G. Dongola, G. Fortuna, and I. Petras, *Fractional Order Systems: Modeling and Control Applications*, World Scientific, Singapore, 2010.
- [7] S. Das, *Functional Fractional Calculus for System Identification and Controls*, Springer-Verlag, Berlin-Heidelberg, Germany, 2009.
- [8] R. A. Ferreira and D. F. Torres, "Fractional h -difference equations arising from the calculus of variations," *Applicable Analysis and Discrete Mathematics*, vol. 5, no. 1, pp. 110–121, 2011.
- [9] D. Mozyrska and M. g. Wyrwas, "The Z-transform method and delta type fractional difference operators," *Discrete Dynamics in Nature and Society*, vol. 2015, Article ID 852734, 12 pages, 2015.
- [10] I. Podlubny, *Fractional Differential Equations*, vol. 198, Academic Press, San Diego, Calif, USA, 1999.
- [11] A. Halanay and J. Samuel, *Differential Equations, Discrete Systems and Control*, Kluwer Academic Publishers, Dordrecht, Netherlands, 1997.
- [12] E. C. Ifeachor and B. W. Jervis, *Digital Signal Processing*, Addison-Wesley, Edinburgh Gate, UK, 1993.
- [13] F. M. Atici and P. W. Eloe, "A transform method in discrete fractional calculus," *International Journal of Difference Equations*, vol. 2, no. 2, pp. 165–176, 2007.
- [14] M. A. Al-Alaoui, "Novel digital integrator and differentiator," *Electronics Letters*, vol. 29, no. 4, pp. 376–378, 1993.
- [15] N. R. O. Bastos, R. A. C. Ferreira, and D. F. M. Torres, "Discrete-time fractional variational problems," *Signal Processing*, vol. 91, no. 3, pp. 513–524, 2011.
- [16] D. Mozyrska, "Multiparameter fractional difference linear control systems," *Discrete Dynamics in Nature and Society*, vol. 2014, Article ID 183782, 8 pages, 2014.
- [17] M. D. Ortigueira, F. J. V. Coito, and J. J. Trujillo, "Discrete-time differential systems," *Signal Processing*, vol. 107, pp. 198–217, 2015.
- [18] P. Ostalczyk, *Discrete Fractional Calculus: Applications in Control and Image Processing*, vol. 14 of *Series in Computer Vision*, World Scientific Publishing Co Pte Ltd, Singapore, 2016.
- [19] R. Stanisławski and K. J. Latawiec, "Stability analysis for discrete-time fractional-order LTI state-space systems. Part I: New necessary and sufficient conditions for the asymptotic stability," *Bulletin of the Polish Academy of Sciences: Technical Sciences*, vol. 61, no. 2, pp. 353–361, 2013.
- [20] R. Stanisławski and K. J. Latawiec, "Stability analysis for discrete-time fractional-order LTI state-space systems. Part II: new stability criterion for FD-based systems," *Bulletin of the Polish Academy of Sciences: Technical Sciences*, vol. 61, no. 2, pp. 363–370, 2013.
- [21] J. Cervera, A. Baños, C. A. Monje, and B. M. Vinagre, "Tuning of fractional PID controllers by using QFT," in *Proceeding of the*

32nd Annual Conference on IEEE Industrial Electronics (IECON '06), pp. 5402–5407, Paris, France, November 2006.

- [22] P. Ostalczyk and D. Mozyrska, “The second form of the variable-, fractional-order discrete-time integrator,” in *Proceedings of the 21st International Conference on Methods and Models in Automation and Robotics, MMAR 2016*, pp. 859–864, pol, September 2016.
- [23] D. Sierociuk, W. Malesza, and M. Macias, “On a new symmetric fractional variable order derivative,” in *Theoretical developments and applications of non-integer order systems*, S. Domek and P. Dworak, Eds., vol. 357, pp. 29–39, Springer, Cham, Heidelberg, Germany, 2016.
- [24] D. Mozyrska and P. Ostalczyk, “Variable-fractional-order Grünwald-Letnikov backward difference selected properties,” in *Proceedings of the 39th International Conference on Telecommunications and Signal Processing, TSP 2016*, June 2016.
- [25] A. A. Kilbas, H. M. Srivastava, and J. J. Trujillo, *Theory and Applications of Fractional Differential Equations*, Elsevier, Amsterdam, Netherlands, 2006.
- [26] A. Oustaloup, *La dérivation non entière: théorie, synthèse et applications*, Hermes, Paris, France, 1995.

Research Article

Fractional Order Memristor No Equilibrium Chaotic System with Its Adaptive Sliding Mode Synchronization and Genetically Optimized Fractional Order PID Synchronization

Karthikeyan Rajagopal, Laarem Guessas, Anitha Karthikeyan, Ashokkumar Srinivasan, and Girma Adam

Centre for Non-Linear Dynamics, Defense University, Addis Ababa, Ethiopia

Correspondence should be addressed to Karthikeyan Rajagopal; rkarthikeyan@gmail.com

Received 12 October 2016; Revised 21 November 2016; Accepted 22 December 2016; Published 26 March 2017

Academic Editor: Ahmed G. Radwan

Copyright © 2017 Karthikeyan Rajagopal et al. This is an open access article distributed under the Creative Commons Attribution License, which permits unrestricted use, distribution, and reproduction in any medium, provided the original work is properly cited.

This paper introduces a fractional order memristor no equilibrium (FOMNE) chaotic system and investigates its adaptive sliding mode synchronization. Firstly the dynamic properties of the integer order memristor no equilibrium system are analyzed. The fractional order memristor no equilibrium system is then derived from the integer order model. Lyapunov exponents and bifurcation with fractional order are investigated. An adaptive sliding mode control algorithm is derived to globally synchronize the identical fractional order memristor systems and genetically optimized fractional order PID controllers are designed and used to synchronize the FOMNE systems. Finally the fractional order memristor no equilibrium system is realized using FPGA.

1. Introduction

Chaotic systems are a special case of nonlinear systems which can be categorized as chaotic if the system possesses at least one positive Lyapunov exponent and hyperchaotic if the system possesses two or more positive Lyapunov exponents. Lyapunov exponents and fractal dimension studies are important in defining the complexity of chaotic and hyperchaotic systems [1, 2]. Chaotic systems found significant importance after the discovery of a 3D weather model by Lorenz [3].

By early 21st century many researchers have announced different chaotic systems such as Chen system [4] Liu system [5], Sundarapandian system [6], Sundarapandian system [7], and Pham system [8]. Chaotic systems with no equilibrium are of great interest in chaos literature. If sum of all the Lyapunov exponents is zero then the system is a conservative system [9].

Memristors popularly known as the fourth fundamental circuit element were characterized as a nonlinear and low power device was proposed by Chua [10, 11]. In 2008

Hewlett-Packard [HP] engineers announced the first physical realization of memristors. In memristor literatures several models had been presented such as linear and nonlinear ion drift model and threshold adaptive memristor model [12–14]. A Murali-Lakshmanan-Chua's circuit with a piecewise linear active flux controlled memristors with hyperchaotic behavior was investigated by Ishaq Ahamed and Lakshmanan [15]. A memristor based hyperchaotic complex Lu system and its adaptive synchronization were studied by Wang et al. [16].

Synchronization of chaotic systems is of great importance when one chaotic oscillator drives the other. Because of high sensitivity to initial conditions two identical chaotic systems may have exponentially diverging state trajectories. Many methods have been proposed in the literature such as active control method [17, 18], adaptive control method [19, 20], extended back stepping control [21, 22], sliding mode control [23, 24], and adaptive sliding mode [25–27].

Fractional calculus [28–31] has fully emerged into a mathematical field with applications in nonlinear controls, electrical and mechanical controls, and so forth. Fraction

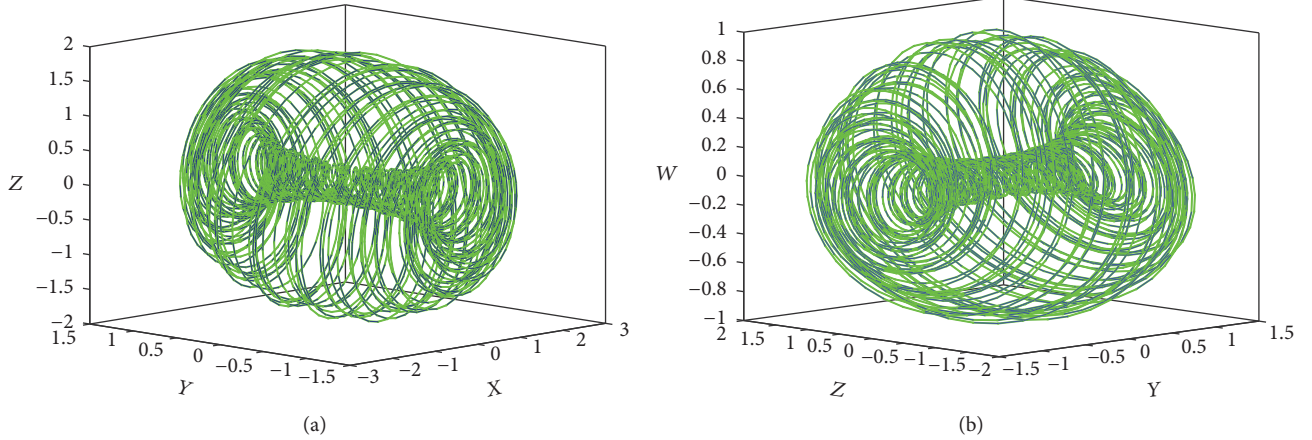


FIGURE 1: 3D state portrait of the novel memristor no equilibrium system (XYZ plane; YZW plane).

chaotic systems have been investigated by many researchers [28–35]. Fractional order controllers [24–27, 36–38] are more effective compared to its integer order models especially in chaos control and synchronization. Fractional order systems with no equilibrium are announced and investigated by Li and Chen [39]. For the numerical simulation of fractional order chaotic system Ivo [40] explained a methodology with a register memory component.

For chaos to exist there should be at least one unstable equilibrium point. Recently many researchers have announced chaotic systems with no equilibrium or one equilibrium [32–34]. Chaotic systems with no equilibrium exhibit hidden attractions as the orbit of attractions does not intersect with any equilibrium points [35, 41]. An algorithmic search methodology was developed by Jafari et al. [42] to discover chaotic flows with no equilibrium.

PID controllers are objects of steady effort for improvements of their quality and robustness. One of the possibilities to improve PID controllers is to use the fractional order controllers (FOPID) with noninteger derivation and integration parts; they generalize the integer order PID controller, used and verified their effectiveness in [38, 40, 43–45], and add more flexibility to control design with accuracy for the real world processes. But finding appropriate parameters values for the FOPID controller is still a difficult task, so in practice control engineers still often use trial and error for the tuning process.

Motivated by the above, in this paper we announce a novel integer order memristor no equilibrium chaotic system. We then derive a fractional order model of the proposed novel system. The dynamic properties of both integer order and fractional order novel systems are investigated. A fractional order adaptive sliding mode control and genetically optimized fractional order PID are proposed to synchronize the identical novel fraction order systems. Finally the proposed fractional order system is implemented in FPGA.

2. Memristor No Equilibrium Chaotic System

In this section we introduce a novel 4D memristor no equilibrium chaotic system (MNECS) with three parameters derived from the Sundarapandian system [46] by including a fourth state which is a combination of state feedback and the flux controlled memristor [47, 48] as described by

$$\begin{aligned}\dot{x} &= az + xy \\ \dot{y} &= 1 - x^2 - z^2 - w^2 \\ \dot{z} &= -bx + yz \\ \dot{w} &= cz - w - w(x)z\end{aligned}\quad (1)$$

and the parameter values are $a = 10$, $b = 9$, and $c = 8.7$ and $w(\cdot)$ is the memductance of a flux controlled memristor characterized by the cubic nonlinearity $w(x) = a_1 + b_1x^2$, $a_1 = 4$, and $b_1 = 0.01$ [47].

Figure 1 shows the state portrait of system (1).

For numerical simulations, we take the initial values of the hyperchaotic system (1) as

$$\begin{aligned}x(0) &= 1, \\ y(0) &= 1, \\ z(0) &= 1, \\ w(0) &= 1.\end{aligned}\quad (2)$$

3. Properties of the 4D Memristor No Equilibrium Chaotic System

3.1. Equilibrium Points. The equilibrium points of system (1) can be found by solving

$$\begin{aligned}0 &= az + xy \\ 0 &= 1 - x^2 - z^2 - w^2 \\ 0 &= -bx + yz \\ 0 &= cz - w - w(x)z.\end{aligned}\quad (3)$$

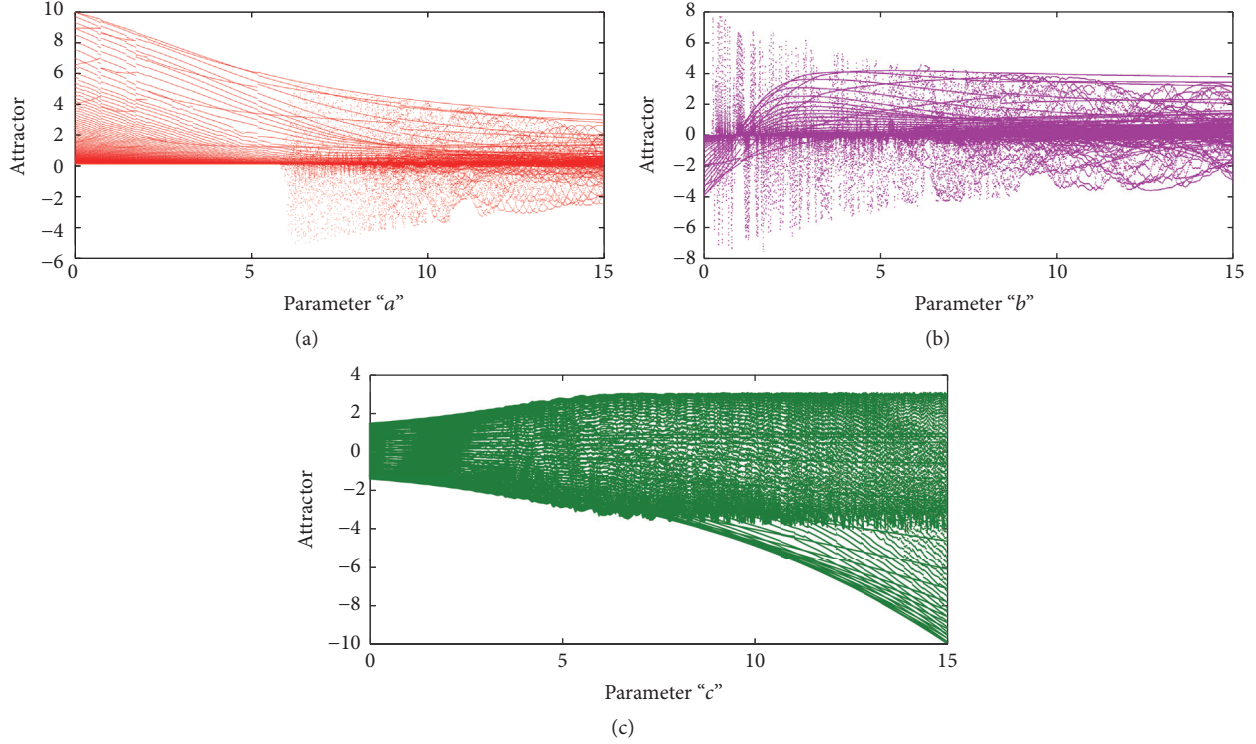


FIGURE 2: (a) Bifurcation plot versus a . (b) Bifurcation plot versus b . (c) Bifurcation plot versus c .

From (3) it can be clearly seen that $az^2 + bx^2 = 0$. As $a > 0$ and $b > 0$ the only solution is $x = z = 0$. It can be seen that $cz - w - w(x)z = 0$ and $x = z = 0$ make $w = 0$; we conclude that $y = 0$. Hence system (1) has no equilibrium points.

3.2. Lyapunov Exponents and Kaplan-Yorke Dimension. The Jacobian matrix of the novel system (1) is calculated as

$$J(X) = \begin{bmatrix} y & x & a & 0 \\ -2x & 0 & -2z & -2w \\ -b & z & y & 0 \\ 0.02xz & 0 & c - 4 - 0.01x^2 & -1 \end{bmatrix}. \quad (4)$$

The eigenvalues of the Jacobian matrix at equilibrium are $\lambda_1 = -1.0000$, $\lambda_2 = 9.4868i$, $\lambda_3 = -9.4868i$, and $\lambda_4 = 0$. The Lyapunov exponents of the system are $L_1 = 0.033426$, $L_2 = 0$, $L_3 = -0.028964$, and $L_4 = -1.005153$. The existence of positive Lyapunov exponents confirms the chaotic behavior of system (1). The sum of all the Lyapunov exponents is negative confirming that the system is dissipative.

The Kaplan-Yorke dimension of a chaotic system is defined as

$$D_{KY} = j + \sum_{i=1}^j \frac{L_i}{L_{j+1}}, \quad (5)$$

where j is the maximum integer such that $\sum L_i < 0$.

$$D_{KY} = 3 + \frac{L_1 + L_2 + L_3}{|L_4|} = 3.004439. \quad (6)$$

3.3. Bifurcation, Bicoherence, and Poincare Map. In order to understand the dynamical behavior of the MNECS, the bifurcation plots are derived for three cases as follows.

Case 1. Fix $b = 9$, $c = 8.7$, $a_1 = 4$, and $b_1 = 0.01$ and vary a between $[0 \ 20]$.

Case 2. Fix $a = 10$, $c = 8.7$, $a_1 = 4$, and $b_1 = 0.01$ and vary b between $[0 \ 20]$.

Case 3. Fix $a = 10$, $b = 9$, $a_1 = 4$, and $b_1 = 0.01$ and vary c between $[0 \ 20]$.

As discussed in [49], the transient behaviors occurring in memristor based nonlinear systems may result in longer simulation times to reach steady states. Hence we used the ode45 solver for numerical simulations. Figures 2(a), 2(b), and 2(c) show the bifurcation plots of the system for the parameters a , b , and c , respectively. The variation in Lyapunov exponents with reference to the parameters a , b , and c is also derived and compared with the bifurcation plots. Figure 3 shows the variation of the Lyapunov exponents with the parameters. As it is observed from Figures 2 and 3, for the values of $8.5 \leq a, b, c \leq 10.5$, the bifurcation plots show

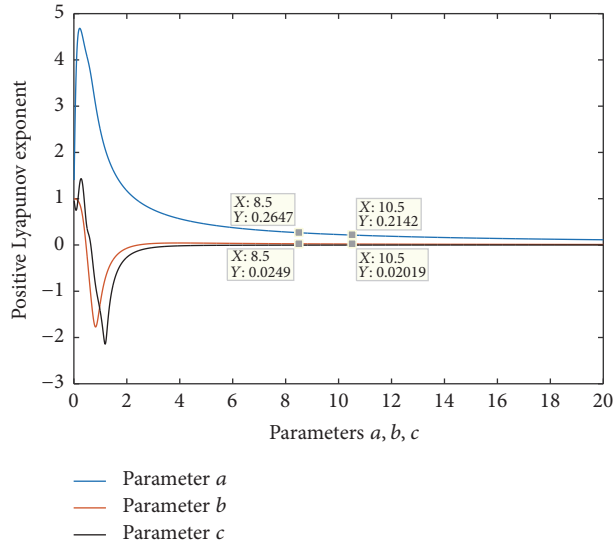


FIGURE 3: Positive Lyapunov exponent for variation in parameters (a, b, c).

denser points confirming the existence of a stable positive Lyapunov exponent.

The regular power spectra investigations cannot be used to analyze nonlinear systems as it does not have the required phase information. Hence researchers have adopted bicoherence or bispectrum analysis to analyze the period doubling sequence occurring in chaotic systems. Bicoherence contour of the novel system (1) as shown in Figure 4 shows the coupling between Fourier modes and is centered about the dominant frequencies composing the limit cycles [50]. As the system exhibits positive Lyapunov exponents, the chaotic behavior of the system increases resulting in period doubling and motions at additional frequencies because of the quadratic interactions between the dominant frequencies and itself. In Figure 4, the dominant frequencies are shown in a circled area which contributes to the bispectrum as indicated.

The autobispectrum with the Fourier coefficients can be derived as

$$G(\omega_1, \omega_2) = E [F(\omega_1)F(\omega_2)F^*(\omega_1 + \omega_2)], \quad (7)$$

where ω_n is the radian frequency and F is the Fourier coefficients of the time series. The normalized magnitude spectrum of the bispectrum known as the squared bicoherence is given by

$$g(\omega_1, \omega_2) = \frac{|G(\omega_1, \omega_2)|^2}{P(\omega_1)P(\omega_2)P(\omega_1 + \omega_2)}, \quad (8)$$

where $P(\omega_1)$ and $P(\omega_2)$ are the power spectra at f_1 and f_2 .

The Poincare map is usually constructed by plotting the value of the state variable for every time it passes through a particular plane. Plotting the value every time it passes through the $x = 0$ plane where x is changing from negative to positive is the normal practice done when studying most

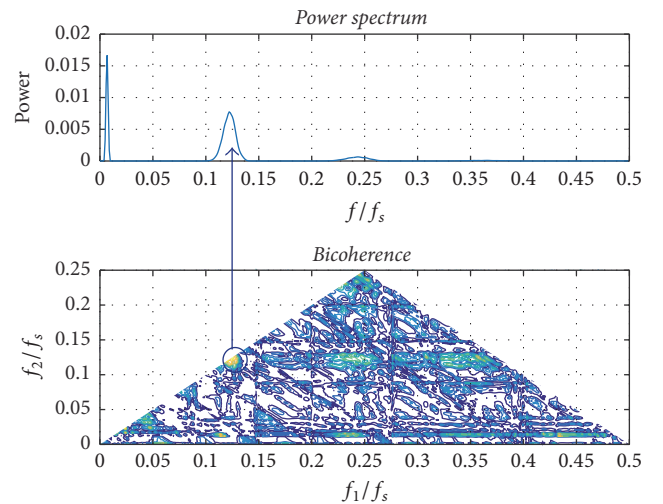


FIGURE 4: Contour of bicoherence for the novel system (1).

of the chaotic attractors. In the case of the proposed novel system (1), the regular method of plotting zero crossing of the x plane is of no interest because of the nature of the system. Hence we plotted the zero crossing of system (1) with reference to the z plane. Figure 5 shows the Poincare sections in the 3D state portrait of system (1). Σ_+ indicates the negative to positive crossing and Σ_- indicates the positive to negative crossing in the z plane.

4. Fractional Order Memristor No Equilibrium Chaotic (FOMNE) System

In this section we derive the fractional order model of the memristor no equilibrium system (1). There are three

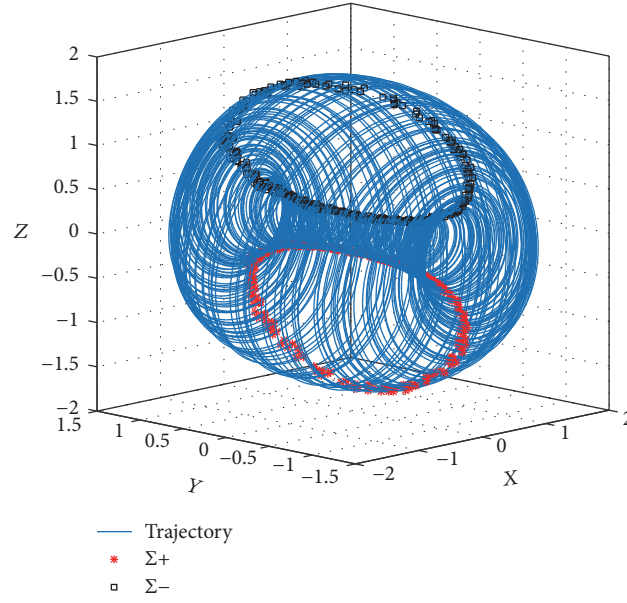


FIGURE 5: Poincare sections in the 3D state portrait of system (1) (XYZ plane).

commonly used definitions of the fractional order differential operator, Grunwald-Letnikov, Riemann-Liouville, and Caputo [28–31].

In this section, we will study the dynamical behavior of fractional order system derived from novel system (1) with the Grunwald-Letnikov (GL) definition, which is defined as

$$\begin{aligned} {}_a D_t^q f(t) &= \lim_{h \rightarrow 0} \left\{ \frac{1}{h^q} \sum_{j=0}^{\lfloor (t-a)/h \rfloor} (-1)^j \binom{q}{j} f(t-jh) \right\} \\ &= \lim_{h \rightarrow 0} \left\{ \frac{1}{h^\alpha} \Delta_h^q f(t) \right\}, \end{aligned} \quad (9)$$

where a and t are limits of the fractional order equation, $\Delta_h^q f(t)$ is generalized difference, h is the step size, and q is the fractional order of the differential equation.

For numerical calculations the above equation is modified as

$${}_{(t-L)} D_t^q f(t) = \lim_{h \rightarrow 0} \left\{ h^{-q} \sum_{j=0}^{N(t)} b_j (f(t-jh)) \right\}. \quad (10)$$

Theoretically fractional order differential equations use infinite memory. Hence when we want to numerically calculate or simulate the fractional order equations we have to use finite memory principal, where L is the memory length and h is the time sampling.

$$N(t) = \min \left\{ \left\lceil \frac{t}{h} \right\rceil, \left\lceil \frac{L}{h} \right\rceil \right\}. \quad (11)$$

The binomial coefficients required for the numerical simulation are calculated as

$$b_j = \left(1 - \frac{a+\alpha}{j} \right) b_{j-1}. \quad (12)$$

Using (10), the fractional order model of system (1) is derived as

$$\begin{aligned} D^{q_x} x &= az + xy \\ D^{q_y} y &= 1 - x^2 - z^2 - w^2 \\ D^{q_z} z &= -bx + yz \\ D^{q_w} w &= cz - w - zw(x), \end{aligned} \quad (13)$$

where $a = 10$, $b = 9$, $c = 8.7$, $a_1 = 4$, $b_1 = 0.01$, q_x, q_y, q_z , and q_w are the fractional orders of the system, and $w(\cdot)$ is the memductance of a flux controller memristor characterized by the nonlinearity $w(x) = a_1 + b_1 x^2$, $a_1 = 4$, and $b_1 = 0.01$ [46]. For numerical simulations, we take the initial values of the hyperchaotic system (1) as $x(0) = 1$, $y(0) = 1$, $z(0) = 1$, and $w(0) = 1$. Figure 6 shows the 3D state portrait of the fractional order system (13) for $q_x = q_y = q_z = q_w = 0.99$.

5. Stability Analysis of FOMNE System

As the FOMNE system has no defined equilibrium points, direct calculation of eigenvalues is impossible and hence we consider the origin $[0, 0, 0, 0]$ as the only time bound trivial solution and use it for stability analysis of the system.

5.1. Commensurate Order. For commensurate FOMNE system of order q , the system is stable and exhibits chaotic oscillations if $|\arg(\text{eig}(J_E))| = |\arg(\lambda_i)| > q\pi/2$, where J_E is the Jacobian matrix at the equilibrium E and λ_i are the eigenvalues of the FOMNE system where $i = 1, 2, 3, 4$. As seen from the FOMNE system, the eigenvalues should remain in the unstable region and the necessary condition for the

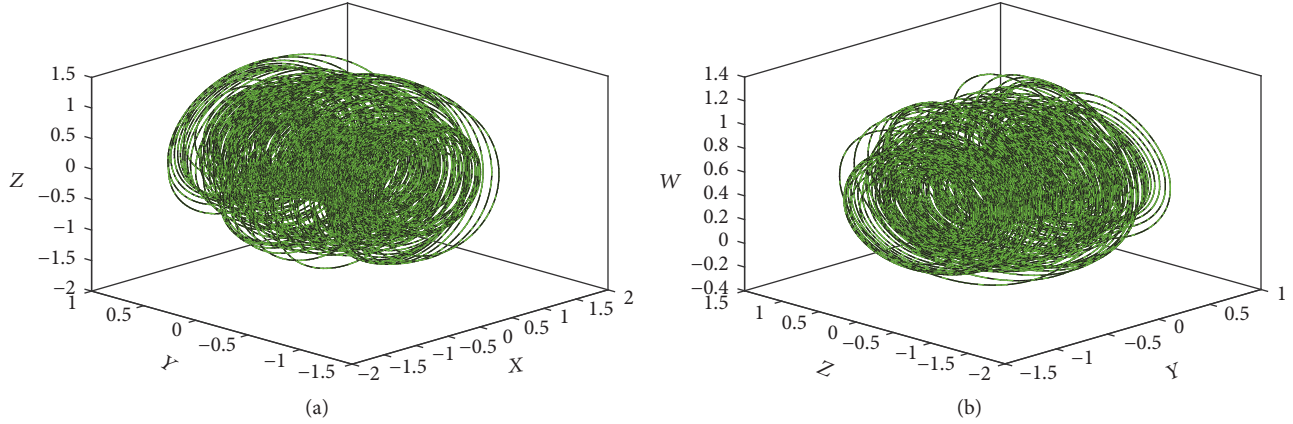


FIGURE 6: 3D state portrait of the FOMNE system (XYZ plane; YZW plane).

FOMNE system to be stable is $q > (2/\pi)\tan^{-1}(|\text{Im } \lambda|/\text{Re } \lambda)$. As the eigenvalues of the system are $\lambda_1 = -1.0000$, $\lambda_2 = 9.4868i$, $\lambda_3 = -9.4868i$, and $\lambda_4 = 0$, it is clearly seen that the value λ_2 is a saddle point and remains in the unstable region contributing to the existence of chaotic oscillations.

5.2. Incommensurate Order. The necessary condition for the FOMNE system to exhibit chaotic oscillations in the incommensurate case is $\pi/2M - \min_i(|\arg(\lambda_i)|) > 0$, where M is the LCM of the fractional orders. If $q_x = 0.9$, $q_y = 0.9$, $q_z = 0.8$, and $q_w = 0.8$, then $M = 10$. The characteristic equation of the system evaluated at the equilibrium is $\det(\text{diag}[\lambda^{Mq_x}, \lambda^{Mq_y}, \lambda^{Mq_z}, \lambda^{Mq_w}] - J_E) = 0$ and by substituting the values of M and the fractional orders $\det(\text{diag}[\lambda^9, \lambda^9, \lambda^8, \lambda^8] - J_E) = 0$, the characteristic equation is $\lambda^{34} - 2\lambda^{27} - 3\lambda^{26} + \lambda^{20} + 5\lambda^{19} + \lambda^{18} + 90\lambda^{17} - 2\lambda^{12} - 4\lambda^{11} - 91\lambda^{10} - 180\lambda^9 + \lambda^4 + \lambda^3 + 90\lambda^2 + 90\lambda$. The approximated solution of the characteristic equation is $\lambda_{34} = 1.414$ whose argument is zero which is the minimum argument and hence the stability necessary condition becomes $\pi/20 - 0 > 0$ which solves for $0.0785 > 0$ and hence the FOMNE system is stable and chaos exists in the incommensurate system.

6. Dynamic Analysis of the Fractional Order Memristor No Equilibrium System

Most of the dynamic properties of the integer order system (1) like the Lyapunov exponents, eigenvalues, and bifurcation with parameters are preserved in the fractional order if $q_i > 0.90$, where $i = x, y, z, w$. The most important analysis of interest when investigating a fractional order system is the bifurcation with fractional order. The resistance of the memristor increases from the initial value until it reaches its maximum R_{off} in a certain time period which is called the saturation time t_{sat} [51]. The fractional order parameter can be used to control the saturation time from a part of a second up to several minutes under the same input voltage [51, 52]. The saturation time can be controlled through the fractional order where it can be less than 1 sec when $\alpha < 0.5$

up to higher values when $\alpha > 0.5$. This specific character of the fractional order memristor is useful in determining the largest positive Lyapunov exponent of the system. Figure 7 shows the 3D state portrait (XYZ plane) of the FOMNE system for various fractional orders $q_x = q_y = q_z = q_w = q$. The largest positive Lyapunov exponent ($L_1 = 0.038174$) of the FOMNE system appears when $q = 0.99$ against its largest integer order Lyapunov exponent ($L_1 = 0.033426$). Hence fractional order chaos suppression/control and synchronization prove efficient than the integer order controls as the systems show the largest positive Lyapunov exponent in fractional order close to 1. It can also be seen that, as the fractional order q decreases, the FOMNE system starts losing its largest positive Lyapunov exponent. When $q \leq 0.9$ the only positive Lyapunov exponent of the system becomes negative and thus the chaotic oscillations in the system disappear.

7. Adaptive Fractional Order Sliding Mode Synchronization

In this section we investigate the adaptive fractional order sliding mode synchronization of identical systems. Let us define a generalized fractional order master system as

$$D^{q_m} x_m = f(x_m) + F(x_m) a, \quad (14)$$

where q_m is the fractional order of the master system and generalized slave system with adaptive controller as

$$D^{q_s} x_s = g(x_s) + G(x_s) b + u(t), \quad (15)$$

where $u(t)$ is the adaptive controller for synchronizing the nonidentical systems and q_s is the fractional order of the slave system.

Let us define the synchronization error as

$$e = x_s - x_m. \quad (16)$$

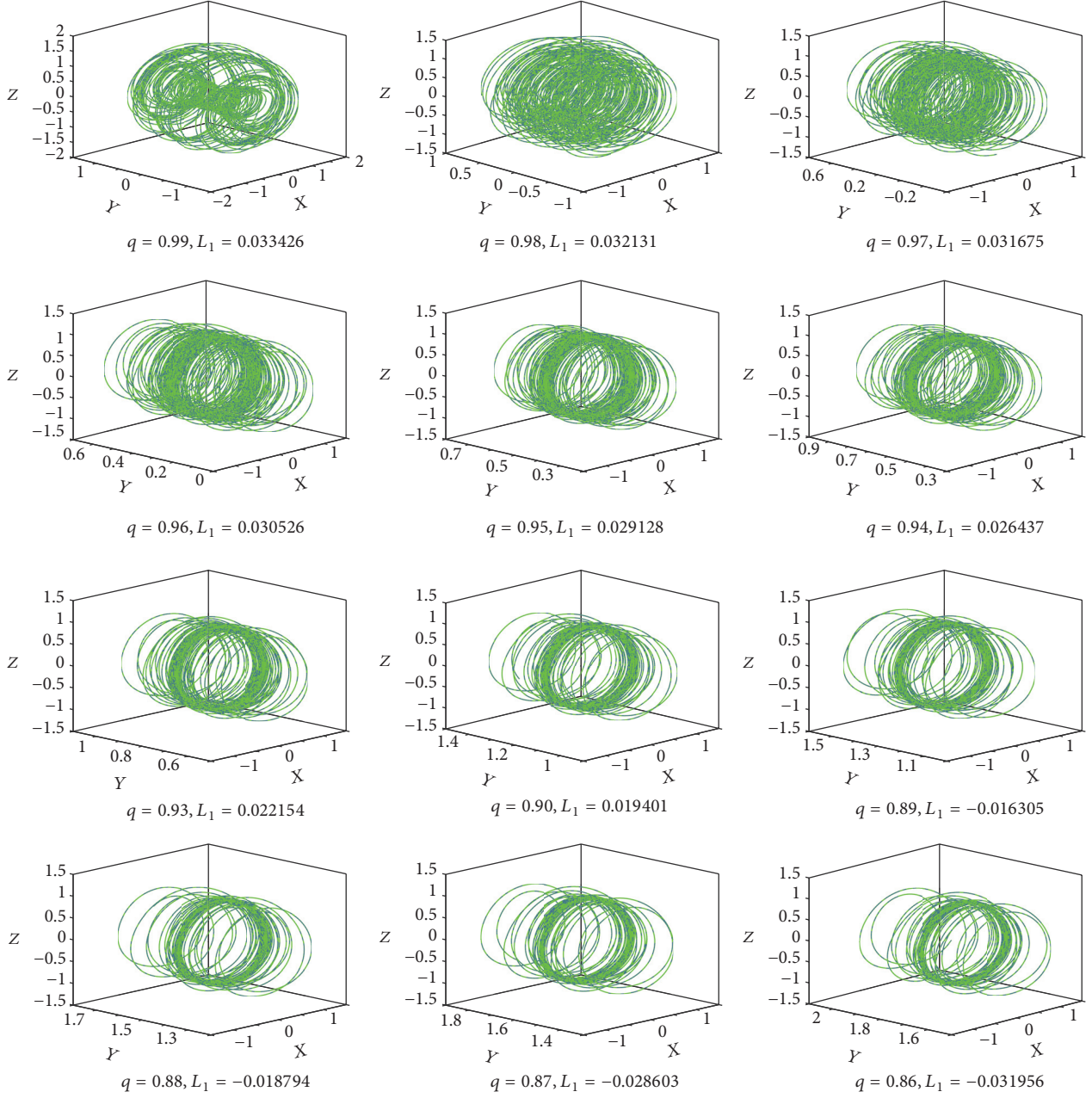


FIGURE 7: 3D state portrait (XYZ plane) of FOMNE system for various fractional orders.

The sliding surface for the integral sliding mode control [26, 27, 36] is defined as

$$s(e) = e + k \int e(\tau) d\tau. \quad (17)$$

The fractional first derivative of the sliding surface is derived as

$$D^q s = D^q e + ke. \quad (18)$$

The fractional order error dynamics are defined as

$$D^q e = D^{q_s} x_s - D^{q_m} x_m. \quad (19)$$

Using (14) and (15) in (19),

$$D^q e = g(x_s) + G(x_s)b + u(t) - f(x_m) - F(x_m)a. \quad (20)$$

Let us define the adaptive controller as

$$u(t) = -g(x_s) - G(x_s)\hat{b} + f(x_m) - F(x_m)\hat{a} - ke - \eta \operatorname{sgn}(s) - \rho s, \quad (21)$$

where k , η , and ρ are positive gain values, \hat{a} and \hat{b} are parameter estimates of master and slave systems, and s is the sliding surface.

Using (21) in (20), the error dynamics simplify to

$$D^q e = G(x_s) [b - \hat{b}] - F(x_m) [a - \hat{a}] - \eta \operatorname{sgn}(s) - \rho s. \quad (22)$$

The Lyapunov candidate function to analyze the stability of the controller is defined as

$$V = \frac{1}{2} s^2 + \frac{1}{2} (b - \hat{b})^2 + \frac{1}{2} (a - \hat{a})^2. \quad (23)$$

The Lyapunov first derivate is derived as

$$\dot{V} = s \cdot \dot{s} + (b - \hat{b}) \left(-\dot{\hat{b}} \right) + (a - \hat{a}) \left(-\dot{\hat{a}} \right). \quad (24)$$

By definition of fractional calculus [29, 30],

$$\dot{x}(t) = D_t^{1-q} \cdot D_t^q x(t). \quad (25)$$

Using (25) in (24),

$$\begin{aligned} \dot{V} = s \cdot D_t^{1-q} \cdot D_t^q s - (b - \hat{b}) \left(D_t^{1-q} \cdot D_t^q \hat{b} \right) \\ - (a - \hat{a}) \left(D_t^{1-q} \cdot D_t^q \hat{a} \right). \end{aligned} \quad (26)$$

Finding the sign of the Lyapunov first derivative using (26) seems difficult and hence we use the modified fractional order Lyapunov method defined by Rajagopal et al. [37] as

$$\frac{1}{2} D_t^q x^2(t) \leq x(t) \frac{1}{2} D_t^q x(t), \quad q \in (0, 1). \quad (27)$$

Using (27), (20), and (18) in (24),

$$\begin{aligned} \dot{V} \leq ks \left[G(x_s) (b - \hat{b}) - F(x_m) (a - \hat{a}) - \eta \operatorname{sgn}(s) \right. \\ \left. - \rho s \right] - (b - \hat{b}) \left(\dot{\hat{b}} \right) - (a - \hat{a}) \left(\dot{\hat{a}} \right). \end{aligned} \quad (28)$$

Let us define the parameter estimate laws as

$$\begin{aligned} D^q \hat{b} &= ks \cdot G(x_s) \\ D^q \hat{a} &= ks \cdot F(x_m). \end{aligned} \quad (29)$$

Using (29) in (28)

$$\dot{V} \leq -\eta |s_w| - \rho s^2 \quad (30)$$

as η and ρ are all positive and \dot{V} is negative definite. Using Barbalat's lemma [53], we conclude that $e_i(t) \rightarrow 0$ as $t \rightarrow \infty$.

7.1. Adaptive Sliding Mode Synchronization of Identical FOMNE Systems. For synchronization let us define the master system as

$$\begin{aligned} D^{q_x} x_m &= az_m + x_m y_m \\ D^{q_y} y_m &= 1 - x_m^2 - z_m^2 - w_m^2 \\ D^{q_z} z_m &= -bx_m + y_m z_m \\ D^{q_w} w_m &= cz_m - w_m - z_m w(x_m) \end{aligned} \quad (31)$$

and the slave system with the adaptive controller is defined as

$$\begin{aligned} D^{q_x} x_s &= \hat{a} z_s + x_s y_s + u_x \\ D^{q_y} y_s &= 1 - x_s^2 - z_s^2 - w_s^2 + u_y \\ D^{q_z} z_s &= -\hat{b} x_s + y_s z_s + u_z \\ D^{q_w} w_s &= \hat{c} z_s - w_s - z_s w(x_s) + u_w, \end{aligned} \quad (32)$$

where \hat{a} , \hat{b} , and \hat{c} are the unknown system parameters and u_x , u_y , u_z , and u_w are the adaptive controllers.

The synchronization error dynamics are defined as

$$\begin{aligned} D^{q_x} e_x &= D^{q_x} x_s - D^{q_x} x_m \\ D^{q_y} e_y &= D^{q_y} y_s - D^{q_y} y_m \\ D^{q_z} e_z &= D^{q_z} z_s - D^{q_z} z_m \\ D^{q_w} e_w &= D^{q_w} w_s - D^{q_w} w_m, \end{aligned} \quad (33)$$

where e_x , e_y , e_z , and e_w are the synchronization errors given by

$$e_i = i_s - i_m \quad (34)$$

and $i = x, y, z, w, s$, and m are slave and master systems, respectively.

Using (31) and (32) in (33), we simplify error dynamics as

$$\begin{aligned} D^{q_x} e_x &= \hat{a} z_s + x_s y_s - az_m - x_m y_m + u_x \\ D^{q_y} e_y &= -x_s^2 - z_s^2 - w_s^2 + x_m^2 + z_m^2 + w_m^2 + u_y \\ D^{q_z} e_z &= -\hat{b} x_s + y_s z_s + bx_m - y_m z_m + u_z \\ D^{q_w} e_w &= \hat{c} z_s - w_s - z_s w(x_s) - cz_m + w_m \\ &\quad + z_m w(x_m) + u_w. \end{aligned} \quad (35)$$

The parameter estimation errors are defined as

$$\begin{aligned} e_a &= a - \hat{a}; \\ e_b &= b - \hat{b}; \\ e_c &= c - \hat{c}. \end{aligned} \quad (36)$$

The first derivatives of (36) are

$$\begin{aligned} D^q e_a &= -D^q \hat{a} \\ D^q e_b &= -D^q \hat{b} \\ D^q e_c &= -D^q \hat{c}. \end{aligned} \quad (37)$$

Let us define the integral sliding surface as

$$s_i = e_i + k_i \int e_i(\tau) d\tau, \quad (38)$$

where $i = x, y, z, w$ are the states, $k_i > 0$, s_i is the sliding surface, and e_i is the synchronization errors. The first derivative of the sliding surface (38) can be derived as

$$D^{q_i} s_i = D^{q_i} e_i + k_i e_i. \quad (39)$$

Let us define the Lyapunov candidate function as

$$V = \frac{1}{2} [s_x^2 + s_y^2 + s_z^2 + s_w^2 + e_a^2 + e_b^2 + e_c^2]. \quad (40)$$

The first derivative of the Lyapunov candidate function (40) is

$$\dot{V} = s_x \dot{s}_x + s_y \dot{s}_y + s_z \dot{s}_z + s_w \dot{s}_w + e_a \dot{e}_a + e_b \dot{e}_b + e_c \dot{e}_c. \quad (41)$$

By definition of fractional calculus [29, 30],

$$\dot{x}(t) = D_t^{1-q} \cdot D_t^q x(t). \quad (42)$$

Applying (42) in (41)

$$\begin{aligned} \dot{V} = & s_x D_t^{1-q} \cdot D_t^q s_x + s_y D_t^{1-q} \cdot D_t^q s_y + s_z D_t^{1-q} \cdot D_t^q s_z \\ & + s_w D_t^{1-q} \cdot D_t^q s_w + e_a D_t^{1-q} \cdot D_t^q e_a + e_b D_t^{1-q} \\ & \cdot D_t^q e_b + e_c D_t^{1-q} \cdot D_t^q e_c. \end{aligned} \quad (43)$$

As observed in (43), analysis of the Lyapunov first derivative is difficult; hence we use the modified fractional order Lyapunov method defined by Rajagopal et al. [37] as

$$\frac{1}{2} D_t^q x^2(t) \leq x(t) \frac{1}{2} D_t^q x(t), \quad q \in (0, 1). \quad (44)$$

Applying (44) in (41),

$$\begin{aligned} \dot{V} \leq & s_x D^{q_x} s_x + s_y D^{q_y} s_y + s_z D^{q_z} s_z + s_w D^{q_w} s_w \\ & + e_a D^q e_a + e_b D^q e_b + e_c D^q e_c \\ \dot{V} \leq & s_x [\hat{a} z_s + x_s y_s - a z_m - x_m y_m + u_x + k_x e_x] \\ & + s_y [-x_s^2 - z_s^2 - w_s^2 + x_m^2 + z_m^2 + w_m^2 + u_y \\ & + k_y e_y] + s_z [-\hat{b} x_s + y_s z_s + b x_m - y_m z_m + u_z \\ & + k_z e_z] + s_w [\hat{c} z_s - w_s - z_s w(x_s) - c z_m + w_m \\ & + z_m w(x_m) + u_w + k_w e_w] - e_a D^q \hat{a} - e_b D^q \hat{b} \\ & + e_c D^q \hat{c}. \end{aligned} \quad (45)$$

After some mathematical simplifications,

$$\begin{aligned} \dot{V} \leq & s_x [\hat{a} e_z + x_s y_s - x_m y_m + u_x + k_x e_x] + s_y [-x_s^2 \\ & - z_s^2 - w_s^2 + x_m^2 + z_m^2 + w_m^2 + u_y + k_y e_y] \\ & + s_z [-\hat{b} e_x + y_s z_s - y_m z_m + u_z + k_z e_z] + s_w [\hat{c} e_z \\ & - w_s - z_s w(x_s) + w_m + z_m w(x_m) + u_w + k_w e_w] \\ & - s_x z_m e_a + s_z x_m e_b - s_w z_m e_c - e_a D^q \hat{a} - e_b D^q \hat{b} \\ & + e_c D^q \hat{c}. \end{aligned} \quad (46)$$

Let us define the adaptive controllers as

$$\begin{aligned} u_x = & -\hat{a} e_z - x_s y_s + x_m y_m - k_x e_x - \eta_x \operatorname{sgn}(s_x) \\ & - \rho_x s_x \\ u_y = & x_s^2 + z_s^2 + w_s^2 - x_m^2 - z_m^2 - w_m^2 - k_y e_y \\ & - \eta_y \operatorname{sgn}(s_y) - \rho_y s_y \\ u_z = & \hat{b} e_x - y_s z_s + y_m z_m - k_z e_z - \eta_z \operatorname{sgn}(s_z) - \rho_z s_z \\ u_w = & -\hat{c} e_z + w_s + z_s w(x_s) - w_m - z_m w(x_m) - k_w e_w \\ & - \eta_w \operatorname{sgn}(s_w) - \rho_w s_w. \end{aligned} \quad (47)$$

And parameter estimation adaptive laws can be defined as

$$\begin{aligned} D^q \hat{a} = & -s_x z_m \\ D^q \hat{b} = & -s_z x_m \\ D^q \hat{c} = & -s_w z_m. \end{aligned} \quad (48)$$

Using the adaptive controllers (47) and the parameter estimation laws (48) in (46),

$$\begin{aligned} \dot{V} \leq & -\eta_x |s_x| - \eta_y |s_y| - \eta_z |s_z| - \eta_w |s_w| - \rho_x s_x^2 \\ & - \rho_y s_y^2 - \rho_z s_z^2 - \rho_w s_w^2 \end{aligned} \quad (49)$$

as $\eta_x, \eta_y, \eta_z,$ and η_w and $\rho_x, \rho_y, \rho_z,$ and ρ_w are all positive and \dot{V} is negative definite. Using Barbalat's lemma [53], we conclude that $e_i(t) \rightarrow 0$ as $t \rightarrow \infty$. For numerical simulations we take the initial conditions as $x_m(0) = 1, y_m(0) = -1, z_m(0) = -1, w_m(0) = 1, x_s(0) = -2, y_s(0) = 3, z_s(0) = -2, w_s(0) = 4,$ and $\hat{a} = 1, \hat{b} = 4,$ and $\hat{c} = 13$. Figure 8 shows the time history of the synchronization errors. Figure 9 shows the adapted parameters.

8. Genetically Optimized Fractional Order PID (FOPID) Controller for the Synchronization of FOMNE Systems

In this section we investigate the synchronization of FOMNE systems using genetically optimized (GA) FOPID controllers (u_x, u_y, u_z, u_w) [38, 44, 45] implemented in feedback loops given by

$$u_i = K_p e_i + K_I \int_0^t e_i d\tau^\beta + K_D \frac{d^\delta e_i}{dt^\delta}, \quad i = x, y, z, w, \quad (50)$$

where u_i is the fractional order PID action control for $i = x, y, z, w$ and δ, β are the fractional order differential and integral operators, e_i is the error signal, and $K_p, K_I,$ and K_D are the proportional, integral, and the derivative gains to synchronize the fractional order model of the memristor no equilibrium system (1). We use genetic algorithm [54, 55] to optimize the controller gains such that the error e_i is minimized. Matlab tools are used for numerical simulations with the following constraints defined.

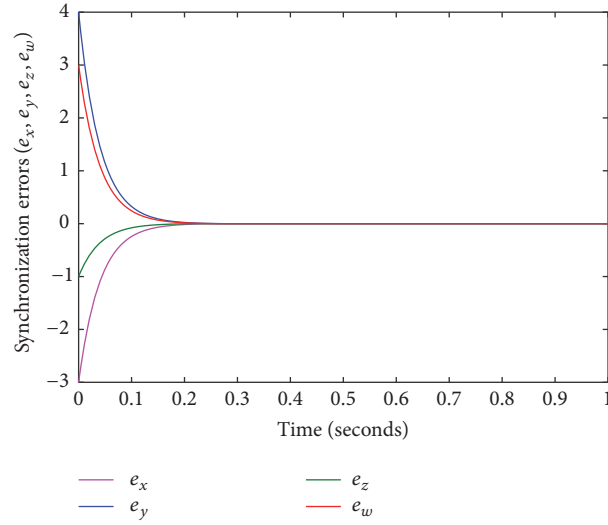


FIGURE 8: Time history of synchronization errors (e_x, e_y, e_z, e_w).

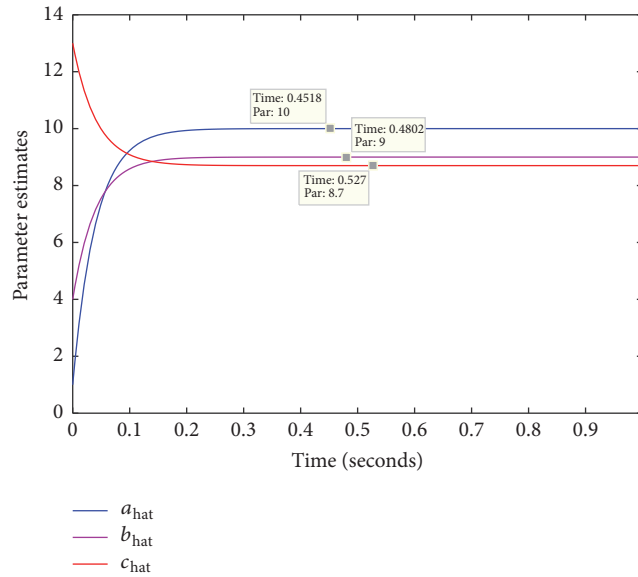


FIGURE 9: Estimated Parameters (a, b, c).

Variable bounds matrix of the proportional, integral, and the derivative gains = $[-0.001, 0.001]$; population size = 80, GA. Genetically, bigger population size give better approximation; number of generations = 100; selection function = stochastic uniform; crossover fraction = 0.8; mutation function = Gaussian; stopping criteria = error performance criterion; length of the chromosome = 12 (decimal codage).

Tuning of PID controllers involves the selection of $K_p, K_I,$ and K_D gains for better control performance which is defined with reference to the required performance index. There are

two important performance indices ISE (Integrated Squared Error) and IAE (Integrated Absolute Error) as given in the following:

$$\begin{aligned} \text{ISE} &= \int_0^{\infty} e_i^2(\tau) d\tau, \\ \text{IAE} &= \int_0^{\infty} |e_i(\tau)| d\tau. \end{aligned} \quad (51)$$

In this paper we use IAE as the objective function and the fitness functions is as given below

$$\text{fitness function} = \frac{1}{\sum \text{abs}(e_i)}, \quad (52)$$

$$e_i = e_x + e_y + e_z + e_w.$$

We synchronize the master system (31) and the slave system (32) using the GA optimized PID controllers with parameters known (Case 1) and parameters unknown (Case 2).

Case 1 (parameters known). In this section we assume that the parameters of the slave system are known. We take the same master system defined by (31) and the slave system (32) is modified with FOPID controllers as given below.

$$\begin{aligned} D^{q_x} x_s &= a z_s + x_s y_s + u_x \\ D^{q_y} y_s &= 1 - x_s^2 - z_s^2 - w_s^2 + u_y \\ D^{q_z} z_s &= -b x_s + y_s z_s + u_z \\ D^{q_w} w_s &= c z_s - w_s - z_s W(x_s) + u_w. \end{aligned} \quad (53)$$

The initial conditions and the parameters are taken as

$$\begin{aligned} x_m(0) &= 1, \\ y_m(0) &= -1, \\ z_m(0) &= -1, \\ w_m(0) &= 1, \\ x_s(0) &= -2, \\ y_s(0) &= 3, \\ z_s(0) &= -2, \\ w_s(0) &= 4, \\ a &= 10, \\ b &= 9, \\ c &= 8.7, \\ a_1 &= 4, \\ b_1 &= 0.01. \end{aligned} \quad (54)$$

The synchronization error dynamics are defined as,

$$\begin{aligned} D^{q_x} e_x &= a e_z + x_s y_s - x_m y_m + u_x \\ D^{q_y} e_x &= x_m^2 - x_s^2 + z_m^2 - z_s^2 + w_m^2 - w_s^2 + u_y \\ D^{q_z} e_x &= -b e_x + y_s z_s - y_m z_m + u_z \\ D^{q_w} e_x &= c e_z - e_w - z_s W(x_s) + z_m W(x_m) + u_w. \end{aligned} \quad (55)$$

Table 1 shows the FOPID gain values of the controllers achieved using genetic algorithm for known parameter values. We get the best solutions tracked over generations for the complete synchronization of the FOMNE systems.

Figure 10 shows the time history of the synchronization errors using genetically optimized fractional order PID controllers; Figure 11 shows the synchronized states and Figure 12 shows the time history of the fractional order PID controllers.

Case 2 (parameters unknown). In this section we assume that the parameters of the slave system are unknown. We take the same master system defined by (31) and the slave system (32) is modified with FOPID controllers as given below.

$$\begin{aligned} D^{q_x} x_s &= \hat{a} z_s + x_s y_s + u_x \\ D^{q_y} y_s &= 1 - x_s^2 - z_s^2 - w_s^2 + u_y \\ D^{q_z} z_s &= -\hat{b} x_s + y_s z_s + u_z \\ D^{q_w} w_s &= \hat{c} z_s - w_s - z_s W(x_s) + u_w, \end{aligned} \quad (56)$$

where \hat{a} , \hat{b} , and \hat{c} are the unknown system parameters of the slave system. The initial conditions are taken as

$$\begin{aligned} x_m(0) &= 1, \\ y_m(0) &= -1, \\ z_m(0) &= -1, \\ w_m(0) &= 1, \\ x_s(0) &= -2, \\ y_s(0) &= 3, \\ z_s(0) &= -2, \\ w_s(0) &= 4, \\ \hat{a} &= 1, \\ \hat{b} &= 4, \\ \hat{c} &= 13. \end{aligned} \quad (57)$$

The synchronization error dynamics are defined as

$$\begin{aligned} D^{q_x} e_x &= \hat{a} z_s + x_s y_s - a z_m - x_m y_m + u_x \\ D^{q_y} e_y &= -x_s^2 - z_s^2 - w_s^2 + x_m^2 + z_m^2 + w_m^2 + u_y \\ D^{q_z} e_z &= -\hat{b} x_s + y_s z_s + b x_m - y_m z_m + u_z \\ D^{q_w} e_w &= \hat{c} z_s - w_s - z_s w(x_s) - c z_m + w_m \\ &\quad + z_m w(x_m) + u_w \end{aligned} \quad (58)$$

and the parameter update laws are defined as

$$\begin{aligned} D^q \hat{a} &= -e_x z_m \\ D^q \hat{b} &= -e_z x_m \\ D^q \hat{c} &= -e_w z_m. \end{aligned} \quad (59)$$

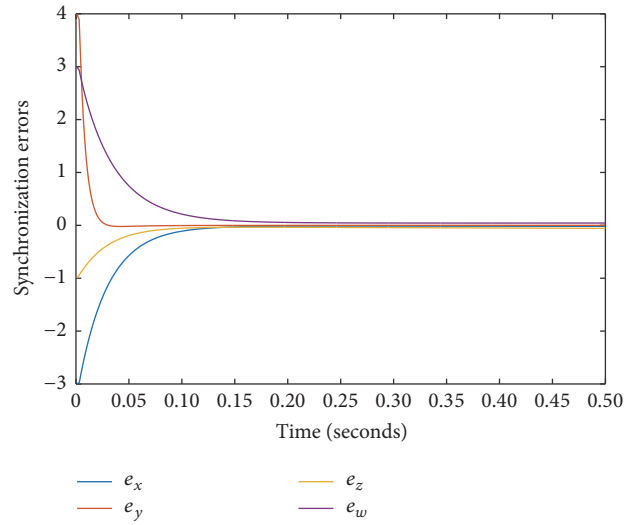
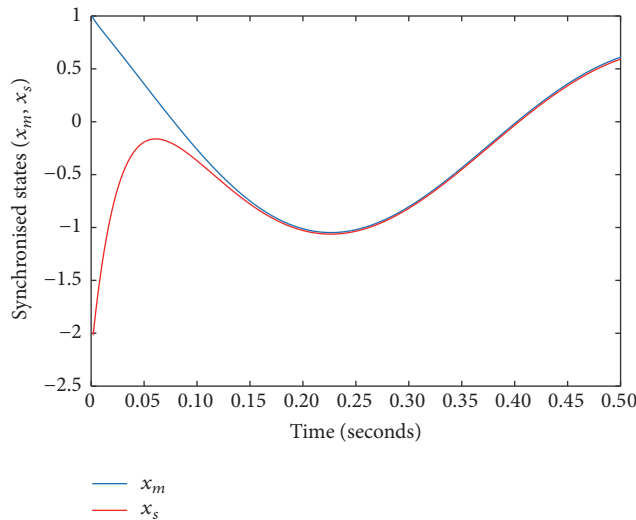
Table 2 shows the FOPID gain values achieved using the genetic algorithm optimization technique for unknown parameters.

TABLE 1: FOPID controller gain values optimized with GA.

FOPID controller	K_p	K_I	K_D
u_x	-0.0271	-0.0095	0.0015
u_y	-0.0469	-0.0809	-0.0029
u_z	-0.0072	0.0011	0.0146
u_w	-0.0199	-0.0063	0.0124

TABLE 2: FOPID controller gain values optimized with GA.

FOPID controller	K_p	K_I	K_D
u_x	-0.0826	-0.1885	-0.0836
u_y	-0.2150	-0.1586	0.0027
u_z	0.1637	-0.1444	0.0888
u_w	-0.2177	-0.0121	0.0304

FIGURE 10: Time history of synchronization errors (e_x, e_y, e_z, e_w).FIGURE 11: State synchronization (x_m, x_s).

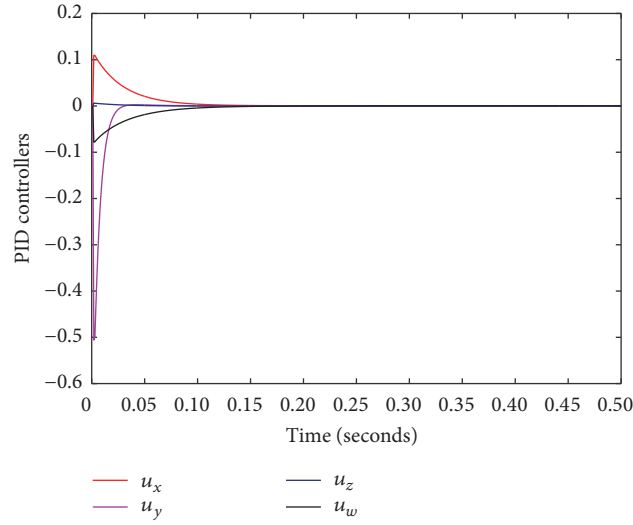


FIGURE 12: Time history of PID controllers u_x , u_y , u_z , and u_w .

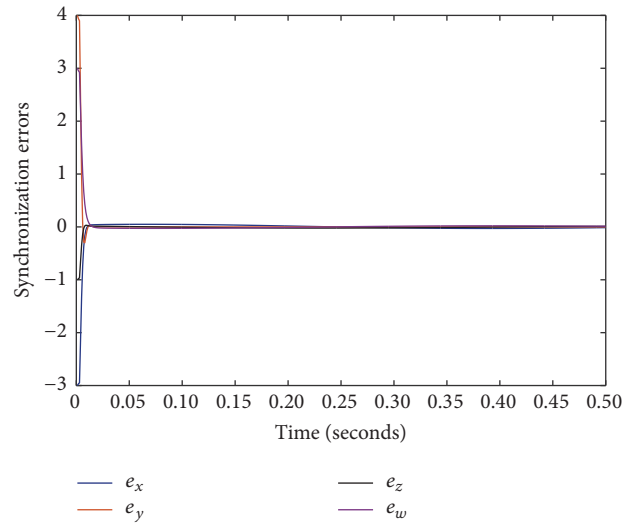


FIGURE 13: Time history of synchronization errors (e_x, e_y, e_z, e_w).

Figure 13 shows the time history of the synchronization errors using genetically optimized fractional order PID controllers, Figure 14 shows the synchronized states, and Figure 15 shows the time history of fractional order PID controllers. Figure 16 shows the time history of the parameter estimates.

As can be seen from Figures 8, 10, and 13, adaptive GA optimized PID control converges much faster ($t = 40$ ms) than adaptive sliding mode control ($t = 190$ ms). Figure 17 shows the comparison of synchronization errors using adaptive sliding mode control (ASMC) and GA optimized PID control (GAPID).

9. FPGA Implementation of the FOMNE System

In this section we discuss the implementation of the novel hyperchaotic system in FPGA using the Xilinx (Vivado)

system generator toolbox in Simulink. Firstly we configure the available built-in blocks of the system generator toolbox. The Add/Sub blocks are configured with zero latency and 32/16-bit fixed point settings. The output of the block is configured to rounded quantization in order to reduce the bit latency. For the multiplier block a latency of 3 is configured and the other settings are the same as in Add/Sub block. Next we will have to design the fractional order integrator which is not a readily available block in the system generator. Hence we implement the integrators using the mathematical relation discussed in (11) and (12) and the value of h is taken as 0.001 and the initial conditions are fed into the forward register. Figure 18 shows the Xilinx schematics of the FOMNE system (13) implemented in Kintex 7 (device = 7k160t; package = fbg484 S) and Figure 19 shows the Xilinx Kintex 7 schematics of the fractional order integrator. Figure 20(a) shows the power consumed by the FOMNE system and Figure 20(b) shows the power consumption for variation in fractional

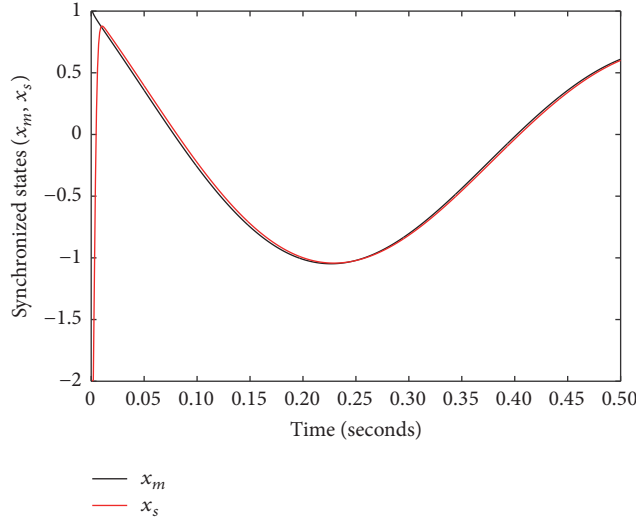


FIGURE 14: State synchronization (x_m, x_s).

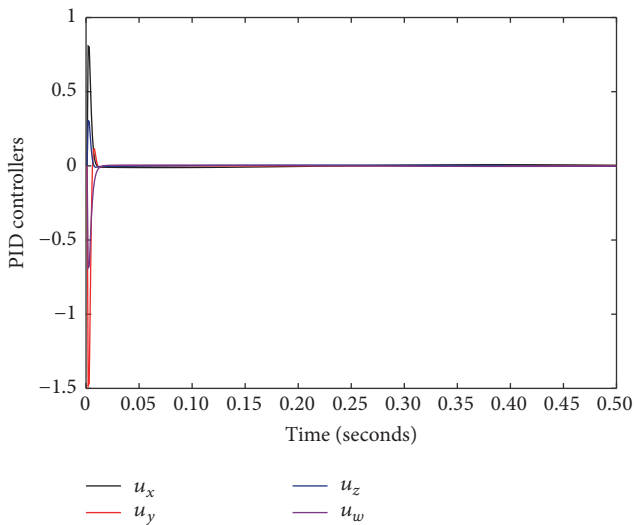


FIGURE 15: Time history of PID controllers u_x, u_y, u_z , and u_w .

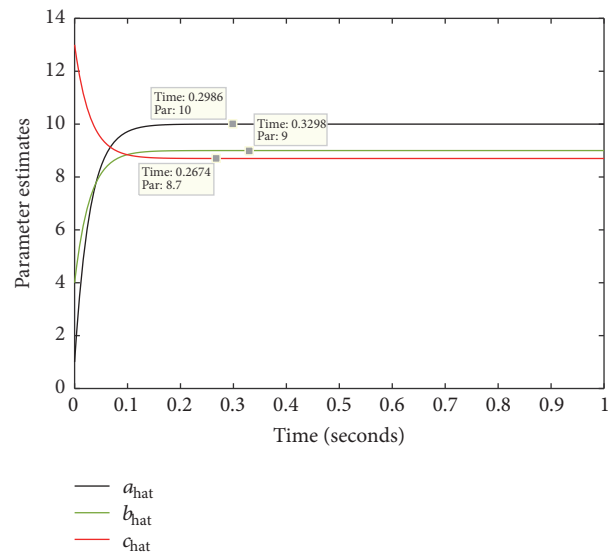


FIGURE 16: Time history of parameter estimates.

orders. As it can be seen from Figure 20(b), the FOMNE system consumes maximum power when its fractional order $q = 0.99$ compared to the integer order 1 thus confirming that the fractional order memristor system exhibits largest Lyapunov exponent compared to the integer order. Figure 21 shows the 2D state portraits of the FOMNE system using Xilinx system generator.

10. Conclusion

In this paper we have announced a novel 4D no equilibrium memristor chaotic system. The dynamic properties of the proposed system are investigated to prove the chaotic behavior of the system. The fractional order model of the 4D no equilibrium memristor chaotic system is derived

from its integer model. Fractional order bifurcation property of the FOMNE system is investigated and it is seen that largest Lyapunov exponent of the system exists when the fractional order is close to 1. The identical FOMNE systems are synchronized using adaptive sliding mode controllers and genetically optimized PID controllers. Numerical simulations are done to validate the theoretical results. Finally the proposed FOMNE system is implemented in FPGA to show that the system is hardware realizable.

Competing Interests

The authors declare that there is no conflict of interests regarding the publication of this paper.

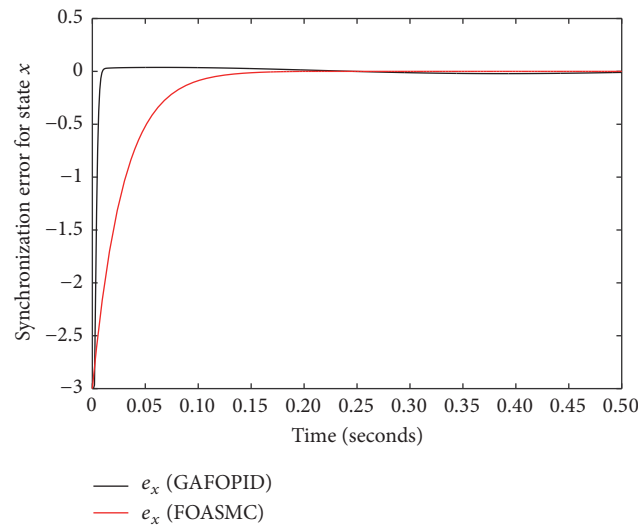


FIGURE 17: Comparison of synchronization errors (ASMC and GAFOPID).

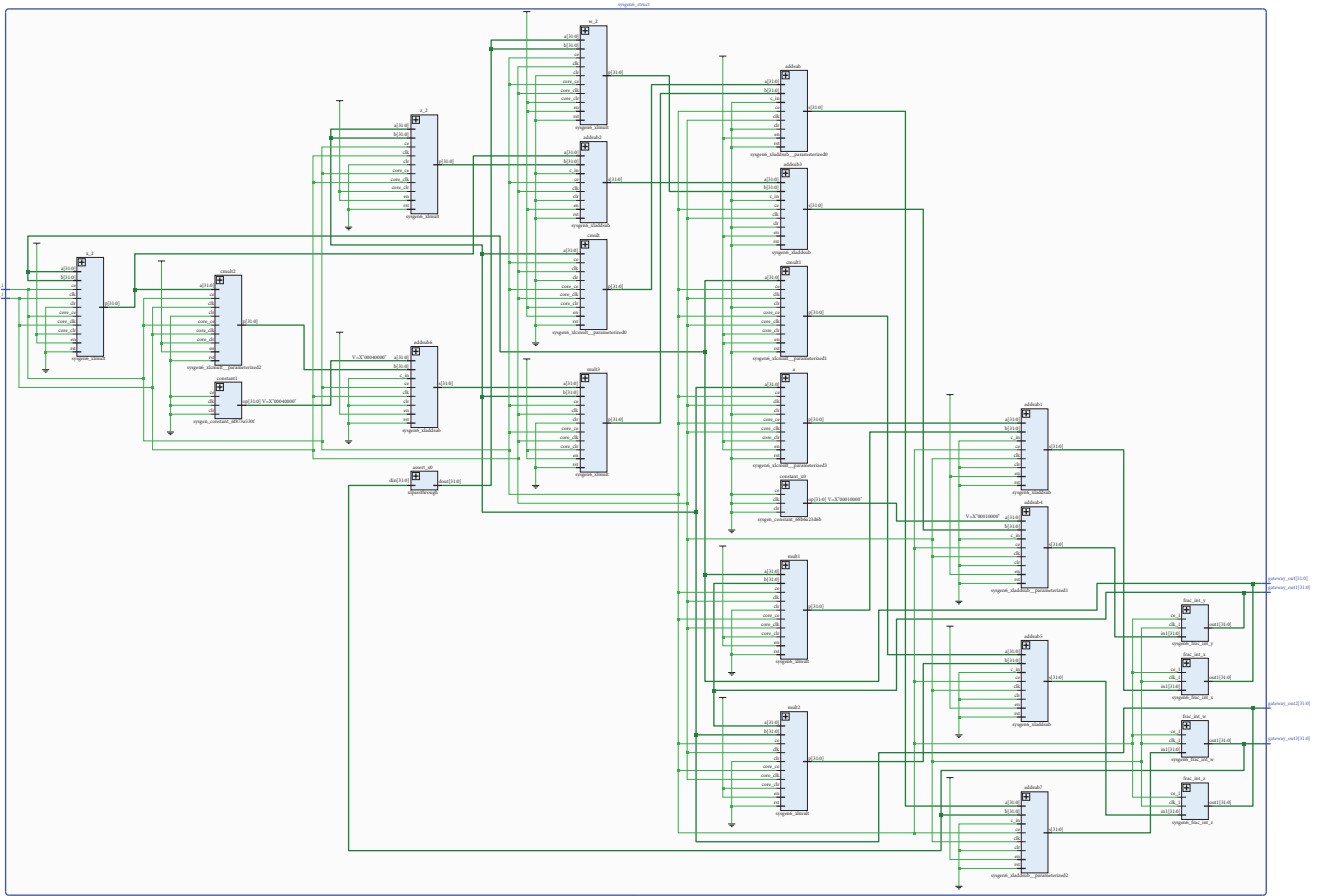


FIGURE 18: Xilinx schematics of the FOMNE system implemented in Kintex 7 (device = 7k160t; package = fbg484 S).

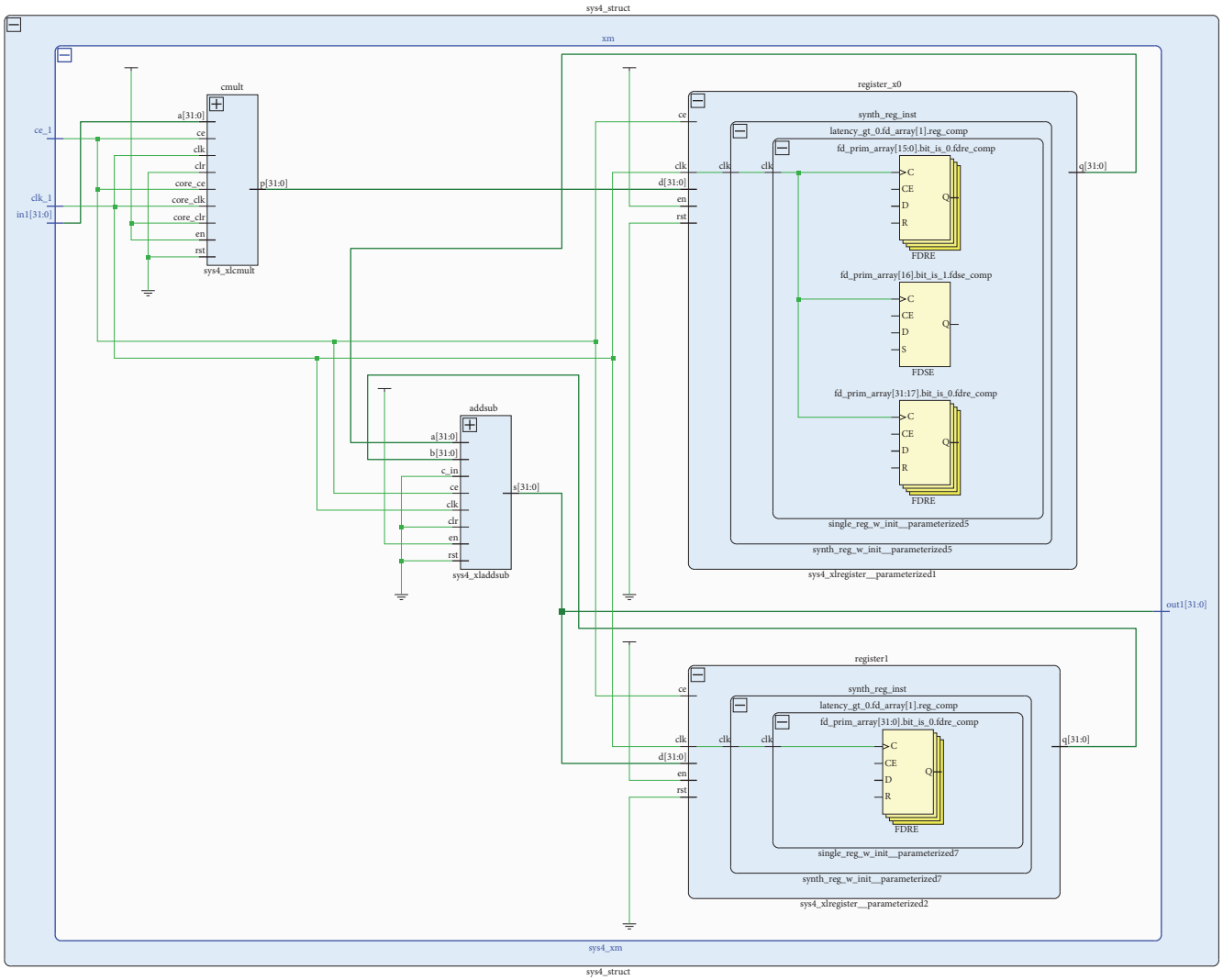


FIGURE 19: Xilinx schematics of the Fractional order integrator implemented in Kintex 7 (device = 7k160t; package = fbg484 S).

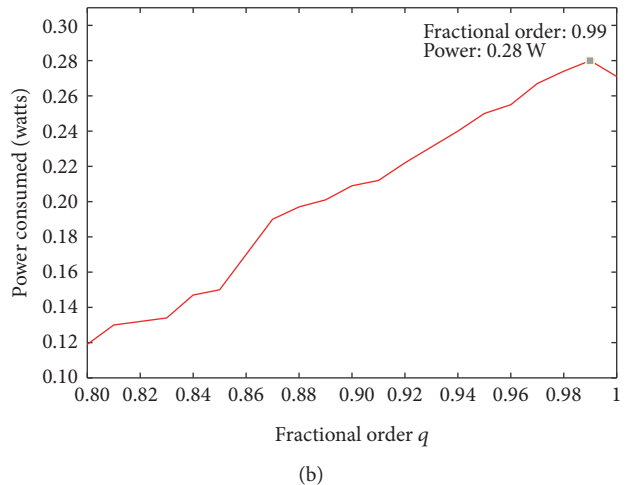
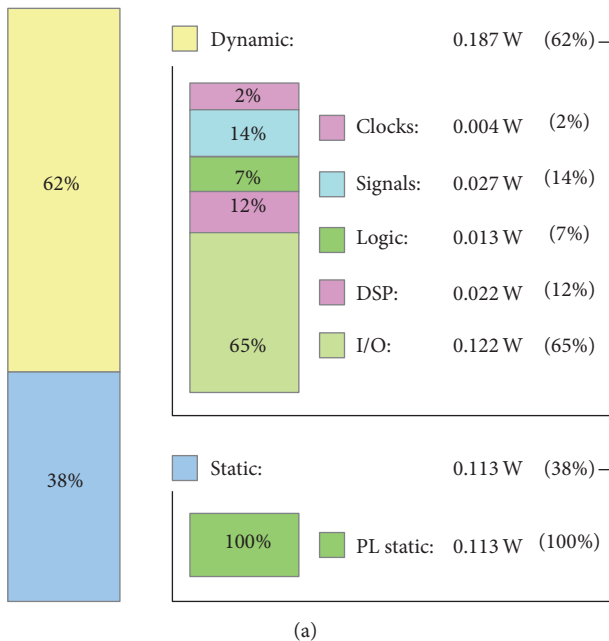


FIGURE 20: (a) Power utilized and (b) power utilization versus fractional order of FOMNE system.

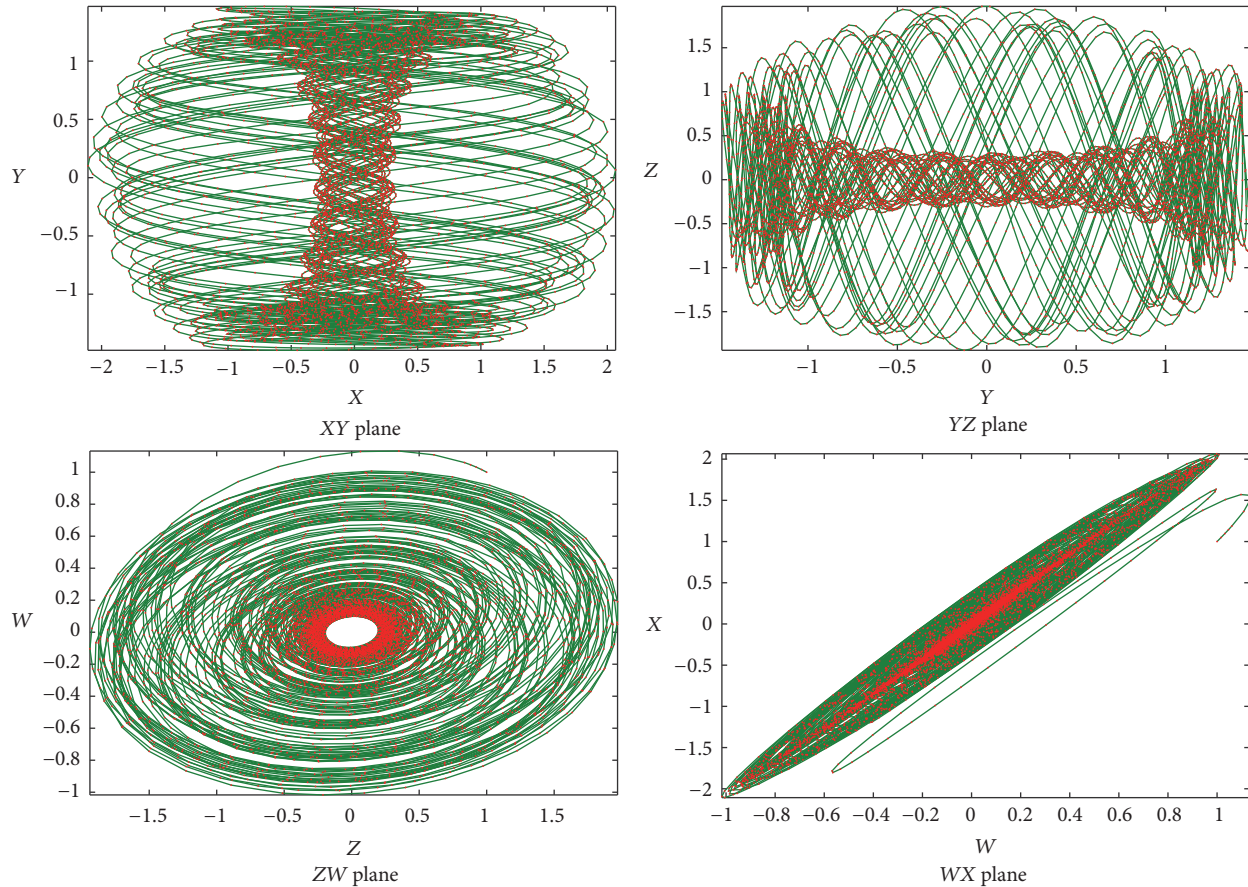


FIGURE 21: 2D state portraits of the FOMENS system implemented using Xilinx system generator (XYZ plane; YZW plane).

References

- [1] T. Geisel, "Chaos, randomness and dimension," *Nature*, vol. 298, no. 5872, pp. 322–323, 1982.
- [2] O. E. RöSSLer, "An equation for hyperchaos," *Physics Letters A*, vol. 71, no. 2-3, pp. 155–157, 1979.
- [3] E. N. Lorenz, "Deterministic nonperiodic flow," *Journal of the Atmospheric Sciences*, vol. 20, pp. 130–141, 1963.
- [4] G. Chen and T. Ueta, "Yet another chaotic attractor," *International Journal of Bifurcation and Chaos*, vol. 9, no. 7, pp. 1465–1466, 1999.
- [5] C. Liu, T. Liu, L. Liu, and K. Liu, "A new chaotic attractor," *Chaos, Solitons and Fractals*, vol. 22, no. 5, pp. 1031–1038, 2004.
- [6] V. Sundarapandian and I. Pehlivan, "Analysis, control, synchronization, and circuit design of a novel chaotic system," *Mathematical and Computer Modelling*, vol. 55, no. 7-8, pp. 1904–1915, 2012.
- [7] V. Sundarapandian, "Analysis and anti-Synchronization of a novel chaotic system via active and adaptive controllers," *Journal of Engineering Science and Technology Review*, vol. 6, no. 4, pp. 45–52, 2013.
- [8] V.-T. Pham, C. Volos, S. Jafari, Z. Wei, and X. Wang, "Constructing a novel no-equilibrium chaotic system," *International Journal of Bifurcation and Chaos*, vol. 24, no. 5, Article ID 1450073, 2014.
- [9] S. Vaidyanathan and C. Volos, "Analysis and adaptive control of a novel 3-D conservative no-equilibrium chaotic system," *Archives of Control Sciences*, vol. 25, no. 3, pp. 333–353, 2015.
- [10] L. O. Chua, "Memristor—the missing circuit element," *IEEE Transactions on Circuit Theory*, vol. 18, pp. 507–519, 1971.
- [11] L. O. Chua and S. M. Kang, "Memristive devices and systems," *Proceedings of the IEEE*, vol. 64, no. 2, pp. 209–223, 1976.
- [12] Z. Birolek, D. Birolek, and V. Biolková, "SPICE model of memristor with nonlinear dopant drift," *Radioengineering*, vol. 18, no. 2, pp. 210–214, 2009.
- [13] R. E. Pino, J. W. Bohl, N. McDonald et al., "Compact method for modeling and simulation of memristor devices: ion conductor chalcogenide-based memristor devices," in *Proceedings of the IEEE/ACM International Symposium on Nanoscale Architectures (NANOARCH '10)*, pp. 1–4, IEEE, Anaheim, Calif, USA, June 2010.
- [14] Á. Rak and G. Csereny, "Macromodeling of the memristor in SPICE," *IEEE Transactions on Computer-Aided Design of Integrated Circuits and Systems*, vol. 29, no. 4, pp. 632–636, 2010.
- [15] A. Ishaq Ahamed and M. Lakshmanan, "Nonsmooth bifurcations, transient hyperchaos and hyperchaotic beats in a memristive Murali–Lakshmanan–Chua circuit," *International Journal of Bifurcation and Chaos*, vol. 23, no. 6, Article ID 1350098, 2013.
- [16] S. Wang, X. Wang, Y. Zhou, and B. Han, "A memristor-based hyperchaotic complex Lü system and its adaptive complex

- generalized synchronization,” *Entropy*, vol. 18, no. 2, article 58, 2016.
- [17] B. A. Idowu, U. E. Vincent, and A. N. Njah, “Synchronization of chaos in non-identical parametrically excited systems,” *Chaos, Solitons and Fractals*, vol. 39, no. 5, pp. 2322–2331, 2009.
- [18] S. Vaidyanathan and K. Rajagopal, “Hybrid synchronization of hyperchaotic Wang-Chen and hyperchaotic Lorenz systems by active non-linear control,” *International Journal of Systems Signal Control and Engineering Application*, vol. 4, no. 3, pp. 55–61, 2011.
- [19] V. Sundarapandian and R. Karthikeyan, “Anti-synchronization of Lü and Pan chaotic systems by adaptive nonlinear control,” *European Journal of Scientific Research*, vol. 64, no. 1, pp. 94–106, 2011.
- [20] V. Sundarapandian and R. Karthikeyan, “Adaptive anti-synchronization of Uncertain Tigan and Li Systems,” *Journal of Engineering and Applied Sciences*, vol. 7, no. 1, pp. 45–52, 2012.
- [21] S. S. Majidabad and H. T. Shandiz, “Discrete-time terminal sliding mode control of chaotic Lorenz system,” *Journal of Control and Systems Engineering*, vol. 1, no. 1, pp. 1–8, 2013.
- [22] A. N. Njah, “Tracking control and synchronization of the new hyperchaotic Liu system via backstepping techniques,” *Nonlinear Dynamics*, vol. 61, no. 1-2, pp. 1–9, 2010.
- [23] O. S. Onma, O. I. Olusola, and A. N. Njah, “Control and synchronization of chaotic and hyperchaotic Lorenz systems via extended backstepping techniques,” *Journal of Nonlinear Dynamics*, vol. 2014, Article ID 861727, 15 pages, 2014.
- [24] B. Wang, Y. Li, and D. L. Zhu, “Simplified sliding mode of a novel class of four-dimensional fractional-order chaos,” *International Journal of Control and Automation*, vol. 8, no. 8, pp. 425–438, 2015.
- [25] C. Yin, S. Dadras, S.-M. Zhong, and Y. Chen, “Control of a novel class of fractional-order chaotic systems via adaptive sliding mode control approach,” *Applied Mathematical Modelling*, vol. 37, no. 4, pp. 2469–2483, 2013.
- [26] H. Liu and J. Yang, “Sliding-mode synchronization control for uncertain fractional-order chaotic systems with time delay,” *Entropy*, vol. 17, no. 6, pp. 4202–4214, 2015.
- [27] S. Wang, Y. Yu, and M. Diao, “Hybrid projective synchronization of chaotic fractional order systems with different dimensions,” *Physica A: Statistical Mechanics and its Applications*, vol. 389, no. 21, pp. 4981–4988, 2010.
- [28] R. Herrmann, *Fractional calculus*, World Scientific Publishing Co., Second edition, 2014.
- [29] D. Baleanu, K. Diethelm, E. Scalas, and J. J. Trujillo, *Fractional Calculus: Models and Numerical Methods*, World Scientific, Singapore, 2014.
- [30] Y. Zhou, *Basic Theory of Fractional Differential Equations*, World Scientific, Singapore, 2014.
- [31] K. Diethelm, *The Analysis of Fractional Differential Equations*, Springer, Berlin, Germany, 2010.
- [32] X. Wang and G. Chen, “A chaotic system with only one stable equilibrium,” *Communications in Nonlinear Science and Numerical Simulation*, vol. 17, no. 3, pp. 1264–1272, 2012.
- [33] X. Wang and G. Chen, “Constructing a chaotic system with any number of equilibria,” *Nonlinear Dynamics*, vol. 71, no. 3, pp. 429–436, 2013.
- [34] Z. Wang, S. Cang, E. O. Ochola, and Y. Sun, “A hyperchaotic system without equilibrium,” *Nonlinear Dynamics*, vol. 69, no. 1-2, pp. 531–537, 2012.
- [35] G. A. Leonov and N. V. Kuznetsov, “Hidden attractors in dynamical systems: from hidden oscillations in Hilbert-Kolmogorov, Aizerman, and Kalman problems to hidden chaotic attractor in Chua circuits,” *International Journal of Bifurcation and Chaos*, vol. 23, no. 1, Article ID 1330002, 69 pages, 2013.
- [36] Z. Wang, X. Huang, and H. Shen, “Control of an uncertain fractional order economic system via adaptive sliding mode,” *Neurocomputing*, vol. 83, pp. 83–88, 2012.
- [37] K. Rajagopal, S. Vaidyanathan, A. Karthikeyan, and P. Duraisamy, “Dynamic analysis and chaos suppression in a fractional order brushless DC motor,” *Electrical Engineering*, 2016.
- [38] T.-Z. Li, Y. Wang, and M.-K. Luo, “Control of fractional chaotic and hyperchaotic systems based on a fractional order controller,” *Chinese Physics B*, vol. 23, no. 8, Article ID 080501, 2014.
- [39] R. H. Li and W. S. Chen, “Fractional order systems without equilibria,” *Chinese Physics B*, vol. 22, Article ID 040503, 2013.
- [40] P. Ivo, *Fractional Order Chaotic Systems*, Matlab Central File Exchange, Math Works, Natick, Mass, USA, 2010, <https://www.mathworks.com/matlabcentral/fileexchange/27336>.
- [41] G. Leonov, N. Kuznetsov, O. Kuznetsova, S. Seldedzhi, and V. Vagitsev, “Hidden oscillations in dynamical systems,” *Transactions on Systems and Control*, vol. 6, pp. 54–67, 2011.
- [42] S. Jafari, J. C. Sprott, and S. M. R. Hashemi Golpayegani, “Elementary quadratic chaotic flows with no equilibria,” *Physics Letters A*, vol. 377, no. 9, pp. 699–702, 2013.
- [43] I. Petráš, “Fractional—order feedback control of a DC motor,” *Journal of Electrical Engineering*, vol. 60, no. 3, pp. 117–128, 2009.
- [44] M. Zamani, M. Karimi-Ghartemani, N. Sadati, and M. Parniani, “Design of a fractional order PID controller for an AVR using particle swarm optimization,” *Control Engineering Practice*, vol. 17, no. 12, pp. 1380–1387, 2009.
- [45] A. Djari, T. Bouden, and A. Boukroune, “Design of a fractional order PID controller, (FOPID) for a class of fractional order MIMO system,” *Journal of Automation and Systems Engineering*, vol. 8, no. 1, pp. 25–39, 2014.
- [46] S. Vaidyanathan and C. Volos, “Analysis and adaptive control of a novel 3-D conservative no-equilibrium chaotic system,” *Archives of Control Sciences*, vol. 25, no. 3, pp. 333–353, 2015.
- [47] Q. Li, H. Zeng, and J. Li, “Hyperchaos in a 4D memristive circuit with infinitely many stable equilibria,” *Nonlinear Dynamics*, vol. 79, no. 4, pp. 2295–2308, 2015.
- [48] Q.-H. Hong, Y.-C. Zeng, and Z.-J. Li, “Design and simulation of chaotic circuit for flux-controlled memristor and charge-controlled memristor,” *Wuli Xuebao/Acta Physica Sinica*, vol. 62, no. 23, Article ID 230502, 2013.
- [49] B. Bao, P. Jiang, H. Wu, and F. Hu, “Complex transient dynamics in periodically forced memristive Chua’s circuit,” *Nonlinear Dynamics*, vol. 79, no. 4, pp. 2333–2343, 2015.
- [50] C. Pezeshki, S. Elgar, and R. C. Krishna, “Bispectral analysis of possessing chaotic motion,” *Journal of Sound and Vibration*, vol. 137, no. 3, pp. 357–368, 1990.
- [51] M. E. Fouda and A. G. Radwan, “On the fractional-order memristor model,” *Journal of Fractional Calculus and Applications*, vol. 4, no. 1, pp. 1–7, 2013.
- [52] Y.-F. Pu and X. Yuan, “Fracmemristor: fractional-order memristor,” *IEEE Access*, vol. 4, pp. 1872–1888, 2016.
- [53] H. K. Khalil, *Nonlinear Systems*, Prentice Hall, New York, NY, USA, 2002.

- [54] L. Guessas and K. Benmahammed, "Adaptive backstepping and pid optimized by genetic algorithm in control of Chaotic," *International Journal of Innovative Computing, Information and Control*, vol. 7, no. 9, pp. 5299–5312, 2011.
- [55] D. E. Goldberg, *Genetic Algorithms in Search, Optimization & Machine Learning*. Addison-Wesley, Boston, Mass, USA, 1989.

Research Article

Dynamics, Circuit Design, and Synchronization of a New Chaotic System with Closed Curve Equilibrium

Xiong Wang,¹ Viet-Thanh Pham,² and Christos Volos³

¹*Institute for Advanced Study, Shenzhen University, Shenzhen, Guangdong 518060, China*

²*School of Electronics and Telecommunications, Hanoi University of Science and Technology, 01 Dai Co Viet, Hanoi, Vietnam*

³*Department of Physics, Aristotle University of Thessaloniki, 54124 Thessaloniki, Greece*

Correspondence should be addressed to Viet-Thanh Pham; pvt3010@gmail.com

Received 9 October 2016; Accepted 18 December 2016; Published 16 February 2017

Academic Editor: Ahmed G. Radwan

Copyright © 2017 Xiong Wang et al. This is an open access article distributed under the Creative Commons Attribution License, which permits unrestricted use, distribution, and reproduction in any medium, provided the original work is properly cited.

After the report of chaotic flows with line equilibrium, there has been much attention to systems with uncountable equilibria in the past five years. This work proposes a new system with an infinite number of equilibrium points located on a closed curve. It is worth noting that the new system generates chaotic behavior as well as hidden attractors. Dynamics of the system with closed curve equilibrium have been investigated by using phase portraits, bifurcation diagram, maximal Lyapunov exponents, and Kaplan–York dimension. In addition, we introduce an electronic implementation of the theoretical system to verify its feasibility. Antisynchronization ability of the new system with infinite equilibria is studied by applying an adaptive control. This study suggests that there exist other chaotic systems with uncountable equilibria in need of further investigation.

1. Introduction

Although chaos has been an object of research since the 1960s, investigating chaotic systems is still a continuing concern within nonlinear dynamics field [1–7]. A great amount of different chaotic systems has been reported in the literature such as modified Lorenz chaotic system [8], jerk-based chaotic oscillators [9], three-dimensional (3D) system [10], 3D autonomous chaotic system with a single cubic nonlinearity [11], chaotic system with butterfly attractor [12], systems with multiscroll chaotic attractors [13–15], or fractional-order chaotic systems [16, 17]. Moreover, the past decade has seen the rapid development of chaos-based applications in many areas from hardware pseudorandom number generators [18], autonomous mobile robots [19], MOS oscillators [20], encryption [21], chaotic masking communication [22], to information processing [23].

Recently, there has been renewed interest in chaotic systems with uncountable equilibria [24] (see the illustration in Figure 1). One of the most important discoveries is the finding of chaotic flows with line equilibrium [24–26]. The presence of parallel lines of equilibrium points [25] and perpendicular lines of equilibria [26] has also been studied.

Recent trends in systems with uncountable equilibria have led to systems with open curve equilibrium [27, 28] and closed curve equilibrium [29]. The issue of finding different shapes of closed curve equilibrium especially has received considerable critical attention [29–31]. Chaotic system with circular equilibrium has been obtained by using a search routine [29]. Gotthans and Petržela have constructed a chaotic flow with square equilibrium [29]. Chaotic system with uncountable equilibria located on a rounded square has been reported in [32]. From the computation point of view, it is now well established that systems with infinite equilibrium can be classified as special systems with “hidden attractor” [33–36], which have not treated much detail [37–39]. Discovering new chaotic systems with closed curve equilibrium is still an attractive research direction.

The main aim of this study is to investigate a novel chaotic system with closed-curve equilibrium. In Section 2, the model and the dynamics of the system are presented. Circuitual implementation of the new system is reported in Section 3 while the ability of antisynchronization of such systems is discussed in Section 4. Finally, Section 5 gives conclusion remarks of our study.

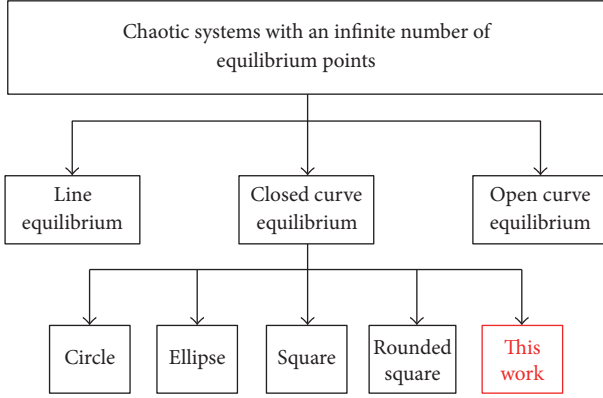


FIGURE 1: Systems with uncountable equilibria in which there has been an increasing interest in discovering different shapes of closed curve equilibrium.

2. Description and Dynamics of the System with Closed Curve Equilibrium

Recently, Gotthans et al. [30] have introduced chaotic systems with circle equilibrium and square equilibrium. Gotthans et al. system with circle equilibrium is given by

$$\begin{aligned}\dot{x} &= z, \\ \dot{y} &= -z(ay + by^2 + xz), \\ \dot{z} &= x^2 + y^2 - 1,\end{aligned}\quad (1)$$

while the system with square equilibrium is described as

$$\begin{aligned}\dot{x} &= z, \\ \dot{y} &= -z(ay + b|y|) - x|z|, \\ \dot{z} &= |x| + |y| - 1,\end{aligned}\quad (2)$$

in which a and b are constants. This investigation is significantly important because authors indicated the existence of chaotic systems with different shapes of equilibrium points [30]. Moreover, by generalizing the systems of Gotthans et al. we may get other new systems with an infinite number of equilibrium.

Based on the systems of Gotthans et al., we concentrate on a general model given by

$$\begin{aligned}\dot{x} &= z, \\ \dot{y} &= -zf_1(x, y, z), \\ \dot{z} &= f_2(x, y),\end{aligned}\quad (3)$$

in which three state variables are x , y , and z . The functions $f_1(x, y, z)$, $f_2(x, y)$ are two arbitrary nonlinear functions. By solving $\dot{x} = 0$, $\dot{y} = 0$, and $\dot{z} = 0$, it is straightforward to obtain

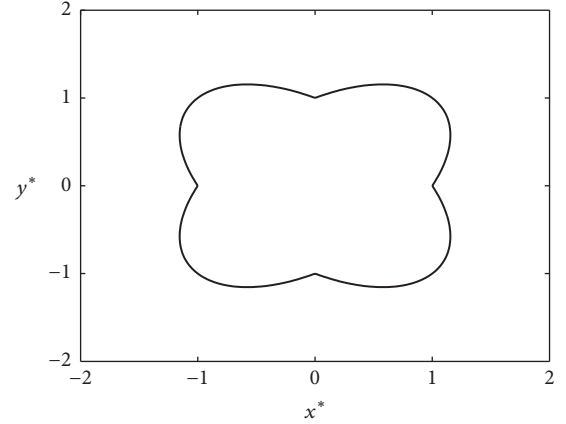


FIGURE 2: The special shape of equilibrium points in the new system (9).

the equilibrium point of general model (3). It means that we calculate

$$z = 0, \quad (4)$$

$$-zf_1(x, y, z) = 0, \quad (5)$$

$$f_2(x, y) = 0. \quad (6)$$

As can be seen from (4), we have $z = 0$. By substituting $z = 0$ into (5) and (6), it is easy to confirm that the equilibrium points of general model (3) are laid on the curve described by (6) in the plane $z = 0$. Therefore numerous systems with closed curve equilibrium can be constructed by selecting appropriate functions $f_1(x, y, z)$ and $f_2(x, y)$.

In this work, we select two nonlinear functions $f_1(x, y, z)$ and $f_2(x, y)$ described by the following forms:

$$f_1(x, y, z) = ay + by^2 + xz, \quad (7)$$

$$f_2(x, y) = x^2 - |xy| + y^2 - 1, \quad (8)$$

in which a and b are two positive parameters. Substituting (7) and (8) into the general model (3), our new system is derived as

$$\begin{aligned}\dot{x} &= z, \\ \dot{y} &= -z(ay + by^2 + xz), \\ \dot{z} &= x^2 - |xy| + y^2 - 1.\end{aligned}\quad (9)$$

Combining (6) and (8), it is simple to verify that system (9) has an infinite number of equilibrium points $E(x^*, y^*, 0)$. Remarkably, such equilibrium points are described by

$$(x^*)^2 - |x^*y^*| + (y^*)^2 = 1. \quad (10)$$

In other words, the proposed system (9) has cloud-shaped curve equilibrium as illustrated in Figure 2. It is interesting to note that the cloud-shaped curve is different from basic shapes like circle, square, or ellipse [29–31]. Furthermore,

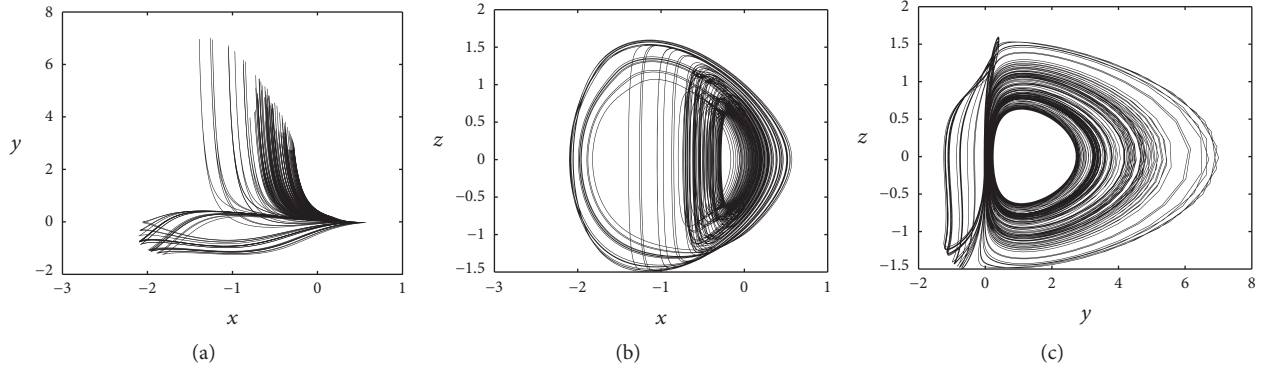


FIGURE 3: Projections of hidden chaotic attractors with cloud-shaped equilibrium in (a) x - y plane, (b) x - z plane, and (c) y - z plane for $a = 4$ and $b = 2.5$.

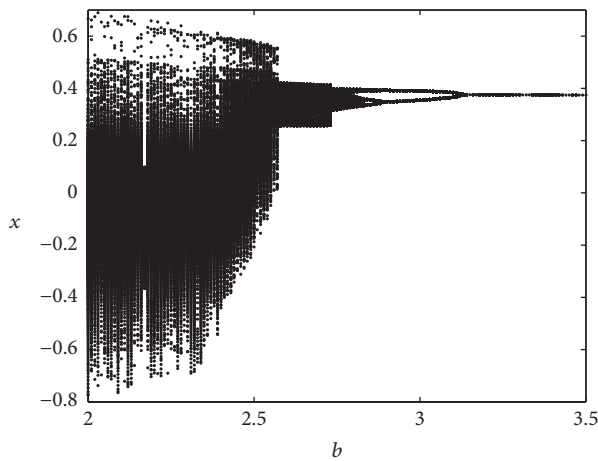


FIGURE 4: Bifurcation diagram of the system with closed curve equilibrium (9) when decreasing the value of the bifurcation parameter b from 3.5 to 2 for $a = 4$.

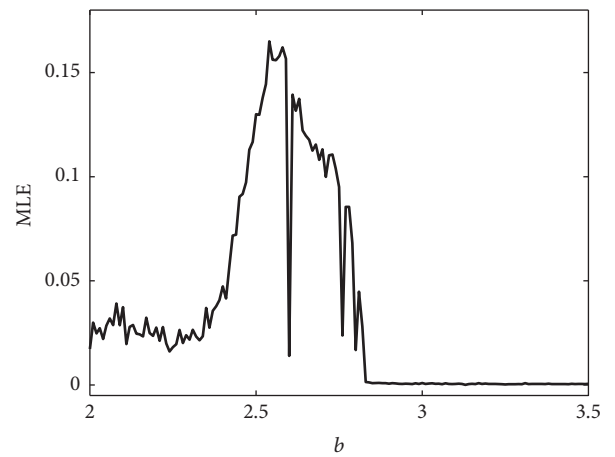


FIGURE 5: Maximal Lyapunov exponents of the system with closed curve equilibrium (9) in the range $2 \leq b \leq 3.5$ for $a = 4$.

system (9) belongs to a rare class of systems with “hidden attractors” [39]. Therefore the investigation of system (9) will enhance our understanding of systems with “hidden attractors” which is an increasingly important area in practical engineering [40–42].

It is worth noting that system (9) with infinite equilibria displays chaotic attractors (see Figure 3) for $a = 4$, $b = 2.5$ and the initial conditions $(x(0), y(0), z(0)) = (0.01, 0.02, 0.01)$. Chaotic behavior of the system is confirmed by the Lyapunov exponents $L_1 = 0.13 > 0$, $L_2 = 0$, and $L_3 = -0.6853$. The well-known Wolf et al.’s method has been used to calculate the Lyapunov exponents [43] and the time of computation is 10,000. In this case, the corresponding Kaplan–York dimension of system (9) is $D_{KY} = 2.1897$. It is noted that unexpected jumps in the values of the local Lyapunov exponents and Lyapunov dimension may occur. Thus the infimum over time interval often gives better estimates. In addition, it is difficult to get the same values of the finite-time local Lyapunov exponents and Lyapunov dimension for different points. Therefore the maximum of the finite-time local Lyapunov dimensions on the grid of point has to be considered [44–46].

By changing the value of the parameter b , the dynamical properties of the system with infinite equilibria (9) are able to be discovered. Figures 4 and 5 display the bifurcation diagram and the diagram of maximal Lyapunov exponents of system (9), respectively. As can be seen from Figures 4 and 5, there is the presence of the classical period doubling route to chaos when decreasing the value of the bifurcation parameter b . The system with cloud-shaped equilibrium generate periodical states in the range of $2.83 \leq b \leq 3.5$. For instance, system (9) can display the period-1 state for $b = 3.25$ (see Figure 6(a)) and the period-2 state for $b = 2.95$ (see Figure 6(b)). For $b < 2.83$, chaotic states are able to be observed in system (9).

3. Circuit Design of the New System with Closed Curve Equilibrium

In order to illustrate the feasibility of the theoretical system with a closed curve of equilibrium points (9), we present its circuitual implementation in this section. For the sake of simplicity, we applied the design approach based on operational amplifiers [47–49]. It is noting that this design approach is not complex and requires common electronic elements only [13,

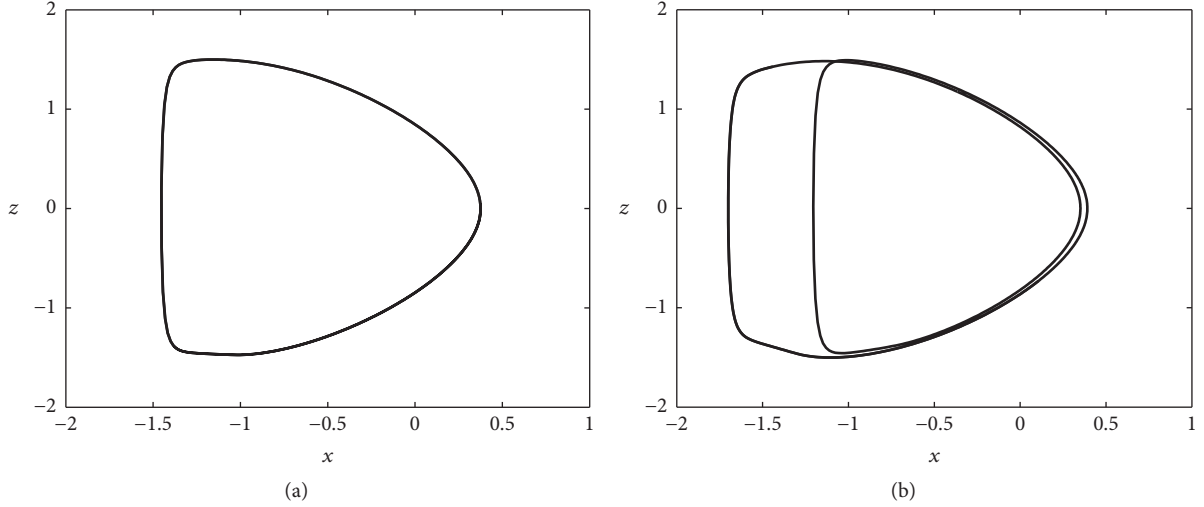


FIGURE 6: Periodical behavior of system (9) represented in the x - z plane: (a) period-1 state ($b = 3.25$) and (b) period-2 state ($b = 2.95$).

50]. Our designed circuit is shown in Figure 7, in which there are three integrators (U_1 - U_3) with corresponding output voltages (v_{C_1} - v_{C_3}). The absolute nonlinearity is realized by the circuitry including two operational amplifiers (U_4, U_5) and two diodes (D_1, D_2).

It is simple to derive the circuitual equation of the circuit in Figure 7:

$$\begin{aligned} \frac{dv_{C_1}}{dt} &= \frac{1}{RC_1} \left(\frac{R}{R_1} v_{C_3} \right), \\ \frac{dv_{C_2}}{dt} &= \frac{1}{RC_2} \left(-\frac{R}{R_2 10V} v_{C_2} v_{C_3} \right. \\ &\quad \left. - \frac{R}{R_3 10^2 V^2} \frac{R_9 + R_{10}}{R_9} v_{C_2}^2 v_{C_3} - \frac{R}{R_4 10^2 V^2} v_{C_1} v_{C_3}^2 \right), \quad (11) \\ \frac{dv_{C_3}}{dt} &= \frac{1}{RC_3} \left(\frac{R}{R_5 10V} v_{C_1}^2 - \frac{R}{R_6 10V} |v_{C_1} v_{C_2}| \right. \\ &\quad \left. + \frac{R}{R_7 10V} v_{C_2}^2 - \frac{R}{R_8} V_1 \right). \end{aligned}$$

The dimensionless system (12) is obtained by normalizing the circuitual equation with $\tau = t/RC$, that is,

$$\begin{aligned} \dot{X} &= \frac{R}{R_1} Z, \\ \dot{Y} &= -\frac{R}{10R_2} YZ - \frac{R}{10^2 R_3} \frac{R_9 + R_{10}}{R_9} Y^2 Z - \frac{R}{10^2 R_4} XZ^2, \quad (12) \\ \dot{Z} &= \frac{R}{10R_5} X^2 - \frac{R}{10R_6} |XY| + \frac{R}{10R_7} Y^2 - \frac{R}{R_8} \frac{V_1}{1V}. \end{aligned}$$

As can be seen in (12), the state variables (X, Y, Z) are equivalent to the voltages of capacitors ($v_{C_1}, v_{C_2}, v_{C_3}$). The dimensionless system (12) corresponds to the proposed system (9) with $a = R/10R_2$ and $b = (R/10^2 R_3)((R_9 + R_{10})/R_9)$.

We select the values of electronic components to realize the theoretical systems (9) for $a = 4$ and $b = 2.5$ as follows:

$R_1 = R_8 = R = 100 \text{ k}\Omega$, $R_2 = 2.5 \text{ k}\Omega$, $R_3 = 4 \text{ k}\Omega$, $R_4 = 1 \text{ k}\Omega$, $R_0 = R_5 = R_6 = R_7 = 10 \text{ k}\Omega$, $R_9 = 11 \text{ k}\Omega$, $R_{10} = 99 \text{ k}\Omega$, $V_1 = 1 \text{ V}_{\text{DC}}$, and $C_1 = C_2 = C_3 = C = 4.7 \text{ nF}$. The PSpice projections of chaotic attractors with infinite equilibria are presented in Figure 8. From Figure 8 we can see that the designed circuit displays chaotic signals. The PSpice results also indicate that the circuit can emulate the theoretical model (9). It is necessary to remark that results of circuit simulation depend on the discretization step. As a result, we should consider the discretization step seriously when simulating electronic circuits, especially in the case of hidden oscillations [51, 52]. Moreover, it is worth noting that realizing the circuit with real analog devices is better than realizing the circuit in PSpice. Therefore, realizing the circuit with real analog devices will be our next work.

4. Antisynchronization of the Identical Systems with Infinite Equilibria

After the investigation of Pecora and Carrol related to synchronization in chaotic systems [53], various synchronization techniques were studied extensively, for example, global chaos synchronization [54], hybrid synchronization [55], ragged synchronizability [56], and so on [57]. Remarkably, the possibility of synchronization of two identical chaotic systems has received considerable attention due to the vital role in practical applications [57, 58]. In this section, we discover the antisynchronization of two new systems with cloud-shaped equilibrium, named the master system and the slave system.

We consider the master system with closed curve equilibrium

$$\begin{aligned} \dot{x}_1 &= z_1, \\ \dot{y}_1 &= -ay_1 z_1 - by_1^2 z_1 - x_1 z_1^2, \\ \dot{z}_1 &= x_1^2 - |x_1 y_1| + y_1^2 - 1, \end{aligned} \quad (13)$$

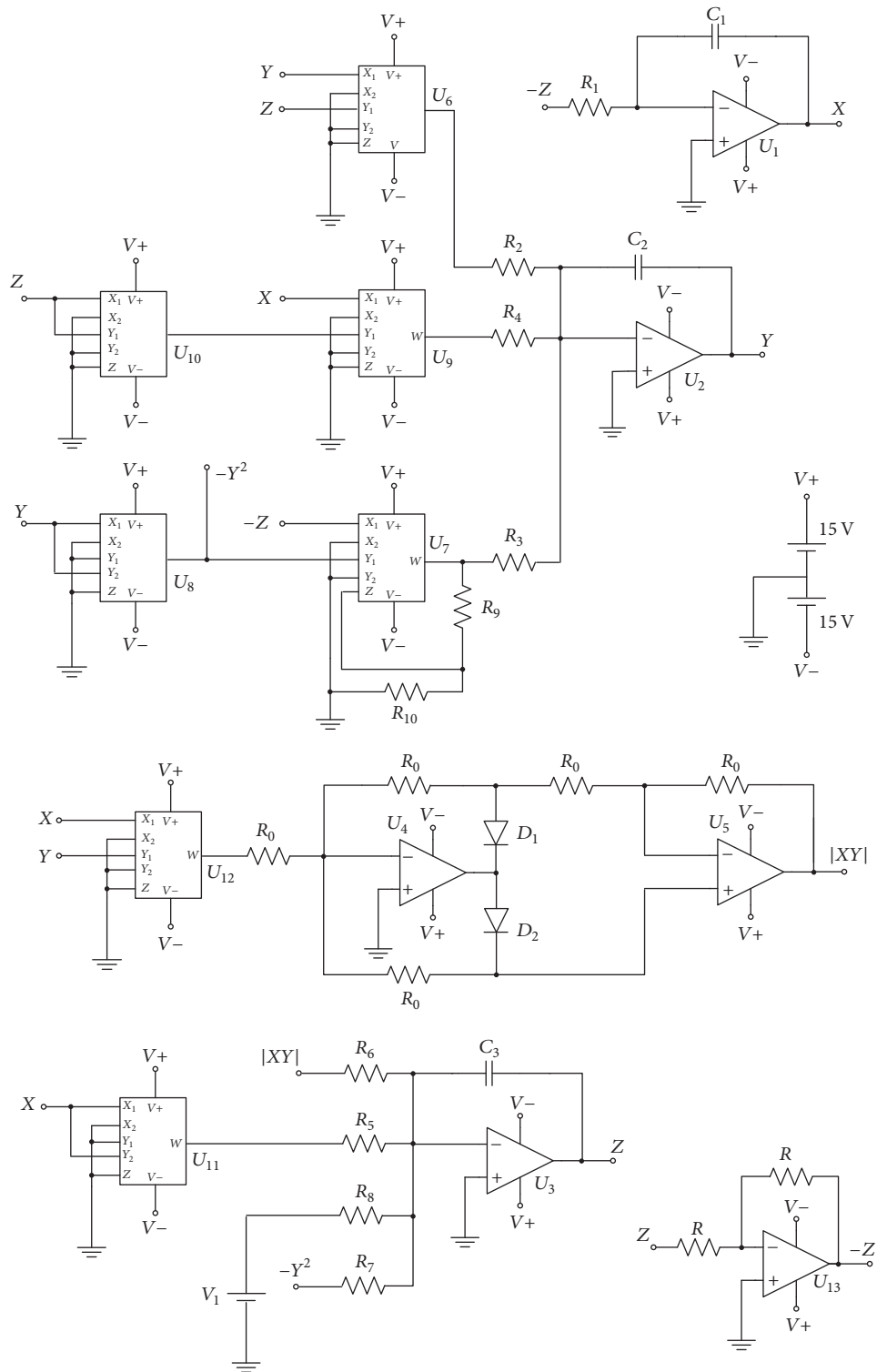


FIGURE 7: The schematic of the circuit which realizes the theoretical chaotic system with closed curve equilibrium (9). Here the values of three capacitors are chosen as $C_1 = C_2 = C_3 = C = 4.7 \text{ nF}$.

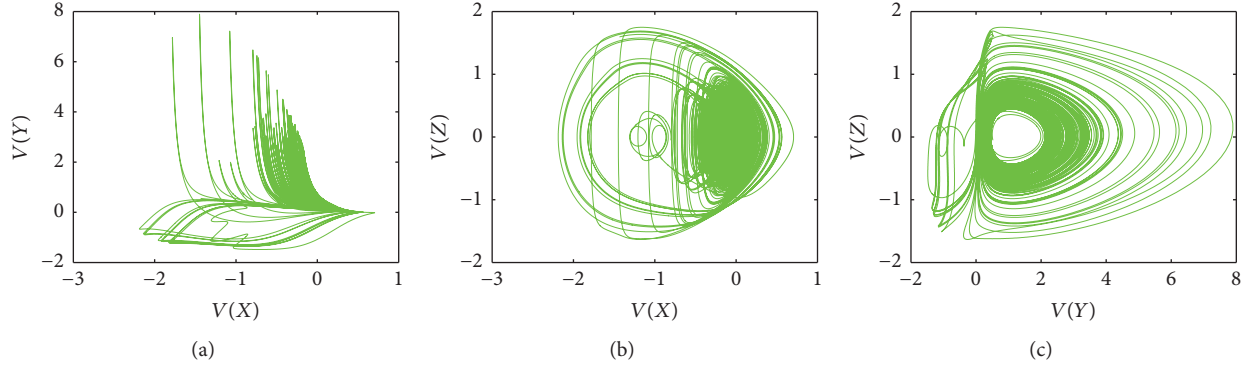


FIGURE 8: PSpice chaotic attractors of the circuit with cloud-shaped equilibrium in (a) X-Y plane, (b) X-Z plane, and (c) Y-Z plane.

in which three state variables are x , y , and z while a and b are two unknown parameters.

The slave system is described by

$$\begin{aligned} \dot{x}_2 &= z_2 + u_x, \\ \dot{y}_2 &= -ay_2z_2 - by_2^2z_2 - x_2z_2^2 + u_y, \\ \dot{z}_2 &= x_2^2 - |x_2y_2| + y_2^2 - 1 + u_z, \end{aligned} \quad (14)$$

in which the adaptive control is $\mathbf{u} = [u_x, u_y, u_z]^T$.

To indicate the difference between the slave system (14) and the master system (13), the state errors are defined as

$$\begin{aligned} e_x &= x_2 - x_1, \\ e_y &= y_2 - y_1, \\ e_z &= z_2 - z_1. \end{aligned} \quad (15)$$

Similarly, we calculate the parameter estimation errors

$$\begin{aligned} e_a &= a - \hat{a}, \\ e_b &= b - \hat{b}, \end{aligned} \quad (16)$$

in which \hat{a} , \hat{b} are the estimations of two unknown parameters a , b , respectively. It is trivial to get the dynamics of the parameter estimation errors:

$$\begin{aligned} \dot{e}_a &= -\dot{\hat{a}}, \\ \dot{e}_b &= -\dot{\hat{b}}. \end{aligned} \quad (17)$$

The aim of our work is to get the antisynchronization between the slave system and the master system; therefore, the adaptive control is proposed by

$$\begin{aligned} u_x &= -e_z - k_x e_x, \\ u_y &= \hat{a}(y_1z_1 + y_2z_2) + \hat{b}(y_1^2z_1 + y_2^2z_2) \\ &\quad + (x_1z_1^2 + x_2z_2^2) - k_y e_y, \\ u_z &= -x_1^2 - x_2^2 + |x_1y_1| + |x_2y_2| - y_1^2 - y_2^2 + 2 - k_z e_z. \end{aligned} \quad (18)$$

In (18), three positive gain constants are k_x , k_y , and k_z while the parameter update law is defined by

$$\begin{aligned} \dot{\hat{a}} &= -e_y(y_1z_1 + y_2z_2), \\ \dot{\hat{b}} &= -e_y(y_1^2z_1 + y_2^2z_2). \end{aligned} \quad (19)$$

The antisynchronization of the slave system (14) and the master system (13) is verified by applying Lyapunov stability theory [59] as follows.

We select the Lyapunov function described by

$$V(e_x, e_y, e_z, e_a, e_b) = \frac{1}{2}(e_x^2 + e_y^2 + e_z^2 + e_a^2 + e_b^2). \quad (20)$$

Therefore, the differentiation of the Lyapunov function is given by

$$\dot{V} = e_x \dot{e}_x + e_y \dot{e}_y + e_z \dot{e}_z + e_a \dot{e}_a + e_b \dot{e}_b. \quad (21)$$

Combining (13)–(16) and (18), we get

$$\begin{aligned} \dot{e}_x &= -k_x e_x, \\ \dot{e}_y &= -e_a(y_1z_1 + y_2z_2) - e_b(y_1^2z_1 + y_2^2z_2) - k_y e_y, \\ \dot{e}_z &= -k_z e_z. \end{aligned} \quad (22)$$

By substituting (17) and (22) into (21), the differentiation of V is rewritten in the form

$$\dot{V} = -k_x e_x^2 - k_y e_y^2 - k_z e_z^2. \quad (23)$$

Obviously, the differentiation of the Lyapunov function \dot{V} is a negative semidefinite function. As a result, it is simple to verify $e_x \rightarrow 0$, $e_y \rightarrow 0$, and $e_z \rightarrow 0$ exponentially as $t \rightarrow \infty$ based on Barbalat's lemma [59]. The complete antisynchronization between the master system and the slave system is proved.

We take an example to illustrate the calculation of the antisynchronization scheme. The parameter values of the master system and slave system are fixed as

$$\begin{aligned} a &= 4, \\ b &= 2.5. \end{aligned} \quad (24)$$

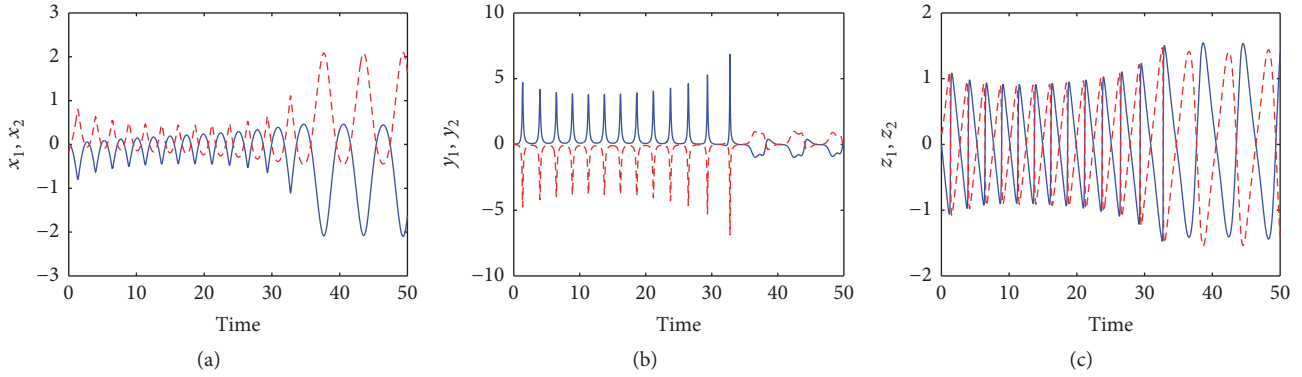


FIGURE 9: Antisynchronization of the slave system and the master system (a) x_1, x_2 state variables, (b) y_1, y_2 state variables, and (c) z_1, z_2 state variables (state variables of the slave system (red dashed lines), state variables of the master system (blue solid lines)).

We assume that the initial states of the master system (13) are

$$\begin{aligned} x_1(0) &= 0.01, \\ y_1(0) &= 0.02, \\ z_1(0) &= 0.01, \end{aligned} \quad (25)$$

while the initial states of the slave system (14) are taken as

$$\begin{aligned} x_2(0) &= -0.19, \\ y_2(0) &= 0.07, \\ z_2(0) &= 0.15. \end{aligned} \quad (26)$$

The positive gain constants are chosen as $k_x = 5$, $k_y = 5$, and $k_z = 5$. For numerical simulations, we take the initial condition of the parameter estimate as

$$\begin{aligned} \hat{a}(0) &= 4.1, \\ \hat{b}(0) &= 2.6. \end{aligned} \quad (27)$$

It is apparent from Figure 9 that there is antisynchronization of the respective states of the systems with cloud-shaped equilibrium (13) and (14). The time-history of the synchronization errors e_x, e_y , and e_z is shown in Figure 10. It is straightforward to verify that Figure 10 depicts the antisynchronization of the master and slave systems.

5. Conclusions

The main goal of the current study is to propose a novel unusual system with infinite number of equilibrium points which lay on a closed curve. Dynamics of the new system have been investigated via different tools such as phase portrait, bifurcation diagram, Kaplan–York dimension, and maximal Lyapunov exponents. The feasibility of the theoretical model is clearly verified by the circuit implementation. In addition, the research also shows that antisynchronization of systems with closed curve equilibrium is obtained by introducing an adaptive control. The findings in this study provide a new understanding of system with infinite equilibria. In terms

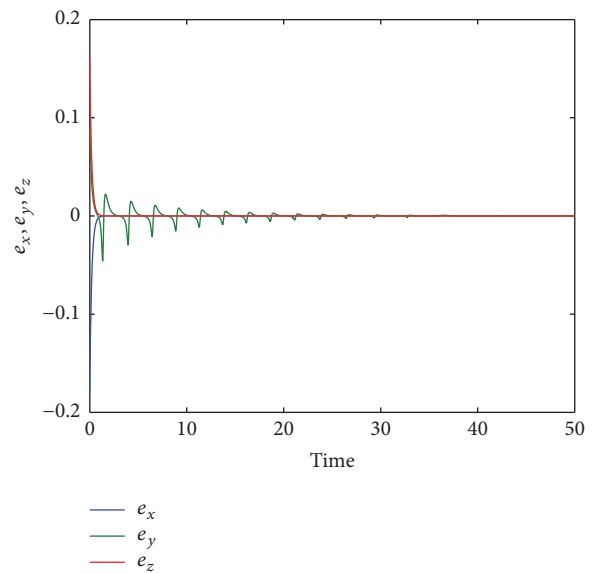


FIGURE 10: Time-history of the antisynchronization errors between the systems with cloud-shaped equilibrium (13) and (14).

of directions for future research, further work could explore chaos-based applications of such new system. For example, chaotic behaviors of other systems which are similar to the new one are useful for generating hardware pseudorandom number [18], controlling motions of autonomous mobile robots [19], or using in secure communications [22].

Competing Interests

The authors declare that there is no conflict of interests regarding the publication of this paper.

Acknowledgments

The authors acknowledge Professor GuanRong Chen, Department of Electronic Engineering, City University of Hong Kong, for suggesting many helpful references. The author Xiong Wang was supported by the National Natural

Science Foundation of China (nos. 11547117 and 61601306) and Shenzhen Overseas High Level Talent Peacock Project Fund (no. 20150215145C).

References

- [1] E. N. Lorenz, "Deterministic nonperiodic flow," *Journal of the Atmospheric Sciences*, vol. 20, no. 2, pp. 130–141, 1963.
- [2] G. R. Chen and T. Ueta, "Yet another chaotic attractor," *International Journal of Bifurcation and Chaos*, vol. 9, no. 7, pp. 1465–1466, 1999.
- [3] J. C. Sprott, "Some simple chaotic flows," *Physical Review E*, vol. 50, no. 2, pp. R647–R650, 1994.
- [4] J. C. Sprott, *Elegant Chaos Algebraically Simple Chaotic Flows*, World Scientific, Singapore, 2010.
- [5] M. P. Aghababa and M. Borjkhani, "Chaotic fractional-order model for muscular blood vessel and its control via fractional control scheme," *Complexity*, vol. 20, no. 2, pp. 37–46, 2014.
- [6] F. Zhang, C. Mu, G. Zhang, and D. Lin, "Dynamics of two classes of Lorenz-type chaotic systems," *Complexity*, vol. 21, no. 1, pp. 363–369, 2015.
- [7] A. T. Azar and S. Vaidyanathan, *Advances in Chaos Theory and Intelligent Control*, Springer, Berlin, Germany, 2016.
- [8] A. G. Radwan, A. M. Soliman, and A. El-Sedeek, "MOS realization of the modified Lorenz chaotic system," *Chaos, Solitons and Fractals*, vol. 21, no. 3, pp. 553–561, 2004.
- [9] A. S. Mansingka, M. A. Zidan, M. L. Barakat, A. G. Radwan, and K. N. Salama, "Fully digital jerk-based chaotic oscillators for high throughput pseudo-random number generators up to 8.77 Gbits/s," *Microelectronics Journal*, vol. 44, no. 9, pp. 744–752, 2013.
- [10] S. Vaidyanathan, "Analysis and adaptive synchronization of eight-term 3-D polynomial chaotic systems with three quadratic nonlinearities," *European Physical Journal: Special Topics*, vol. 223, no. 8, pp. 1519–1529, 2014.
- [11] V. Sundarapandian and I. Pehlivan, "Analysis, control, synchronization and circuit design of a novel chaotic system," *Mathematical and Computer Modelling*, vol. 55, no. 7-8, pp. 1904–1915, 2012.
- [12] I. Pehlivan, I. M. Moroz, and S. Vaidyanathan, "Analysis, synchronization and circuit design of a novel butterfly attractor," *Journal of Sound and Vibration*, vol. 333, no. 20, pp. 5077–5096, 2014.
- [13] A. Akgul, I. Moroz, I. Pehlivan, and S. Vaidyanathan, "A new four-scroll chaotic attractor and its engineering applications," *Optik*, vol. 127, no. 13, pp. 5491–5499, 2016.
- [14] A. G. Radwan, A. M. Soliman, and A. S. Elwakil, "1-D digitally-controlled multiscroll chaos generator," *International Journal of Bifurcation and Chaos*, vol. 17, no. 1, pp. 227–242, 2007.
- [15] M. A. Zidan, A. G. Radwan, and K. N. Salama, "Controllable V-shape multiscroll butterfly attractor: system and circuit implementation," *International Journal of Bifurcation and Chaos*, vol. 22, no. 6, Article ID 1250143, 2012.
- [16] A. Hajipour and H. Tavakoli, "Analysis and circuit simulation of a novel nonlinear fractional incommensurate order financial system," *Optik*, vol. 127, no. 22, pp. 10643–10652, 2016.
- [17] E. Zambrano-Serrano, E. Campos-Cantón, and J. M. Muñoz-Pacheco, "Strange attractors generated by a fractional order switching system and its topological horseshoe," *Nonlinear Dynamics*, vol. 83, no. 3, pp. 1629–1641, 2016.
- [18] M. L. Barakat, A. S. Mansingka, A. G. Radwan, and K. N. Salama, "Generalized hardware post-processing technique for chaos-based pseudorandom number generators," *ETRI Journal*, vol. 35, no. 3, pp. 448–458, 2013.
- [19] C. K. Volos, I. M. Kyprianidis, and I. N. Stouboulos, "A chaotic path planning generator for autonomous mobile robots," *Robotics and Autonomous Systems*, vol. 60, no. 4, pp. 651–656, 2012.
- [20] A. G. Radwan, A. M. Soliman, and A.-L. El-Sedeek, "An inductorless CMOS realization of Chua's circuit," *Chaos, Solitons & Fractals*, vol. 18, no. 1, pp. 149–158, 2003.
- [21] C. K. Volos, I. M. Kyprianidis, and I. N. Stouboulos, "Image encryption process based on chaotic synchronization phenomena," *Signal Processing*, vol. 93, no. 5, pp. 1328–1340, 2013.
- [22] S. Çiçek, A. Ferikoğlu, and I. Pehlivan, "A new 3D chaotic system: dynamical analysis, electronic circuit design, active control synchronization and chaotic masking communication application," *Optik*, vol. 127, no. 8, pp. 4024–4030, 2016.
- [23] V. E. Bondarenko, "Information processing, memories, and synchronization in chaotic neural network with the time delay," *Complexity*, vol. 11, no. 2, pp. 39–52, 2005.
- [24] S. Jafari and J. C. Sprott, "Simple chaotic flows with a line equilibrium," *Chaos, Solitons & Fractals*, vol. 57, pp. 79–84, 2013.
- [25] C. Li and J. C. Sprott, "Chaotic flows with a single nonquadratic term," *Physics Letters A*, vol. 378, no. 3, pp. 178–183, 2014.
- [26] C. Li, J. C. Sprott, Z. Yuan, and H. Li, "Constructing chaotic systems with total amplitude control," *International Journal of Bifurcation and Chaos*, vol. 25, no. 10, Article ID 1530025, 2015.
- [27] Y. Chen and Q. Yang, "A new Lorenz-type hyperchaotic system with a curve of equilibria," *Mathematics and Computers in Simulation*, vol. 112, pp. 40–55, 2015.
- [28] V.-T. Pham, S. Jafari, C. Volos, S. Vaidyanathan, and T. Kapitaniak, "A chaotic system with infinite equilibria located on a piecewise linear curve," *Optik*, vol. 127, no. 20, pp. 9111–9117, 2016.
- [29] T. Gotthans and J. Petrzela, "New class of chaotic systems with circular equilibrium," *Nonlinear Dynamics*, vol. 81, no. 3, pp. 1143–1149, 2015.
- [30] T. Gotthans, J. C. Sprott, and J. Petrzela, "Simple chaotic flow with circle and square equilibrium," *International Journal of Bifurcation and Chaos*, vol. 26, no. 8, Article ID 1650137, 2016.
- [31] V.-T. Pham, S. Jafari, X. Wang, and J. Ma, "A chaotic system with different shapes of equilibria," *International Journal of Bifurcation and Chaos*, vol. 26, no. 4, Article ID 1650069, 5 pages, 2016.
- [32] V.-T. Pham, S. Jafari, C. Volos, A. Giakoumis, S. Vaidyanathan, and T. Kapitaniak, "A chaotic system with equilibria located on the rounded square loop and its circuit implementation," *IEEE Transactions on Circuits and Systems II: Express Briefs*, vol. 63, no. 9, pp. 878–882, 2016.
- [33] G. A. Leonov, N. V. Kuznetsov, O. A. Kuznetsova, S. M. Seldedzhi, and V. I. Vagitsev, "Hidden oscillations in dynamical systems," *Transaction on Systems and Control*, vol. 6, pp. 54–67, 2011.
- [34] G. A. Leonov, N. V. Kuznetsov, and V. I. Vagitsev, "Localization of hidden Chua's attractors," *Physics Letters. A*, vol. 375, no. 23, pp. 2230–2233, 2011.
- [35] G. A. Leonov, N. V. Kuznetsov, and V. I. Vagitsev, "Hidden attractor in smooth Chua systems," *Physica D*, vol. 241, no. 18, pp. 1482–1486, 2012.

- [36] G. A. Leonov and N. V. Kuznetsov, "Hidden attractors in dynamical systems. From hidden oscillations in Hilbert-Kolmogorov, Aizerman, and Kalman problems to hidden chaotic attractor in Chua circuits," *International Journal of Bifurcation and Chaos*, vol. 23, no. 1, Article ID 1330002, 2013.
- [37] S. Brezetskyi, D. Dudkowski, and T. Kapitaniak, "Rare and hidden attractors in Van der Pol-Duffing oscillators," *European Physical Journal: Special Topics*, vol. 224, no. 8, pp. 1459–1467, 2015.
- [38] T. Kapitaniak and G. A. Leonov, "Multistability: uncovering hidden attractors," *European Physical Journal: Special Topics*, vol. 224, no. 8, pp. 1405–1408, 2015.
- [39] D. Dudkowski, S. Jafari, T. Kapitaniak, N. V. Kuznetsov, G. A. Leonov, and A. Prasad, "Hidden attractors in dynamical systems," *Physics Reports*, vol. 637, pp. 1–50, 2016.
- [40] P. R. Sharma, M. D. Shrimali, A. Prasad, N. V. Kuznetsov, and G. A. Leonov, "Control of multistability in hidden attractors," *European Physical Journal: Special Topics*, vol. 224, no. 8, pp. 1485–1491, 2015.
- [41] Z. T. Zhusubaliyev, E. Mosekilde, A. N. Churilov, and A. Medvedev, "Multistability and hidden attractors in an impulsive Goodwin oscillator with time delay," *European Physical Journal: Special Topics*, vol. 224, no. 8, pp. 1519–1539, 2015.
- [42] Z. T. Zhusubaliyev and E. Mosekilde, "Multistability and hidden attractors in a multilevel DC/DC converter," *Mathematics and Computers in Simulation*, vol. 109, pp. 32–45, 2015.
- [43] A. Wolf, J. B. Swift, H. L. Swinney, and J. A. Vastano, "Determining Lyapunov exponents from a time series," *Physica D*, vol. 16, no. 3, pp. 285–317, 1985.
- [44] N. V. Kuznetsov, "The Lyapunov dimension and its estimation via the Leonov method," *Physics Letters A*, vol. 380, no. 25–26, pp. 2142–2149, 2016.
- [45] N. V. Kuznetsov, T. A. Alexeeva, and G. A. Leonov, "Invariance of Lyapunov exponents and Lyapunov dimension for regular and irregular linearizations," *Nonlinear Dynamics*, vol. 85, no. 1, pp. 195–201, 2016.
- [46] G. A. Leonov, N. V. Kuznetsov, N. A. Korzhemanova, and D. V. Kusakina, "Lyapunov dimension formula for the global attractor of the Lorenz system," *Communications in Nonlinear Science and Numerical Simulation*, vol. 41, pp. 84–103, 2016.
- [47] S. Bouali, A. Buscarino, L. Fortuna, M. Frasca, and L. V. Gambuzza, "Emulating complex business cycles by using an electronic analogue," *Nonlinear Analysis. Real World Applications*, vol. 13, no. 6, pp. 2459–2465, 2012.
- [48] W.-J. Zhou, Z.-P. Wang, M.-W. Wu, W.-H. Zheng, and J.-F. Weng, "Dynamics analysis and circuit implementation of a new three-dimensional chaotic system," *Optik*, vol. 126, no. 7–8, pp. 765–768, 2015.
- [49] Q. Lai and L. Wang, "Chaos, bifurcation, coexisting attractors and circuit design of a three-dimensional continuous autonomous system," *Optik*, vol. 127, no. 13, pp. 5400–5406, 2016.
- [50] L. Fortuna, M. Frasca, and M. G. Xibilia, *Chua's Circuit Implementation: Yesterday, Today and Tomorrow*, World Scientific, Singapore, 2009.
- [51] G. Bianchi, N. V. Kuznetsov, G. A. Leonov, M. V. Yuldashev, and R. V. Yuldashev, "Limitations of PLL simulation: hidden oscillations in MatLab and SPICE," in *Proceedings of the 7th International Congress on Ultra Modern Telecommunications and Control Systems and Workshops (ICUMT '15)*, pp. 79–84, October 2015.
- [52] G. Bianchi, N. V. Kuznetsov, G. A. Leonov, S. M. Seledzhi, M. V. Yuldashev, and R. V. Yuldashev, "Hidden oscillations in SPICE simulation of two-phase Costas loop with non-linear VCO," *IFAC-PapersOnLine*, vol. 49, no. 14, pp. 45–50, 2016.
- [53] L. M. Pecora and T. L. Carroll, "Synchronization in chaotic systems," *Physical Review Letters*, vol. 64, no. 8, pp. 821–824, 1990.
- [54] S. Vaidyanathan and S. Rasappan, "Global chaos synchronization of n-scroll Chua circuit and Lur'e system using backstepping control design with recursive feedback," *Arabian Journal for Science and Engineering*, vol. 39, no. 4, pp. 3351–3364, 2014.
- [55] A. Ouannas, A. T. Azar, and R. Abu-Saris, "A new type of hybrid synchronization between arbitrary hyperchaotic maps," *International Journal of Machine Learning and Cybernetics*, pp. 1–8, 2016.
- [56] A. Stefanski, P. Perlikowski, and T. Kapitaniak, "Ragged synchronization of coupled oscillators," *Physical Review E*, vol. 75, no. 1, Article ID 016210, 2007.
- [57] S. Boccaletti, J. Kurths, G. Osipov, D. L. Valladares, and C. S. Zhou, "The synchronization of chaotic systems," *Physics Reports A*, vol. 366, no. 1–2, pp. 1–101, 2002.
- [58] L. Fortuna and M. Frasca, "Experimental synchronization of single-transistor-based chaotic circuits," *Chaos*, vol. 17, no. 4, Article ID 043118, 2007.
- [59] H. K. Khalil, *Nonlinear Systems*, Prentice Hall, New Jersey, NJ, USA, 3rd edition, 2002.

Research Article

A Novel Chaotic System without Equilibrium: Dynamics, Synchronization, and Circuit Realization

Ahmad Taher Azar,^{1,2} Christos Volos,³ Nikolaos A. Gerodimos,⁴ George S. Tombras,⁴ Viet-Thanh Pham,⁵ Ahmed G. Radwan,^{2,6} Sundarapandian Vaidyanathan,⁷ Adel Ouannas,⁸ and Jesus M. Munoz-Pacheco⁹

¹Faculty of Computers and Information, Benha University, Benha, Egypt

²Nanoelectronics Integrated Systems Center (NISC), Nile University, Giza, Egypt

³Department of Physics, Aristotle University of Thessaloniki, 54124 Thessaloniki, Greece

⁴Faculty of Physics, Department of Electronics, Computers, Telecommunications and Control, National and Kapodistrian University of Athens, 15784 Athens, Greece

⁵School of Electronics and Telecommunications, Hanoi University of Science and Technology, 01 Dai Co Viet, Hanoi, Vietnam

⁶Engineering Mathematics and Physics, Cairo University, Giza, Egypt

⁷Research and Development Center, Vel Tech University, Avadi, Chennai, Tamil Nadu 600062, India

⁸Laboratory of Mathematics, Informatics and Systems (LAMIS), University of Larbi Tebessi, 12002 Tebessa, Algeria

⁹University of Puebla, Puebla, PUE, Mexico

Correspondence should be addressed to Christos Volos; chvolos@gmail.com

Received 21 October 2016; Revised 12 December 2016; Accepted 22 December 2016; Published 2 February 2017

Academic Editor: Carlos Gershenson

Copyright © 2017 Ahmad Taher Azar et al. This is an open access article distributed under the Creative Commons Attribution License, which permits unrestricted use, distribution, and reproduction in any medium, provided the original work is properly cited.

A few special chaotic systems without unstable equilibrium points have been investigated recently. It is worth noting that these special systems are different from normal chaotic ones because the classical Shilnikov criterion cannot be used to prove chaos of such systems. A novel unusual chaotic system without equilibrium is proposed in this work. We discover dynamical properties as well as the synchronization of the new system. Furthermore, a physical realization of the system without equilibrium is also implemented to illustrate its feasibility.

1. Introduction

A considerable amount of literature has been published on chaotic systems in last decades, for example, Lorenz's system [1], Rössler's system [2], Chen and Ueta's system [3], simple chaotic flows [4, 5], memristive chaotic system with heart-shaped attractors [6], chaotic circuit based on memristor [7, 8], MOS-transistors based oscillators [9, 10], mixed analog-digital designs [11], fully digital realization of chaotic systems [12, 13], or electromechanical oscillator [14]. Complexity of chaotic systems has been used in various engineering applications from asymmetric color pathological image encryption [15, 16], control and synchronization [17, 18], a chaotic video

communication scheme via WAN remote transmission [19], and image encryption with avalanche effects [20] to audio encryption scheme [21] and so on.

It is now well established from a variety of studies that equilibrium points play a vital role in our understanding of chaos in nonlinear systems [22–24]. In general, conventional chaotic systems have unstable equilibria and we are able to verify chaos in such systems with the Shilnikov criterion [25, 26]. However, recent researches have consistently shown that chaotic behavior can be observed in three-dimensional (3D) systems with no equilibrium [27].

The study of systems without equilibria has a long history, describing various electromechanical models with rotation

and electrical circuits with cylindrical phase space. One of the first such examples has been described by Arnold Sommerfeld in 1902 [28], by studying the oscillations caused by a motor driving an unbalanced weight and discovered the resonance capture, which is called ‘‘Sommerfeld effect.’’ This phenomenon represents the failure of a rotating mechanical system to be spun up by a torque-limited rotor to a desired rotational velocity due to its resonant interaction with another part of the system [29, 30]. Many decades later, in 1984–85, Nosé [31] and Hoover [32] have led the study with their proposed dynamical system without equilibria and its various modifications, where hidden chaotic oscillations can be found [4, 33–36].

Systematic search routine was developed by Jafari et al. to determine simple quadratic flows with no equilibria [24, 27]. Wang and Chen found a new system without equilibrium while studying a chaotic system with any number of equilibria [24]. Wei discovered dynamical properties of a no-equilibrium chaotic system by applying a constant to the Sprott D system [37]. Multiple attractors in a three-dimensional system with no-equilibrium point were reported in [38]. Akgul et al. designed a random number generator with a 3D chaotic system without equilibrium point [39]. In addition, 4D no-equilibrium systems with hyperchaos were presented in [40–42]. It is interesting to note that chaotic systems without equilibrium display ‘‘hidden attractors’’ [43–46]. There has been considerable interest in discovering hidden attractors because they cannot be localized by applying common computational procedures [47–52].

This study makes a contribution to research on systems with hidden attractors by exploring a new chaotic system without equilibrium. In the next section, the description and dynamics of the no-equilibrium system are presented. Synchronization of two new chaotic systems without equilibrium is studied in Section 3. The theoretical system has been realized by an electronic circuit as reported in Section 4. Finally, conclusion remarks are drawn in the last section.

2. Description and Dynamics of the System without Equilibrium

Jafari et al. have introduced an effective approach for investigating potential systems without equilibrium [27]. Authors constructed general models and applied a systematical search routine to obtain seventeen simple flows with no equilibrium [27]. Motivated by Jafari et al.’s systems, in this work we consider a general form as follows:

$$\begin{aligned}\dot{x} &= y, \\ \dot{y} &= z, \\ \dot{z} &= a_0|x| + a_1y + a_2z + a_3y^2 + a_4z^2 + a_5xy + a_6xz \\ &\quad + a_7yz + a_8,\end{aligned}\tag{1}$$

in which three state variables of the general form are x , y , and z , while nine parameters are a_i ($i = 0, \dots, 8$) with $a_0 \neq 0$. An absolute nonlinearity has been included in (1) because it is a

potential term for designing nonlinear systems with special characteristics [53, 54].

In order to find the equilibrium of system (1), we solve the three following equations:

$$y = 0,\tag{2}$$

$$z = 0,\tag{3}$$

$$\begin{aligned}a_0|x| + a_1y + a_2z + a_3y^2 + a_4z^2 + a_5xy + a_6xz \\ + a_7yz + a_8 = 0.\end{aligned}\tag{4}$$

By substituting (2), (3) into (4), we have

$$|x| = -\frac{a_8}{a_0}.\tag{5}$$

It is easy to verify that the equation is inconsistent for

$$a_0a_8 > 0.\tag{6}$$

In other words, in this case the general model (1) has no equilibrium.

By applying a systematic search procedure [27] into (1), a simple three-dimensional system is obtained in the following form:

$$\begin{aligned}\dot{x} &= y, \\ \dot{y} &= z, \\ \dot{z} &= -a|x| - y + 3y^2 - xz - b,\end{aligned}\tag{7}$$

in which three state variables are x , y , and z while two positive parameters are a, b ($a > 0, b > 0$). According to condition (6), it is trivial to verify that there is no equilibrium in the new system (7).

It is interesting that system (7) can generate chaotic signals although there is the absence of equilibrium. For $a = 0.35$, $b = 0.05$ and the initial conditions $(x(0), y(0), z(0)) = (0.1, 0.1, 0.1)$, system (7) generates chaotic behavior as shown in Figure 1. As can be seen in Figure 1, chaotic waveforms and broadband spectra indicate the chaoticity of system (7). In addition, chaotic phase portraits of system (7) are illustrated in Figure 2. Calculated Lyapunov exponents and Kaplan-York dimension of the system without equilibrium (7) are $L_1 = 0, 0594$, $L_2 = 0$, $L_3 = -0.358$, and $D_{KY} = 2.1659$, respectively. In other words, system (7) has hidden attractors, which is important for a wide range of scientific and engineering processes [55–58]. In our work, the well-known algorithm of Wolf et al. [59] has been applied to calculate Lyapunov exponents. The time of the computation is 10,000. It is noted that, due to the different values of the finite-time local Lyapunov exponents and Lyapunov dimension for different points, the maximum of the finite-time local Lyapunov dimensions on the grid of point has to be considered [60–62].

Dynamics of the system without equilibrium have been investigated by changing the value of the bifurcation parameter a in the range from 0.2 to 0.36. Figures 3 and 4 show the bifurcation diagram and the diagram of maximal Lyapunov exponents (MLEs) of the no-equilibrium system. As can be

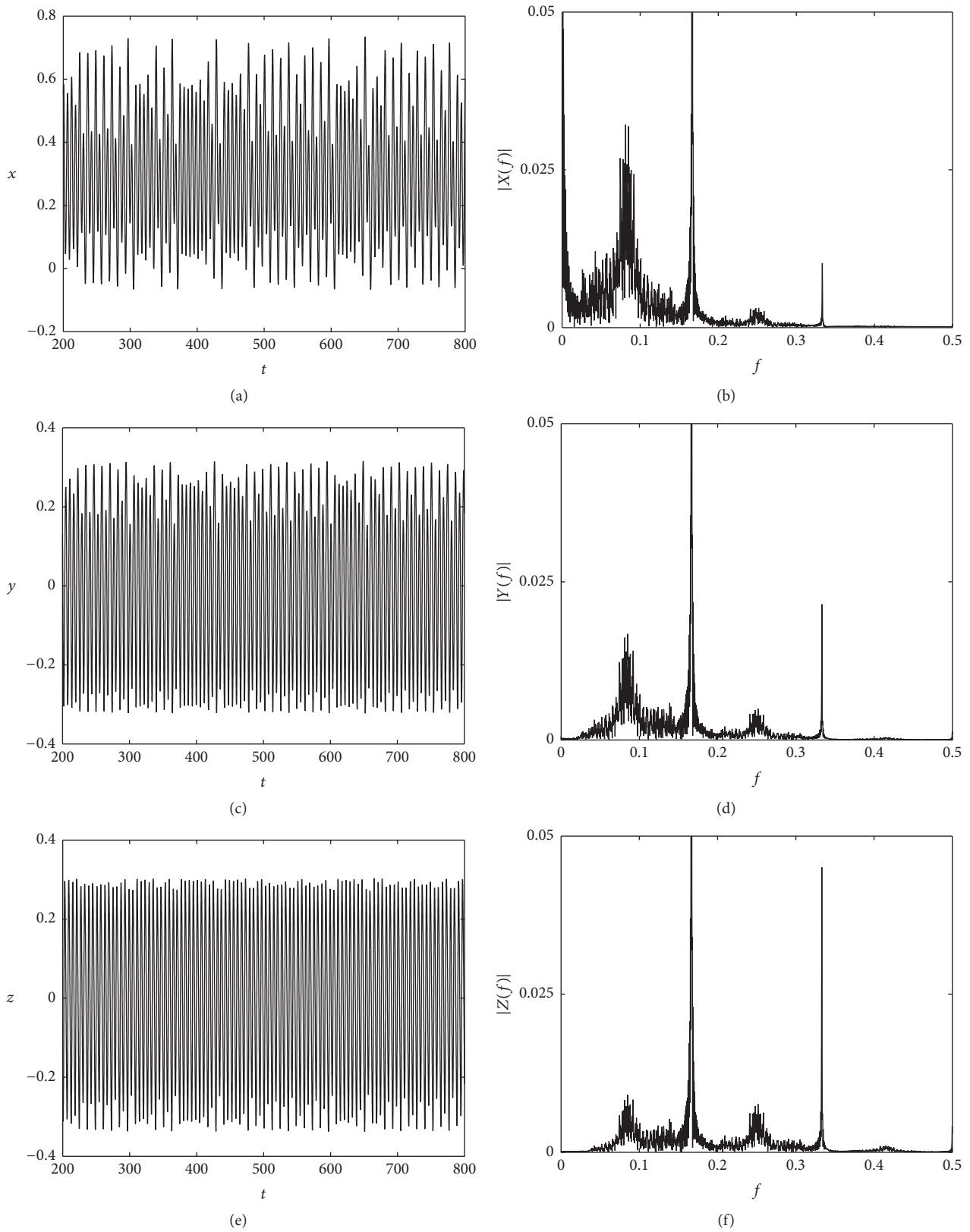


FIGURE 1: Chaotic waveform and the frequency spectra generated from system (7): (a) time series of $x(t)$, (b) single-sided amplitude spectrum of $x(t)$, (c) time series of $y(t)$, (d) single-sided amplitude spectrum of $y(t)$, (e) time series of $z(t)$, and (f) single-sided amplitude spectrum of $z(t)$.

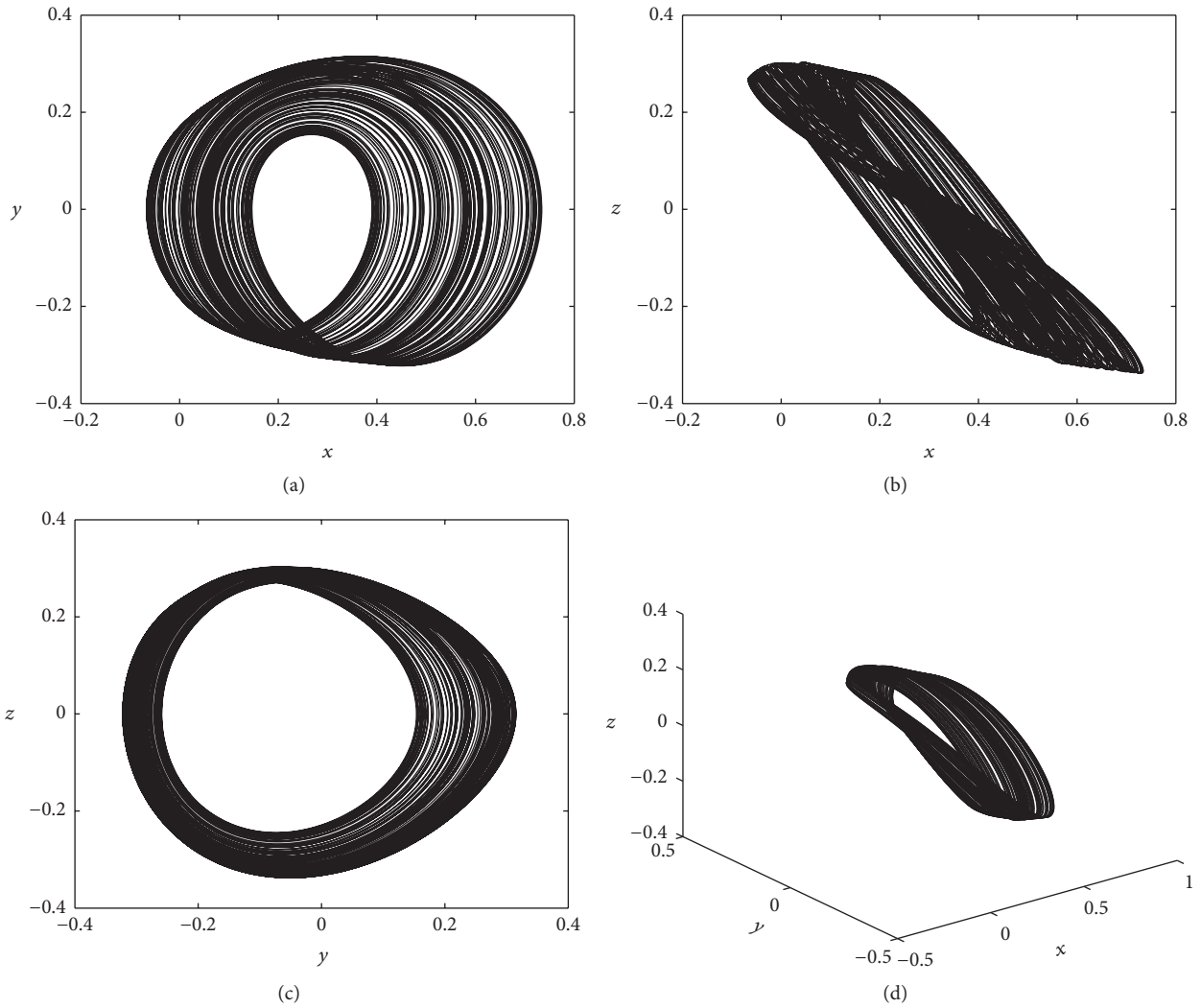


FIGURE 2: Four views of the chaotic attractors in system without equilibrium (7) in (a) x - y plane, (b) x - z plane, (c) y - z plane, and (d) x - y - z space for $a = 0.35$, $b = 0.05$, and the initial conditions $(x(0), y(0), z(0)) = (0.1, 0.1, 0.1)$.

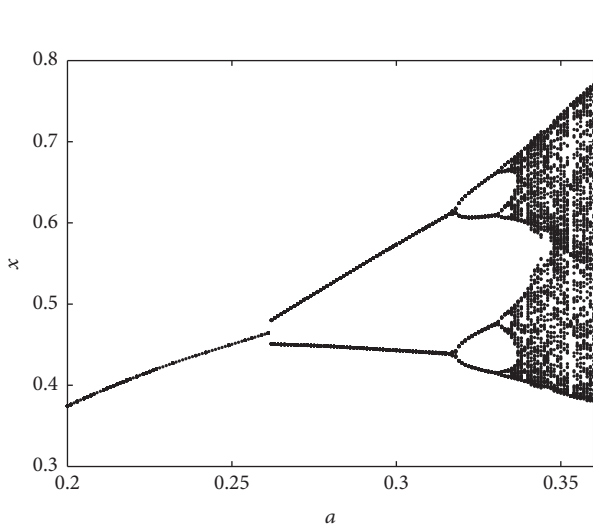


FIGURE 3: Bifurcation diagram of the system without equilibrium (7) for $b = 0.05$ and $a \in [0.2, 0.36]$.

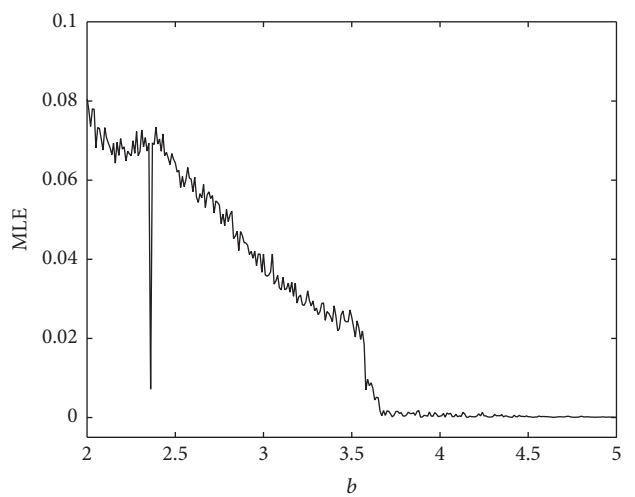


FIGURE 4: Maximum Lyapunov exponents of the system without equilibrium (7) for $b = 0.05$ when changing the value of the parameter a from 0.2 to 0.36.

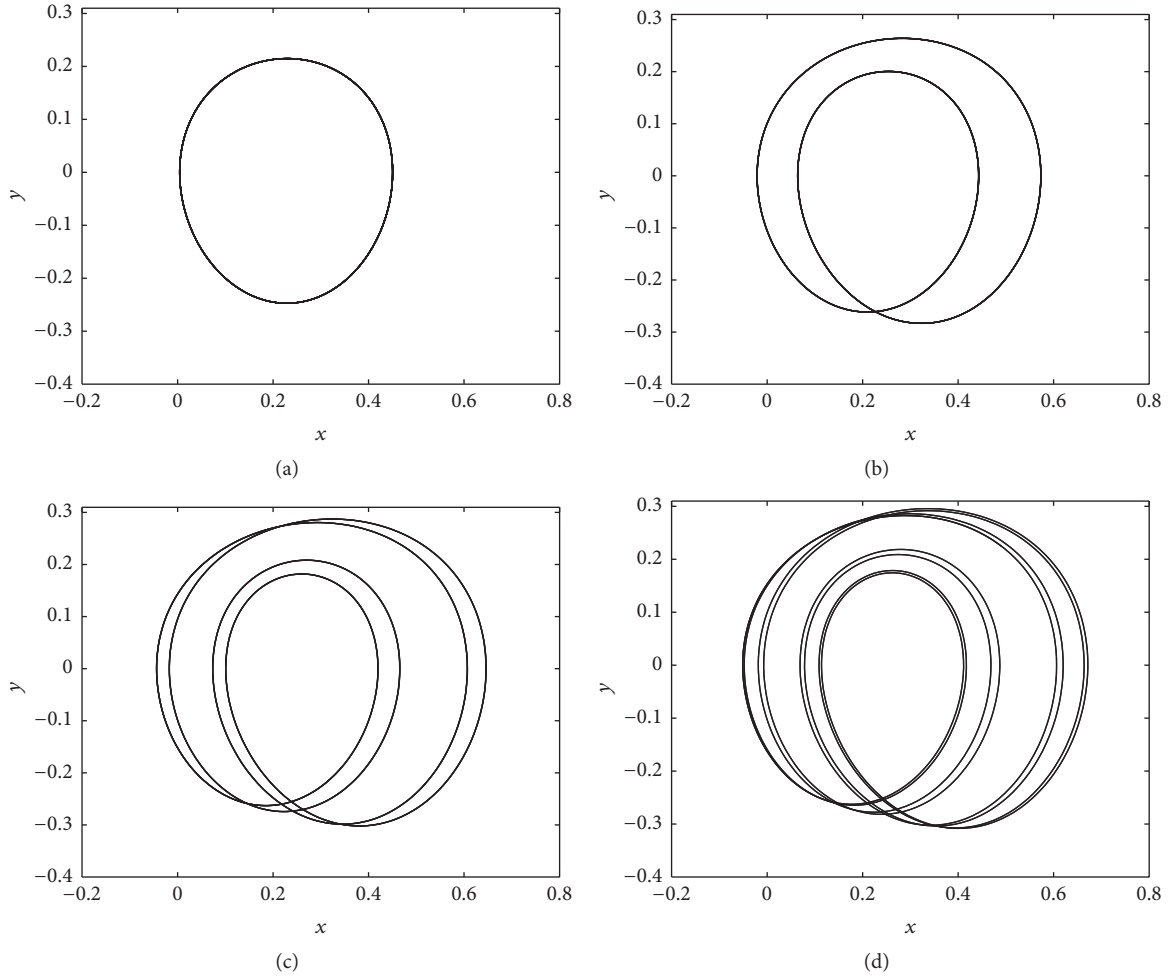


FIGURE 5: Four views of limit cycles in the system without equilibrium (7) in (a) period-1 oscillation ($a = 0.25$), (b) period-2 oscillation ($a = 0.3$), (c) period-4 oscillation ($a = 0.325$), and (d) period-8 oscillation ($a = 0.333$) for the initial conditions $(x(0), y(0), z(0)) = (0.1, 0.1, 0.1)$ and $b = 0.05$.

seen from Figures 3 and 4, system (7) displays periodical oscillations for $a < 0.335$. For instance, different periodical oscillations of system (7) are illustrated in Figure 5. For $a \geq 0.335$, complex behaviors of the system can be observed. Moreover, it is easy to verify the presence of a period-doubling route to chaos when increasing the value of the parameter a .

3. Synchronization of Two Identical Systems without Equilibrium

The past decade has seen the rapid development of synchronization schemes for numerous chaotic systems because synchronization plays a critical role in practical applications [63–67]. Therefore, when investigating a new chaotic system it is important to consider its synchronization ability. In this section, we study the synchronization of two new systems without equilibrium (the master and slave systems) via an adaptive controller, which has been reported as an effective approach [68–70].

Here the master system without equilibrium is presented by

$$\begin{aligned}\dot{x}_1 &= y_1, \\ \dot{y}_1 &= z_1, \\ \dot{z}_1 &= -a|x_1| - y_1 + 3y_1^2 - x_1z_1 - b,\end{aligned}\tag{8}$$

where three state variables are x_1 , y_1 , and z_1 and the unknown system parameters are a , b . The slave system without equilibrium is given by

$$\begin{aligned}\dot{x}_2 &= y_2 + u_x, \\ \dot{y}_2 &= z_2 + u_y, \\ \dot{z}_2 &= -a|x_2| - y_2 + 3y_2^2 - x_2z_2 - b + u_z,\end{aligned}\tag{9}$$

in which x_2 , y_2 , and z_2 are system's variables and $\mathbf{u} = [u_x, u_y, u_z]^T$ is an adaptive control. By calculating the difference

between the slave system and the master system, the state errors are defined as

$$\begin{aligned} e_x &= x_2 - x_1, \\ e_y &= y_2 - y_1, \\ e_z &= z_2 - z_1. \end{aligned} \quad (10)$$

As a result, the state error dynamics are calculated by

$$\begin{aligned} \dot{e}_x &= \dot{x}_2 - \dot{x}_1, \\ \dot{e}_y &= \dot{y}_2 - \dot{y}_1, \\ \dot{e}_z &= \dot{z}_2 - \dot{z}_1. \end{aligned} \quad (11)$$

The parameter estimation error is denoted as e_a

$$e_a = a - \hat{a}, \quad (12)$$

where the estimation of the unknown parameter (a) is \hat{a} . By differentiating (12), we get

$$\dot{e}_a = -\dot{\hat{a}}. \quad (13)$$

We design an adaptive control to synchronize the slave system without equilibrium (9) with the master system (8) without equilibrium as follows:

$$\begin{aligned} u_x &= -e_y - k_x e_x, \\ u_y &= -e_z - k_y e_y, \\ u_z &= e_y - 3(y_2^2 - y_1^2) + x_2 z_2 - x_1 z_1 + \hat{a}(|x_2| - |x_1|) \\ &\quad - k_z e_z. \end{aligned} \quad (14)$$

In the adaptive control (14), three positive gain constants are k_x , k_y , and k_z while the parameter update law is constructed by

$$\dot{\hat{a}} = e_z (|x_1| - |x_2|). \quad (15)$$

It is simple to verify that the slave system (9) and the master system (8) are synchronized when applying the proposed adaptive control (14). We prove this result by using the selected Lyapunov function:

$$V(e_x, e_y, e_z, e_a) = \frac{1}{2} (e_x^2 + e_y^2 + e_z^2 + e_a^2). \quad (16)$$

From (16), we have the differentiation of V :

$$\dot{V} = e_x \dot{e}_x + e_y \dot{e}_y + e_z \dot{e}_z + e_a \dot{e}_a. \quad (17)$$

By combining (8), (9), and (14), synchronization error dynamics are achieved as

$$\begin{aligned} \dot{e}_x &= -k_x e_x, \\ \dot{e}_y &= -k_y e_y, \\ \dot{e}_z &= -e_a (|x_2| - |x_1|) - k_z e_z. \end{aligned} \quad (18)$$

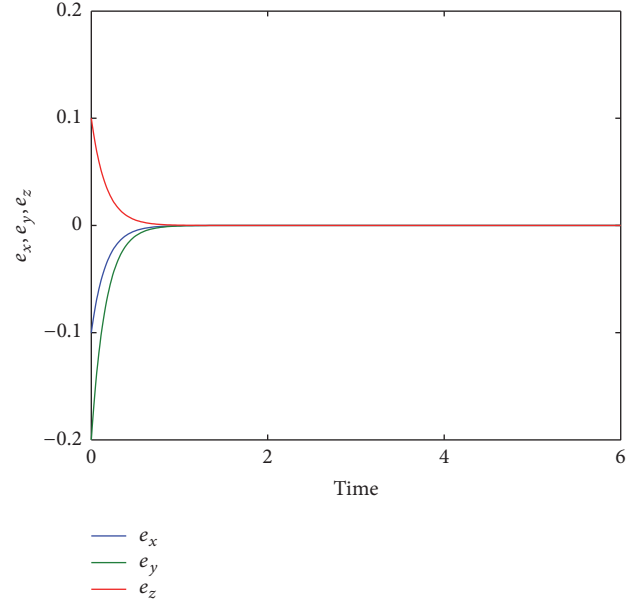


FIGURE 6: Time-history of the synchronization errors between the slave system without equilibrium (9) and the master system without equilibrium (8).

Finally, by substituting (13) and (18) into (17), the differentiation of the Lyapunov function can be simplified as

$$\dot{V} = -k_x e_x^2 - k_y e_y^2 - k_z e_z^2. \quad (19)$$

Obviously, the differentiation of V is a negative semidefinite function. Therefore, according to Barbalat's lemma [71], we have $e_x \rightarrow 0$, $e_y \rightarrow 0$, and $e_z \rightarrow 0$ exponentially as $t \rightarrow \infty$. As a result, the synchronization between the slave system (9) and the master system (8) is verified.

In order to confirm the calculation of the synchronization scheme, we consider an example where the parameter values of the master system and the slave system are fixed as

$$\begin{aligned} a &= 0.35, \\ b &= 0.05. \end{aligned} \quad (20)$$

The initial states of the master system are assumed as

$$\begin{aligned} x_1(0) &= 0.1, \\ y_1(0) &= 0.1, \\ z_1(0) &= 0.1, \end{aligned} \quad (21)$$

while the initial states of the slave system are selected as

$$\begin{aligned} x_2(0) &= 0, \\ y_2(0) &= -0.1, \\ z_2(0) &= 0.2. \end{aligned} \quad (22)$$

We take the positive gain constants which are $k_x = 6$, $k_y = 6$, and $k_z = 6$ and set the initial condition of the parameter estimate, that is,

$$\hat{a}(0) = 0.3. \quad (23)$$

The time-history of the synchronization errors e_x , e_y , e_z is reported in Figure 6. Furthermore, the time series of the

master and the slave systems are illustrated in Figure 7. From Figures 6 and 7 it is straightforward to see the synchronization of the slave system and the master system.

4. Realization of the Proposed System without Equilibrium

The issue of realizing theoretical chaotic models has received considerable critical attention due to its practical applications [65, 72–76]. Thus, an electronic circuit for realizing the proposed system without equilibrium (7) is introduced in this section. We rescaled three state variables of system without equilibrium (7), that is, $X = 10x$, $Y = 10y$, and $Z = 10z$, to get enough larger signals in our electronic circuit. Therefore, the system without equilibrium (7) is transformed into the following equivalent system:

$$\begin{aligned}\dot{X} &= Y, \\ \dot{Y} &= Z, \\ \dot{Z} &= -a|X| - Y + \frac{3}{10}Y^2 - \frac{1}{10}XZ - 10b.\end{aligned}\quad (24)$$

Figure 8 shows the schematic of the circuit for realizing system (24). As shown in Figure 8, there are three integrators (U_3 – U_5) implemented with operational amplifiers. The circuit of absolute nonlinearity ($|X|$) is based on two operational amplifiers (U_6, U_7) and two diodes (D_1, D_2). By applying Kirchhoff's circuit laws into the designed circuit, the following circuital equation is derived:

$$\begin{aligned}\dot{X} &= \frac{1}{RC}Y, \\ \dot{Y} &= \frac{1}{RC}Z, \\ \dot{Z} &= \frac{1}{RC} \left(-\frac{R}{R_a}|X| - Y + \frac{R}{R_1 10V}Y^2 - \frac{1}{10V}XZ - V_b \right).\end{aligned}\quad (25)$$

The variables X , Y , and Z in (25) correspond to the voltages in the outputs of three integrators (U_3 , U_4 , and U_5), respectively. It is simple to verify that system (25) is equivalent to the system without equilibrium (24) by normalizing it with $\tau = t/RC$. In order to get $a = 0.35$ and $b = 0.05$, the electronic components have been selected as $R = 10 \text{ k}\Omega$, $R_a = 28.571 \text{ k}\Omega$, $R_1 = 3.333 \text{ k}\Omega$, $C = 10 \text{ nF}$, and $V_b = 0.5 \text{ V}_{\text{DC}}$. The power supplies of all active devices are $\pm 15 \text{ V}_{\text{DC}}$. Implementation of the circuit on a breadboard is shown in Figure 9. We have measured signals in the real circuit by using oscilloscope. Experimental results are reported in Figure 10, which display a good agreement with numerical results in Figure 2.

5. Conclusions

The present study provides an additional system without equilibrium, which has received significant attention in

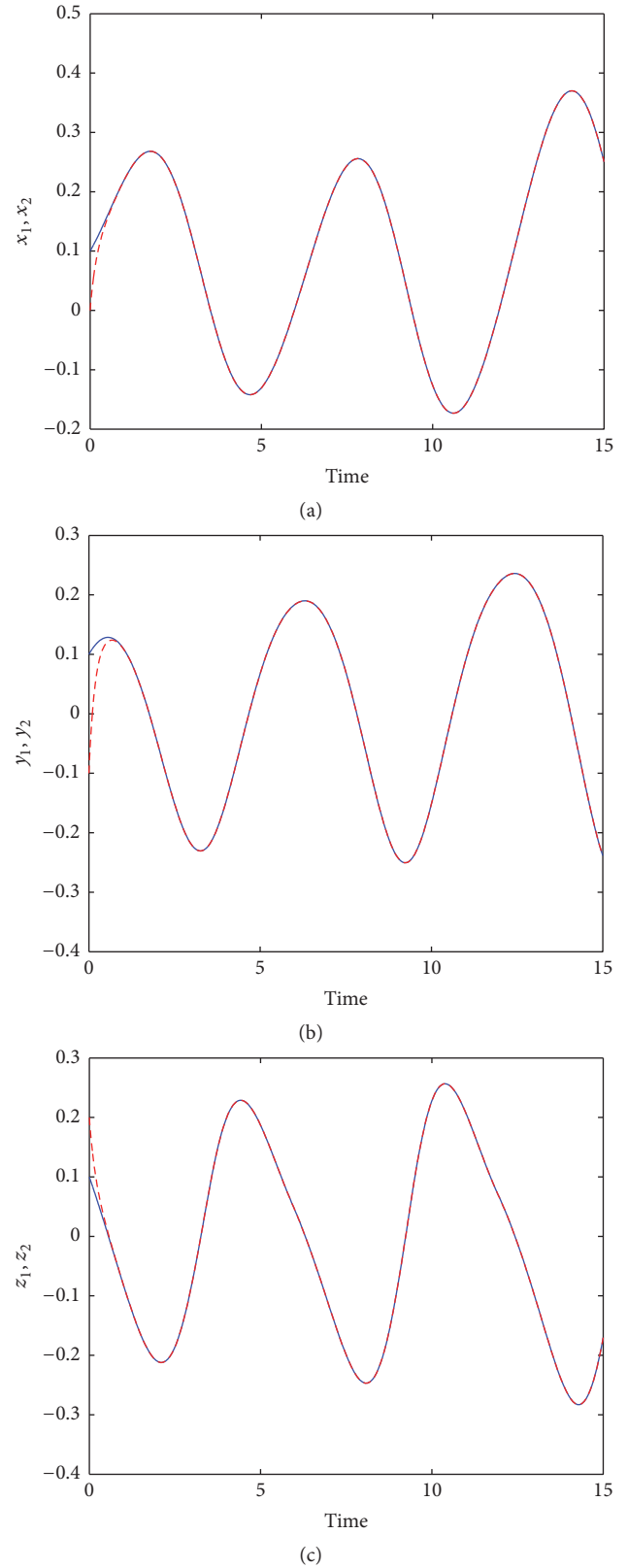


FIGURE 7: Time series of the master system (blue solid) and the slave systems (red dashed): (a) x_1 and x_2 , (b) y_1 and y_2 , and (c) z_1 and z_2 .

the research community recently. Dynamics of the proposed system are studied by numerical tools and physical

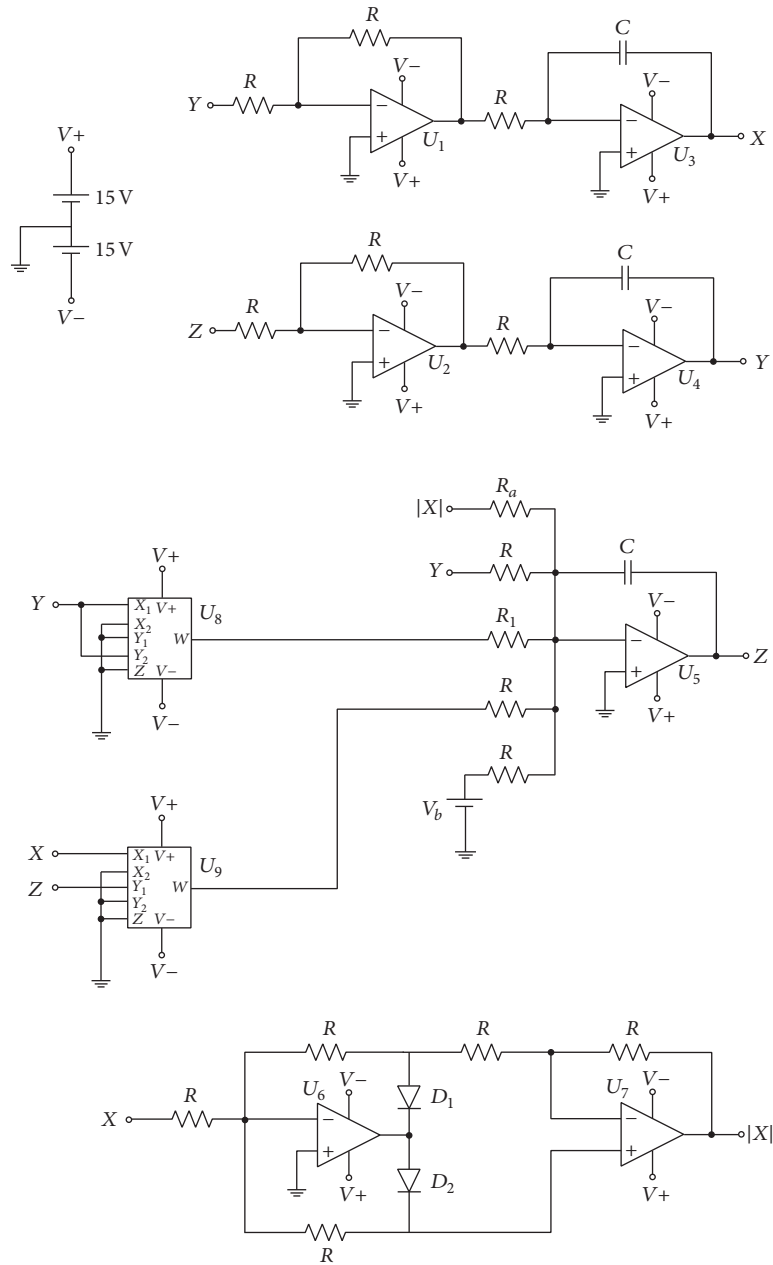


FIGURE 8: Schematic of the circuit including 16 resistors, seven operational amplifiers, two analog multipliers, two diodes, and three capacitors.

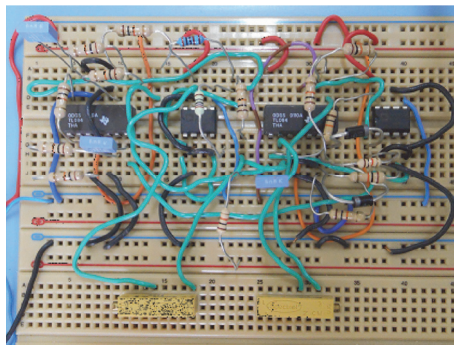


FIGURE 9: Physical realization of the theoretical system by using common electronic components.

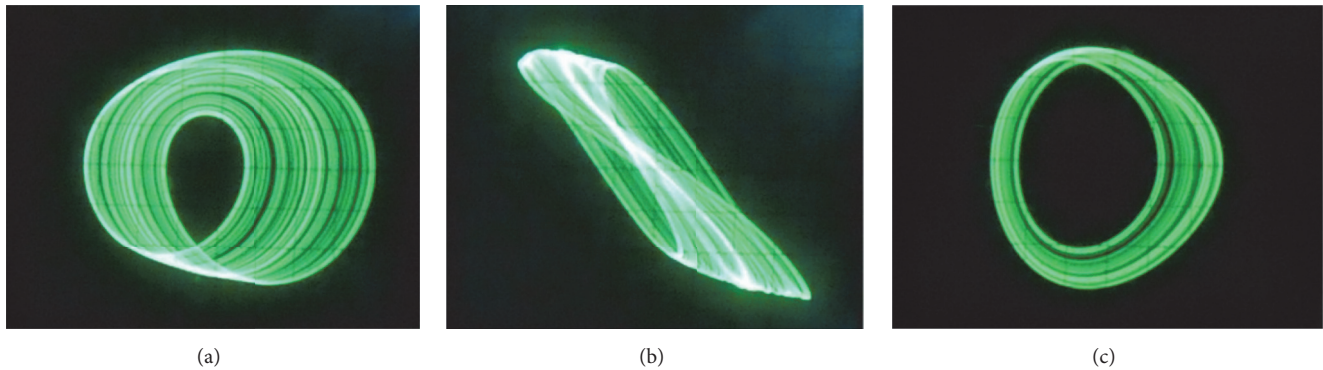


FIGURE 10: Captured chaotic attractors of the designed circuit in (a) X-Y plane, (b) X-Z plane, and (c) Y-Z plane.

implementation. It is interesting that the system can generate chaotic signals despite the fact that there is an absence of equilibrium. The system is realized easily by using common electronic components; therefore, it would be interesting to assess the practical application of the new system. Further studies related to the possible real-time applications of the system will be investigated in our future works.

Competing Interests

The authors declare that there is no conflict of interests regarding the publication of this paper.

Acknowledgments

The authors acknowledge Professor GuanRong Chen, Department of Electronic Engineering, City University of Hong Kong, for suggesting many helpful references.

References

- [1] E. Lorenz, "Deterministic nonperiodic flow," *Journal of the Atmospheric Sciences*, vol. 20, pp. 130–141, 1963.
- [2] O. Rössler, "An equation for continuous chaos," *Physics Letters A*, vol. 57, pp. 397–398, 1976.
- [3] G. Chen and T. Ueta, "Yet another chaotic attractor," *International Journal of Bifurcation and Chaos in Applied Sciences and Engineering*, vol. 9, no. 7, pp. 1465–1466, 1999.
- [4] J. C. Sprott, "Some simple chaotic flows," *Physical Review E*, vol. 50, no. 2, pp. R647–R650, 1994.
- [5] J. C. Sprott, *Elegant Chaos Algebraically Simple Chaotic Flows*, World Scientific, Singapore, 2010.
- [6] J. Wu, L. Wang, G. Chen, and S. Duan, "A memristive chaotic system with heart-shaped attractors and its implementation," *Chaos, Solitons & Fractals*, vol. 92, pp. 20–29, 2016.
- [7] R. Wu and C. Wang, "A new simple chaotic circuit based on memristor," *International Journal of Bifurcation and Chaos in Applied Sciences and Engineering*, vol. 26, no. 9, Article ID 1650145, 11 pages, 2016.
- [8] A. G. Radwan, K. Moaddy, and I. Hashim, "Amplitude modulation and synchronization of fractional-order memristor-based Chua's circuit," *Abstract and Applied Analysis*, vol. 2013, Article ID 758676, 10 pages, 2013.
- [9] A. G. Radwan, A. M. Soliman, and A.-L. El-Sedeek, "An inductorless CMOS realization of Chua's circuit," *Chaos, Solitons and Fractals*, vol. 18, no. 1, pp. 149–158, 2003.
- [10] A. G. Radwan, A. M. Soliman, and A.-L. El-Sedeek, "MOS realization of the conjectured simplest chaotic equation," *Circuits, Systems, and Signal Processing*, vol. 22, no. 3, pp. 277–285, 2003.
- [11] A. Radwan, A. Soliman, and A. S. Elwakil, "1-D digitally-controlled multiscroll chaos generator," *International Journal of Bifurcation and Chaos*, vol. 17, no. 1, pp. 227–242, 2007.
- [12] M. A. Zidan, A. G. Radwan, and K. N. Salama, "Controllable V-shape multiscroll butterfly attractor: system and circuit implementation," *International Journal of Bifurcation and Chaos*, vol. 22, no. 6, Article ID 1250143, 2012.
- [13] A. S. Mansingka, M. Affan Zidan, M. L. Barakat, A. G. Radwan, and K. N. Salama, "Fully digital jerk-based chaotic oscillators for high throughput pseudo-random number generators up to 8.77 Gbits/s," *Microelectronics Journal*, vol. 44, no. 9, pp. 744–752, 2013.
- [14] A. Buscarino, C. Famoso, L. Fortuna, and M. Frasca, "A new chaotic electro-mechanical oscillator," *International Journal of Bifurcation and Chaos in Applied Sciences and Engineering*, vol. 26, no. 10, Article ID 1650161, 7 pages, 2016.
- [15] H. Liu, A. Kadir, and Y. Li, "Asymmetric color pathological image encryption scheme based on complex hyper chaotic system," *Optik*, vol. 127, pp. 5812–5819, 2016.
- [16] A. G. Radwan, S. H. AbdElHaleem, and S. K. Abd-El-Hafiz, "Symmetric encryption algorithms using chaotic and non-chaotic generators: a review," *Journal of Advanced Research*, vol. 7, no. 2, pp. 193–208, 2016.
- [17] K. Moaddy, A. G. Radwan, K. N. Salama, S. Momani, and I. Hashim, "The fractional-order modeling and synchronization of electrically coupled neuron systems," *Computers & Mathematics with Applications*, vol. 64, no. 10, pp. 3329–3339, 2012.
- [18] A. G. Radwan, K. Moaddy, K. N. Salama, S. Momani, and I. Hashim, "Control and switching synchronization of fractional order chaotic systems using active control technique," *Journal of Advanced Research*, vol. 5, no. 1, pp. 125–132, 2014.
- [19] Z. Lin, S. Yu, C. Li, J. Lü, and Q. Wang, "Design and smartphone-based implementation of a chaotic video communication scheme via WAN remote transmission," *International Journal of Bifurcation and Chaos in Applied Sciences and Engineering*, vol. 26, no. 9, Article ID 1650158, 8 pages, 2016.
- [20] L. Min, X. Yang, G. Chen, and D. Wang, "Some polynomial chaotic maps without equilibria and an application to image

- encryption with avalanche effects,” *International Journal of Bifurcation and Chaos*, vol. 25, no. 9, Article ID 1550124, 2015.
- [21] H. Liu, A. Kadir, and Y. Li, “Audio encryption scheme by confusion and diffusion based on multi-scroll chaotic system and one-time keys,” *Optik*, vol. 127, no. 19, pp. 7431–7438, 2016.
- [22] J. Lü and G. Chen, “Generating multiscroll chaotic attractors: theories, methods and applications,” *International Journal of Bifurcation and Chaos in Applied Sciences and Engineering*, vol. 16, no. 4, pp. 775–858, 2006.
- [23] X. Wang and G. Chen, “A chaotic system with only one stable equilibrium,” *Communications in Nonlinear Science and Numerical Simulation*, vol. 17, no. 3, pp. 1264–1272, 2012.
- [24] X. Wang and G. Chen, “Constructing a chaotic system with any number of equilibria,” *Nonlinear Dynamics*, vol. 71, no. 3, pp. 429–436, 2013.
- [25] L. P. Shilnikov, “A case of the existence of a countable number of periodic motions,” *Soviet Mathematics. Doklady*, vol. 6, pp. 163–166, 1965.
- [26] L. Shilnikov, A. Shilnikov, D. Turaev, and L. Chua, *Methods of Qualitative Theory in Nonlinear Dynamics*, World Scientific, Singapore, 1998.
- [27] S. Jafari, J. C. Sprott, and S. M. R. H. Golpayegani, “Elementary quadratic chaotic flows with no equilibria,” *Physics Letters A*, vol. 377, no. 9, pp. 699–702, 2013.
- [28] A. Sommerfeld, “Beitrage zum dynamischen ausbau der festigkeitslehre,” *Zeitschrift des Vereins Deutscher Ingenieure*, vol. 46, pp. 391–394, 1902.
- [29] R. Evan-Iwanowski, *Resonance Oscillations in Mechanical Systems*, Elsevier, Amsterdam, The Netherlands, 1976.
- [30] M. Eckert, *Arnold Sommerfeld: Science, Life and Turbulent Times 1868–1951*, Springer, New York, NY, USA, 2013.
- [31] S. Nosé, “A molecular dynamics method for simulations in the canonical ensemble,” *Molecular Physics*, vol. 52, no. 2, pp. 255–268, 1984.
- [32] W. G. Hoover, “Canonical dynamics: equilibrium phase-space distributions,” *Physical Review A*, vol. 31, no. 3, pp. 1695–1697, 1985.
- [33] H. A. Posch, W. G. Hoover, and F. J. Vesely, “Canonical dynamics of the Nosé oscillator: stability, order, and chaos,” *Physical Review A. Third Series*, vol. 33, no. 6, pp. 4253–4265, 1986.
- [34] J. C. Sprott, W. G. Hoover, and C. G. Hoover, “Heat conduction, and the lack thereof, in time-reversible dynamical systems: generalized Nosé-Hoover oscillators with a temperature gradient,” *Physical Review E*, vol. 89, no. 4, Article ID 042914, 2014.
- [35] J. C. Sprott, “Strange attractors with various equilibrium types,” *European Physical Journal: Special Topics*, vol. 224, no. 8, pp. 1409–1419, 2015.
- [36] L. Wang and X.-S. Yang, “The invariant tori of knot type and the interlinked invariant tori in the Nosé-Hoover oscillator,” *The European Physical Journal B*, vol. 88, article 78, 5 pages, 2015.
- [37] Z. Wei, “Dynamical behaviors of a chaotic system with no equilibria,” *Physics Letters A*, vol. 376, no. 2, pp. 102–108, 2011.
- [38] J.-L. Zuo and C.-L. Li, “Multiple attractors and dynamic analysis of a no-equilibrium chaotic system,” *Optik*, vol. 127, no. 19, pp. 7952–7957, 2016.
- [39] A. Akgul, H. Calgan, I. Koyuncu, I. Pehlivan, and A. Istanbulu, “Chaos-based engineering applications with a 3D chaotic system without equilibrium points,” *Nonlinear Dynamics*, vol. 84, no. 2, pp. 481–495, 2016.
- [40] Z. Wang, S. Cang, E. O. Ochola, and Y. Sun, “A hyperchaotic system without equilibrium,” *Nonlinear Dynamics. An International Journal of Nonlinear Dynamics and Chaos in Engineering Systems*, vol. 69, no. 1-2, pp. 531–537, 2012.
- [41] Z. Wei, R. Wang, and A. Liu, “A new finding of the existence of hidden hyperchaotic attractors with no equilibria,” *Mathematics and Computers in Simulation*, vol. 100, pp. 13–23, 2014.
- [42] Z. Wang, J. Ma, S. Cang, Z. Wang, and Z. Chen, “Simplified hyper-chaotic systems generating multi-wing non-equilibrium attractors,” *Optik*, vol. 127, no. 5, pp. 2424–2431, 2016.
- [43] G. A. Leonov, N. V. Kuznetsov, O. A. Kuznetsova, S. M. Seledzhi, and V. I. Vagitsev, “Hidden oscillations in dynamical systems,” *WSEAS Transactions on Systems and Control*, vol. 6, no. 2, pp. 54–67, 2011.
- [44] G. A. Leonov, N. V. Kuznetsov, and V. I. Vagitsev, “Localization of hidden Chua’s attractors,” *Physics Letters. A*, vol. 375, no. 23, pp. 2230–2233, 2011.
- [45] T. Kapitaniak and G. A. Leonov, “Multistability: uncovering hidden attractors,” *European Physical Journal: Special Topics*, vol. 224, no. 8, pp. 1405–1408, 2015.
- [46] D. Dudkowski, S. Jafari, T. Kapitaniak, N. V. Kuznetsov, G. A. Leonov, and A. Prasad, “Hidden attractors in dynamical systems,” *Physics Reports*, vol. 637, pp. 1–50, 2016.
- [47] G. A. Leonov, N. V. Kuznetsov, and V. I. Vagitsev, “Hidden attractor in smooth Chua systems,” *Physica D. Nonlinear Phenomena*, vol. 241, no. 18, pp. 1482–1486, 2012.
- [48] G. A. Leonov and N. V. Kuznetsov, “Hidden attractors in dynamical systems: From hidden oscillation in Hilbert-Kolmogorov, Aizerman and Kalman problems to hidden chaotic attractor in Chua circuits,” *International Journal of Bifurcation and Chaos in Applied Sciences and Engineering*, vol. 23, no. 1, Article ID 1330002, 69 pages, 2013.
- [49] G. A. Leonov, N. V. Kuznetsov, M. A. Kiseleva, E. P. Solovyeva, and A. M. Zaretskiy, “Hidden oscillations in mathematical model of drilling system actuated by induction motor with a wound rotor,” *Nonlinear Dynamics*, vol. 77, no. 1-2, pp. 277–288, 2014.
- [50] G. A. Leonov, N. V. Kuznetsov, and T. N. Mokaev, “Hidden attractor and homoclinic orbit in Lorenz-like system describing convective fluid motion in rotating cavity,” *Communications in Nonlinear Science and Numerical Simulation*, vol. 28, no. 1-3, pp. 166–174, 2015.
- [51] Q. Li, H. Zeng, and J. Li, “Hyperchaos in a 4D memristive circuit with infinitely many stable equilibria,” *Nonlinear Dynamics. An International Journal of Nonlinear Dynamics and Chaos in Engineering Systems*, vol. 79, no. 4, pp. 2295–2308, 2015.
- [52] S. Brezetskiy, D. Dudkowski, and T. Kapitaniak, “Rare and hidden attractors in Van der Pol-Duffing oscillators,” *The European Physical Journal Special Topics*, vol. 224, no. 8, pp. 1459–1467, 2015.
- [53] B. Munmuangsaen, J. C. Sprott, W. J. Thio, A. Buscarino, and L. Fortuna, “A simple chaotic flow with a continuously adjustable attractor dimension,” *International Journal of Bifurcation and Chaos in Applied Sciences and Engineering*, vol. 25, no. 12, Article ID 1530036, 2015.
- [54] C. Li, J. C. Sprott, Z. Yuan, and H. Li, “Constructing chaotic systems with total amplitude control,” *International Journal of Bifurcation and Chaos*, vol. 25, no. 10, Article ID 1530025, 2015.
- [55] A. Chudzik, P. Perlikowski, A. Stefanski, and T. Kapitaniak, “Multistability and rare attractors in van der pol-duffing oscillator,” *International Journal of Bifurcation and Chaos in Applied Sciences and Engineering*, vol. 21, no. 7, pp. 1907–1912, 2011.

- [56] P. R. Sharma, M. D. Shrimali, A. Prasad, N. V. Kuznetsov, and G. A. Leonov, "Control of multistability in hidden attractors," *European Physical Journal: Special Topics*, vol. 224, no. 8, pp. 1485–1491, 2015.
- [57] Z. T. Zhusubaliyev, E. Mosekilde, A. N. Churilov, and A. Medvedev, "Multistability and hidden attractors in an impulsive Goodwin oscillator with time delay," *European Physical Journal: Special Topics*, vol. 224, no. 8, pp. 1519–1539, 2015.
- [58] Z. T. Zhusubaliyev and E. Mosekilde, "Multistability and hidden attractors in a multilevel DC/DC converter," *Mathematics and Computers in Simulation*, vol. 109, pp. 32–45, 2015.
- [59] A. Wolf, J. B. Swift, H. L. Swinney, and J. A. Vastano, "Determining Lyapunov exponents from a time series," *Physica D: Nonlinear Phenomena*, vol. 16, no. 3, pp. 285–317, 1985.
- [60] N. V. Kuznetsov, "The Lyapunov dimension and its estimation via the Leonov method," *Physics Letters A*, vol. 380, no. 25–26, pp. 2142–2149, 2016.
- [61] N. V. Kuznetsov, T. A. Alexeeva, and G. A. Leonov, "Invariance of LYapunov exponents and LYapunov dimension for regular and irregular linearizations," *Nonlinear Dynamics. An International Journal of Nonlinear Dynamics and Chaos in Engineering Systems*, vol. 85, no. 1, pp. 195–201, 2016.
- [62] G. A. Leonov, N. V. Kuznetsov, N. A. Korzhemanova, and D. V. Kusakin, "Lyapunov dimension formula for the global attractor of the Lorenz system," *Communications in Nonlinear Science and Numerical Simulation*, vol. 41, pp. 84–103, 2016.
- [63] S. Banerjee, *Chaos Synchronization and Cryptography for Secure Communication*, IGI Global, Hershey, Pa, USA, 2010.
- [64] J. L. Mata-Machucaa, R. Martínez-Guerra, R. Aguilar-López, and C. Aguilar-Ibañez, "A chaotic system in synchronization and secure communications," *Communications in Nonlinear Science and Numerical Simulation*, vol. 17, no. 4, pp. 1706–1713, 2012.
- [65] C. K. Volos, I. M. Kyprianidis, and I. N. Stouboulos, "Image encryption process based on chaotic synchronization phenomena," *Signal Processing*, vol. 93, no. 5, pp. 1328–1340, 2013.
- [66] R. Aguilar-López, R. Martínez-Guerra, and C. A. Perez-Pinacho, "Nonlinear observer for synchronization of chaotic systems with application to secure data transmission," *The European Physical Journal Special Topics*, vol. 223, no. 8, pp. 1541–1548, 2014.
- [67] S. Çiçek, A. Ferikoğlu, and I. Pehlivan, "A new 3D chaotic system: dynamical analysis, electronic circuit design, active control synchronization and chaotic masking communication application," *Optik*, vol. 127, no. 8, pp. 4024–4030, 2016.
- [68] C. Hua and X. Guan, "Adaptive control for chaotic systems," *Chaos, Solitons & Fractals*, vol. 22, no. 1, pp. 55–60, 2004.
- [69] G. Feng and G. Chen, "Adaptive control of discrete-time chaotic systems: a fuzzy control approach," *Chaos, Solitons & Fractals*, vol. 23, no. 2, pp. 459–467, 2005.
- [70] S.-Y. Li, C.-H. Yang, C.-T. Lin, L.-W. Ko, and T.-T. Chiu, "Adaptive synchronization of chaotic systems with unknown parameters via new backstepping strategy," *Nonlinear Dynamics*, vol. 70, no. 3, pp. 2129–2143, 2012.
- [71] H. K. Khalil, *Nonlinear Systems*, Prentice Hall, Upper Saddle River, NJ, USA, 3rd edition, 2002.
- [72] M. s. Yalcin, J. A. Suykens, and J. Vandewalle, "True random bit generation from a double-scroll attractor," *IEEE Transactions on Circuits and Systems. I. Regular Papers*, vol. 51, no. 7, pp. 1395–1404, 2004.
- [73] G. Y. Wang, X. L. Bao, and Z. L. Wang, "Design and implementation of a new hyperchaotic system," *Chinese Physics B*, vol. 17, pp. 3596–3602, 2008.
- [74] C. K. Volos, I. M. Kyprianidis, and I. N. Stouboulos, "A chaotic path planning generator for autonomous mobile robots," *Robotics and Autonomous Systems*, vol. 60, no. 4, pp. 651–656, 2012.
- [75] D. Valli, B. Muthuswamy, S. Banerjee et al., "Synchronization in coupled Ikeda delay systems experimental observations using Field Programmable Gate Arrays," *The European Physical Journal Special Topics*, vol. 223, pp. 1465–1479, 2014.
- [76] A. Akgul, I. Moroz, I. Pehlivan, and S. Vaidyanathan, "A new four-scroll chaotic attractor and its engineering applications," *Optik*, vol. 127, no. 13, pp. 5491–5499, 2016.